Characterising the Post-Collision Tumbling Dynamics and Attitude Control Retrieval of Solar-Sails

Lorenz Alexander Vinzenz Veithen

TU Delft

Characterising the Post-Collision Tumbling Dynamics and Attitude Control Retrieval of Solar-Sails

by

Lorenz Alexander Vinzenz Veithen

A thesis submitted to the Delft University of Technology in partial fulfilment of the requirements for the degree of Master of Science in Aerospace Engineering

Thesis committee:

Chair:	Dr. W. van der Wal
Supervisors:	Dr. J. Heiligers
	Dr. O. Çelik
External examiner:	Dr. D. Dirkx

An electronic version of this thesis is available at `http://repository.tudelft.nl/`.

Faculty of Aerospace Engineering · Delft University of Technology

Preface

With this document, I close one of the most eventful chapters in my life. I cannot thank myself enough for having the guts to go abroad for my studies from an early age, I will forever be grateful for the five years I spent in Delft and the opportunities that they gave me both inside and outside the classroom. From ambitious student-led projects and research initiatives to collaborations with other institutions, what makes Delft so special are the projects available to students next their studies. These opportunities have taught my most valuable lesson yet, that with patience and dedication, one's wildest ambitions are within reach.

However, all of this would never have been possible without the help of the many people part of my inner circle. Starting with my parents who have always believed in my capabilities and supported me in my adventures, Nanie without whom I would probably still be struggling with basic arithmetic, Nono for always making sure that I would not burn-out, my sister for making sure that my ego does not inflate too much, and my amazing girlfriend Alicia for always cheering me up and having supported me for all these years. To all of you, I want to say one word: Merci. I would also want to thank all the friends I made along the way in Delft, Lausanne, and Munich, but I would rather not turn this text into a bulleted-list, you will recognise yourself.

Last but certainly not least, I also want to extend my gratitude to both my supervisors, Jeannette Heiligers and Onur Çelik, without whom this research would have been much less glorious. Your feedback throughout the project has been invaluable.

Lorenz Veithen

Delft, August 2024

Contents

Nomenclature

List of Abbreviations

ACS Attitude Control System

ACS3 Advanced Composite Solar-Sail System (ACS3)

ADR Active Debris Removal

AEP Artificial Equilibrium Points

AoA Angle of Attack

AoP Argument of Pericenter

CoM Centre of Mass

CoP Centre of Pressure

DAS Debris Assessment Software

DCAM Deployable Camera

DCAM Differential Dynamic Programming

DoF Degree of Freedom

DRAMA Debris Risk Assessment and Mitigation Analysis

ECEF Earth-Centered Earth-Fixed

ECI Earth-Centered Inertial

EGO Extended Geostationary Orbit

EISCAT European Incoherent Scatter Radar

EoL End of Life

EoM Equation of Motion

ESA European Space Agency

ESO Escape Orbits

GDP Gross Domestic Product

GEO Geostationary Orbit

GHO GEO-superGEO Crossing Orbits

GNSS Global Navigation Satellite Systems

GSM Generalised Sail Model

GTO GEO Transfer Orbit

HAO High Altitude Earth Orbit

HEO Highly Eccentric Earth Orbit

HNKO Highly Non-Keplerian Orbits

HVI HyperVelocity Impact

I-SRP Ideal Solar Radiation Pressure model

IADC Inter-Agency Space Debris Coordination Committee

IGO Inclined Geosynchronous Orbit

IKAROS Interplanetary Kite-craft Accelerated by Radiation Of the Sun

JAXA Japan Aerospace Exploration Agency

JPL Jet Propulsion Laboratory

LAGEOS Laser Geodynamics Satellites

LEGEND LEO-to-GEO Environment Debris

LEO Low Earth Orbit

LMO LEO-MEO Crossing Orbits

LTE Local Truncation Error

MASTER Meteoroid And Space debris Terrestrial Environment Reference

MEE Modified Equinoctial Elements

MEO Medium Earth Orbit

MGO MEO-GEO Crossing Orbits

MMI Mass Moment of Inertia

MODs Meteoroids and Orbital Debris

N-M Nelder-Mead

N/A Not Applicable

NASA National Aeronautics and Space Administration

NSO Navigation Satellites Orbit

O-SRP Optical Solar Radiation Pressure model

ORDEM Orbital Debris Engineering Model

ORSAT Object Reentry Survival Analysis Tool

PPT Pulse Plasma Thruster

PRP Planetary Radiation Pressure

R&D Research and Development

RAAN Right Ascension of Ascending Node

RADAR RAdio Detection And Ranging

RCD Reflectivity Control Device

RKF Runge-Kutta-Fehlberg

RTN Radial, Transverse, and Normal

SBS Sail-Boom Subsystem

SCARAB Spacecraft Atmospheric Reentry and Aerothermal Breakup

SDT Space Debris Telescope

SRP Solar Radiation Pressure

SSB Solar System Barycenter

SSBM NASA Satellite Standard Breakup Model

SSO Sun-Synchronous Orbit

TIRA Tracking and Imaging Radar

TUDAT TU Delft Astrodynamics Toolbox

UFO Undefined Orbit

USA United States of America

WBS Work Breakdown Structure

List of Roman Symbols

$\hat{\boldsymbol{N}}$ Normal unit vector of the RTN frame [-]

$\hat{\boldsymbol{R}}$ Radial unit vector of the RTN frame

$\hat{\boldsymbol{T}}$ Tangential unit vector of the RTN frame [-]

$\tilde{\boldsymbol{T}}$ Non-dimensional torque [-]

$\boldsymbol{a}$ Acceleration vector [m/s/s]

$\boldsymbol{b}_{\mathcal{BI}_{\oplus}}$ Rotation matrix from the inertial to the body-fixed frame [-]

$\boldsymbol{F}$ Force vector [N]

$\boldsymbol{f}$ Force vector exerted by a single reflective surface

$\boldsymbol{F}_{\alpha,\zeta,\rho}$ Force vectors relative to absorption, transmission, and reflection of photons [N]

$\boldsymbol{G}$ Resultant torque in the torque allocation optimization [Nm]

$\boldsymbol{g}$ Torque of a vane in the torque allocation optimization [Nm]

$\boldsymbol{I}$ Identity matrix [-]

$\boldsymbol{I}_{\mathcal{B}}$ Inertia tensor [kg m^2]

$\boldsymbol{n}$ Surface normal direction vector of a given surface [-]

$\boldsymbol{n}_s$ Sunlight direction vector [-]

$\boldsymbol{p}$ Linear momentum vector [kg m /s]

$\boldsymbol{q}$ Quaternion elements vector [-]

$\boldsymbol{r}$ Position vector [m]

$\boldsymbol{r}_{\odot}$ Position vector of the spacecraft with respect to the Sun's centre of mass [km]

$\boldsymbol{r}_p$ Position vector of a hypervelocity impact [m]

$\boldsymbol{r}_{v_0}$ Default vane centroid position vector [m]

$\boldsymbol{r}_{v_1}$ Rotated vane centroid position vector [m]

$\boldsymbol{R}_x, \boldsymbol{R}_y, \boldsymbol{R}_z$ Euler rotation matrices

$\boldsymbol{T}$ Torque vector [Nm]

$\boldsymbol{v}$ Velocity vector [m/s]

$\boldsymbol{X}$ State vector

$\boldsymbol{y}$ Directional effective area [m^2]

$\mathcal{G}$ 1x12 vector of variables of the torque allocation optimization [Nm]

$\tilde{s}_x$ Non-dimensional spline in the $\tilde{T}_{x,\mathcal{B}} - \tilde{T}_{z,\mathcal{B}}$ plane

$\tilde{s}_y$ Non-dimensional spline in the $\tilde{T}_{y,\mathcal{B}} - \tilde{T}_{z,\mathcal{B}}$ plane

A Spacecraft cross-sectional area in the direction of flight [m^2]

a Semi-major axis [m]

a_0 Characteristic acceleration [m/s/s]

A_h	Hole area [m^2]
a_p	Ellipse semi-major axis [-]
A_{SRP}	Surface area on which the Solar Radiation Pressure is acting [m^2]
B	Lambertian coefficient [-]
c	Speed of light in vacuum [m/s]
C_R	Reflection coefficient [-]
d	Diameter [m]
d_p	Projectile diameter [m]
E	Total or relativistic energy [J]
e	Eccentricity [-]
f	Modified Equinoctial Element [-]
g	Modified Equinoctial Element [-]
h	Modified Equinoctial Element [-]
I	Parameter of the MEE translational dynamics equations [-]
i	Inclination [deg]
I_{sp}	Specific impulse [s]
k	Modified Equinoctial Element [-]
L	True longitude [deg]
$L_\odot$	Sun's luminosity [W]
l_c	Average geometrical length of a debris [m]
l_v	Side length of the vanes [m]
$l_{x,y,z}$	X-Y-Z geometric length of a debris [m]
M	Mean anomaly [deg]
m	Spacecraft mass [kg]
m_0	Rest mass [kg]
m_r	Relativistic mass [kg]
m_{s_i}	The ith moving mass of a sliding mass system[kg]
n	Orbital mean motion [rad/s]
$N_{>l_c}$	Number of fragments generated per size [-]
N_d	Number of fragments in Earth orbit [-]
O	Reference frame origin [-]
P	Solar Radiation Pressure [N/m^2]
p	Semi-latus rectum [km]
P_{max}	Maximum achievable Solar Radiation Pressure at a given distance from the Sun [N/m^2]
q_i	The ith quaternion element (i=1,2,3,4) [-]
$r_\odot$	Distance to the Sun's centre of mass [km]
r_ξ	Scalar factor defining the vane sigmoid transition [-]
r_a	Apocenter radius [km]
R_E	Earth equatorial radius [km]
R_J	Jupiter equatorial radius [km]
r_p	Pericenter radius [km]
R_V	Venus equatorial radius [km]
S	Area [m^2]
S	Surface [m^2]
s	Substituting element in MEE translational equations of motion [-]
S_{ellipse}	Ellipse area [m^2]
T	Period [s]
t	Time [s]
t	Time variable [s]
T_ω	Period of attitude motion [s]
T_{eq}	Equilibrium temperature [K]
t_{max}	Material maximum penetrated thickness [m]
t_t	Target thickness [m]
U	Gravitational potential [J/kg]
u	Set element [-]
v	Moving speed [m/s]
V_I	Impact velocity [km/s]
v_s	Threshold spallation velocity of an HVI [m/s]
v_z	Transition velocity of an HVI [m/s]

W	Radiative flux [W/m^2]
w	Substituting element in MEE translational equations of motion [-]
$W_{incident}$	Incident radiative flux [W/m^2]
X	A set [-]
x	A subset [-]

List of Greek Symbols

α	Absorption optical coefficient of a given material [-]
α_s	Sun cone angle [deg]
β	Solar sail lightness number [-]
β_E	Momentum enhancement factor [-]
β_s	Sun clock angle [deg]
$\boldsymbol{\Delta p}$	Linear momentum transferred to a target body [kg m / s]
$\hat{\boldsymbol{\omega}}_{\mathcal{B}}$	Rotational velocity vector direction [-]
$\boldsymbol{\omega}_{\mathcal{B}}$	Rotational velocity vector between the body-fixed and inertial frames, expressed in the body-fixed frame [rad/s]
$\boldsymbol{\tau}$	Torque vector exerted by a single reflective surface [Nm]
ΔS	Area difference [m^2]
$\Delta t_{detumbling}$	Detumbling time [s]
ΔV	Velocity increment [m/s]
$\Delta_{r,t,n}$	Perturbing accelerations in the RTN frame [m/s/s]
ϵ	Emissivity [-]
η	Efficiency fractor [-]
γ	Steepness parameter of the sigmoid transition between two vane angles [-]
κ	Scaling factor [-]
λ_i	Scaling factor [-]
λ_v	Vane inner angle [deg]
μ	Gravitational parameter [m^3/s^2]
Ω	Right Ascension of Ascending Node [deg]
ω	Argument of pericenter [deg]
ϕ_g	Second rotational degree of freedom of the gimball mass [deg]
ϕ_p	Projectile azymuth angle [deg]
ϕ_v	Second rotational degree of freedom of the vanes [deg]
ρ	Reflection optical property of a given material [-]
ρ_d	Diffuse reflection optical property of a given material [-]
ρ_s	Specular reflection optical property of a given material [-]
σ	Standard deviation
σ_{sail}	Sail loading [kg/m^2]
σ_{SB}	Stefan-Boltzmann constant [W/(m^2 K^4)]
τ	Orbital lifetime [years]
θ	Angle between the surface normal of a given surface and the sunlight vector in the body-fixed frame [deg]
θ	True anomaly [deg]
θ_g	First rotational degree of freedom of the gimball mass [deg]
θ_p	Projectile zenith angle [deg]
θ_s	Angle between a surface normal of a reflective surface and the sunlight vector [deg]
θ_v	First rotational degree of freedom of the vanes [deg]
$\theta_{z,\mathcal{B}}$	Angle of rotation around the $Z_{\mathcal{B}}$ [deg]
ξ	A vane angle [deg]
ζ	Transmission optical property of a given material [-]

List of Subscripts

0	Initial
$\mathcal{B}$	Body-fixed reference frame
$\mathcal{I}_{\odot}$	Sun-Centred Inertial reference frame
$\mathcal{I}_{\oplus}$	Earth-Centred Inertial reference frame

$\mathcal{R}$	Earth-Centred Earth-Fixed reference frame
$\mathcal{S}$	Radial, Transverse, and Normal reference frame
$\mathcal{V}$	Vane reference frame
$\odot$	Sun
$\oplus$	Earth
DT	Detumbling
eff	Effective
fin	Final
Gyro	Gyroscopic
LTT	Long-Term Tumbling
pr	Previous iteration
rel	Relative
tb	Third body
tr	Truncated
b	Back surface
CG	Center of gravity
ch	Convex hull
d	Desired
e	Ejecta
f	Front surface
g	Gymball mass
h	Hole
I	Impact
i	The ith element
p	Projectile
r	Relativistic
s	Associated with the Sun
SRP	Solar Radiation Pressure
t	Target
v	Vane
w	Wing

List of Superscripts

$*$	Optimal
i	Vane or wing index

List of Figures

List of Tables

Summary

With the steadily increasing number of artificial objects in Earth orbit, the Low Earth Orbit (LEO) and geostationary orbit (GEO) protected regions have become hostile environments to modern satellites. These numerous objects also increase the likelihood of the onset of a self-sustaining collisional cascading process once the number of objects reaches a critical threshold, called the Kessler syndrome. Such process would result in the denial of access to key orbital regions. To delay the onset of the Kessler syndrome, Active Debris Removal (ADR) missions have been proposed to remove large defunct satellites from orbit. One promising ADR method makes use of solar-sails, which leverage the momentum of photons to generate a thrust force. This property makes them particularly attractive for long-term missions, especially if they make use of propellantless Attitude Control Systems (ACS). A particularly attractive ACS makes use of four actuated tip-vanes with two degrees of freedom each to orient the sail using the Solar Radiation Pressure (SRP) force. However, solar-sails have a large surface area, making them particularly vulnerable to HyperVelocity impacts (HVI) with space debris, which can result in a significant momentum transfer upon collision with a supporting boom. This momentum transfer could then result in a loss of attitude control, which is directly linked to the sail orbital dynamics.

This thesis therefore investigates the effect of tumbling dynamics on the sail coupled attitude-orbit dynamics, and assesses the capabilities of a state-of-the-art vane-based attitude controller to recover the attitude control of the sail. Particular focus is placed on studying the sensitivity of the results with respect to the sailcraft reflective properties, orbital regime, and the number of degrees-of-freedom of each vane. The reference sail model and orbit used throughout the work are inspired from the Advanced Composite Solar-Sail System (ACS3) mission.

The sail dynamics are modelled through the coupled attitude-orbit equations of motions, in a central gravity field including the SRP perturbing acceleration and torque. However, the gravity gradient torque is neglected. The sail is assumed to be in its fully deployed state and is assumed to be a constant mass rigid body with flat reflective surfaces. Therefore, the sail structural dynamics are neglected. The main sail reflective surfaces have fixed positions in the body-fixed frame, but the vanes can rotate along two degrees-of-freedom (DoF). Additionally, a vane system controller aiming to time-optimally stabilise the attitude motion of the sailcraft is designed with a particular focus on the computational efficiency. This thesis extended the capabilities of such controller from previous literature to include non-ideal reflectance models of the vanes, a self-shadowing constraint, and variations in the number of degrees-of-freedom of each vane. The TU Delft Astrodynamics Toolbox is used to develop this numerical simulation.

The analysis of the long-term tumbling dynamics of the sail was performed by considering rotational velocities in the sail plane up to 15 deg/s in magnitude and assessing the deviations from the nominal orbit after 30 days. The tumbling dynamics resulted in an eccentricity growth which is slower than the growth which would be experienced by a continuously Sun-pointing spacecraft. Therefore, the overall effect of the tumbling motion is to reduce the effect of the SRP perturbing acceleration on the sailcraft orbit, compared to a continuously Sun-pointing sailcraft. This reduction is independent of the rotational velocity magnitude (under the assumption that the attitude motion is significantly faster than the orbital motion), but long-term effects depend on the tumbling axis direction in the sail body-fixed frame. Over long periods of time, this eccentricity growth could result in a re-entry of the sailcraft if it is in a low orbit. Sensitivity studies revealed that larger deviations from the initial orbit are experienced at higher orbital altitudes and in orbits with a smaller eclipse fraction. Additionally, sails with more efficient reflective properties result in larger deviations. On the short-term, the overall effect of the tumbling dynamics can be modelled as a Sun-pointing sailcraft with a sail area reduced by 57.56% ($\approx 1 - \frac{4}{3\pi}$) and the same spacecraft mass. On the long-term, the movement of the Earth around the Sun causes a rotation of the local sunlight direction, which changes the direction of the tumbling axis with respect to the local sunlight, resulting in deviations from this simplified model.

The analysis of the detumbling performance of the sail considered combinations of one-, two-, and three-axis tumbling scenarios (in the body-fixed frame) up to 15 deg/s. Additionally, three-axis tumbling

scenarios up to 100 deg/s were considered over their first six orbits to determine the maximum rotational velocity which can be handled by the vane controller. A vane system composed of four actuated tip-vanes with two rotational DoF demonstrated that it can detumble the sailcraft from initial rotational velocities up to 26 deg/s using ideally reflective vanes, and 20 deg/s for vanes with the reflective properties of the ACS3 sail material. For rotational velocity magnitudes below 8 deg/s, the vane system is capable of stabilising the sailcraft at a rate of 2 deg/s per day with ideally reflective vanes and 1.3 deg/s with vanes made of the ACS3 sail material. For higher rotational velocities, the detumbling time grows non-linearly. Furthermore, tumbling scenarios with a rotational velocity vector in the sail plane were found to be the most challenging to stabilise due to the coupling between the $X_{\mathcal{B}}$ and $Y_{\mathcal{B}}$ rotational velocity components in the body-fixed frame. This coupling results in a quickly changing direction of the optimal detumbling torque, which is difficult to follow for the ACS. At last, the system is found to be robust to the failure of a single vane and to environmental effects, with the eclipse time being the only environmental aspect affecting the system performance, resulting in a down-time.

The results from the analysis of the detumbling performance were linked to the momentum transfer which could result from a hypervelocity impact. The vane system can stabilise a sailcraft after a hypervelocity impact with a projectile linear momentum up to 0.13 kgm/s. Particularly, head-on collisions result in the largest attitude disturbance and yield rotational velocities in the sail plane, which are the most difficult to detumble. In general, collisions with aluminium debris with a diameter larger than 5 mm would result in a tumbling motion which cannot be handled by the vane system. However, only 0.001% of the impactors in the orbital region of the ACS3 mission target orbit are expected to be larger than 1 mm.

1

Introduction

Since the early days of the space age, human reliance on space activities has tremendously increased, ranging from climate change monitoring to television. However, these technological advancements have come at the cost of the increasing number of objects in Earth orbit, contributing to a congested environment prone to the onset of a self-sustaining collisional cascading process called the Kessler syndrome [1]. This syndrome poses a major threat to the access to protected orbital regimes such as the Low Earth Orbit and the Geostationary orbit.

It has now become clear that space debris removal missions are necessary to prevent the onset of the Kessler syndrome. Solar sailing is a promising propellant-free propulsion method which generates a thrust force by interacting with the photons reaching the sail, thereby providing a continuous acceleration which is not bound to any on-board reaction mass. This latter characteristic makes solar sails particularly attractive for long-term missions, such as the removal of multiple defunct satellites with a single sailcraft. However, using solar sails for a space debris removal mission would involve a long-term presence in a debris rich environments which are particularly dangerous to solar sails due to their large surface area, making them prone to high-energy impacts with micrometeoroids and space debris.

As the survivability of a sailcraft in such environments has not been considered in details by the literature, this thesis will consider the global topic of solar sails in a debris rich environment. A specific research objective and the associated research questions will be formulated based on a review of the literature. The structure of this thesis is as follows. First, Chapter 2 presents an extensive literature review considering the fields of space debris, solar sails, and hypervelocity impacts, and concludes with the research questions addressed in this thesis. Then, Chapter 3 gives an overview of the methods used throughout this work. Second, a research paper describing the specific methodology developed for, and the results produced by this work, is given in Part II. At last, Chapter 4 provides some final conclusions and recommendations, as well as answers to the research questions.

Part I

Background Information

2

Literature Review

This chapter presents a brief review of literature to determine the research questions and objectives of this work. First, a global overview of the current space debris problematic is given in Section 2.1, diving into the current challenges and proposed methods to tackle the crisis. Second, the state of solar-sail technology is presented in Section 2.2 with a focus on Solar Radiation Pressure models, attitude control, and sailcraft trajectories. Third, Section 2.3 describes aspects of on-orbit hypervelocity impact literature. At last, the research questions and objectives of the thesis are given in Section 2.4.

2.1. Space Debris Problematic

Since the launch of Sputnik 1 in 1957 [2], mankind's dependence on space activities has steadily grown. Ranging from global communication to Global Navigation Satellite Systems (GNSS), disaster early warning systems, and climate-change monitoring, space technologies have shaped humankind significantly [3]. However, while Sputnik 1 remained in orbit for three months, Vanguard 1, launched by the United States of America (USA) in 1958, will remain in Medium-Earth Orbit (MEO) for the next 200 years despite having been inactive since 1964 [4]. Since Vanguard 1, thousands of inactive satellites and rocket upper stages have been added to the list of orbital debris.

However, uncontrollable objects remaining in Earth orbit only form part of the problem. In 1978, Kessler and Cour-Palais [1] theorised the onset of on-orbit collisions between uncontrollable objects in Earth orbit. Satellite collisions produce numerous smaller debris which can in turn collide with other large satellites, thereby creating more debris, and so on [1]. When the number of objects in the considered orbital region is sufficiently high, a self-sustaining collisional cascading process could take place [5]. This phenomenon, called the Kessler syndrome, poses a significant threat to space activities in Earth orbit through the creation of a fatal debris cloud for all upcoming missions. This problem is intensified by the recent trends of the NewSpace, with thousands of satellites launched to form mega-constellations in Low Earth Orbit (LEO) [6]. Additionally, thousands of debris are also created from other space events such as explosions or anti-satellite weapon tests [7, 8]. Kessler and Cour-Palais [1] predicted that satellite collisions would become a new source of space debris by the year 2000, however, this process started as early as 1991 with a collision between a Cosmos satellite and a mission-related debris [9]. Since then, numerous other collisions occurred, including the Cosmos-Iridium collision in 2009, which is the first collision between two intact spacecraft [8].

To delay the onset of the Kessler syndrome, the European Space Agency (ESA) has implemented guidelines applicable to future Earth-orbit missions to mitigate the production of space debris. At the end of 2023, ESA published the Zero Debris Approach and related charter [10], adding and revising key requirements to the Space Debris Mitigation Requirements list. The most important of these are listed as[1]:

1. The duration of the disposal phase in low-Earth orbit has been reduced from 25-year to a maximum of five years, with an additional consideration for the mission's total collision risk with space debris during this disposal phase, and more stringent requirements for satellite constellations.
2. The probability of successful disposal must be larger than 90%, with more stringent requirements for large constellations.

[1] URL: `https://esoc.esa.int/new-space-debris-mitigation-policy-and-requirements-effect`. Accessed online on 17/02/2024.

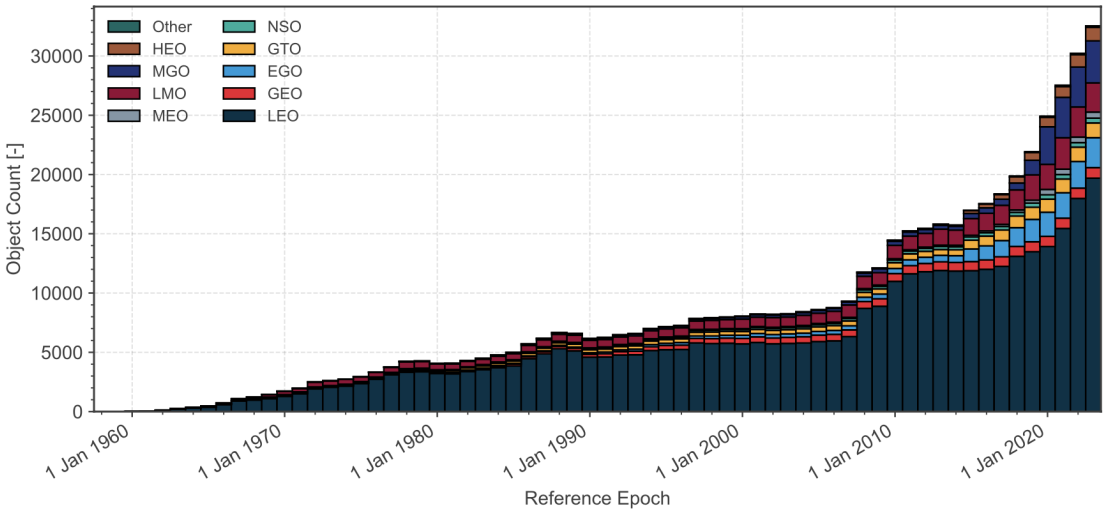

Figure 2.1: Evolution of the number of objects catalogued in all orbits by orbital regime. Please consult the list of abbreviations for the abbreviations definitions [11].

3. Space objects operating in protected orbital regions, which are not considered to be “low risk”, must be equipped with interfaces to facilitate servicing by an active debris removal mission in case they fail in orbit.
4. Introduction of a new set of requirements related to collision avoidance and space traffic coordination based on current best practices, such as response time in case of a collision warning;
5. Introduction of preliminary requirements on the emerging issues of avoiding the generation of space debris in lunar orbits and limiting interferences with radio and optical astronomy.

However, these debris mitigation guidelines only partially contribute to a solution for the space debris crisis. Even if all launches were to be stopped as of 2024, the Kessler syndrome would continue to develop and the cascading effect would end up denying access to some orbital regions [11]. This justifies the need for debris removal missions seeking to de-orbit (or place in dedicated graveyard orbits) satellites which did not have a sustainable End of Life (EoL) strategy.

In the following, an overview of the space debris literature is given. First, the current state of the debris environment and its projections are described in Section 2.1.1. This is followed by a discussion of the state of the art of space debris environment modelling in Section 2.1.2 including topics on orbital decay, breakup modelling, debris spread, and how these aspects are blended together to present assessments of the current environment and generate reliable projections on its trend. At last, Section 2.1.3 will describe methods and guidelines aiming to remediate the space debris crisis in the future.

2.1.1. Background and Trends

Each year, the European Space Agency publishes the Space Environment Report, which gives an up-to-date description of the space debris environment and recent trends [11]. The information given in this subsection is derived from the September 2023 version of this report (issue 7, revision 1), unless stated otherwise.

Figure 2.1 shows an overview of the number of catalogued objects, differentiated by their orbital regime, over time. From this figure, it appears that the number of catalogued objects is steadily increasing over time for all orbital regions, with the majority of the objects present in LEO. However, the object counts recorded are likely underestimated due to the limited capabilities of the space surveillance system to detect and track objects, despite the continuous improvements in sensor performances. Following, Figure 2.2 shows the evolution of the launch traffic in LEO and the Geostationary Orbit (GEO) for different funding types. From that figure, it appears that the launch activity in LEO has boomed in the late 2010s due to the commercial sector (Figure 2.2a), while the number of launches to GEO has levelled-off around 25-30 objects per year (Figure 2.2b). By comparing Figures 2.1 and 2.2, it can be concluded that the recent rapid growth in the number of catalogued objects is likely a result of the launch activity in LEO. The latter has

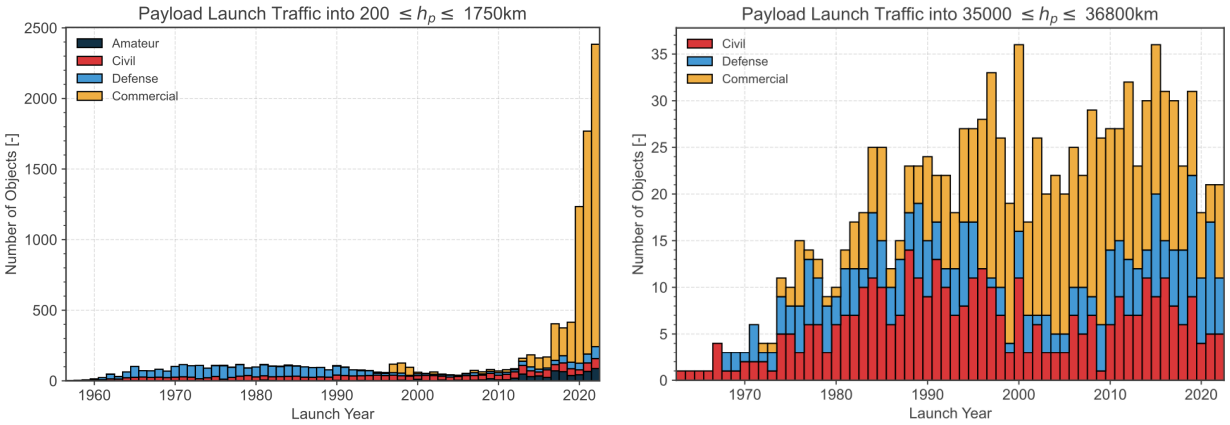

(a) Evolution of the launch traffic in Low Earth Orbit per funding type.

(b) Evolution of the launch traffic in geostationary orbit per funding type.

Figure 2.2: Evolution of launches in Low Earth Orbit and geostationary orbit [11].

greatly increased as a result of the deployment of mega-constellations such as Starlink and OneWeb from 2019 onwards [12], which is also seen in Figure 2.1 from the rapid evolution after 2019.

The steep increase in (uncontrollable) man-made objects in LEO strongly increases the risk of collisions where spacecraft are broken up in several smaller pieces, contributing to the cascading effect described by Kessler and Cour-Palais [1]. Combining the effects of accidental collisions to the fragmentation events arising from explosions and intended collisions, the protected LEO region has become dangerous to operational satellites, and collision avoidance manoeuvres have become common practice. As an example, the International Space Station (ISS) had to perform 37 manoeuvres to avoid catalogued debris since 1999, with seven in 2022 and 2023 alone [13]. Despite, the natural cleaning mechanism resulting from the atmospheric drag slowing down spacecraft below 600 km altitude within 25-year, debris mitigation guidelines are necessary to limit the number of objects in LEO [11]. Figures 2.3a and 2.3b show the share of payload and rocket body clearance compliance to the previous 25-year guideline as a function of the EoL year. Particularly considering the successful attempts to comply to the guideline, it appears that an increasingly greater share of missions take actions to limit debris generation. Furthermore, the aforementioned natural cleaning process is not present at GEO altitudes, meaning that the launch traffic shown in Figure 2.2b adds up over time. The Geostationary Orbit has therefore been recognised as a limited natural resource, and a dedicated graveyard orbit where satellites reaching their EoL shall be moved to was defined [14]. Figure 2.3c shows the share of payload clearance compliance as a function of the EoL year, illustrating that while a greater share of missions successfully attempt disposal actions in GEO, early missions did not follow these disposal guidelines and remain in the crowded space to this date. This observation is further supported by Figure 2.3d, which shows the share of rocket-body clearance from GEO and LEO for launches to GEO as a function of the launch year. In this figure, it appears that an increasingly larger share of rocket bodies are cleared from the protected regions, and the share of GEO crossing objects has steadily declined. Overall, Figure 2.3 indicates that the threat of the Kessler syndrome and the associated debris mitigation guidelines have had a clear effect on the space market.

The predicted evolution of the number of objects larger than 1 cm in LEO and of the number of catastrophic collisions in Earth orbit, are given in Figures 2.4a and 2.4b respectively. Both figures display a case without further launches in grey and an extrapolation of the current launch traffic trends in red, showing that both the number of objects and the number of catastrophic collisions will increase over the next 200 years for both scenarios. From these figures, it can then be concluded that even if all launches had ceased as of 2023 onwards, the cascading catastrophic collisions in LEO would continue and the number of objects larger than 1 cm would grow steadily, meaning that the Kessler syndrome has already started. However, this growth of the debris population in LEO would be much worse if the current trends were to continue as is. These conclusions are further supported by Figure 2.5, which shows the absolute and relative number of fragmentation events per event cause through the years. From Figure 2.5b particularly, it appears that the collisions are becoming a significant cause of fragmentation events, as predicted by

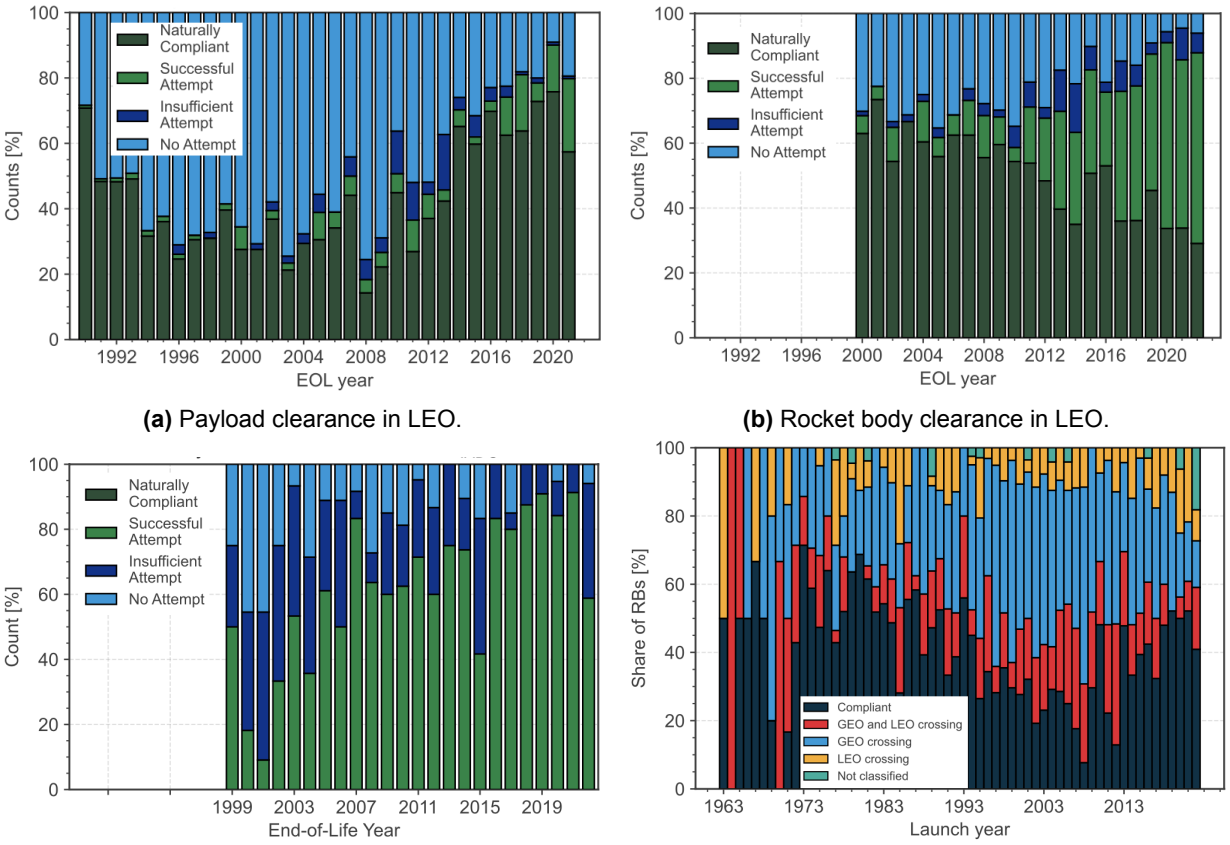

(a) Payload clearance in LEO.

(b) Rocket body clearance in LEO.

(c) Payload clearance in GEO.

(d) Rocket body clearance in GEO.

Figure 2.3: Compliance of payloads and rocket bodies in protected regions (Low Earth Orbit and geostationary ring) according to the previous 25-year guideline [11].

Kessler and Cour-Palais [1], although significantly accelerated in comparison to the original prediction due to the recent boom in launch traffic. These collisions can be classified into three types [5]:

1. **Negligible non-catastrophic**: collisions which only produce few debris, such as with a thin surface (such as a solar-sail membrane). The mass of debris generated is then limited by the mass of the colliding fragment.
2. **Non-catastrophic**: collisions contributing to the short-term evolution of the environment only, generally between a fragment and an intact object. The generated debris are too small to be catalogued and to contribute to the long-term collisional cascading as they are unlikely to cause a catastrophic breakup upon collision with another target mass of a similar size, but pose a significant threat to operational satellites on the short-term.
3. **Catastrophic**: collisions contributing to both the short-term and long-term evolution of the environment by producing populations of smaller and larger debris. About 40 Joules per gram of target mass are necessary for such a fragmentation event to occur [15], which is equivalent to a 1.6 g debris colliding with a 1U CubeSat at 10 km/s. However, note that this number was derived from experiments, rather than physics contrary to what is implied in most literature [16]. Additionally, catastrophic collisions produce 90 to 100 fragments, which are able to catastrophically break up a target mass of the same size.

However, the number of objects reported in Figure 2.1 is also a reflection of the limited debris detection and tracking capabilities, meaning that a great number of small debris is not catalogued and models are necessary to estimate the debris flux for a given orbit. This was achieved with ESA's Meteoroid And Space debris Terrestrial Environment Reference (MASTER-8) software [17], and reported in [11]. Figure 2.6a shows some results from the MASTER-8 debris environment model, with Figure 2.6a giving the estimated number of space debris objects in Earth orbit as a function of their size, and Figure 2.6b giving the spatial

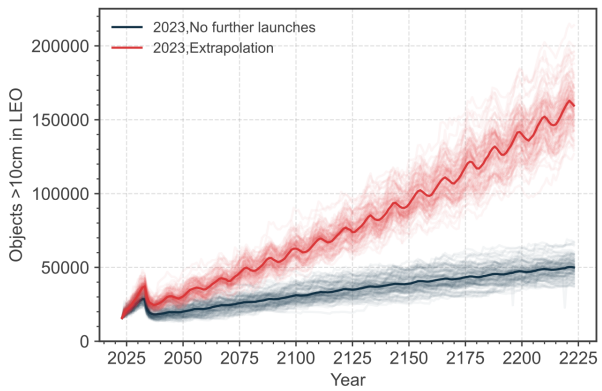

(a) Evolution of the number of objects larger than 1 cm in Low Earth Orbit.

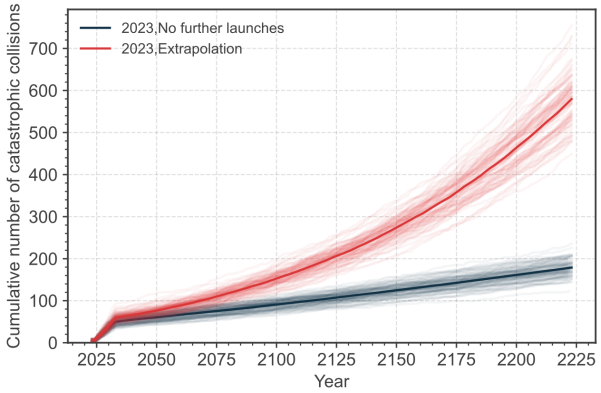

(b) Cumulative number of catastrophic collisions.

Figure 2.4: Evolution of the debris environment by extrapolation of current trends and in case launches had ceased completely as of the first of January 2023 [11].

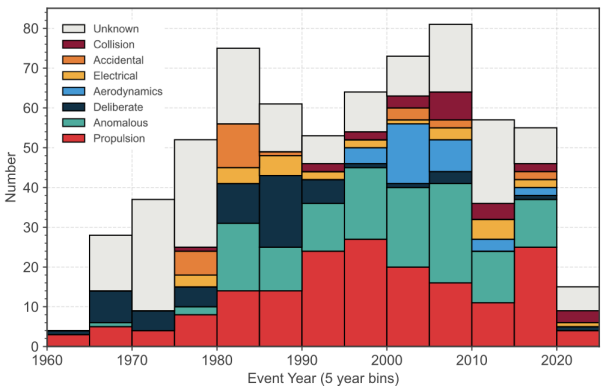

(a) Absolute number of fragmentation events per event cause.

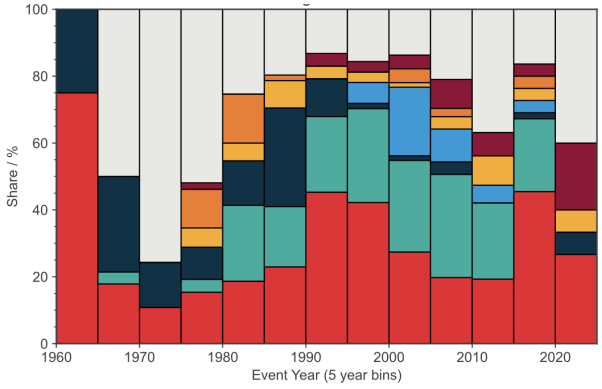

(b) Relative number of fragmentation events per event cause.

Figure 2.5: Historical trend of fragmentation event per cause [11]. Note that the 2020-2025 bin is not complete.

density of 1 cm and 10 cm debris as a function of the orbital altitude in LEO. From these figures, it can be observed that smaller debris dominate the space environment. Furthermore, 1-10 cm debris are the most harmful to operational spacecraft due to their low detectability but very high kinetic energy [18]. While, shielding, although expensive, can be sufficient to protect spacecraft from debris below 1 cm [19], it is insufficient for larger debris. Further considering the spatial density of objects in LEO through Figure 2.6b, it appears that the debris flux is much smaller at low altitudes, due to the thicker atmosphere as a result of the aforementioned cleaning mechanism. This results in the majority of the debris being present between 500 and 1000 km altitude.

Overall, it is obvious that the Kessler syndrome is still a large threat to space activities, and that the slow cascading process might have already started. The majority of payloads and rocket bodies in LEO and GEO at least attempt to comply with the debris mitigation guidelines, with a significant success rate (with respect to the recently updated 25-year standard). However, even with 100% compliance to the new five years guideline for all future launches, the onset of the Kessler syndrome will continue (see Figure 2.4b). Furthermore, based on Figure 2.4, ESA[2] states that limiting the number of launches is neither feasible (due to the mandating difficulty) nor helpful (as the number of debris will still steadily increase). Kessler et al. [5] therefore emphasised the need for Active Debris Removal (ADR) missions which target selected defunct satellites based on their collision likelihood.

[2]URL: `https://www.esa.int/Space_Safety/Space_Debris/Active_debris_removal`. Accessed online on 20/02/2024.

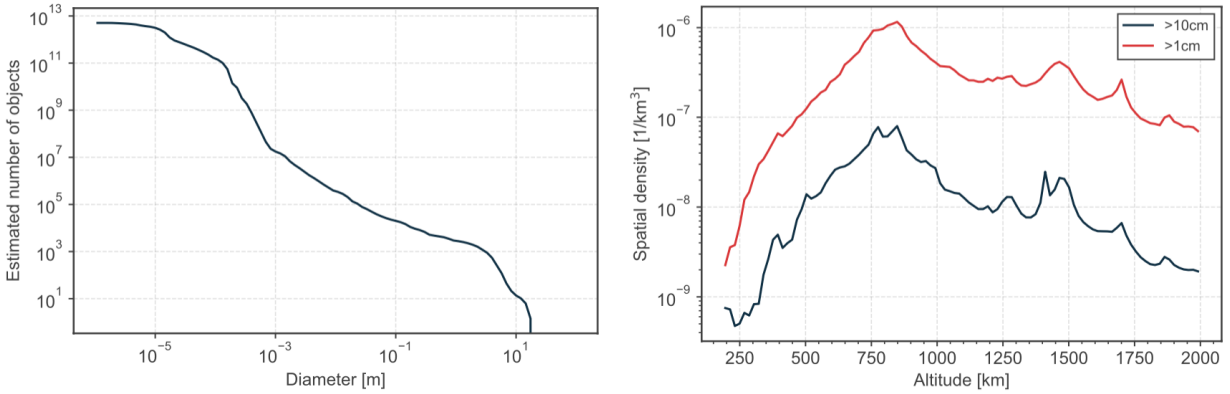

(a) Estimated number of space debris objects as function of the object size in Earth orbit.

(b) Density profiles in LEO for different space debris size ranges.

Figure 2.6: Non-catalogued and modelled objects following the MASTER space debris environment model from ESA [17, 11].

Furthermore, the Kessler syndrome is a major threat to the world economy, with a 1.95% projected negative damage to the global Gross Domestic Product (GDP) [20]. As ADR is the only feasible approach to prevent it on long-term, space debris monitoring and removal has been classified as an emerging space market [21]. Despite the lack of clear economic incentives, a number of companies and space agencies have launched ADR development programs focusing primarily on large defunct satellites. However, while some demonstrator missions have been successful [22, 23, 24], no large scale mission has yet been launched and Research & Development (R&D) programs continue to this day with missions such as Clear Space 1 [25, 25].

2.1.2. Debris Field Models

Accurate modelling of the space debris environment is fundamental to better assess appropriate adaption and mitigation approaches. To this end, a number of aspects are reviewed in the following. First, general indications on the rate of orbital decay are given in Section 2.1.2.1. Section 2.1.2.2 then describes key elements of breakup models for both high- and low-velocity impacts. Subsequently, the debris spread as a result of an on-orbit catastrophic event is described in Section 2.1.2.3. At last, models of the current debris population and methods to estimate the current and future risks of collision are presented in Section 2.1.2.4.

2.1.2.1. Orbital Decay

Orbital decay is a direct result of the interaction of the spacecraft with the Earth's atmosphere. For an eccentric orbit, the main effect of atmospheric drag is to gradually drive the orbital eccentricity to zero by decreasing the apogee significantly and only slightly altering the perigee. As a result, the orbit circularises before decaying until a critical orbital altitude, at which the spacecraft burns up [26]. Accurate estimations of orbital lifetime are complex to obtain due to the complicated dynamical environment and the uncertainties in the atmospheric models, however, rough estimates can be obtained from fundamental principles by only accounting for the atmospheric drag, as described by Vukovich and Kim [26]. These estimates are only valid for circular orbits close to the critical altitude (pericentre radius $r_p \leq 150$ km). For elliptic orbits, the decay of r_p can only be estimated under assumptions of linear decrease of the eccentricity, until the orbit becomes circular [26]. To predict the long-term behaviour of the space debris population and assess the capabilities of end of life strategies, significantly more accurate methods are required.

A high-fidelity orbital simulation was used by Alessi et al. [27] to estimate the lifetime of various area-to-mass ratio (A/m, with A the cross-sectional area of the spacecraft in the direction of flight, and m its mass) satellites starting from different LEO circular orbits, and is shown in Figure 2.7. This plot was obtained by considering the NRLMSISE-00 atmospheric model, which is the industry standard for orbital lifetime estimates [28]. This result demonstrates the importance of the area-to-mass ratio under the influence of atmospheric drag, as a factor of 10 difference in the lifetime is found at an altitude of 750 km between $A/m = 0.1$ m^2/kg and $A/m = 0.012$ m^2/kg. The high-fidelity results from Figure 2.7 can be compared to the debris population generated from a typical fragmentation event through Figure 2.8, which gives

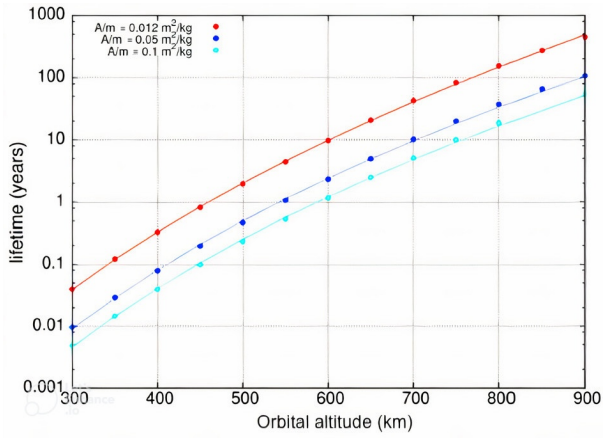

Figure 2.7: Estimated lifetime of satellites in circular orbits at different LEO altitudes and for area-to-mass ratios of 0.1, 0.05, and 0.012 m^2/kg, adapted from [27].

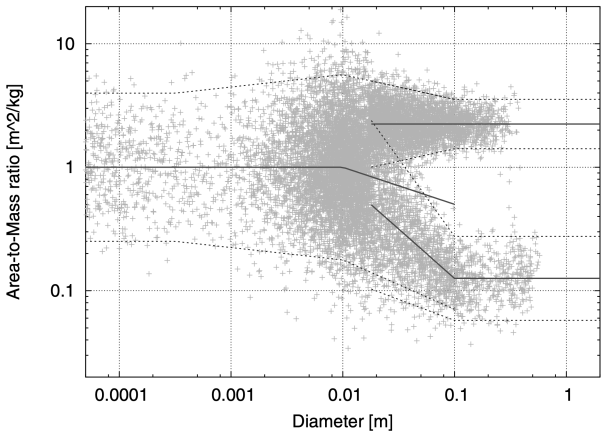

Figure 2.8: Bi-modal area-to-mass distributions A/m for a Pegasus breakup event, with means and $\pm 2\sigma$ dispersions as a function of the characteristic length, based on the NASA breakup model [18].

the bi-modal A/m of debris resulting from a Pegasus breakup event based on the NASA breakup model discussed in Section 2.1.2.2. This figure shows that most debris have an area-to-mass ratio between 0.1 and 4 m^2/kg, meaning that they will re-enter the atmosphere more quickly than predicted by Figure 2.7.

While the decay of circular orbits has been studied in detail [26], only few studies considered the complex dynamical interplay at play. Liu and Wang [29] found that high-altitude satellites at large inclinations are also significantly affected by third-body perturbations from the Moon and the Sun. These accelerations cause a growth of the eccentricity while keeping the semi-major axis mostly constant, meaning that the pericentre plunges towards the primary body and atmospheric entry results. Additionally, Liu and Wang [29] showed that the gravitational bulges resulting from the oblateness of the primary body have a stabilising effect preventing this eccentricity growth and natural decay. These results were further confirmed and generalised to a wider class of dynamical perturbing accelerations by Alessi et al. [27], who analysed the dynamical environment in LEO and identified critical inclinations at which perturbations different from atmospheric drag contribute significantly to the spacecraft re-entry. Some key results are showcased in Figure 2.9, where Figure 2.9a shows the effect of different combinations of initial eccentricity and semi-major axis on the orbital lifetime, and Figure 2.9b shows the effect of lunisolar gravitational resonance. The latter particularly highlights that the lunisolar gravitational resonance has a non-negligible impact on the orbital lifetime. These results demonstrate that perturbations other than atmospheric drag can largely decrease the orbital lifetime of a satellite.

High-fidelity pieces of software permitting to simulate the orbital decay and atmospheric entry of orbiting objects exist, such as the Object Reentry Survival Analysis Tool (ORSAT) [30] and Spacecraft Atmospheric Reentry and Aerothermal Breakup (SCARAB) [31], developed by the National Aeronautics and Space Administration (NASA) and ESA respectively. Both these models have been validated on simple shapes and are the industry standard [32, 33]. Some models are open source, such as the Debris Risk Assessment and Mitigation Analysis (DRAMA) from ESA and Debris Assessment Software (DAS) from NASA [33], however, these make use of simplifying assumptions and models limiting their capabilities [34]. Other numerical codes exist [35, 36], but most of the aforementioned make use of a low-fidelity aerodynamics approach. This limitation was tackled by Kumar et al. [33] who considered the variation in drag coefficient due to the Angle of Attack (AoA), vehicle shape, and motion.

However, these studies are only as accurate as the models of the upper atmosphere and solar activity (which is an input to atmosphere models) [37]. Particularly, the effect of the solar activity on LEO satellites was analysed by Khodairy et al. [38], showing that it had a non-negligible effect on the thermosphere and therefore the drag force acting on LEO satellites. Determining the accuracy of these recent models is complex due to their dependence on time and space, but maximum deviations of the order of 10% for state-of-the-art atmospheric models in the high atmosphere (up to 1200 km) are expected [39].

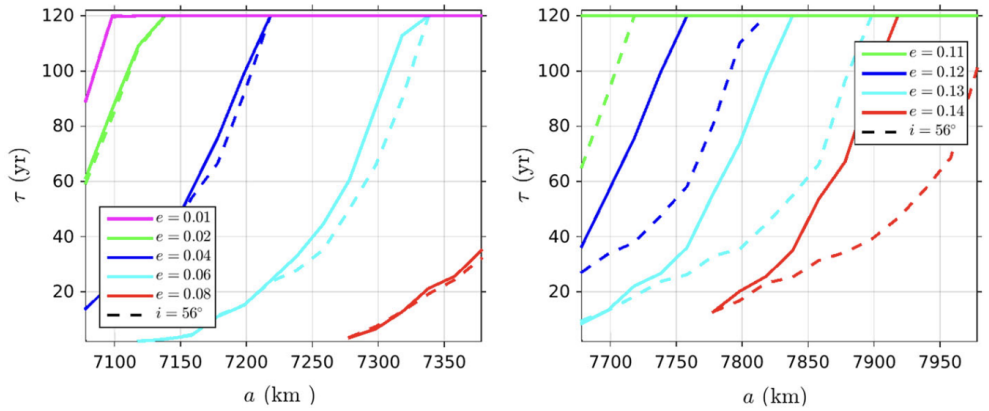

(a) Comparison of the lifetime computed in correspondence of the $i = 56°$ critical inclination (dashed curve) or non-critical inclination (solid curves). Left: $a \in [7078.14 : 7378.14]$ km. Right: $a \in [7678.14 : 7978.14]$ km. Initial epoch 2020, $C_R(A/m) = 0.024$ m^2/kg, $\Omega = 0°$, $\omega = 90°$.

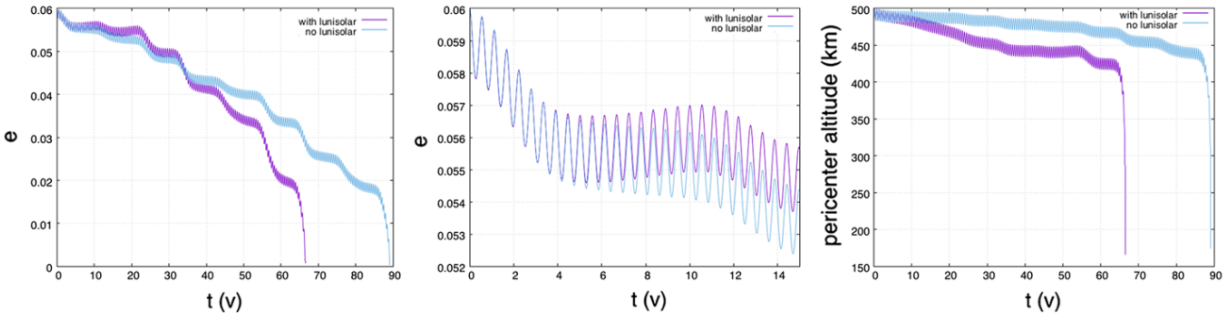

(b) Comparison of the lifetime computed when the effect of drag is combined with a lunisolar gravitational resonance (purple), and when lunisolar perturbations do not act (blue). Left: eccentricity behaviour over time. Middle: detailed behaviour at the time when the relative eccentricity increase takes place. Right: pericentre altitude behaviour in time. Initial condition: $a = 7300.14$ km, $e = 0.06$, $i = 56°$, $\Omega = 0°$, $\omega = 90°$, epoch 2020, $C_R(A/m) = 0.012$ m^2/kg.

Figure 2.9: Key results from the dynamical study of Alessi et al. [27].

2.1.2.2. Breakup Modelling

As defined by Kessler et al. [5], on-orbit catastrophic events contribute to both the short-term and long-term evolution of the environment by producing populations of smaller and larger debris. These fragmentation events can be the result of a collision or an explosion. Breakup events are also predicted to be the largest source of new debris in the future [1, 40], therefore requiring reliable models to be implemented in space debris environment software.

These events can be modelled in various different ways, ranging from physics-based hydrocodes using detailed knowledge of collision geometries and colliding bodies [16] to simple semi-empirical models [41]. On the one hand, while the former can be used to assess the collision characteristics of a specific event known with great details, it is too computationally intensive to be used in debris environment simulations. On the other hand, semi-empirical methods permit to obtain an estimate of the most important metrics of fragmentation events at a low computational cost and without the need for detailed information about the event [41]. For these reasons, semi-empirical models have been used widely in literature for space debris environment modelling and predictions.

The NASA Satellite Standard Breakup Model (SSBM) developed by Johnson et al. [42] for the EVOLVE 4.0 software, a long-term debris environment analysis code, has become the baseline of all subsequent debris environment models (see Section 2.1.2.4) [16]. This model was introduced as an update to the model in [43], which underestimated the generation of fragments smaller than 10 cm and treated all debris as spheres with a density as a function of the fragment diameter [42]. Furthermore, the SSBM is a semi-empirical model fitted to data from ground tests and observations of on-orbit events [16], meaning that the update from [42] was the result of an updated database of such events. Using the average of the three principal geometric axes of a fragment $l_c = (l_x + l_y + l_z)/3$ as independent variable, the model uses

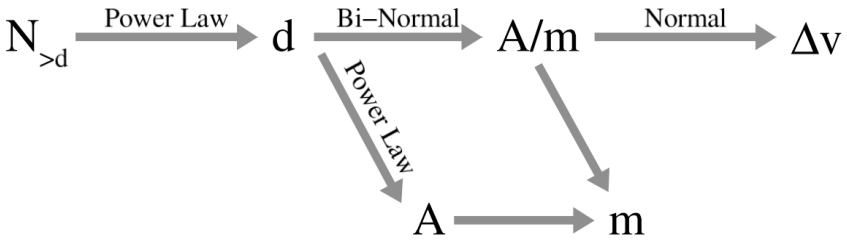

Figure 2.10: Conceptual outline of the size-based derivation of cross-section A, mass m,and imparted velocity ΔV in the NASA breakup model [18].

the total colliding mass and collision velocity to determine the number of fragments generated per size ($N_{>l_c}$) well as their area-to-mass ratio and velocity distributions. The basic principle behind the model is outlined in Figure 2.10 and described in detail in [18, p. 67-76], with $d = l_c$. Additionally, the model distinguishes between explosions and collisions, as well as catastrophic and non-catastrophic collisions based on the 40 J/g criterion from McKnight, Maher, and Nagl [15].

As a semi-empirical model, the improvement of the SSBM is an ongoing process, with new fragmentation events data providing a strong basis to enhancements of the model [44, 45]. However, more fundamental issues present in the original version have been corrected over time, such as the fundamental laws of mass, momentum, and energy conservation [46, 47]. Future improvements could tackle the issues described below.

Considering collisions, the SSBM was designed based on hypervelocity collisions (like in LEO), but collisions are also possible at much smaller relative velocities (a few hundreds of meters per second) within the GEO region [48]. However, Hanada [48] showed that while the size distribution and size-to-area conversion model of the SSBM match low-velocity collision experimental results quite well (accounting for some corrections), the fragment velocity increment ΔV and A/m models do not match these results sufficiently well. As the focus of collisions has been primarily in LEO, no updates to the model have been presented in literature to account for those deviations.

Furthermore, the SSBM was developed at a time when LEO satellites were significantly heavier (600-1000 kg) and larger than in current days [49]. As a result, recent trends of the NewSpace era deviate significantly from many state-of-the-art debris models such as the SSBM. Diserens, Lewis, and Fliege [49] showed that the model significantly deviates from observations of more recent explosions and collisions in terms of number of fragments, by over-predicting the number of larger debris fragments and under-predicting the number of small debris fragments. Such deviations from reality can lead to a significant impact on the debris environment predictions [50], as will be seen in Section 2.1.2.4. To tackle this problem, new collision scenarios and geometries could be generated using high-fidelity numerical simulations as presented by Schimmerohn et al. [16]. This would permit to tune the SSBM to new parameters involving the collision geometry and different mass ratios between the colliding bodies, by considering a larger database of fragmentation events. Particularly, Schimmerohn et al. [16] found that the collision geometry and secondary fragment impacts, both unaccounted for by the SSBM, have a large influence on the resulting fragment cloud characteristics.

2.1.2.3. Debris Spread

The dispersion of the debris from the Cosmos-Iridium collision was studied by Wang [51], resulting in Figure 2.11 which shows the orbit of these debris seven days, three months, one year, and three years after the collision. In this figure, most of the fragments created by the collision have orbital speeds that are close to the speed of their parent satellite, and therefore follow orbits that are close to the orbit of the parent satellite. However, small differences in the distribution of fragment speeds cause the fragment orbits to precess at different rates. Considering Figure 2.11d, three years after the collision, the Cosmos fragments are spread into a shell around the Earth which is concentrated at the altitude of the original Cosmos satellite [51]. The spread of a debris cloud after a fragmentation event follows four general stages [52, 53] as described below.

1. The velocity of the majority of the debris is dominated by the original velocity of the spacecraft at the

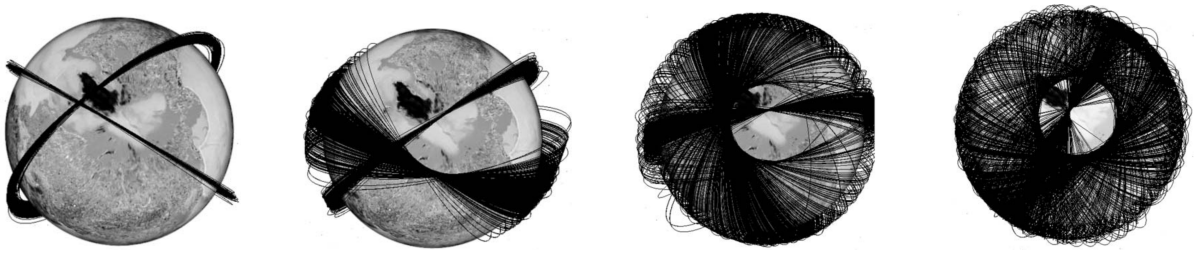

(a) 7 days after the collision. **(b)** 3 months after the collision. **(c)** 1 year after the collision. **(d)** 3 years after the collision.

Figure 2.11: Spread over time of debris orbits from the Cosmos-Iridium collision in 2009 [51].

time of the fragmentation. As a result, these debris form an ellipsoid flying in formation in similar but different orbits.

2. The differences in semi-major axis imparted by the event results in a spread in the orbital period, meaning that the ellipsoid stretches until the entire initial orbital plane of the satellite is covered. Within a few hours, the ellipsoid elongates in a toroid as seen in Figure 2.11a, having a pinch point where the event took place. The density of the debris cloud is greatest at the pinch point.
3. As a result of the Earth oblateness perturbing acceleration, the toroid starts to expand, as the Right Ascension of the Ascending Node (RAAN), Ω and argument of pericentre (AoP), ω, precess. The precessions of the RAAN and AoP are mostly dominated by the J_2 effect and are given by [18],

$$\dot{\Omega} = -\frac{3nR_E^2 J_2}{2p^2}\cos(i) \qquad (2.1a) \qquad\qquad \dot{\omega} = \frac{3nR_E^2 J_2}{4p^2}\left(4 - 5\sin^2(i)\right) \qquad (2.1b)$$

where n is the mean motion, R_E is the Earth radius, i is the inclination, and $p = a(1-e^2)$ is the semi-latus rectum, a is the semi-major axis, and e is the eccentricity. As a result, the pinch point also rotates North- or Southwards. This is shown in Figures 2.11b and 2.11c at two different evolution levels of this stage. The spread in orbital planes yields a decrease in debris density at the pinch point. However, the fanning out of the orbital planes results in the creation of Northern and Southern nodes at the extreme declinations (latitudes). The precession of the pinch point continues until it reaches these Northern and Southern nodes, at which point the debris density will increase again.
4. After several years, the debris are distributed around the Earth, with maximum declinations reaching the value of the inclination of the original spacecraft.

These four stages are easily modelled through integration of the Gauss perturbation equations [54] accounting for major perturbations[3] for the debris field predicted by one of the breakup models presented in Section 2.1.2.2. Furthermore, the stages described above are valid for the debris remaining in orbit. However, in LEO, a significant portion of the generated objects will directly fall in the atmosphere. For the Cosmos-Iridium collision which happened at an altitude of 770 km, approximately one third of the debris directly de-orbited [53].

2.1.2.4. Debris Environment Modelling

Two main methods exist to model the space debris environment: simple source-sink models and full three-dimensional analyses [55].

Source-sink models offer a straightforward model of the amount of debris in orbit, by considering fragmentation events and new launches as sources, and the atmospheric decay as a sink [56]. This is illustrated in Figure 2.12, which shows a graphical representation of the source-sink model for the number of orbital objects in Earth orbit. The model resembles a physical bath system where the water level is dependent on the water inflow and outflow. However, a key difference between the orbital debris system and such a bath system is that the growth in debris from fragmentation events depends on the number of debris in the system [56]: there is a reinforcing feedback and a balancing feedback, both based on the number of debris in the considered region. Such a simple system follows a differential equation of the form,

$$\frac{\mathrm{d}N_d}{\mathrm{d}t} = A - BN_d + CN_d^2 \qquad (2.2)$$

[3] such as Earth oblateness, atmospheric drag, and Solar Radiation Pressure

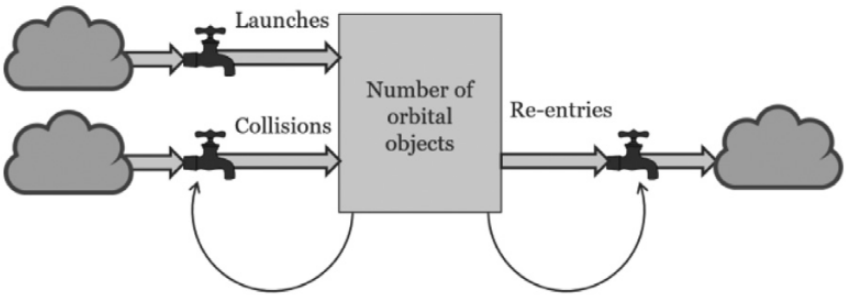

Figure 2.12: Representation of the orbital debris system in the source-sink model [56].

where N_d is the number of debris in the system and A, B, and C are constants. Eq. (2.2) permits to make general predictions on the future evolution of the system. Source-sink models are aimed at understanding general trends of the environment and performing sensitivity studies on predictions, rather than seeking to model the environment as accurately as possible [55]. For example, Lewis [56] used such a system to demonstrate that the linear growth often found in predictions on 200 years periods, like the ones given by Figure 2.4, are only the beginning of an exponential growth noticeable in 1000-year projections.

Sophisticated three-dimensional models have been developed to make high-fidelity assessments and predictions on the space debris environment [55]. These models then permit to infer predictions on a wider range of parameters than solely the number of objects in the studied orbital regions. ESA's MASTER-8 model [57] and NASA's Orbital Debris Engineering Model (ORDEM) 3.1 [58] form the state of the art in terms of orbital debris engineering models [59]. However, the modelling approaches of each software are very different.

The modelling philosophy behind the MASTER population can be described as simulating all known debris generating events in history and their sink mechanisms, to obtain an artificial population [40]. This population can then be used to make future predictions according to specified scenarios and derive flux information on spacecraft of known geometries and mission planning. Additionally, the three-dimensional nature (on grid cells) of the software permits to determine the collision geometry information such as the direction and impact velocity [59]. This modelling approach requires a number of source models for the release mechanism of the different debris ranging from fragmentation events to sodium-potassium droplets [59], each having individual orbital, material composition, size and mass distributions. Overall, the generation of the historic population follows an iterative procedure [59]: (1) object generation through the various source models; (2) correlation of the simulated debris population with the catalogued data (diameters larger than 10 cm); (3) validation of the model through available measurements of the space environment including dedicated missions such as the Tracking and Imaging Radar (TIRA), the European Incoherent Scatter Radar (EISCAT) and ESA's Space Debris Telescope (SDT). The latest release of the MASTER population provides a description of the debris environment until the 1st of November 2016 reference epoch and permits predictions until 2046, taking into account objects larger than 1 µm. On the Inter-Agency Space Debris Coordination Committee (IADC) level, the MASTER population and underlying models have been utilized to estimate the efficacy of space debris mitigation efforts and underline the need for corrective action [40]. Typical results of the MASTER-8 release were shown in Figure 2.6.

The ORDEM software is data-driven, meaning that measurement data is used to scale initial reference models of the debris environment [59], based on the NASA LEO-to-GEO Environment Debris (LEGEND) [60] model which gives the baseline for most sub-populations. The LEGEND model is a full-scale three-dimensional debris evolutionary model that replaced the EVOLVE software (for which the SSBM was originally developed) in 2003 [60], and is capable of providing debris characteristics as functions of time, altitude, longitude and latitude. ORDEM is then capable of providing fluxes of debris for a given year, but no information on the collision geometry or source of the debris can be derived [59].

Horstmann et al. [59] recently compared the MASTER and ORDEM models, permitting to make an objective assessment on regions where the space debris environment is well-modelled, as well as regions where additional information may be needed. Examples of comparison of both models are shown in Figures 2.13 and 2.14, which show comparisons of the cumulative total flux for a Sun-Synchronous Orbit (SSO) and

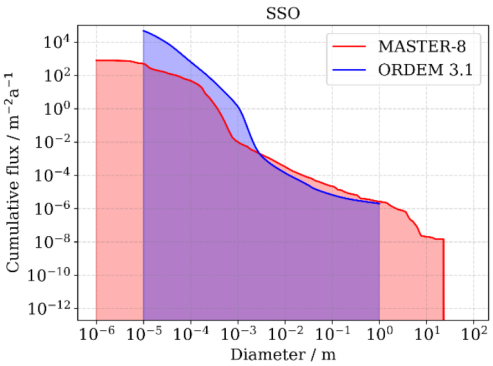

(a) Cumulative total flux for a sun-synchronous orbit at 800 km altitude.

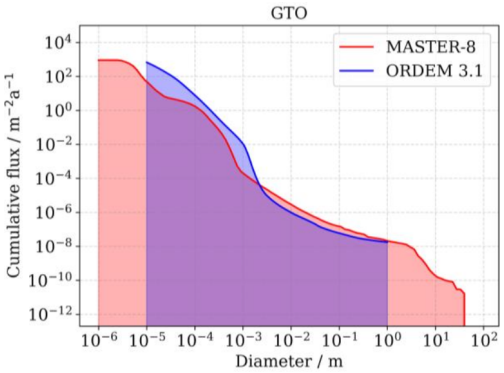

(b) Cumulative total flux for a typical GTO with an apogee altitude of 35 149 km and a perigee altitude of 109 km.

Figure 2.13: Cumulative total flux comparisons between MASTER-8 and ORDEM 3.1 for a Sun-synchronous Orbit (SSO) and a Geosynchronous Transfer Orbit (GTO) [59].

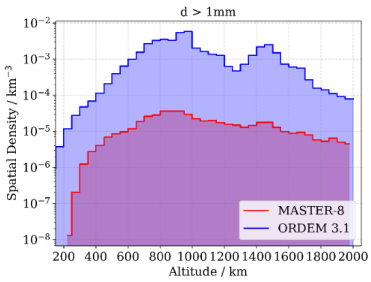

(a) Spatial density in LEO for objects with a diameter larger than 1 mm.

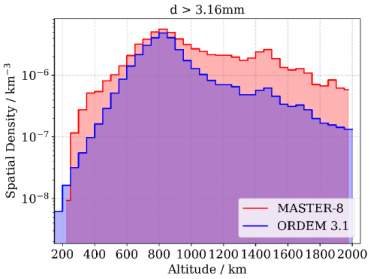

(b) Spatial density in LEO for objects with a diameter larger than 3.16 mm.

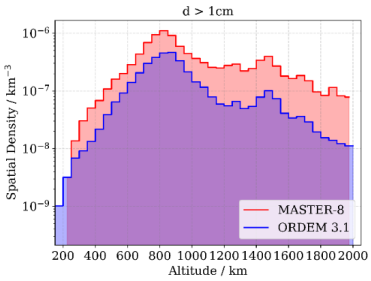

(c) Spatial density in LEO for objects with a diameter larger than 1 cm.

Figure 2.14: Spatial density comparisons between MASTER-8 and ORDEM 3.1 [59].

a GTO, and of the spatial density in LEO for different object size ranges, respectively. From these figures, it appears that the models agree best in orbital regions and debris sizes where good data is available, and much more poorly where measurements are lacking (such as in the critical millimetre size range and Sun-Synchronous Orbit altitudes) [59]. Particularly, modelling the sub-millimeter diameter regime is complex due to the lack of data on which the models can be calibrated. This is seen in Figure 2.14, where deviations between the two models are much larger in Figure 2.14a than in Figure 2.14c.

2.1.3. Space Debris Remediation

Aside from regulations indicating the maximum duration of a complete passivisation of an inactive spacecraft, a number of remediation strategies have been considered in the literature. The detection, tracking and imaging of space debris is a first step towards mitigating the problematic. Having a good knowledge of the debris population in key orbital regions and of the position of major debris serves multiple purposes; particularly, validation of the space debris environment models presented in Section 2.1.2.4 and prediction of the trajectory of catalogued objects to determine the need for future collision avoidance manoeuvres of active satellite [61]. The LEO region is generally monitored using RAdio Detection And Ranging (RADAR) technology, while optical telescopes are used for GEO objects [61]. Other methods exist, but are less common. RADAR technology relies on the concept of echo, where continuous or pulsed radio waves are sent from the antenna and reflections are detected to gain information on the body [62]. Continuous waves permit to evaluate the frequency shift between the incident and reflected signals (yielding information on the object's velocity) and pulsed signals permit to determine the distance to the target. More information on the different types of RADAR systems can be found in the review from Muntoni et al. [62]. The global spaced debris monitoring system is capable of detecting objects larger than 5–10 cm in LEO and 0.3-1.0

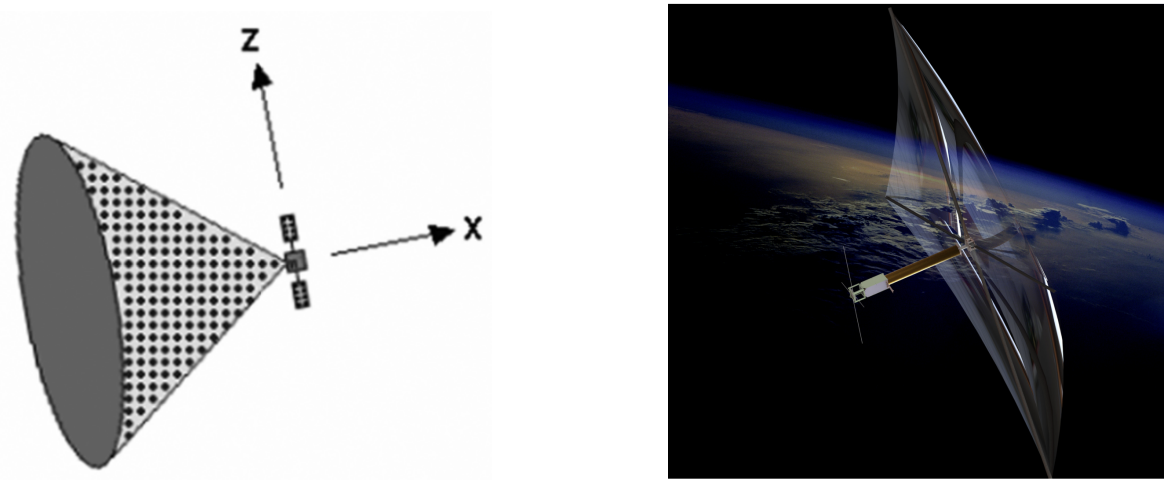

(a) Drag sail from [66].

(b) Inflatable drag enhancement device from [71].

Figure 2.15: Example of drag enhancement devices.

m at higher altitude [62].

Another remediation strategy is the use of Active Debris Removal missions to de-orbit or move a defunct satellite to a graveyard orbit. Numerous concepts have been suggested in literature, ranging from expanding foam systems and robotic extensible arms to laser-based methods [63], but most missions capable of removing large bodies from orbit require the removal spacecraft to be in close vicinity to the target object. As a result, the vast majority of missions being developed aim to target a single spacecraft.

At last, A key aspect of space debris mitigation is the need for clear EoL strategies which comply with the requirements specified by [10]. These permit spacecraft to more quickly re-enter the atmosphere or to be transferred to a graveyard orbit, thereby freeing up space for future missions. In the following, methods applicable to the two most important protected regions are considered in some detail: LEO and GEO. Additionally, MEO and Highly Eccentric Orbit (HEO) cases are briefly discussed due to their possible interference with the aforementioned protected regions. However, please note that the very recent change from 25 to five years EoL guideline means that the majority of available literature still considers the former to evaluate system performances. The shorter guideline means that more efficient designs, or combinations of various methods may be necessary to comply.

Low Earth Orbit EoL: In LEO, spacecraft disposal can occur either by boosting to an orbit above 2000 km altitude (graveyard orbit), or by de-orbiting it [64]. These two approaches were compared by Alsup et al. [65], showing that the former option is only preferred for satellites above 1300 km altitude (in terms of ΔV expenditure). While entering a graveyard orbit is only possible with some sort of propulsion, three main methods can be used to de-orbit a spacecraft in LEO: thrusters, tethers, and drag enhancement [66].

With the presence of a residual atmosphere in Low Earth Orbit, atmospheric disposal is considered to be the most effective method to comply with the debris mitigation guidelines [64]. At altitudes where the atmosphere is too thin for the natural decay rate to comply with space debris mitigation guidelines, drag enhancement devices can be used. Three types of such systems exist: drag sails, solar-sails (taking advantage of both the Solar Radiation Pressure and atmospheric drag), and inflatables [64]. The drag sail and inflatable concepts are shown in Figure 2.15, but all aim to increase the area-to-mass ratio of the spacecraft. Based on studies from [67, 68, 69], Roberts and Harkness [66] concludes that the original 25-year guideline can be fulfilled single-handedly by such a device up to altitudes of 700-1000 km. Furthermore, aero-stable drag enhancement devices can be deployed easily even if the spacecraft is tumbling, and can be designed to collapse at specific altitudes to ensure a maximum aerodynamic heating on the spacecraft bus during the reentry [66]. The overall concept has been studied thoroughly, and some on-orbit demonstrations have been made [70, 71, 23]. Furthermore, Alessi et al. [27] presented natural highways using the dynamical resonances associated to the high-degree geopotential harmonics, lunisolar perturbations, and Solar Radiation Pressure, permitting to explore new optimal de-orbiting strategies.

The presence of the Earth magnetic field can also be leveraged to produce Lorentz forces using an electrodynamic tether [72]. The interaction between the device and the electromagnetic field converts kinetic energy into electric energy, thereby producing an artificial drag force [73]. Such a system can be carried by the spacecraft and only deployed at EoL after a signal from the ground station is received. However, an electrodynamic tether consists of a very long (500 m - 5 km) flexible conductor attached to the body of the satellite [73, 72], making its deployment rather complex for tumbling satellites [74]. Additionally, ensuring the dynamical stability of such system requires dissipation strategies to reduce the amplitude of the tether oscillation [75] and collision of a space debris with a long tether could render the EoL strategy ineffective.

The more traditional approach consists of using the available propulsion system on-board to initiate reentry. If the spacecraft is expected to not completely burn-up in the atmosphere, this permits to perform a controlled reentry targeting unpopulated areas [64]. However, this approach implies that the spacecraft is still active.

Geostationary Orbit EoL: Spacecraft in GEO can smoothly and reliably reach a graveyard orbit above the GEO belt. This approach has therefore been the standard for a sustainable disposal of these satellites [76]. However, even this graveyard orbit is becoming crowded, and missions aiming to clean up this region have been considered as any collision in the graveyard orbit would create GEO-crossing debris [77]. Furthermore, while the disposal of GEO satellites is done with relative ease, Morand et al. [76] found that the disposal of satellites in geosynchronous orbits[4] are much more tedious to perform with long-term sustainability. Cabot Costa [78] investigated a number of disposal strategies for these satellites.

MEO and HEO EoL: The MEO region is primarily occupied by telecommunication satellites and is significantly less populated than the LEO and GEO regions [79]. It is therefore less of a concern with respect to the onset of the Kessler syndrome. However, Rossi et al. [80] pointed out that the use of unstable graveyard orbits can result in dangerous crossings with the LEO region on the long-term, yielding an increased collision risk. Furthermore, the high orbital altitudes render the de-orbiting of the spacecraft through atmospheric drag unfeasible, leaving two approaches: disposal to long-term stable graveyard or to eccentricity build-up orbits [81]. While the former is similar to the GEO case, the latter aims to select a disposal orbit that maximises eccentricity growth (from perturbations described by Rossi et al. [80]) and results in an atmospheric entry within 200 years. The disadvantage of this approach is that it will enter the LEO and GEO protected regions at some point during its evolution. However, these passes are predicted to be very short and have a negligible effect on the spatial density of each region [81].

Highly eccentric orbits are characterised by a perigee close to LEO and an apogee above 40,000 km (often above 60,000 km) [11]. Having the perigee in LEO, the common approach is to provoke an atmospheric entry. However, the high velocity of these satellites around the perigee can pose ground hazards. Therefore, the disposal of objects in HEO through atmospheric entry should be planned carefully [82]. Alternatively, a graveyard orbit is available, although Colombo et al. [83] mentions that re-entry is definitely the more sustainable solution. Furthermore, similar to MEO satellites, the main points of concern are the passes through the LEO and GEO protected regions, requiring careful planning [82].

2.2. Solar-Sail Technology

Practical spacecraft propulsion is bound to the third law of Newton, stating that for every action (force) in nature, there is an equal and opposite reaction [84]. In other words, spacecraft propulsion is a momentum exchange process. Conventional systems have relied on chemical propulsion, which provides high thrust at low specific impulse. The low efficiency of these systems has prompted a lot of research on plasma propulsion (electric or ionic) which were proposed in the early 1900s [85, 86] but has only been actively developed since 1957 [87]. However, while plasma propulsion allows for significant mass savings for both long-term interplanetary cruise and planetocentric orbital operations [88, 89], it is still constrained by the amount of propellant taken on-board. This limits both the total ΔV which can be gained by the spacecraft, and the mission lifetime [90].

solar-sailing technology provides an elegant solution to the reliance on the presence of reaction mass on-board [91], by interacting with the space environment [92], and thereby greatly resolving the aforementioned limitations of spacecraft propulsion. While some spacecraft interact with the gravitational attraction of a

[4] Orbits at geostationary altitude but non-zero inclinations.

body [93], an atmosphere [94, 95] or the solar wind to exchange momentum [96, 97], sailcraft leverage the Solar Radiation Pressure (SRP) [92]. Similarly to a ship sailing the sea by manoeuvring a sail to orient the wind force in a desired direction, solar-sails use a reflective surface to gain momentum from the photons reaching it and orient the resulting force to follow a desired trajectory [92]. However, the momentum carried by an individual photon is very small, meaning that a very large number of photons need to be intercepted to result in a significant force, and a great reflective sail area is necessary [91]: only about 9 N/km^2 can be generated at 1 AU by a perfect reflector [91, 92]. Therefore, the spacecraft mass to sail area ratio should be small to generate a significant acceleration on the spacecraft.

As solar-sails are not constrained by a finite source of reaction mass, they are only limited by the lifetime of their film membrane in the space environment [91], which can last decades. This makes the concept particularly relevant to the de-orbiting of multiple satellites to mitigate or delay the aforementioned Kessler syndrome. In the following sections, a review of the state-of-the-art of solar-sail technology is presented.

2.2.1. Historical Background

The first notion of Solar Radiation Pressure dates back to 1610, when Johannes Kepler observed that the Sun may cause the tails of comets to point outward from it [98]. This was noted in a correspondence with Galileo, yielding the first recorded observations that light may exert a force [99, 92]. However, the mechanism behind this force was not understood until 1873 when Maxwell [100] predicted the existence of radiation pressure as a consequence of the unified theory of electromagnetic radiation, showing that electromagnetic fields carry both energy and momentum. This quantitative prediction was experimentally verified in the 1900s by Lebedew [101] and Nichols and Hull [102], while a number of science fiction authors wrote about spaceships propelled by mirrors around the same period [91]. It is only in the 1920s, however, that practical solar-sailing concepts were proposed by Tsiolkovsky [103] and Tsander [104] (the latter quoting a report from the author from 1924). Despite these early publications, the field remained dormant until the 1950s, when Wiley [105] and Garwin [106] rediscovered the concept independently, describing it as a unique and elegant method yielding a continuous and propellantless thrust. In 1961, a probe balloon named “Echo-1” was launched by NASA to measure Solar Radiation Pressure in space for the first time [107]. Shortly after, in 1963 Arthur C. Clarke published his well-known short story *The Wind from the Sun*, popularising the concept of solar-sailing to many engineers reading science fiction [91].

The unique capabilities of solar-sails have raised great interest from the scientific community to apply the concept to a wide array of missions ranging from interstellar exploration to geoengineering [108, 109]. A number of these mission applications have been reviewed by Macdonald and McInnes [110]. Of particular interest to this work are the applications of solar-sails in Earth orbit, including active debris removal missions [111]. solar-sails have been considered to lower the perigee of high-altitude orbits until atmospheric drag takes over, and the spacecraft re-enters the atmosphere [112, 113]. According to Borja and Tun [112], the de-orbiting of a geosynchronous satellite could be achieved in less than 5.8 years.

As the field gained in popularity, solar-sailing was considered in the context of many missions. Zhao, Wu, and Li [114] provide an overview of the research schemes and hotspots in the solar-sailing field, including key missions having contributed to the state-of-the-art of the field. Of particular interest is the first serious design study of a solar-sail for a rendezvous mission with the Halley comet at its perihelion in the mid-1980s [115]. Although the use of solar-sailing was dropped in favour of electric propulsion due to the complexity of deployment (and the mission ended up never flying) [91], the lessons learned from this mission laid solid foundations for solar-sailing technology [99]. Much later, in 2010, the Interplanetary Kite-craft Accelerated by Radiation Of the Sun (IKAROS) sailcraft from the Japan Aerospace Exploration Agency (JAXA) was launched and successfully demonstrated a number of key technologies [116, 99]. IKAROS, shown in-flight in Figure 2.16a, is widely regarded as a major milestone in solar-sailing technology. More recently, the Lightsail-2 spacecraft launched in 2019 demonstrated that solar-sails are a viable propulsion method for CubeSats [117, 114]. Furthermore, the 12U CubeSat Advanced Composite Solar-Sail System (ACS3) from NASA was launched on the 23rd of April 2024, with two main technology demonstration objectives given by Wilkie [118]: (1) to deploy and characterise the ACS3 deployable composite boom technology solar-sail; (2) to characterise the Solar Radiation Pressure thrust of the deployed solar-sail via controlled orbit raising and lowering, and to attempt to identify the fundamental flexible body structural dynamic vibration modes of the deployed solar-sail (extended mission objective). Figure 2.16b shows the full system ground deployment test of the ACS3 Sail-Boom Subsystem (SBS) prototype unit. In this figure, the development sails shown are slightly smaller than the flight ACS3 sail membranes. However, composite booms, sail folding, sail and

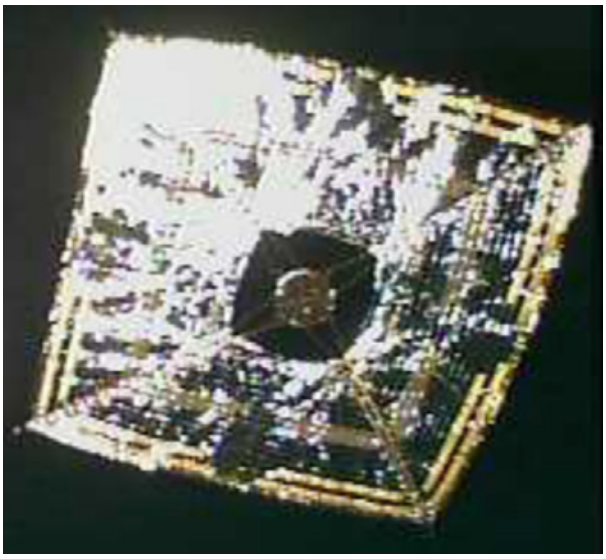

(a) Solar-sailing IKAROS in the interplanetary field, captured by the Deployable Camera (DCAM) on the 14th of June 2010 [116].

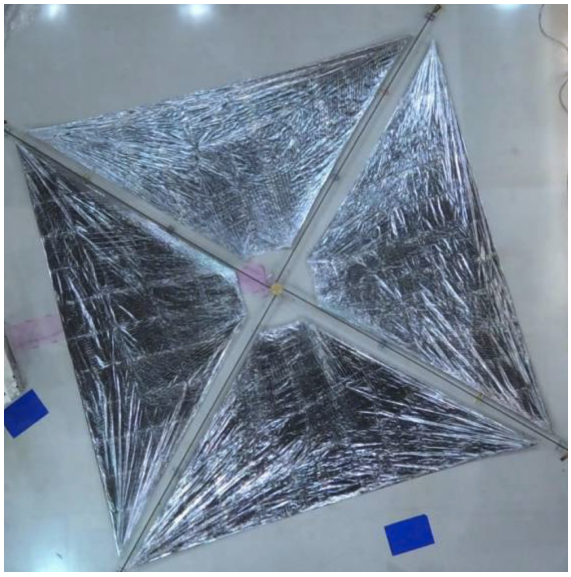

(b) ACS3 prototype unit during the full system ground deployment test of the SBS [118].

Figure 2.16: The IKAROS and ACS3 solar-sails.

Table 2.1: Environmental forces on the Galileo spacecraft in Newtons [119, 99]. The position in the solar system is given as (spacecraft-Sun distance; distance to central body in terms of its equatorial radius R, if any).

Source	**Near Venus** (0.7 AU; $10R_V$)	**Near Earth** (1 AU; $10R_E$)	**Interplanetary** (3 AU; N/A)	**Near Jupiter** (5 AU; $10R_J$)
Solar Radiation	1.7E-4	9E-5	1.1E-5	3.3E-6
Solar Wind	5.9E-8	3.1E-8	3.6E-9	1.1E-9
Meteoroids	1.6E-10	1.1E-10	9.4E-9	4.2E-9
Newtonian Drag	3.4E-9	7.9E-11	5.3E-11	5.7E-11
Magnetic Field	5.4E-14	1.9E-13	2.1E-11	1.6E-9

boom stowage, sail-to-boom tip attachment, and sail root spring tensioning are representative of the flight SBS design.

2.2.2. Solar Radiation Pressure

A spacecraft navigating throughout the solar system will experience a number of forces alongside gravity, the source of these forces ranges from SRP to meteoroids impacts and magnetic field interactions. Following the estimations of the magnitude of these perturbing forces on the Galileo spacecraft at different positions in the solar system shown in Table 2.1 [119], it is clear that the SRP provides the largest momentum exchange capabilities (largest force) and is the most consistent throughout the solar system. In the interplanetary environment, SRP forces are also more steady and predictable than other environmental forces [99]: at 1 AU, various measurements over the years provided ranges of solar fluxes[5] spanning only from 1360 to 1370 W/m^2 (based on solar cycles) [120]. The relatively large thrust potential and reliability offered by the Solar Radiation Pressure provided great attention to the use of solar-sails for interplanetary missions.

In LEO, accelerations due to the oblateness of the Earth, atmospheric drag, and the Moon gravity can be orders of magnitude larger than the SRP acceleration of a conventional spacecraft [120]. According

[5] which is directly related to the SRP, as demonstrated below.

to Macdonald [121], solar-sails are inappropriate for Earth orbits below 750 km due to the atmospheric drag. However, more recent studies found that orbit raising from a minimum altitude ranging from 400 to 600 km (depending on the solar activity) is feasible [122]. Moreover, Carzana, Visser, and Heiligers [123] demonstrated the feasibility of using a solar-sail in Earth orbit by developing an efficient and accurate technique to optimise these solar-sail trajectories in the presence of gravitational and atmospheric perturbations. Nevertheless, solar-sails remain attractive for Earth-bound missions despite the complexity of dynamical environment thanks to their propellantless nature and usability for long-term missions.

2.2.2.1. Existence and Estimation of SRP

The SRP magnitude can be derived from either quantum mechanics or the theory of electromagnetism, as described by McInnes [91]. In this work, a simple derivation based on the quantum mechanics description of light is presented following Fu, Sperber, and Eke [99], to demonstrate the existence of SRP and its value. Starting with the mass-energy equivalence equation from Einstein [124],

$$E = m_r c^2, \tag{2.3}$$

where E is the total or relativistic energy, m_r is the relativistic mass, and c is the speed of light. With the definition of the relativistic mass given by [125],

$$m_r = \frac{m_0}{\sqrt{1 - v^2/c^2}},$$

where m_0 is the rest mass of the particle and v is the moving speed of the particle. Note however that this work does not consider solar-sails travelling at relativistic speeds and $m \approx m_0 \approx m_r$. Nevertheless, Eq. (2.3) can be written as,

$$E^2 = (m_r c^2)^2 = \frac{m_0^2}{1 - (v/c)^2} c^4.$$

This expression can be further developed using,

$$\frac{1}{1 - (v/c)^2} = 1 + \frac{(v/c)^2}{1 - (v/c)^2},$$

and the definition of linear momentum of a particle $p = m_r v$,

$$E^2 = m_0^2 c^4 \left(1 + \frac{(v/c)^2}{1 - (v/c)^2}\right) = (m_0 c^2)^2 + \frac{m_0^2 c^2 v^2}{1 - (v/c)^2} = (m_0 c^2)^2 + m_r^2 v^2 c^2 = (m_0 c^2)^2 + (pc)^2. \tag{2.4}$$

From the second term on the right-hand-side of Eq. 2.4, it is clear that massless photons can carry momentum that can then be leveraged by solar-sails. Based on this equation, a formulation for the SRP on a given surface area A_{SRP} can be derived. Assuming a uniform beam of photons hitting a flat surface of area A_{SRP} orthogonally, and assuming that all the momentum from the photons transfers to the surface, the time derivative of Eq. (2.4) is obtained as [99],

$$2\frac{\mathrm{d}E}{\mathrm{d}t} = 2\frac{\mathrm{d}(pc)}{\mathrm{d}t} = 2c\frac{\mathrm{d}p}{\mathrm{d}t},$$

where the time derivative of the total energy can be expressed as $\frac{\mathrm{d}E}{\mathrm{d}t} = W A_{SRP}$, with W the radiative flux. The time rate of change of linear momentum is the magnitude of the force resulting from the momentum exchange ($\frac{\mathrm{d}p}{\mathrm{d}t} = f_{SRP}$) [84]. This results in,

$$2WA = 2cf_{SRP} \Leftrightarrow P = \frac{f_{SRP}}{A_{SRP}} = \frac{W}{c}, \tag{2.5}$$

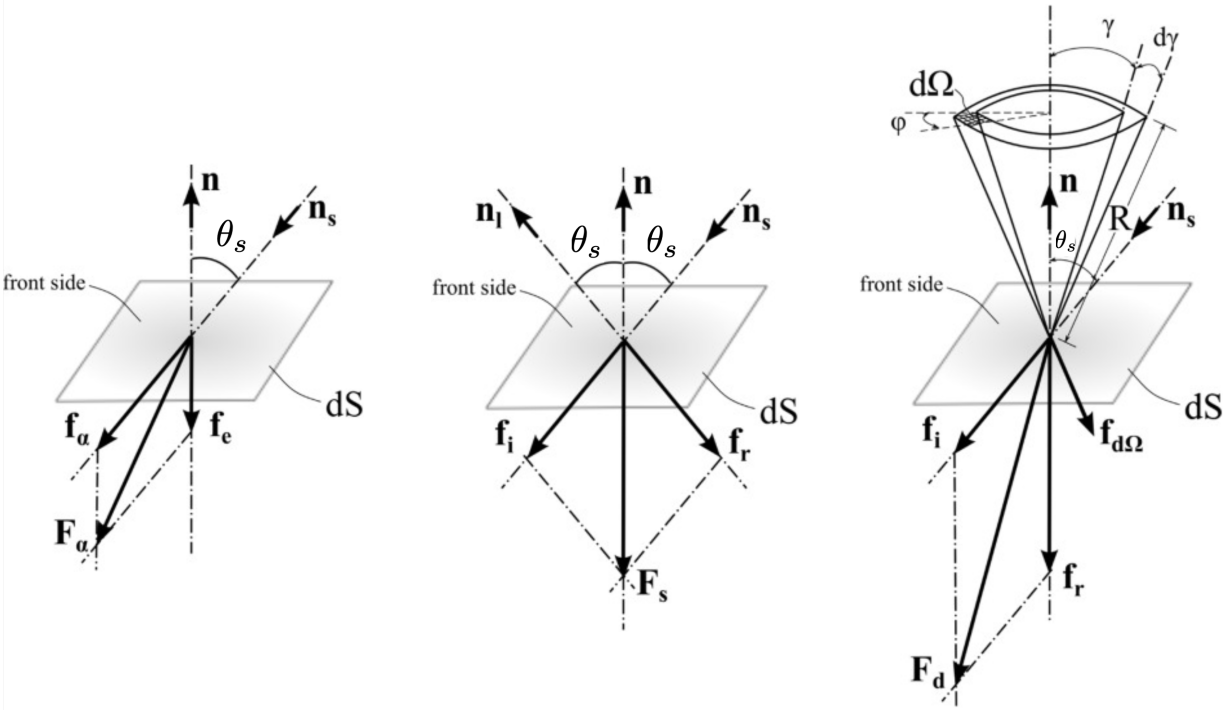

(a) Absorption and emission cases. **(b)** Specular reflection case. **(c)** Diffuse reflection case.

Figure 2.17: Forces acting on a surface dS under the influence of Solar Radiation Pressure [99].

where P is the Solar Radiation Pressure on the A_{SRP} surface area. This shows that the solar pressure at a given point in space depends on the radiative flux coming from the Sun, which follows the inverse squared rule [99, 91],

$$W(r_\odot) = \frac{L_\odot}{4\pi r_\odot^2}, \tag{2.6}$$

where $r_\odot$ is the distance from the Sun's centre of mass at which W is evaluated, and $L_\odot = 3.84E26$ W is the luminosity of the Sun [99]. Note that Eq. (2.6) assumes a point-like Sun [126]. The incident radiative flux on a surface inclined by an angle θ_s with respect to the sunlight is then given by,

$$W_{incident}(r_\odot, \theta_s) = W(r_\odot)\cos(\theta_s). \tag{2.7}$$

Finally, the SRP experienced by an object at $r_\odot$ is maximum when all photons are reflected back to the Sun (meaning that photons are reflected with an equal but opposite velocity and $\theta_s = 0$). The maximum SRP is then given by,

$$P_{max}(r_\odot) = 2\frac{W(r_\odot)}{c}. \tag{2.8}$$

Therefore, the effectivity of a solar-sail depends on the distance from the radiating body, the orientation of the sail, and its efficiency in reflecting the photons. The latter aspect will be considered in detail below. Based on this model for Solar Radiation Pressure, the forces exerted on the sail material element can be derived.

2.2.2.2. Photon-Sail Interaction

In the following, the physics of photon-sail interaction is described, based on the assumption of a point-like Sun. The equations are derived for an infinitesimal surface dS and can later be integrated for any shape (flat plate, sphere, and so on) either analytically [127, 126] or numerically. When a photon encounters a

solar-sail, it is either absorbed, transmitted, or reflected. Additionally, the spacecraft being a grey body, photons are also emitted from both sides of $\mathrm{d}S$. Considering the probability of absorption α, transmission ζ and reflection ρ, the following holds [99],

$$\alpha + \zeta + \rho = 1. \tag{2.9}$$

These probabilities can also be considered as optical parameters of the sail membrane. The total force on the infinitesimal element $\mathrm{d}S$ then becomes,

$$\mathrm{d}\boldsymbol{F} = \alpha \mathrm{d}\boldsymbol{F}_{\alpha} + \zeta \mathrm{d}\boldsymbol{F}_{\zeta} + \rho \mathrm{d}\boldsymbol{F}_{\rho}, \tag{2.10}$$

where $\mathrm{d}\boldsymbol{F}$ is an infinitesimal force vector and $\mathrm{d}\boldsymbol{F}_{\alpha,\zeta,\rho}$ are the infinitesimal force vectors generated due to the absorption, transmission, and reflection of photons respectively. As transmitted photons go through the sail without change of momentum (although they may be refracted), they do not result in a net propulsive force on the spacecraft and $\mathrm{d}\boldsymbol{F}_{\zeta} = 0$ [127]. Figure 2.17 provides an overview of the sail-photon interaction cases related to absorption in Figure 2.17a, and related to reflection in Figures 2.17b and 2.17c. In these figures, $\boldsymbol{n}$ is the surface normal vector of $\mathrm{d}S$ and $\boldsymbol{n}_s$ is the sunlight vector. As absorbed and emitted radiation are inherently linked, they are generally considered together, as shown in Figure 2.17a, where $\boldsymbol{f_{\alpha}}$ and $\boldsymbol{f_e}$ are the force vectors resulting from the absorption and emission of photons respectively, and $\boldsymbol{F}_{\alpha}$ is the resultant of these forces. The emitted radiation is directly linked to the equilibrium temperature, T_{eq}, of the body which can be estimated through the classical Stefan-Boltzmann law by equating the emitted and absorbed power (P_{ϵ} and P_{α}) [128],

$$P_{\alpha} = P_{\epsilon} \Leftrightarrow \alpha W \cos(\theta_s)\mathrm{d}S = \mathrm{d}S T_{eq}^4 \sigma(\epsilon_f + \epsilon_b) \Leftrightarrow T_{eq} = \sqrt[4]{\frac{\alpha W \cos\theta_s}{\sigma_{SB}(\epsilon_f + \epsilon_b)}}, \tag{2.11}$$

where ϵ_b and ϵ_f are the emissivities of the front and back of the sail respectively, $\sigma_{SB} = 5.670374419E{-}8$ W/(m^{2}K^4) is the Stefan-Boltzmann constant. Based on this result, $\mathrm{d}\boldsymbol{F}_{\alpha}$ can be expressed as [99],

$$\mathrm{d}\boldsymbol{F}_{\alpha} = \frac{W\cos(\theta_s)}{c}\mathrm{d}S\left(\underbrace{\boldsymbol{n}_s}_{absorption} + \underbrace{\frac{\epsilon_b B_b - \epsilon_f B_f}{\epsilon_f + \epsilon_b}\boldsymbol{n}}_{emission}\right) \tag{2.12}$$

where B_b and B_f are the Lambertian coefficients of the front and back surfaces of the sail, and were included because the behaviour of the re-emitted energy flux follows Lambert's diffuse dissipation for a flat surface [126]. Note that this equation assumes no temperature difference between the front and back side of the sail, which is validated by Forward [127] who showed that the difference is below 0.1 K. It is clear from Eq. (2.12) that the thermal emission component is zero if both sides of the sail have the same optical properties. Additionally, note that the absorbed force component is in the same direction as the incoming light rays, while the force associated to thermal emission is normal to the sail element considered.

Continuing, two types of reflection can take place: specular or diffusive reflection of the incident photons. The former is illustrated in Figure 2.17b and refers to the case in which all the photons are reflected according to the cosine law [126]. In this figure, $\boldsymbol{f_r}$ and $\boldsymbol{f_i}$ refer to the force vectors of generated by the incident and (specularly) reflected photon beams respectively, and F_s is the resultant of these forces. The photons are reflected along $\boldsymbol{n}_I$ lying in the plane defined by $\boldsymbol{n} \times \boldsymbol{n}_s$ with $\boldsymbol{n} \cdot \boldsymbol{n}_I = \boldsymbol{n} \cdot \boldsymbol{n}_s$. The resultant force then acts along $\boldsymbol{n}$ and is given by [99],

$$\mathrm{d}\boldsymbol{F}_s = -\frac{2W}{c}\cos^2(\theta_s)\mathrm{d}S\boldsymbol{n}, \tag{2.13}$$

where $\mathrm{d}F_s$ is the infinitesimal force generated by the specular reflection process. Diffusive reflection is scattered in all directions, with the most common model being Lambert diffusion, meaning that it appears equally bright at all viewing angles [126, 99]. Figure 2.17c describes the forces at play in such diffusive

process, where $\boldsymbol{F_d}$ is the force resulting from $\boldsymbol{f_i}$ and $\boldsymbol{f_r}$ (in this case diffusely reflected), and $\boldsymbol{f_r}$ is itself the resultant of all $\boldsymbol{f_{d\Omega}}$ from the diffusive reflection process. Fu, Sperber, and Eke [99] derived that the force generated by a photon reflected diffusively is given by,

$$\mathrm{d}\boldsymbol{F}_d = \frac{W\cos\theta_s}{c}(\boldsymbol{n}_s - B_f\boldsymbol{n})\mathrm{d}S \tag{2.14}$$

where $\mathrm{d}\boldsymbol{F}_d$ is the infinitesimal force generated by the diffusive reflection process and B_f takes the value of $2/3$ for a Lambert surface. Finally, combining Equations (2.10), (2.12), (2.13), and (2.14) results in the total force on element $\mathrm{d}S$ [99],

$$\mathrm{d}\boldsymbol{F} = \frac{W}{c}\left(\alpha\cos\left(\theta_s\right)\left(\boldsymbol{n}_s + \frac{\epsilon_b B_b - \epsilon_f B_f}{\epsilon_f + \epsilon_b}\boldsymbol{n}\right) - 2\rho_s\cos^2\left(\theta_s\right)\boldsymbol{n} + \rho_d\cos\left(\theta_s\right)\left(\boldsymbol{n}_s - B_f\boldsymbol{n}\right)\right)\mathrm{d}S \tag{2.15}$$

where $\rho = \rho_s + \rho_d$, the probabilities of specular and diffuse reflections, respectively. While these formulations assume a point-like luminous body, meaning that it is distant enough, McInnes [91] and Koblik, Polyakhova, and Sokolov [126] discussed the effects of considering an extended (non-point-like finite body) body to compute the radiation pressure force. However, the present work considers a solar-sail in orbit around the Earth, where Sun rays can be considered as parallel due to the large Sun-Earth distance [129]. Additionally, more details on the comparison between point-like and spherical-like models of the Sun are also given by Markhoos [130].

2.2.2.3. Overview of SRP Force Models

A great number of models describing the forces on a complete solar-sail have been proposed in literature based on the formulations of infinitesimal forces on an element $\mathrm{d}S$ presented in the previous section. Note that the models presented below are also more generally applicable to arbitrary spacecraft, rather than solar-sails only, and that they all assume parallel sun-rays [99].

The simplest SRP force model available is the cannonball model, which approximates the spacecraft's shape as a sphere [131], resulting in a constant force (at a given point in space) both in magnitude and direction (collinear with the Sun-spacecraft vector). The model also simplifies the photon-sail interaction through the use of a reflection coefficient, C_r, taking values between 1 (absorbed) and 2 (fully specularly reflected). This results in,

$$\boldsymbol{F}_{SRP}^{cannonball} = WA_{SRP,eff}C_r\boldsymbol{r}_{\odot} \tag{2.16}$$

where $\boldsymbol{r}_{\odot}$ is the position vector of the spacecraft with respect to the Sun, $A_{SRP,eff}$ is an effective surface area[6] on which the SRP is acting, and $\boldsymbol{F}_{SRP}^{cannonball}$ is the force vector resulting from the SRP based on the cannonball model. According to McMahon and Scheeres [132], the model was democratised by the very precise orbit determination results for the Laser Geodynamics Satellites (LAGEOS) using the cannonball model [133]. However, LAGEOS were spheres, making the model particularly applicable for this specific case and its accuracy non-generalisable. In practice, the model fails to capture the true dynamics and is too simple for solar-sail mission studies.

A similarly simplistic model which is more suited to solar-sailing technology is the Ideal SRP force model (I-SRP), relying on the assumption of a flat sail and perfectly specularly reflected sunlight [99]. This results in,

$$\boldsymbol{F}_{SRP}^{I-SRP} = \eta\frac{-2W}{c}\cos^2\left(\theta_s\right)A_{SRP}\boldsymbol{n} \tag{2.17}$$

where an efficiency factor $0 < \eta < 1$ was added to characterise the loss of thrust due to other effects. This model is widely used in literature [134, 135, 136, 137], and is particularly suited for feasibility studies or preliminary mission analysis. Particularly, the SRP force is always aligned with the sail surface normal,

[6] Selected to be representative of the average area exposed to the photons over time.

which permits to obtain noise-free insights of the dynamics in preliminary studies. However, in practice, the reflection of photons deviates from this model due to manufacturing limitations in making a perfectly specularly reflecting surface.

A more complex and realistic solar-sail model is the Optical SRP force model (O-SRP), which uses the complete model given by Eq. (2.10) on a flat surface and assuming all parameters to be known constants, this results in [91, 99],

$$\boldsymbol{F}_{SRP}^{O-SRP} = \frac{WA}{c}\left(\alpha\cos\left(\theta_s\right)\left(\boldsymbol{n}_s + \frac{\epsilon_b B_b - \epsilon_f B_f}{\epsilon_f + \epsilon_b}\boldsymbol{n}\right) - 2\rho_s\cos^2\left(\theta_s\right)\boldsymbol{n} + \rho_d\cos\left(\theta_s\right)\left(\boldsymbol{n}_s - B_f\boldsymbol{n}\right)\right). \quad (2.18)$$

The O-SRP is widely used in literature [138, 139, 140, 141, 142] because it permits to capture the tangential force component generated by the sail-photon interaction, contrary to the I-SRP model. Typical values of the optical coefficients in Eq. (2.18) are given by the front surface of the ACS3 with $\alpha = 0.1$, $\rho_s = 0.74$, $\rho_d = 0.16$, $\epsilon_f = 0.03$, and ϵ_b = 0.6 [143]. These coefficients illustrate that state-of-the-art sail surfaces are quite far from perfectly specularly reflecting properties ($\rho_s = 1$).

Note that for each of these models macroscopic holes in the sail should be accounted for by considering an effective surface area, and microscopic holes can be considered through the transmittance of the membrane [127]. Furthermore, all models described until now have relied on the flat surface assumption, however, the forces obtained from different surfaces can be summed up together by considering different parts of the spacecraft as separate flat panels. This results in the so-called N-plates model [131]. Note that this model is generally considered for conventional spacecraft, rather than solar-sails.

A number of more refined models have been derived based on the O-SRP formulation. These models are generally considered too refined for preliminary analysis of solar-sails dynamics [99], but could prove useful to verify the development results on a more realistic sail model. Furthermore, they remain useful for validation studies. Therefore, key ones are briefly described in the following.

The Generalised Sail Model (GSM) for solar-sails of arbitrary shapes was derived by Rios-Reyes and Scheeres [144] and further demonstrated in [145]. The papers derived compact expressions for the total sail force and moment in terms of tensors and dyads, permitting to characterise the entire sail shape using 19 parameters, assuming that the sail shape is fixed and no self-shadowing occurs. This permits to compute the forces and moments analytically, by describing the deviations from the O-SRP model for flat sails in tensors obtained by integrating the differential forces generated by differential areas [146]. A number of studies have used this model [147, 148, 149, 150, 151], as it is considered to be one of the most comprehensive models proposed in literature.

However, the GSM fails to capture the dependence of optical properties on the sail attitude, the distance to the luminous body, and the sail roughness (microirregularities). This was taken into account by Mengali et al. [152] to develop a model (labelled N-SRP hereafter) based on the experimental data of the Aurora project presented by Vulpetti and Scaglione [153], showing that the light incidence angle has the largest effect of the three considered independent variables. Mengali et al. [152] found differences of 5-10% in optimal interplanetary transfer times between the O- and N-SRP models[7], which may be neglected for preliminary studies.

Another aspect that has not been taken into account in the previous models is the degradation of the optical properties as a function of time. This was developed by Dachwald et al. [154] (this model is labelled OD-SRP hereafter), and used by McInnes [155] to determine a closed-form solution for solar-sail spiral trajectories including membrane degradation. Dachwald et al. [154] found that the O-SRP model was most sensitive to the values of ϵ_f, ρ_s and ρ_d, while the rest could safely be assumed constant for first order analysis. The model simulations degradation as an exponential decay of key optical parameters to a final value in relation to the radiation dose it was subject to [99]. Furthermore, Dachwald et al. [156] showed that the impact of the solar-sail degradation has a potentially very significant effect on optimal transfer times and time histories for a number of trajectories in the solar system and to Lagrange points. As the present work will focus on the relation between the solar-sail and a debris field at a given time or on short periods of time, this model was discarded.

[7] But the time histories become significantly different for large surface roughness.

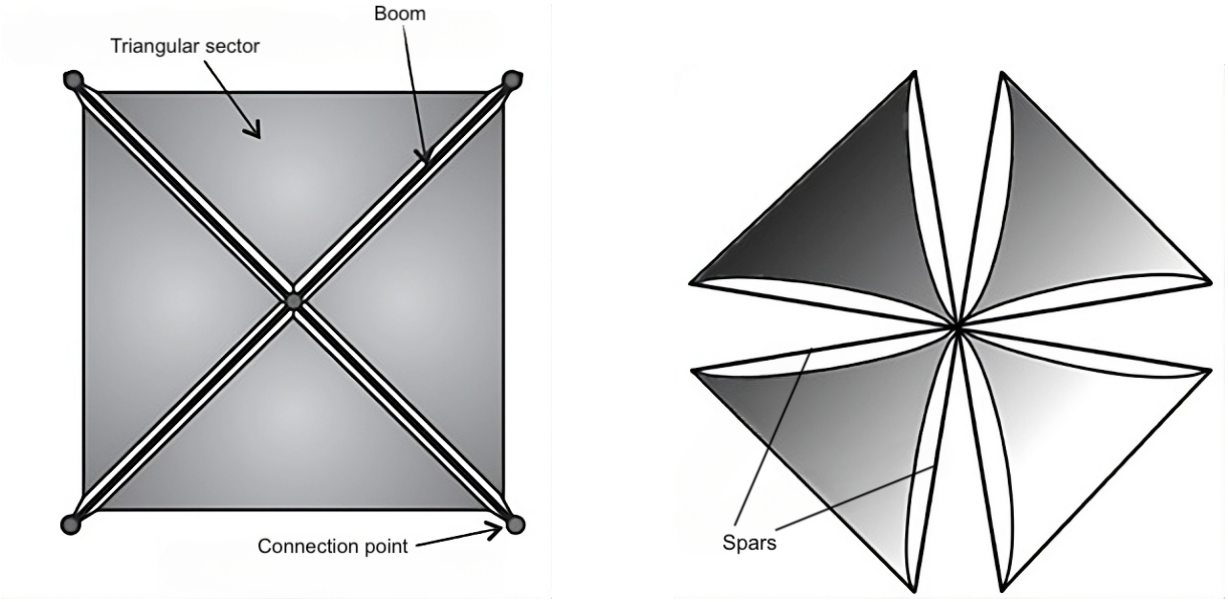

(a) Square sail configuration from [163].

(b) Quad sail configuration [99].

Figure 2.18: Rigid solar-sail configurations.

The dependence between the sail shape and the SRP itself can also have an effect on the resultant SRP force, such as wrinkling and billowing [157, 158, 159]. Additionally, relativistic effects need to be considered for very fast sails [160, 99], but this is not applicable to the present work studying a solar-sail in Earth orbit.

It is clear that the models briefly presented above only incorporate specific aspects of modelling a realistic sail. Further work should focus on combining these aspects into a single cohesive solar-sail model which would bring the state-of-the-art closer to realistic sails. However, while such model is the logical path forward in literature, such a high accuracy is rarely required and may result in an added programming and computational effort. Simpler models such as the O-SRP can be sufficient to assess key features of solar-sail technology.

2.2.3. Types of solar-sails and Sail Performance Metrics

solar-sails are generally classified as either rigid or non-rigid sails, where the former makes use of a supporting structure to retain its shape while the latter uses the centripetal acceleration arising from its rotational motion [99]. Note that different methods of attitude control will be required for each type. Both types of solar-sails will be shortly discussed below along examples of configurations available to both. Then, key sail performance metrics will be described.

2.2.3.1. Rigid Sails

According to Wie [161] and Fu, Sperber, and Eke [99], the rigid sail type is the most likely to be adopted for near-term missions. A number of rigid solar-sail configurations exist, all based on the presence of a supporting structure aiding the sail deployment and retaining the sail shape [91]. For each alternative, spars connect a central hub with the edge of the sail membrane, but the exact number of spars depends on the configuration chosen [99]. The minimum-weight configuration is a standard square sail with four spars joining the corners of the square, as shown in Figure 2.18. However, this configuration does not allow independent movement of the different quadrants, which may be desirable for attitude control purposes [99]. This is allowed by the quad configuration illustrated in Figure 2.18b, at the cost of a higher structural mass fraction (2 spars per quadrant). Similarly, a number of other variants exist [162]. The LightSail-2, which demonstrated solar-sailing capabilities in 2019, was a square rigid sail [117].

2.2.3.2. Non-Rigid Sails

Only two configurations fall in the non-rigid category: the heliogyro and the disc solar-sails.

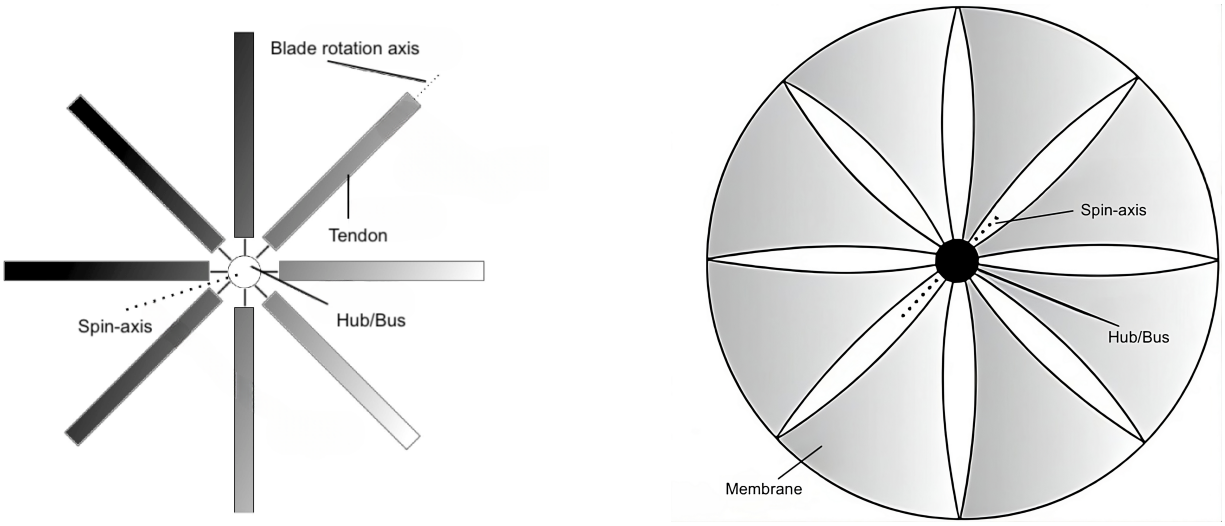

(a) Heliogyro configuration from [99].

(b) Disc sail configuration [99].

Figure 2.19: Non-rigid solar-sail configurations.

The heliogyro concept presented in Figure 2.19a divides the sail area into blades spread around a centre hub containing the spacecraft bus [164]. The blades are long, slender, and maintained in tension through the spin-induced centripetal force. The blades are weighted at their tips and attached to tendons to aid the force distribution throughout the blade [99]. The main advantage of this configuration is its ability to quickly and periodically change the pitch of each blade independently, permitting to directly generate a body torque used for attitude control (complete 3-axis control is possible [165]), as well as its ease of packing and deployment which do not require a stiffening structure of mechanisms [164]. According to Wilkie et al. [165] the most in-depth study of the design concept dates back to the work performed at the Jet Propulsion Laboratory (JPL) in 1977 for the Comet Halley rendezvous mission [166, 167], but the concept found a renewed interest over the past decade [168, 169, 170]: “Our initial efforts have been encouraging and lead us to conclude that a credible, near-term heliogyro technology demonstration mission is possible at an affordable cost” [165, p.18].

The disc solar-sail shown in Figure 2.19b consists of a continuous film held flat through spin-induced tension. This offers the same potential advantages as the heliogyro concept, but avoids the extremely long and slender blades [91]. One key difference with the heliogyro, however, is that no inclination of parts of the sail is possible, meaning that Centre of Mass (CoM) based attitude control methods are required. Additionally, some structural elements may be used to provide stiffness to the sail [91]. Note, however, that disc sails are not necessarily circular [99]: The IKAROS sail from JAXA, which was square but non-rigid, launched in 2010 belongs to this category [171].

2.2.3.3. Sail Performance Metrics

With such a variety of basic configurations available, general Figures of Merit (FoM) are required to allow for performance comparisons. Three key metrics have been commonly used in literature to evaluate and compare the performance of solar-sails. The most common metric is the characteristic acceleration a_0 [91],

$$a_0 = \frac{2\eta P_{max}(r_\odot = 1\ \text{AU})}{\sigma_{sail}} = \frac{2\eta P_{max}(r_\odot = 1\ \text{AU}) A_{SRP}}{m}, \tag{2.19}$$

where $\sigma_{sail} = m_/ A_{SRP}$ is the sail loading. The characteristic acceleration characterises the maximum acceleration generated by the solar-sail in a Sun-facing attitude at 1 AU [91, 99]. Furthermore, note that the sail loading number is also a common figure of merit in itself. A third performance metric is given by the sail lightness number,

$$\beta = \frac{2P_{max}(r_\odot) A_{SRP}}{\mu_\odot m / r_\odot^2}, \tag{2.20}$$

Table 2.2: Characteristic acceleration, lightness number, and sail loading of the ACS3, IKAROS, NanoSail-D2, and LightSail-2 missions.

Mission	Launch year	a_0 [mm/s/s]	β [-]	σ_{sail} [kg/m^2]
ACS3 [143]	2024	0.0454	0.0077	0.2
LightSail-2 [173]	2019	0.0590	0.0099	0.154
NanoSail-D2 [173]	2010	0.0227	0.0038	0.4
IKAROS [173]	2010	0.0062	0.0010	1.55

where $\mu_\odot$ is the gravitational parameter of the Sun. This number describes the ratio between the maximum solar radiation acceleration (the sail is facing the Sun) and the solar gravitational acceleration. β remains constant independently of where it is measured, as both the SRP and gravitational attraction follow the inverse square law. This is shown by rewriting Eq. (2.20) using Eq. (2.6) and Eq. (2.8),

$$\beta = \frac{4W(r_\odot)A_{SRP}}{c\mu_\odot m/r_\odot^2} = \frac{4L_\odot A_{SRP}}{c4\pi r_\odot^2 \mu_\odot m/r_\odot^2} = \frac{L_\odot}{c\pi\mu_\odot}\frac{A_{SRP}}{m}, \tag{2.21}$$

where clearly, the right-hand-side is independent of the position of the sail with respect to the Sun. Furthermore, both the sail characteristic acceleration and lightness numbers can be written in terms of the sail loading as [172, 92],

$$a_0 = \frac{9.08 \cdot 10^{-6}}{\sigma_{sail}} \tag{2.22a}$$

$$\beta = \frac{1.53 \cdot 10^{-3}}{\sigma_{sail}}. \tag{2.22b}$$

Table 2.2 provides an overview of the performance metrics of key solar-sailing missions.

2.2.4. Attitude Control

The direction of the thrust generated by a solar-sail is dictated by its attitude, meaning that the sailcraft requires an accurate and robust Attitude Control System (ACS) to follow a desired trajectory. However, conventional systems (such as reaction/momentum wheels and control moment gyros) are ineffective for spacecraft with a large Mass Moment of Inertia (MMI), like sailcraft in full deployed state [161]. Additionally, the propellantless nature of solar-sails motivates the use of a propellantless ACS to not diminish the primary attractive feature of solar-sails [92]. Therefore, SRP-based control methods making use of the shift between the Centre of Pressure (CoP) and CoM of the spacecraft have been studied in great detail for solar-sails [99]. In practice, sailcraft are designed to have their CoP and CoM coincide in default state, and the ACS shifts one of them to generate a moment on the structure. While this type of ACS was never implemented as the primary system on flown solar-sails, the use of SRP to control the attitude of a spacecraft was validated in-flight for both Earth-orbiting and interplanetary spacecraft through the use of flaps or asymmetrical twisting of solar panels to generate windmill torques [161]. In the following, the most common attitude control methods used for solar-sails are shortly presented.

While the methods presented below are classified based on whether they shift the CoP or CoM, some methods are only available to rigid sails. The lack of structural rigidity of non-rigid sailcrafts prevents the use of ACS relying on mechanisms or moving masses, and moving the CoM off the spin axis would be unwise. Additionally, the attitude control concept of non-rigid sails needs to be compatible with the spinning motion (periodic ACS). However, concepts available to non-rigid sails are generally also available to rigid spacecraft. [99]

2.2.4.1. Centre of Mass Offset Methods

Figure 2.20 presents the two most promising mass-based ACS for solar sails. In these figures, $\boldsymbol{T}$ gives the resultant torque of the ACS, and the centres of mass and pressure are indicated by *cm* and *cp* respectively.

Figure 2.20a presents the gimbaled mass method (where the mass and length of the rod are exaggerated). The concept relies on the shift of the CoM through the two rotational degrees of freedom of the rod (θ_g, ϕ_g) [99]. However, as the gimbal mass m_g is generally much smaller than the sail mass, the centre of mass will only have a very small out-of-plane component. Therefore, it is often assumed to remain in the

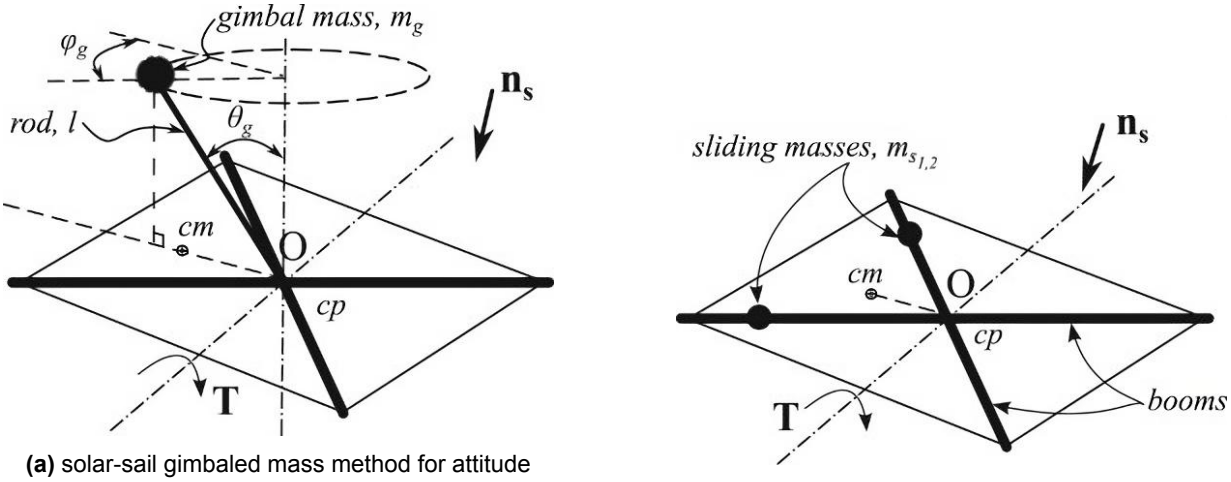

(a) solar-sail gimbaled mass method for attitude control.

(b) solar-sail sliding mass method for attitude control.

Figure 2.20: Centre of mass based attitude control methods [99].

sail plane, meaning that spin torques are not achievable [99]. The spacecraft bus can also be used as gimbal mass for mass efficiency [92]. Sperber, Fu, and Eke [174] presented the nonlinear equations of motion of a three-dimensional gimbaled solar-sail along algorithms for attitude control.

The second method aiming to change the position of the CoM for attitude control is presented in Figure 2.20b, and consists of trimming the centre of mass by moving ballasts ($m_{s_{1,2}}$) in the sail booms [175, 99]. Each mass has a single degree of freedom, and could consist of payload elements. Romagnoli and Oehlschlägel [176] presented a high-performance controller for this concept, extending the work of Wie and Murphy [177] and Bolle and Circi [178]. According to Fu, Sperber, and Eke [99], this approach particularly has great potential for future missions.

As these methods cannot provide three-axis attitude control, they need to be supplemented by an additional method [92]. This also permits to add redundancy to the system. For example, Wie [179] studied a system using a gimbaled mass with control vanes (see Figure 2.21a below) and Murphy, Murphey, and Gierow [180] derived three-axis stabilisation by gimbaling a mass on an extended boom.

2.2.4.2. Centre of Pressure Offset Methods

Figure 2.21 shows a number of ACS relying on shifting the CoP of the sail with respect to the total spacecraft centre of mass with little to no impact on the CoM position.

Figure 2.21a shows the control vane method applied to a square sail, however, the method can be applied to any rigid solar-sail [99]. The concept resembles aircraft control surfaces which create a torque by asymmetrically deflecting the airflow on small portions of the wing, except that, in this case, light is reflected instead [175]. The vanes are positioned at the end of the supporting booms to allow for a large moment arm, and possess two rotational Degrees of Freedom (DoFs) to allow for three-axis stabilisation. However, the system becomes over-constrained when more than three total DoFs are present (two DoFs per vane) [175], rendering the control system design laborious: determining the control torque from a known state is straightforward, but determining the right vane angles to obtain a specified torque through the eight control inputs is challenging [99]. A simplified control problem, limiting the movement of each vane to the plane defined by the sail normal and the boom direction, was studied by Wie [179]. Subsequently, the under-constrained control allocation problem was studied by Choi and Damaren [181] who found that any desired rotation can be achieved in approximately two hours at 1 AU. Additionally, issues relative to self-shadowing and deployment sensitivity have been tackled by Kun [182] and Quadrelli and West [183], respectively [99].

Figure 2.21b presents a reflectivity-based attitude control method, aiming to change the reflectivity of portions of the sail-film to shift the CoP of the sail [99]. The reflectivity of the sail membrane is changed through Reflectivity Control Devices (RCDs) which switch between specular (ON) and diffuse reflection (OFF) by becoming more or less transparent [184]. As described in Section 2.2.2.2, diffuse and specular

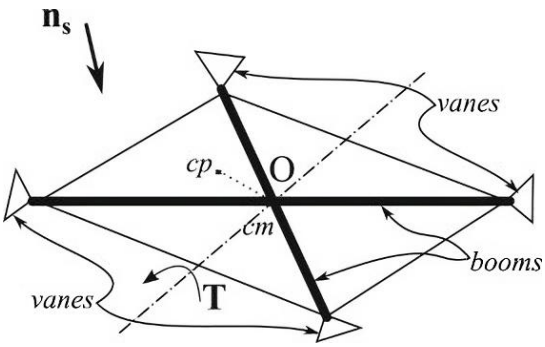

(a) Solar-sail vane method for attitude control.

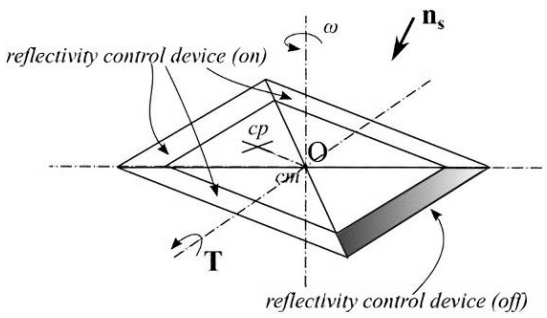

(b) Solar-sail reflectivity method for attitude control.

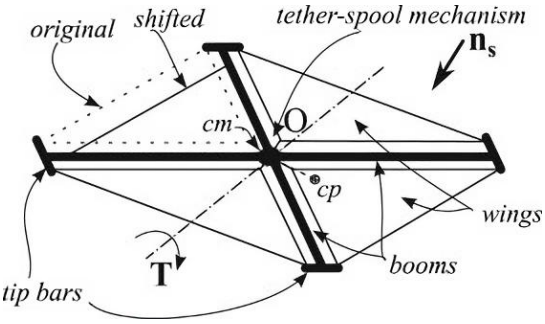

(c) Solar-sail shifted wings method for attitude control.

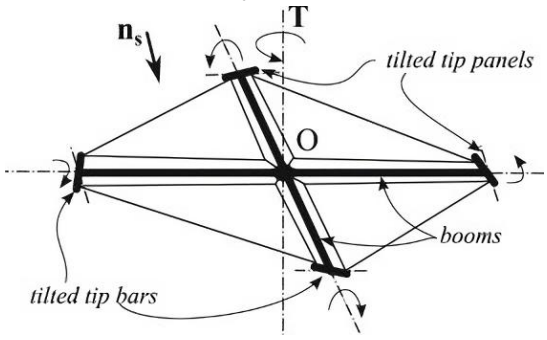

(d) Solar-sail twisted wings method for attitude control.

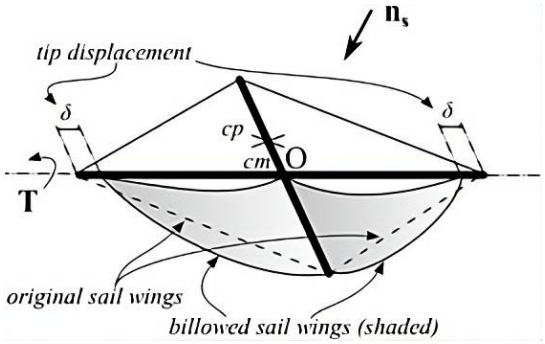

(e) Solar-sail billowed wings method for attitude control

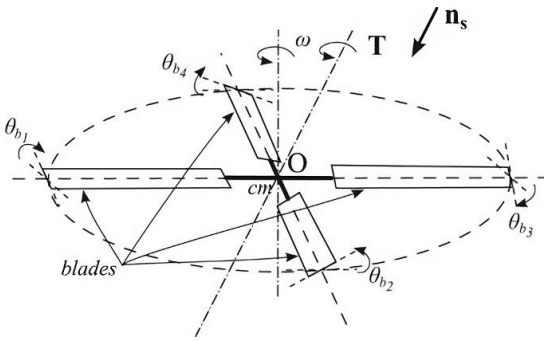

(f) Heliogyro solar-sail attitude control concept.

Figure 2.21: Centre of pressure based attitude control methods [99].

reflections generate different forces on the sail material, meaning that a torque can be generated. The devices are positioned directly on top of the sail material, providing minute and continuous control inputs. This concept was successfully demonstrated by JAXA with the IKAROS spacecraft [184], providing a stable and oscillation-free (in the sail material) ACS for non-rigid solar-sails. Note, however, that no windmill torque can be applied in the flat sail case [99]. Furthermore, a more advanced version of the method was studied by Borggräfe et al. [185] by considering electro-chromic coating across the complete sail in both continuous and discrete fashion.

Figures 2.21c and 2.21d illustrate two concepts relying on controlled deformations of the sail through actuation of the boom tips. The former is the shifted wings concept, which decreases the area of a portion of the sail (here a quadrant) by shifting its boom-attachment point while maintaining tension in the surface[8] [99]. The latter is the twisted wing concept, which consists of rotating a boom around its length to incline a specific quadrant of the sail [99]. The combination of both methods was introduced by Wie [179], giving full three-axis attitude control (the former cannot introduce a spin torque).

[8]Note that a significant portion of the spacecraft mass should be in the centre of the sail to avoid major shifts in the sail CoM.

The billowed wing concept, also called “tip displacement method” is presented in Figure 2.21e. The billowing phenomenon refers to the “inflation” of the sail material due to the solar pressure (similarly to the effect of wind on a ship’s sail), and is present on all solar-sails [186]. While this effect is generally considered as a disturbance of force models, it can also be controlled to perform three-axis attitude control [99]. The system was thoroughly analysed in [187, 188, 189], providing a thorough mathematical treatment of the ACS and the deformation of the sail film under SRP. The method is particularly suited to large sails, for which the influence of wrinkling is negligible, and only requires simple mechanisms in comparison to other concepts such as the twisted/shifted wings or control vanes [99].

The heliogyro configuration was described in Section 2.2.3, having a very distinctive layout resembling a windmill or helicopter. This geometry permits the design of an ACS using blade pitching to shift the CoP of the sail with respect to the spacecraft centre O (where the CoM will usually be located) [99]. Due to the spin necessary to maintain tension in the blades, the blade pitching occurs periodically, permitting to achieve three-axis attitude control. The simplest heliogyro model relies on the assumption of rigid blades, however, very high length-to-width ratios are common and the lack of a supporting structure renders blade structural dynamics non-negligible [190]. Blomquist [190] reviewed several blade models and studied heliogyros with length-to-width ratios in the 1000s. Wilkie et al. [191] found no intractable stability and control issues for the heliogyro solar-sail concept. Pimienta-Penalver [192] further improved the discrete-mass heliogyro blade model. Additionally, several pitching methods and ways to combine them to generate a specified torque were presented by Guerrant and Lawrence [193].

2.2.4.3. Passive Methods

Passive attitude control methods aim to maintain a particular attitude with respect to an external body, such as the Sun. This is achieved through specific geometries which converge towards a Sun-pointing attitude under the influence of SRP. A variety of configurations have been considered, ranging from spherical balloons and two-folding sails made of unequal reflective rectangular plates to conical sails [92]. Providing a theoretical basis to passive stability design, Hu, Gong, and Li [194] performed a linear stability analysis to determine the general passive stability criteria for three-axis stabilisation of axisymmetric curved solar-sails. However, a detailed review of these configurations is outside the scope of this work.

Passive attitude control can also be achieved through spin-stabilisation, which permits to average thrust vector misalignments [161]. These thrust vector misalignments can arise from sail shape uncertainties or manufacturing defects producing an undesired CoM to CoP offset and introducing a constant torque, destabilising the sail [99]. Furthermore, spin-stabilisation can be leveraged to passively station-keep the sail by cancelling aerodynamic, gravitational, and solar radiation disturbance torques, as studied by Lawrence and Whorton [195] and Gong, Li, and Zhu [196]. When spin-stabilisation is employed, active attitude control comes back to controlling the precession and nutation of the spin-axis.

2.2.4.4. Other Attitude Control Systems

Other concepts have been proposed through literature, such as the use of Pulse Plasma Thrusters (PPTs) [175]. While the concept defeats the propellantless purpose of solar-sails, Wie et al. [197] explains that the large moment arm would permit to significantly reduce the reaction mass requirement: Gong and Li [198] found that only 0.1 kg of propellant would be necessary for a Venus transfer of a 20 m-side square sail with PPTs having an a specific impulse, I_{sp}, of 700s and a thrust level of 150 mN. Additionally, this removes the direct Sun-dependence of the ACS, meaning that attitude control is feasible during eclipse time if enough energy is stored in a battery system. However, PPTs require significant power consumption and could introduce translational dynamics if not properly accounted for [175]. The system is considered to be a suitable back-up system or as a primary system for short missions [199].

Another system is shown in Figure 2.22, combining both CoP and CoM shifts and is applicable to any solar-sail type [200]. It consists of a series of moving-mass booms attached to the spacecraft bus and extended by reflective surfaces with a single DoF (along the axis they are positioned on), resulting in full three-axis control capabilities of the sail. According to Adeli, Theodorou, and Lappas [200], one of the main advantages of such system is that the ACS is completely decoupled from the sail, meaning that it can be scaled and integrated with any sail deployment mechanism. The trim-control mass part of this ACS was also demonstrated through ground testing [200].

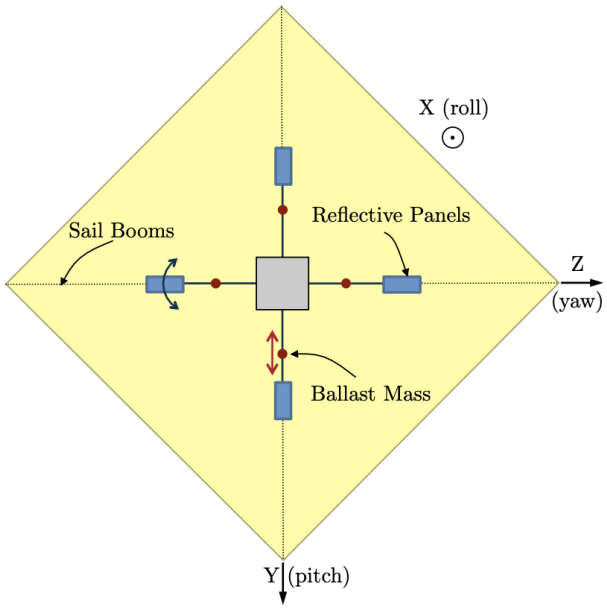

Figure 2.22: Scalable bus-based attitude control system concept [200].

2.2.5. solar-sail Trajectories

In their most basic dynamical framework, solar-sail trajectories can be considered in a system with the gravitational attraction of the centre body and the SRP force arising from the Sun. In the Sun-centred case, the dynamic equations of a solar-sail then become [92],

$$\begin{cases} \dot{\boldsymbol{r}}_{\mathcal{I}_\odot} = \boldsymbol{v}_{\mathcal{I}_\odot} \\ \dot{\boldsymbol{v}}_{\mathcal{I}_\odot} = -\frac{\mu_\odot}{||\boldsymbol{r}_{\mathcal{I}_\odot}||^3}\boldsymbol{r}_{\mathcal{I}_\odot} + \beta\frac{\mu_\odot}{||\boldsymbol{r}_{\mathcal{I}_\odot}||^4}(\boldsymbol{r}_{\mathcal{I}_\odot}\cdot\boldsymbol{n}_{\mathcal{I}_\odot})^2\boldsymbol{n}_{\mathcal{I}_\odot} \end{cases} \tag{2.23}$$

where $\boldsymbol{r}_{\mathcal{I}_\odot}$, $\boldsymbol{v}_{\mathcal{I}_\odot}$, and $\boldsymbol{n}_{\mathcal{I}_\odot}$ are the sailcraft position, velocity and surface normal vectors expressed in an inertial reference frame $\mathcal{I}_\odot$ ($X_{\mathcal{I}_\odot}$, $Y_{\mathcal{I}_\odot}$, $Z_{\mathcal{I}_\odot}$) with origin at the centre of mass of the Sun. In this reference frame, $X_{\mathcal{I}_\odot}$ points in the direction of the vernal equinox at the J2000 epoch, $Z_{\mathcal{I}_\odot}$ is perpendicular to the ecliptic plane, and $Y_{\mathcal{I}_\odot}$ completes the right-handed reference frame. In this set of equations, the I-SRP model was used to express the SRP force on the sail. The primary performance metric is often the transfer time, due to the propellantless nature of the solar-sail [92]. Earth-centred trajectories, on the other hand, have been considered to be much more complex due to the wider range of perturbations from the Earth higher-order gravitational terms, atmospheric drag, and magnetosphere [99]. These perturbations have rendered the development of Earth-centred control laws more complex than for heliocentric trajectories, resulting in some authors advocating against the use of solar-sails in Earth orbit [99]. As a result, only few studies have considered Earth-centred dynamics and control. Furthermore, the complex dynamical environment renders the methods and results from literature only valid under simplifying assumptions on the orbit shape and orientation with respect to the Sun, and for limited orbital transfer cases [123]. However, the use of solar-sails in Earth orbit has recently gained more interest and was shown to be feasible despite the complexity of the dynamical environment (orbit raising is possible from altitudes as low as 400 to 600 km depending on the solar activity) [123].

Several early studies on the topic of solar-sailing dynamics and control in Earth orbit have been performed based on the very simplistic models described by McInnes [91] of an ideal solar-sail (I-SRP model) in an unperturbed environment around the Earth. These studies include analytical control laws where different independent laws are blended together [201] and specific mission applications such as the GeoSail mission [202]. The latter particularly demonstrated the existence of a non-Keplerian orbit permitting to artificially precess the orbit apse line, meaning that the orbit is not fixed in inertial space anymore (like Keplerian orbits). This is shown in Figure 2.23, which displays the GeoSail mission orbital evolution over 30 days. Other works based on the same simplified model considered Earth escape trajectories [203, 204]. However, perturbations such as the aerodynamic drag and planetary radiation pressure can result

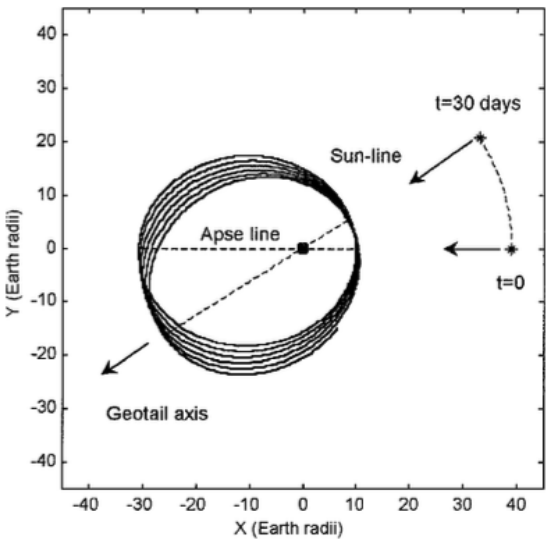

Figure 2.23: GeoSail mission orbit evolution over 30 days [202].

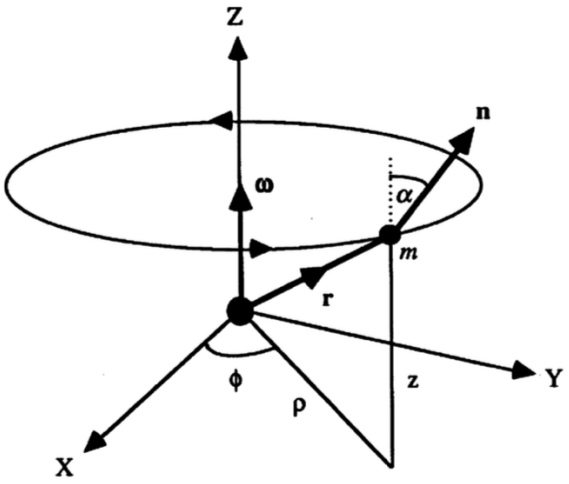

Figure 2.24: Displaced orbit with thrust-induced acceleration [207].

in accelerations of the same order of magnitude or greater than the SRP, meaning that these studies have little applicability to high-fidelity mission design for Earth orbiting solar-sails [123]. Furthermore, prior studies to these that did consider perturbations neglected basic constraints such as non-negative altitudes [205], with Macdonald and McInnes [204] being the first study to implement such a constraint while retaining the optimality (in two-body dynamics).

Another type of trajectories which was studied around the same time period are Highly Non-Keplerian Orbits (HNKOs). These orbits have been defined by McKay et al. [206] as dynamical cases where the time-averaged acceleration exerted by the spacecraft over a full orbit ($||\bar{a}||$, eg., through a sail thrust or electric propulsion) is at larger or equal to the combined gravitational and centripetal acceleration experienced by the object ($||\nabla \boldsymbol{v}||$, as viewed in a reference frame rotating at a given angular velocity relative to an inertial frame). This can be formulated as, $||\bar{a}||/||\nabla \boldsymbol{v}|| \geq 1$, although no definition is widely agreed upon. Displaced Earth-centred orbits, shown illustrated in Figure 2.24, are examples of these cases and have been shown to be generally controllable by McInnes [207]. The basic principle relies on the use of a low (but continuous) thrust to displace the orbital plane such that it does not pass through the centre of mass of the centre body anymore [206]. These non-Keplerian orbits can then be patched between each other and to Keplerian orbits (by zeroing the thrust), resulting in increasingly more complex trajectories [208, 209]. It must be noted, however, that since solar-sails require a direct exposition to the sunlight to generate their thrust, displaced orbits which include eclipse periods are infeasible. Furthermore, these orbits have been shown to be controllable under two-body dynamics with the addition of SRP, which means that the displaced orbit must be far enough from the centre body for key perturbations (such as atmospheric drag, oblateness of the centre body, and so on) to be negligible.

Among the limited studies of solar-sails in a perturbed planet-centred environment, some considered the coupling of the SRP force with Planetary Radiation Pressure (PRP) [210, 211]. Particularly, in eclipse, PRP is the only source of thrust which can be leveraged to continue an orbital transfer despite the lack of direct sunlight. Neglecting PRP in the dynamical model was also shown to lead to significant errors (up to 55% relative error in altitude in LEO) [122]. Other studies considered SRP and aerodynamics-based optimal control laws [212, 213] and drag-induced active debris removal and de-orbiting capabilities, as discussed in Section 2.1.3. More recently, Carzana, Visser, and Heiligers [123] developed a novel approach to optimise Earth-bound solar-sail trajectories from any steering law and in any orbital regime, thereby opening the door to more general solar-sailing around the Earth than the previous limited studies. Furthermore, Leemans, Carzana, and Heiligers [214] used Differential Dynamic Programming (DDP) to find optimal Earth-centred solar-sail trajectories, which further permits to optimise constrained trajectories in the perturbed Earth environment.

This subsection has been focused on planet-centred trajectories, however, a much wider variety of solar-sail trajectories have been studied in literature for cases which are not specifically planet-centred. These generally make use of the free low-thrust propulsion bound to solar-sailing to generate non-Keplerian orbits [206]. An extended version of the three-body problem then arises with the photogravitational three-body problem [91], yielding displaced Lagrangian points (or surfaces depending on the thrust level achievable) and displaced halo orbits, which are only subsets of Artificial Equilibrium Points (AEP) and periodic orbits about AEPs respectively [206]. Similarly to planet-centred displaced orbits, displaced orbits about the Sun are also achievable [91]. Low-cost transfers can also be designed with specific invariant manifolds [215, 92], and interplanetary transfers can benefit from very unconventional concepts such as the H-reversal [216] or solar-photonic assists [217] to gain great amounts of momentum quickly. Note that all the examples mentioned above, except the H-reversal and solar photonic assist, are more generally applicable to low-thrust propulsion systems. However, many of these were first studied through solar-sails as they become most attractive for propellantless systems [206].

2.3. On-Orbit Collision Research

While the use of a solar-sail in Earth orbit for ADR has various advantages, the large spacecraft cross-sectional area increases significantly the risk of collision with Meteoroids and Orbital Debris (MODs). Although collisions with a large debris remain unlikely, collisions with thousands of smaller MODs can be expected [218]. Despite collision velocities up to 10 km/s for space debris and 70 km/s for meteoroids, these Hypervelocity Impacts (HVI) generally remain non-catastrophic for conventional spacecraft [219], in contrast to the collisions modelled by the SSBM described in Section 2.1.2.2. As a result, the spacecraft remains generally intact but some small (mostly non-trackable) debris are produced [5]. Although definitions vary in literature, HVIs refer to the scenario in which the impact velocity becomes so large that the strength of the materials is sufficiently small in comparison to inertial forces and the solid target material then behaves like a fluid [220].

In this section, a brief introduction to the field is given. First, Section 2.3.1 provides a general description of the physics related to hypervelocity impacts. Second, Section 2.3.2 describes the state-of-the-art in terms of the understanding of the momentum transfer arising from HVIs. At last, Section 2.3.3 provides a brief description of the key features of hole growth and hole diameter estimations, as the primary solar-sail degradation effect of HVIs.

2.3.1. Hypervelocity Impact Physics

The physics of hypervelocity impact are essentially the same for both orbital debris and meteoroids, meaning that the processes described below are similar in both cases [221]. To gain an understanding of the physical process of HVIs, both hydrocodes and hypervelocity experiments have been used [222, 223, 224, 18, 225], permitting to determine the influence of different parameters under well-controlled conditions.

In the simplest case, when a spherical projectile hits a ductile target at low-velocities, plastic deformation of the target prevails. As the impact velocity is increased, the projectile tends to breakup and melt, leaving a characteristic crater and starting the particle ejection process described below. Increasing the impact velocity further, elastic and plastic stress–strain behaviour prevails, density and compressibility effects set in, and finally thermal properties become important. After impact with the target, compression waves travelling in the material steepen until a shockwave carrying jumps in density, pressure, grid-point velocity, and internal energy is formed. For targets of finite thickness, free boundaries (for example, the other end of a thin plate) reflect the compression waves forming the shock as tensile waves, and superposition of both types can yield plastic deformations on the other side of the plate with respect to the impact. Different impact damages are shown in Figure 2.25, demonstrating damages ranging from complete fracture when exceeding cohesive material strength (left most) to plastic deformation (right most). In this figure, d_p is the projectile diameter, t_t is the target object thickness, and $\boldsymbol{V}_I$ is the impact velocity vector. These impacts put the target materials under extreme conditions, reaching around 10,000 K and 100 GPa in temperature and pressure, respectively, for high velocities and slender bodies, and happen within time scales of microseconds only. [18]

The effects of HVIs on the spacecraft depend strongly on the size and relative velocity of the impactor [229]. However, aspects such as the impact geometry, impactor shape and density, target thickness, and

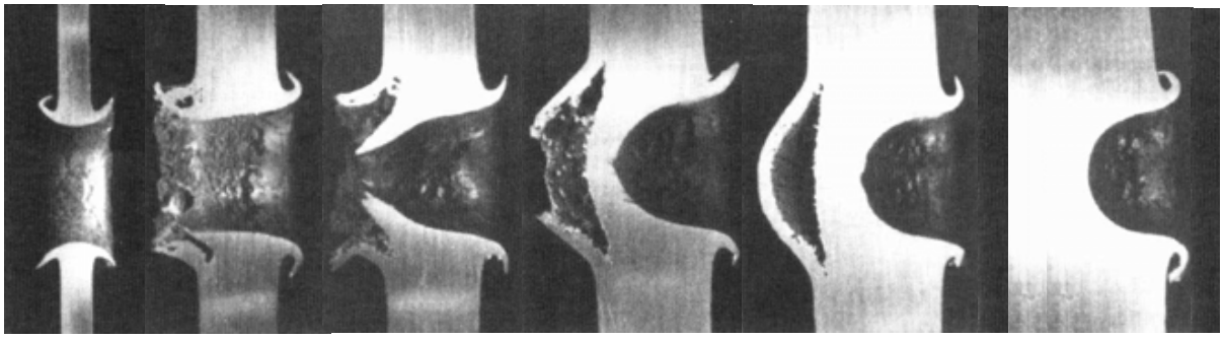

Figure 2.25: Single-wall impact damage characteristics on aluminium 1100 targets, as a function of the relative target thickness $t_t/d_p = 1.0, 2.4, 2.8, 3.4, 3.9, 10.0$ (left to right), for an impact by a glass projectile of diameter $d_p = 3.2$ mm at a velocity of $||\boldsymbol{V}_I|| = 6$ km/s (note: display of right most target is truncated in thickness) [226, 18].

so on can also play a significant role on the overall effect of the impact [221]. Drolshagen [228] described the main effects of hypervelocity impacts on a spacecraft, and grouped them as follows[9]:

1. **Cratering and ejecta**
   - Surface erosion and degradation leading to a change in thermal, optical or electrical properties.
   - Degradation of sensors and mirrors, including impacts on internal instruments by secondary ejecta.
   - Degradation of windows (even relatively small craters require the exchange of Space Shuttle windows).
   - Sealing problems if for example exposed hatches have to be closed.
2. **Plasma effects**
   - Electrical interference.
   - Current flow.
   - Triggering of electrostatic discharges.
   - Light flashes.
3. **Structural damage**
   - Penetration of spacecraft walls, leading to structural damage of subsystems.
   - Penetration of pressurised vessels (tanks, manned mod- ules, coolant loops).
   - Cutting of cables or tethers.
   - Short circuits.
   - Damage to exposed focal plane arrays like CCDs.
   - Complete destruction of impacted spacecraft or spacecraft subsystem by larger object.
4. **Momentum transfer**
   - Change of attitude.
   - Loss of target lock.
   - Loss of formation flying.

Of particular importance to gossamer structures, despite having received very little attention from literature [221], is the momentum transfer resulting from such a collision with a debris having a significant kinetic energy. This effect is generally small for conventional spacecraft, but can become significant for high area-to-mass ratio satellites due to the large moment arm of collisions occurring at the extremes of the structure [218]. The impulse endured from such a collision could possibly result in disruptions in the attitude of the sail [230], which, for a solar-sail, is inherently linked to the orbital motion. Furthermore, this risk is intensified by the low-thrust nature of a solar-sail, which may result in difficulties to perform collision avoidance manoeuvres with respect to larger trackable debris under short warning times. The literature surrounding HVI momentum transfers will be reviewed in Section 2.3.2.

Furthermore, during an impact, ejecta particles resulting from the HVI further contribute to the momentum transfer. In particular, they result in momentum enhancement, meaning that more momentum is transferred

[9] Taken directly from [228, p. 2]

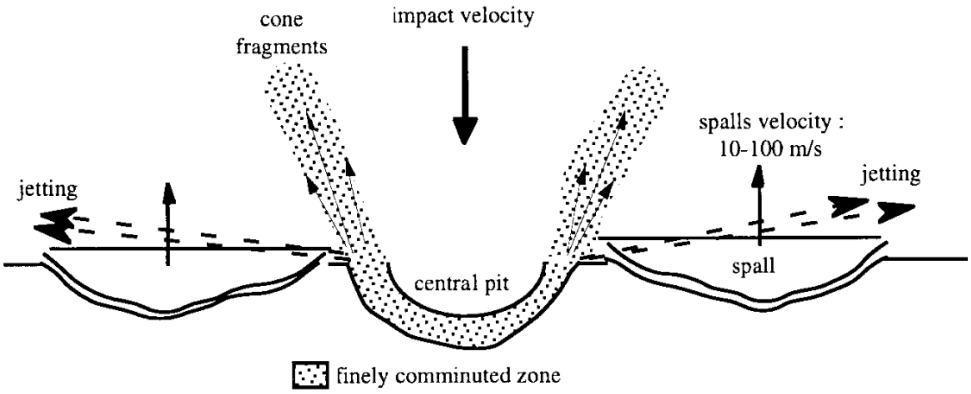

(a) Sketch of main impact crater features resulting from a normal impact [227].

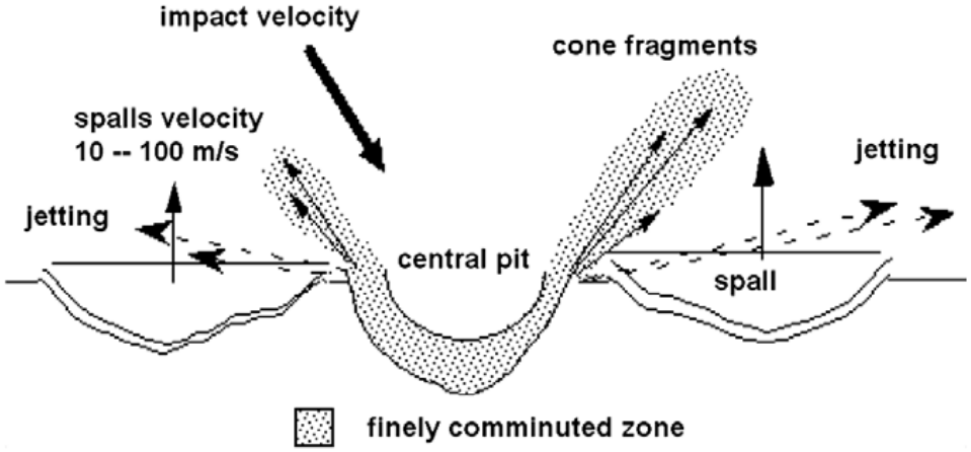

(b) Sketch of main impact crater features resulting from an oblique impact [228].

Figure 2.26: Main impact crater features resulting from a normal (a) and oblique (b) impact.

to the target than the original particle contained [219]. They come as either back-scattered (particles ejected on the side of the impact) or downrange scattered (particles ejected on the other side) ejecta [227]. The latter can form up to 75% of the secondary particles for HVI with thin targets. Rival and Mandeville [227] categorised the ejecta from hypervelocity collisions in three different kinds, as illustrated in Figure 2.26 for both normal and oblique collisions:

1. **Jetting fragments** are small, high velocity particles ejected at grazing angles during the early stages of the impact. Jetting happens before the impactor has completely penetrated the target and is completely independent from the melt and vapour production during the formation of the crater [231].
2. **Cone fragments** are small, high velocity particles ejected at constant elevation angle, creating a cone shape around the crater.
3. **Spall fragments** are large ejecta expelled at low velocities and normal to the impact surface, due to the tensile rupture of the material near to the cone site [221].

2.3.2. Momentum Transfer in Hypervelocity Impacts

Momentum is expressed as the product of the mass of an object and its velocity vector, and is always conserved in an isolated system. Therefore, in the case of a hypervelocity impact, when a projectile strikes the target object with an impact velocity V_I, momentum is transferred between the projectile, the target, and any ejecta mass arising from the collision [221]. As the ejecta fragments can be expelled backwards (relative to the velocity of the incoming projectile), more momentum than originally contained by the projectile can be transferred to the target body [232]. This phenomenon is generally considered through a momentum enhancement factor β_E [233], which characterises the additional momentum gained by the target relative to the momentum of the projectile.

During a hypervelocity impact, the momentum of the projectile is conserved in various forms [234]:

1. The internal momentum of the target object.
2. The ejecta from the impact zone of the particulate on the target body.
3. The material spalled from the non-impact surface of the target body (downrange ejecta).
4. The momentum in the same direction as the incoming particulate of all downrange ejecta when penetration of the target occurs. This also includes the original projectile momentum if full-penetration occurs.

For the same impact velocity, very small particles will only trigger process (a). As the particle size (and mass) increases, processes (b)-(c)-(d) start to occur [234]. In this work, relatively large projectiles will be considered, meaning that all these sources will become relevant. However, only the added momentum to the target object is of interest, and other processes only need to be accounted to allow an accurate estimation of the former. The momentum gained by the target can be expressed as follows [235],

$$m_t \Delta \boldsymbol{v_t} = m_p \boldsymbol{v_p} - \sum m_e \boldsymbol{v_e} = \beta_E m_p \boldsymbol{v_p}, \tag{2.24}$$

where m_t and $\Delta \boldsymbol{v_t}$ are the target object mass and velocity increment after the collision processes have completely occurred, m_p and $\boldsymbol{V_p}$ are the mass and velocity of the projectile prior to the impact, and m_e and $\boldsymbol{V_e}$ are the mass and velocity of the ejecta fragments. In other words, $\beta_E = 1 - \text{sign}(\boldsymbol{p}_e \cdot \boldsymbol{p}_p)||\boldsymbol{p}_e||/||\boldsymbol{p}_p||$ where $\boldsymbol{p}$ is the linear momentum vector of the ejecta (e) or particle (p). The ejecta momentum can be expressed as $\boldsymbol{p}_e = \boldsymbol{p}_{back} + \boldsymbol{p}_{down}$ (linear momentum of the back- and downrange scattered fragments respectively), where $(\boldsymbol{p}_{back} \cdot \boldsymbol{p}_p) < 0$ and $(\boldsymbol{p}_{down} \cdot \boldsymbol{p}_p) > 0$. Meaning that in case no downrange ejecta are generated, and no perforation occurs ($\boldsymbol{p}_{down} = \boldsymbol{0}$), $(\boldsymbol{p}_e \cdot \boldsymbol{p}_p) < 0$ and momentum enhancement occurs ($\beta_E > 1$) [221]. McDonnell [219] showed that the theoretical limit for the momentum enhancement process can be derived from conservation of energy as,

$$\beta_E < \sqrt{\frac{m_t}{m_p}}. \tag{2.25}$$

Thick targets have gained more attention recently due to the applicability of HVIs to the deflection of potentially dangerous asteroids. Particularly, Walker and Chocron [233] found that in this case, β_E is maximised when the impactor density is close to that of the target, and the projectile shape is close to a sphere. Across the different configurations tested in their numerical computations, the momentum enhancement remained between a factor of 1 to 3 for aluminium projectiles with impact velocities ranging from 1 to 10 km/s [233]. Furthermore, the momentum enhancement factor was found to be most sensitive to the tensile strength of the target material: for a lower tensile strength of a ductile material, the material fractures more and ejects more material upon impact. Therefore, for the same projectile kinetic energy, as the ejected mass increases, its velocity decreases (from the conservation of energy) and the momentum enhancement increases [233]. While the work performed by Walker and Chocron [233] remained primarily computational, Hayashi et al. [236] studied thick targets of ductile material (aluminium) through experiments, showing that momentum enhancement increases if the impact velocity is increased and the target thickness is decreased. Additionally, they found that the ejecta scattering angle varies according to the thickness of the target [236]. At last, McDonnell [219] refined the formula proposed by Nysmith and Denardo [237] the highest velocity data reported at the time, yielding,

$$\beta_E = 1 + 0.144 \frac{(||\boldsymbol{V}_I|| - 0.55)^2}{||\boldsymbol{V}_I||}. \tag{2.26}$$

The ACS3 foil has a thickness of 2.115 µm [118], meaning that standard solar-sail foils will be considered as thin or very thin ($t_t/d_p < 0.1$ [238]) in the HVI sense for a significant portion of the impacts it is subjected to. In practice, any collision with objects larger than ≈ 20 µm will may be considered under the thin target limit, which is still a significant portion of objects in Earth orbit according to Figure 2.6. The ACS3 booms, however, are hollow and up to 0.26 mm thick [118], making them significantly thicker than the sail foil. Additionally, their hollow structure means that two impacts occur (one with each side) during an HVI which is expected to increase the momentum transfer, although this configuration has not been studied in detail before. Therefore, solar-sail booms cannot be considered in the thin target limit, contrary to solar-sail foil.

Little experimental work was performed on momentum transfer overall, and none considered very thin targets to the best of the author's knowledge (most of the work on very thin targets considered hole growth). Nevertheless, the early work performed by Nysmith and Denardo [237] presented some qualitative assessments of the momentum transfer for different impact regimes as a function of the impact velocity, as described in Figure 2.27. While this qualitative plot refers to a single t_t/d_p ratio at different velocities, the graph is expected to shrink or expand horizontally for different ratios. That is, for a higher (lower) t_t/d_p, a greater (smaller) velocity is necessary to enter phase II, meaning that the graph is expanded (shrank) horizontally. The four phases of momentum transfer shown in Figure 2.27 are as follows [237]:

1. **Phase I:** the target has not been perforated nor spalled and the ejecta momentum is relatively small. More momentum is gained by the target as the impact velocity increases. Impacts with semi-infinitely thick targets lie in this category. During this phase, all the momentum of the projectile is absorbed by the target.
2. **Phase II:** at the threshold spallation velocity, v_s, material starts spalling at the rear of the target and the spray momentum (momentum from spalled material at the rear of the target) increases from zero. This reduces the gained target momentum as, which might even become negative for some t/d_p ratios. Throughout phase II, all components from the momentum balance vary smoothly.
3. **Phase III:** at the transition velocity, v_z, material is also spalled from the front surface, which causes an increase in target and ejecta momentum (the grey zone in Figure 2.27 shows that the process is a somewhat random and poorly understood). This spallation phenomenon from the front surface means that the target essentially becomes thin: the front and back surfaces become similar.
4. **Phase IV:** the momentum gained by the target is zero, which happens to very thin targets at velocities up to ≈ 8 km/s and to thick targets at much higher velocities. All the momentum is transferred to ejecta and spray (and remaining projectile fragment if not perforation occurred).

In addition, for very thin targets, McDonnell [219] suggested a scaling of Eq. (2.26) based on the Giotto data [234], yielding,

$$\beta_E = \left(1 + 0.144\frac{(V_I - 0.55)^2}{V_I}\right)\left(\frac{t_t}{t_{max}}\right), \tag{2.27}$$

where t_{max} is the maximum penetrated thickness of the material, which is a function of the area-time product. The maximum penetrated thickness of a given material provides the maximum expected penetration of the material as a result of the trajectory of area-time product [239]. Equation (2.27) shows that the gained target momentum indeed goes to zero for very thin targets.

One shortcoming of experimental works on hypervelocity impacts is the limited achievable impact velocity. This was tackled by the Giotto mission from ESA, which rendezvoused with comet Halley in 1986, and carried a dust impact detection system able to cover a mass range from 10^{-17} to 10^{-3} grams [240]. This system permitted to characterise the momentum transfer resulting from hypervelocity impacts from small particles on the dust shield, with relative velocities of the order of 68 km/s, many times higher than the 10 km/s achievable in conventional experimental setups [234]. In particular, this permitted highlighting the relationship between β_E and the impact velocity, as $10 \leq \beta_E \leq 68$ were found [234]. These values are significantly higher than anything measured prior to the Giotto mission [219].

Furthermore, the cumulative effects of this momentum transfer from meteoroids and space debris on the attitude and the trajectory of conventional and high area-to-mass ratio spacecraft have been considered by [218, 230] through the use of the MASTER MODs population. While the effect was found to be very small for both the trajectory and attitude propagations, it was more pronounced for spacecraft having a large area. The ejecta model present in MASTER-2009 from Rival and Mandeville [227] (qualitatively described in the previous subsection) was used by Sagnières and Sharf [230] to determine the momentum enhancement for the different configurations.

While this subsection provided a general understanding of momentum enhancement and which aspects are most relevant to solar-sails, defining an appropriate model for each impact scenario is a complex task. In particular, two cases of impact can be distinguished: impact with a supporting structural element and impact with the solar-sail foil. While the thin target models could be applicable to solar-sail foils, literature up to this point primarily focused on flat plate target objects of monolithic material. Only few studies considered composite structures and hollow booms such as the ones considered for rigid sails [241, 242, 221].

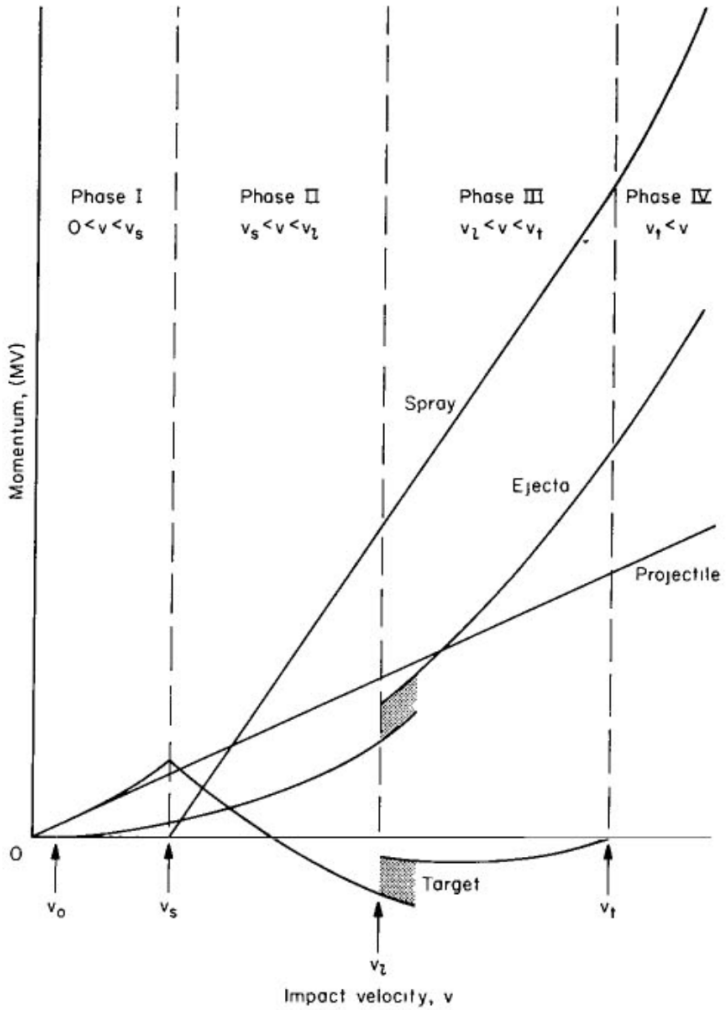

Figure 2.27: Representation of the division of the projectile momentum for a typical t_t/d_p ratio [237].

2.3.3. Solar-sail Degradation From Hypervelocity Impacts

Aside from the aforementioned momentum transfer, hypervelocity impacts also cause structural damages to the sail, the most important of which are holes in the foil that reduce the effective area of the sail. Additionally, these holes may result in a residual disturbance torque due to their asymmetric distribution. Fortunately, Edwards et al. [224] found through experiments that typical solar-sail foil materials (Aluminium coated Mylar^{TM}, Teonex^{TM}, and Colorless Polyimide) do not have a tendency to rip apart under hypervelocity impacts, even after continued exposure to radiation doses representative of long-term missions.

As seen earlier, HVIs result in a crater on the target body, however, if the projectile has enough kinetic energy, full penetration of a thin sheet is also possible. Key features of the hole growth phenomenon are summarised by Hosseini and Abbas [243] as follows:

1. Both clear lips or fine lips revealing a clean hole are possible depending on the impact velocity and characteristics of the target and projectile. These characteristic lips are clearly seen on either sides of the penetration hole in Figure 2.25
2. For perforated targets, the hole diameter is usually greater than the projectile diameter. In certain cases, however, the hole diameter can be smaller due to: (1) elastic recovery of the lips; (2) the projectile got burnt or vaporised upon impact; (3) the projectile got damaged because it is weaker than the target material.
3. Greater collision velocities result in increased hole diameter because of the greater inertia of the lips.
4. Thicker targets result in larger hole diameters due to an increased inertia of the lips.
5. For spherical targets, oblique impacts result in elliptical craters while normal impacts result in circular

Table 2.3: Model constants for hole diameter predictions of hypervelocity impact on thin plates.

Model	C_1	p_1	p_2	p_3	p_4	$f(\theta_I)$	C_2
General [243]	2.800	-0.035	0.335	0.113	0.516	$\cos^{-0.026}(\theta_I)$	0.6
Normal shock [248]	3.32	0	0.38	0	0.17	1	0
Minor axis oblique shock [248]	4	0	1.60	0	0.41	$\cos^{0.38}(\theta_I)$	1.22
Major axis oblique shock [248]	1.68	0	0.24	0	0.0014	$e^{0.83\theta_I}$	0

craters.

For solar-sail materials particularly, Edwards et al. [224] found that the damage area (area of the circumscribing circle containing all damages from the impact) is never more than twice as large as the hole area for normal strikes. A number of studies have attempted to develop empirical formulas capable of predicting the final hole diameter (assuming penetration) in thin targets, due to the applicability of the results to the design of bumper plates to shield spacecraft components from MODs [244, 245, 243, 246]. In this purpose, De Chant [247] derived a general formula for the diameter of the perforated hole in a thin plate based on fluid dynamics as follows,

$$\frac{d_h}{d_p} = C_1 \left(\frac{\rho_p}{\rho_t}\right)^{p_1} \left(\frac{V_I}{c_t}\right)^{p_2} \left(\frac{V_I}{c_p}\right)^{p_3} \left(\frac{t_t}{d_p}\right)^{p_4} f(\theta_I) + C_2, \tag{2.28}$$

where $C_{1,2}$ and p_{1-4} are constants of the model, ρ_p and ρ_t are the densities of the projectile and target material respectively, c_p and c_t are the speeds of sound in the projectile and target materials respectively, d_h is the hole diameter, t_t is the target thickness, and $f(\theta_I)$ is a function of θ_I, which is the impact obliquity. This model resembles many of the other empirical models in literature and takes into account the most important geometrical and material properties necessary to describe the behaviour of shock waves in solid materials [243]. Table 2.3 shows different values and formulations of the constants in Eq. (2.28), resulting from various analyses. Based on a total of 1314 data points, Hosseini and Abbas [243] fitted the constants of the equation by considering d_h as the mean diameter (average of major and minor axes for elliptical holes formed by oblique shocks), as shown in the first row of Table 2.3. This model results in a mean error of 7.21%. Furthermore, for cases where only a single material is used for both the projectile and target, this model was found to perform only slightly worse than independent models developed specifically for these cases specifically. Dhote and Verma [248] further considered the one-material case through simulations in ANSYS Autodyn-3D non-linear hydrocode and generated a wide array of data to fit Eq. (2.28), determining three models: one for normal collisions, and two for oblique ones (one determines the major axis and the other the minor axis of the resulting ellipsoid). The constants of these models are shown in the second, third and fourth rows of Table 2.3 and their associated absolute percentage error is given in Figure 2.28.

Although HVIs on the sail foil are not expected to result in a momentum transfer, the holes resulting from these impacts will result in a residual body-fixed torque. Based on the models described by Eq. (2.28) and Table 2.3, the hole diameter (and area) generated by an HVI can be obtained for different collision geometries, and the residual torque can be obtained from,

$$\boldsymbol{\tau}_{\text{res}} = -\boldsymbol{r}_{I,\mathcal{B}} \times \left(\frac{A_h}{A_{SRP}}\right) \boldsymbol{F}_{SRP}, \tag{2.29}$$

where $A_h = \frac{\pi}{4} d_h^2$ is the hole area and $\boldsymbol{r}_{I,\mathcal{B}}$ is the body-fixed position of the impact on the sail. The body-fixed frame has its origin at the CoM of the sail, its $X_{\mathcal{B}}$-axis along one of the booms, $Z_{\mathcal{B}}$-axis in the direction of the sail surface normal, and its $Y_{\mathcal{B}}$-axis completes the right-handed coordinate system. The residual torque given by Eq. (2.29) then needs to be counter-balanced by the ACS.

2.4. Research Questions and Objectives

In the previous sections, the developments and state-of-the-art of three different fields have been presented.

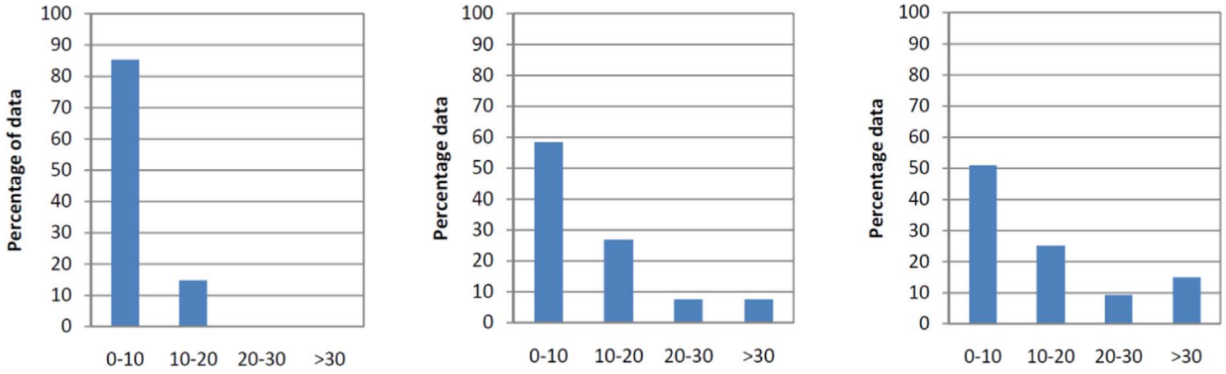

(a) Normal impact hole diameter.

(b) Oblique impact minor hole diameter.

(c) Oblique impact major hole diameter.

Figure 2.28: Histogram of absolute percentage error for the different models derived by [248].

First, it was made clear that the space debris problematic has reached a critical point where active measures need to be taken to guarantee the access to LEO and GEO protected regions on the long-term [11]. The number of objects in Earth orbit is steadily increasing, and the number of collisions between these objects is projected to further grow in the future even if no more launches were to take place [56]. Mitigating the space debris crisis and delaying the onset of the Kessler syndrome takes place through three main points of focus: (1) assessment of the debris environment through debris detection and tracking, permitting to perform collision avoidance manoeuvres and validate high-fidelity debris environment models [61]; (2) implementation of effective end-of-life strategies for the most important orbital regimes [10]; and (3) active debris removal of defunct satellites having a large risk of collision with other debris [11].

Solar-sails have been considered in the past as a system permitting to de-orbit high-altitude satellites using the SRP force to decelerate the spacecraft and later act as a drag sail to facilitate atmospheric entry. Additionally, their propellant-free nature also provides a great opportunity for long-term missions aiming to travel to multiple different defunct satellites to initiate their re-entry or to move them into a higher graveyard orbit. However, the momentum carried by a single photon is extremely small, and large sails are necessary to generate a significant acceleration [91]. The long predicted mission duration and increased surface area with respect to conventional spacecraft results in a significantly increased risk of collision with orbital debris or meteoroids. For solar-sails, a relatively large debris impacting the sail on its sail foil or a supporting boom would likely not result in a complete catastrophic breakup of the sail, but could result in a significant momentum transfer and disturbance of its attitude.

Collisions with an orbital debris or a meteoroid are generally referred to as hypervelocity impacts, as they occur at impact velocities of the order of kilometres per second. The momentum carried by the colliding debris in these HVIs is distributed among the target body, ejecta from the collision crater, spalled material from the non-impacted surfaces, and downrange ejecta [234]. While for very thin target materials (with respect to the colliding projectile) such as solar-sail foils, the momentum transfer to the spacecraft approaches zero [237], large amounts of momentum can be transferred through collisions with thicker or hollow targets such as the supporting booms of a rigid sail [236]. Furthermore, while the effect of the momentum transfer on the attitude and orbital dynamics of conventional spacecraft was found to be rather small [230, 218], the large area of a solar-sail will result in a much greater number of collisions than on conventional spacecraft. Additionally, in case a debris transferred a lot of momentum through a collision on one of the tips of the sail, the large moment arm could result in greater attitude dynamics perturbations than predicted by Sagnières and Sharf [230] and result in a tumbling motion.

As the attitude of a solar-sail directly dictates its thrust direction, an uncontrolled tumbling motion would have direct implications on the spacecraft orbital dynamics [91]. However, whether the retrieval of attitude control is feasible using the propellant-free attitude control methods presented in Section 2.2.4 in the complex dynamical environment of Earth-bound satellites is unclear. While [199] claims that these attitude control systems cannot recover by themselves from tumbling and that independent thrusters would be necessary, no simulation backed-up this statement for the propellantless ACS described in this work.

While the use of solar-sails in Earth orbit is certainly attractive, the current state and trends of the space debris environment raises a number of questions on how safe it is to navigate a solar-sail in debris rich regions. This work aims to answer one of these questions by considering the effect of a high-energy on-orbit collision on the sail attitude and trajectory dynamics, and assessing the capability of state-of-the-art propellantless attitude control system to bring back the sail attitude to a pre-determined state. The research objective of this thesis can then be formally stated as follows:

Research Objective

To characterise the effect of a high-energy on-orbit debris/solar-sail collision with an orbital debris on the sailcraft attitude and trajectory dynamics and assess the capability of an actuated tip-vane system to retrieve attitude control from a tumbling state.

The study of the structural dynamics involved in hypervelocity impact is considered outside the scope of this work. Therefore, expected values of momentum transfer based on previous experimental work or models will be used as inputs for orbital and attitude dynamics simulations. Furthermore, while the orbital dynamics resulting from the tumbling motion will be considered, only the retrieval of a stable attitude control will be investigated. That is, optimal transfers between the resulting orbit (after attitude stabilisation is reached) and the nominal orbit (prior to the collision) will not be considered. To pursue this research objective, the following research questions will be answered:

Research Question 1

What is the effect of the tumbling motion on the sail trajectory?

Research Question 2

Under which tumbling conditions is the attitude control recovery achievable using a vane-based attitude control system?

(a) *Is a robust back-up attitude control system necessary to recover attitude control after such collision?*
(b) *How long does it take to retrieve attitude control from an initially tumbling state ?*
(c) *What parameters influence the recovery time the most?*

Research Question 3

What collision geometries are the most difficult to recover from?

In order to answer these questions, the case study of the ACS3 spacecraft will first be used as a baseline to develop all the tools and methods necessary. A detailed work breakdown structure and gantt chart of the work performed throughout this thesis are given in Appendix B.

3

Materials and Methods

This chapter presents the general methods employed throughout the thesis to design the six-degrees-of-freedom simulator which was used to perform all numerical simulations in this work. Methodologies specific to the research objectives of this work can be found in the accompanying paper after this chapter. The methods presented below are broadly divided into the dynamical environment presented in Section 3.1 and the numerical environment presented in Section 3.2. The software was developed using the TU Delft Astrodynamics Toolbox [249]. A complete verification of the software developed is given in Appendix A.

3.1. Dynamical Environment

This section presents the dynamical environment used to develop the numerical simulation. The sail dynamics have been modelled through the coupled attitude-orbit equations of motion, neglecting the sail structural dynamics. First, Section 3.1.1 starts by giving the reference frames used to define the sail dynamics. Then the coupled attitude-orbit equations are given through Section 3.1.2 and Section 3.1.3, which gives the equations of motion of the sail orbital dynamics and attitude dynamics respectively, and Section 3.1.4 summarises the resulting state model representation. This is followed by Section 3.1.5, which presents the selection of the relevant perturbing accelerations and torques of the sailcraft dynamics. At last, Section 3.1.6 briefly discusses the ephemeris and shape models of the planetary bodies used in the simulation.

3.1.1. Reference Frames

In this subsection, the most relevant reference frames are briefly presented[1]:

- The **Earth-Centred Inertial** (ECI) reference frame, denoted by $\mathcal{I}_\oplus$, is used to formulate the orbital and attitude equations of motion. The frame origin $O_{\mathcal{I}_\oplus}$ is at the centre of mass of the Earth, the $Z_{\mathcal{I}_\oplus}$-axis points North along the rotational axis of the Earth, the $X_{\mathcal{I}_\oplus}$-axis points in the direction of the vernal equinox[2], and $Y_{\mathcal{I}_\oplus}$ completes the right-handed coordinate system [250]. Additionally, the frame orientation is defined by the direction of these axes at the J2000 time (January 1st 2000, at 12:00), after which they are fixed in place ($Z_{\mathcal{I}_\oplus}$ does not follow the axis of rotation of the Earth). It is noted that the ECI is a pseudo-reference frame due to the acceleration of the Sun on Earth's centre of mass, but this simplification is acceptable for Earth-orbiting satellites [250]. This reference frame is given in Figure 3.1.
- The **Earth-Centred Earth-Fixed Reference Frame** (ECEF) reference frame, denoted by $\mathcal{R}$, is used by dynamical models which require the orientation of the Earth, such as the spherical harmonics expansion of the gravitational field of the centre body. The frame coincides with the ECI reference frame at the J2000 epoch, but then rotates with the Earth. Therefore, its origin $O_\mathcal{R}$ is at the Earth centre of mass, the $Z_\mathcal{R}$-axis points towards the North, the $X_\mathcal{R}$-axis intersects the equator at zero longitude, and $Y_\mathcal{R}$ completes the right-handed coordinate system [251]. This reference frame is given in Figure 3.1.

[1] Note that all reference frames considered are right-handed

[2] This is the intersection of the Earth's equatorial plane with the ecliptic plane (the plane of the Earth's orbit around the Sun) at the J2000 epoch.

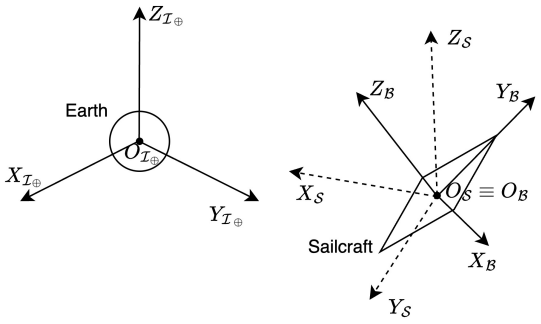

Figure 3.1: The ECI, RTN, and body-fixed reference frames.

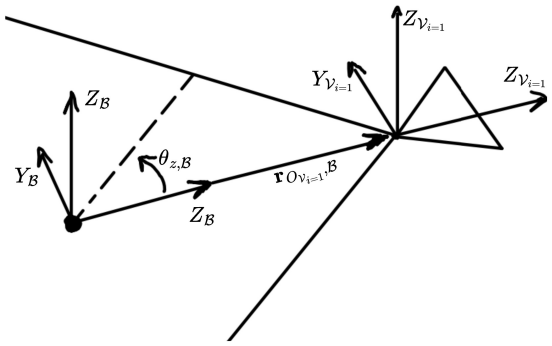

Figure 3.2: Vane reference frame of a given vane (numbered 1).

- The **Radial, Transverse, and Normal** (RTN) frame, denoted by $\mathcal{S}$, is a spacecraft-centered frame with its origin $O_{\mathcal{S}}$ at the sailcraft centre of mass, $X_{\mathcal{S}}$ parallel to the radial position vector, $Z_{\mathcal{S}}$ in the direction of the orbital angular momentum vector (perpendicular to the orbital plane), and $Y_{\mathcal{S}}$ completes the right-handed coordinate system [252]. This reference frame is used to define the perturbation accelerations for the translational dynamical system.

$$\hat{\boldsymbol{X}}_{\mathcal{S}} = \frac{\boldsymbol{r}_{\mathcal{I}_\oplus}}{||\boldsymbol{r}_{\mathcal{I}_\oplus}||} \quad (3.1a) \qquad \hat{\boldsymbol{Z}}_{\mathcal{S}} = \frac{\boldsymbol{r}_{\mathcal{I}_\oplus} \times \boldsymbol{v}_{\mathcal{I}_\oplus}}{||\boldsymbol{r}_{\mathcal{I}_\oplus} \times \boldsymbol{v}_{\mathcal{I}_\oplus}||} \quad (3.1b) \qquad \hat{\boldsymbol{Y}}_{\mathcal{S}} = \frac{\hat{\boldsymbol{Z}}_{\mathcal{S}} \times \hat{\boldsymbol{X}}_{\mathcal{S}}}{||\hat{\boldsymbol{Z}}_{\mathcal{S}} \times \hat{\boldsymbol{X}}_{\mathcal{S}}||} \quad (3.1c)$$

- The **body-fixed** reference frame, denoted by $\mathcal{B}$, is used to define the attitude dynamics (relative to the inertial frame) of the body, as well as define the dynamics of the vane ACS. Its origin $O_{\mathcal{B}}$ is at the spacecraft centroid with the $Z_{\mathcal{B}}$-axis pointing in the direction of the sail normal vector, the $X_{\mathcal{B}}$ points along a reference boom of the sail, and $Y_{\mathcal{B}}$ completes the right-handed coordinate system. For the most common case of a square sail with perpendicular booms, $Y_{\mathcal{B}}$ then also points in the direction of a boom. An example of this reference frame for a square sail is given in Figure 3.1.
- The **vane-fixed** reference frame of the i$^{\text{th}}$ vane, denoted by $\mathcal{V}_i$, is used to define the movements of the vanes as part of the sail attitude system. The reference frame origin $O_{\mathcal{V}_i}$ is located at the vane attachment point (where actuators can act on the vane orientation), $X_{\mathcal{V}_i}$ is aligned with the associated boom direction and points outwards, $Z_{\mathcal{V}_i}$ is in the direction of the body-fixed $Z_{\mathcal{B}}$-axis, and $Y_{\mathcal{V}_i}$ completes the right-handed frame, as illustrated in Figure 3.2. In this figure, $\theta_{z,\mathcal{B}}$ is the rotation angle along the $Z_{\mathcal{B}}$ axis and $\boldsymbol{r}_{O_{\mathcal{V}_{i=1}}}$ is the position vector of the attachment point of the vane considered. Furthermore, note that the frame does not move with the vane during its movement.

To change from one frame to another, rotation matrices along each unit axis of a given right-handed reference frame. The X, Y, and Z-axis rotation matrices are given by $\boldsymbol{R}_x(\cdot)$, $\boldsymbol{R}_y(\cdot)$, and $\boldsymbol{R}_z(\cdot)$ where $(\cdot)$ is a given rotation angle around the considered axis [251],

$$\boldsymbol{R}_x(\cdot) = \begin{bmatrix} 1 & 0 & 0 \\ 0 & \cos(\cdot) & \sin(\cdot) \\ 0 & -\sin(\cdot) & \cos(\cdot) \end{bmatrix} \quad (3.2a) \qquad \boldsymbol{R}_y(\cdot) = \begin{bmatrix} \cos(\cdot) & 0 & -\sin(\cdot) \\ 0 & 1 & 0 \\ \sin(\cdot) & 0 & \cos(\cdot) \end{bmatrix} \quad (3.2b)$$

$$\boldsymbol{R}_z(\cdot) = \begin{bmatrix} \cos(\cdot) & \sin(\cdot) & 0 \\ -\sin(\cdot) & \cos(\cdot) & 0 \\ 0 & 0 & 1 \end{bmatrix} \quad (3.2c)$$

3.1.2. Orbital Dynamics

The movement of a body in orbit can be described using Newton's second law of motion, stating that the time rate of change of linear momentum is equal to the magnitude of the force inducing the momentum exchange ($\frac{\mathrm{d}\boldsymbol{p}}{\mathrm{d}t} = \boldsymbol{F}$) in an inertial reference frame [84]. For cases where the mass of the body is constant, this permits to write $\boldsymbol{F} = m\boldsymbol{a}$, where $\boldsymbol{a}$ is the acceleration vector of the body and $\boldsymbol{F}$ is an external force

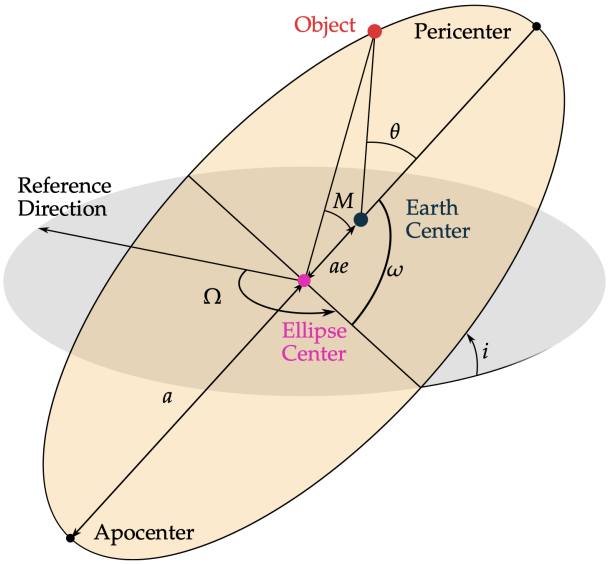

Figure 3.3: Kepler orbit definition using Kepler elements.

acting on the body. Therefore, the general form of the translational equations of motion can be expressed in Cartesian coordinates as,

$$\frac{\mathrm{d}\boldsymbol{r}_{\mathcal{I}_\oplus}}{\mathrm{d}t} = \dot{\boldsymbol{r}}_{\mathcal{I}_\oplus} \tag{3.3a}$$

$$\frac{\mathrm{d}\dot{\boldsymbol{r}}_{\mathcal{I}_\oplus}}{\mathrm{d}t} = \ddot{\boldsymbol{r}}_{\mathcal{I}_\oplus} = \frac{\boldsymbol{F}_{\mathcal{I}_\oplus}}{m} \tag{3.3b}$$

where $\boldsymbol{r}$ is the Cartesian position vector in the inertial reference frame. In this work, the equations of motions are all expressed in the ECI reference frame, as all the cases considered involve a solar-sail in Earth orbit. The general form given by Eq. (3.3), also called the Cowell formulation, is only one way among numerous alternatives to formulate the equations of motion. The Cowell formulation is particularly robust and suitable for propagation of orbital dynamics in highly perturbed environments [253], however, the large oscillations in all components of the state vector (position and velocity Cartesian components) also make it less computationally efficient. For lightly perturbed cases, such as a solar-sail in Earth orbit subject to SRP from the Sun, a formulation based on a single fast element and five slow elements is more efficient, such as the Gauss perturbation equations which have been used extensively in the literature [54].

The Gauss perturbation equations can be expressed in Keplerian or Modified Equinoctial Elements (MEE) form. The former provides a more intuitive representation of the orbit and its dynamics, using the semi-major axis a, eccentricity e, inclination i, Right Ascension of the Ascending Node (RAAN) Ω, the argument of pericenter ω, and the true anomaly θ (and mean anomaly M), as shown in Figure 3.3. However, the equations of motion employing the Keplerian form have singularities at $e = 0$, $i = 0°$, $e = +\infty$, and $i = 180°$ [254]. As near-circular orbits will be considered in this work, the MEE form propagated in time, which only have a singularity at $i = 0°$ or at $i = 180°$ depending on the formulation, was used throughout this research. The MEE can be directly linked to Keplerian elements through [249],

$$p = \begin{cases} a(1-e^2) & e \neq 1 \\ 2a & e = 1 \end{cases} \tag{3.4a}$$

$$f = e\cos\left(\omega + I\Omega\right) \tag{3.4b}$$

$$g = e\sin\left(\omega + I\Omega\right) \tag{3.4c}$$

$$h = \tan^I\left(\frac{i}{2}\right)\sin\Omega \tag{3.4d}$$

$$k = \tan^I\left(\frac{i}{2}\right)\cos\Omega \tag{3.4e}$$

$$L = \omega + I\Omega + \theta \tag{3.4f}$$

where $I = \pm 1$ in depending on the initial orbit at the start of the simulation: $I = 1$ gives a singularity in $i = 180°$ and $I = -1$ gives a singularity in $i = 0°$. The time formulation of the MEE's equations of motion is given by Betts [255],

$$\frac{\mathrm{d}p}{\mathrm{d}t} = \frac{2p}{w}\sqrt{\frac{p}{\mu_\oplus}}\Delta_t, \tag{3.5a}$$

$$\frac{\mathrm{d}f}{\mathrm{d}t} = \sqrt{\frac{p}{\mu_\oplus}}\left[\Delta_r \sin L + ((w+1)\cos L + f)\frac{\Delta_t}{w} - (h\sin L - k\cos L)\frac{g\Delta_n}{w}\right], \tag{3.5b}$$

$$\frac{\mathrm{d}g}{\mathrm{d}t} = \sqrt{\frac{p}{\mu_\oplus}}\left[-\Delta_r \cos L + ((w+1)\sin L + g)\frac{\Delta_t}{w} + (h\sin L - k\cos L)\frac{f\Delta_n}{w}\right], \tag{3.5c}$$

$$\frac{\mathrm{d}h}{\mathrm{d}t} = \sqrt{\frac{p}{\mu_\oplus}}\frac{s^2\Delta_n}{2w}\cos L, \tag{3.5d}$$

$$\frac{\mathrm{d}k}{\mathrm{d}t} = \sqrt{\frac{p}{\mu_\oplus}}\frac{s^2\Delta_n}{2w}\sin L, \tag{3.5e}$$

$$\frac{\mathrm{d}L}{\mathrm{d}t} = \sqrt{\mu_\oplus p}\left(\frac{w}{p}\right)^2 + \frac{1}{w}\sqrt{\frac{p}{\mu_\oplus}}(h\sin L - k\cos L)\Delta_n, \tag{3.5f}$$

with,

$$s^2 = 1 + h^2 + k^2, \tag{3.6a}$$

$$w = 1 + f\cos L + g\sin L, \tag{3.6b}$$

where Δ_r, Δ_t, and Δ_n are the components of the disturbing acceleration in the RTN frame.

3.1.3. Attitude Dynamics

The forces acting on the body can also induce a perturbation of the attitude dynamics of a body, if applied asymmetrically, resulting in a perturbing torque. Such torque could be the result of the Solar Radiation Pressure or the gravity gradient. The full rotational state is defined by $\boldsymbol{b}_{\mathcal{I}_\oplus\mathcal{B}}$, which describes the body's orientation with respect to the inertial frame (in the form of a rotation matrix from the body-fixed frame to the inertial frame), and $\boldsymbol{\omega}_{\mathcal{I}_\oplus\mathcal{B},\mathcal{B}}$, the body's angular velocity vector with respect to the inertial frame and expressed in the body fixed frame. The latter is referred to as $\boldsymbol{\omega}_\mathcal{B}$ hereafter in brevity. In this work, the propagated body is assumed to be a rigid body of a constant mass, meaning that the body's inertia tensor $\boldsymbol{I}_\mathcal{B}$ is constant. This permits to write [251],

$$\dot{\boldsymbol{\omega}}_{\mathcal{I}_\oplus\mathcal{B},\mathcal{B}} = (\boldsymbol{I}_\mathcal{B})^{-1}\left(\boldsymbol{T}_\mathcal{B} - \boldsymbol{\omega}_{\mathcal{I}_\oplus\mathcal{B},\mathcal{B}} \times \left(\boldsymbol{I}_\mathcal{B}\boldsymbol{\omega}_{\mathcal{I}_\oplus\mathcal{B},\mathcal{B}}\right)\right), \tag{3.7}$$

where $\boldsymbol{T}_\mathcal{B}$ is an external torque acting on the spacecraft, expressed in the body-fixed frame. Equation (3.7) gives Euler's attitude equation of motion for a rigid body, which may also be valid for very small variations of $\dot{\boldsymbol{I}}_\mathcal{B}$ if $\boldsymbol{I}_\mathcal{B}$ is updated often enough [256]. Particularly, the movement of the vanes in the body-fixed frame is assumed to have a negligible effect on the sail inertia tensor. Equation (3.7) can be expressed in various forms, such as Euler angles, unified state model, Rodrigues parameters and quaternions [257], but the quaternions form is used throughout this work. The quaternion formulation is singularity-free, which is important when considering a tumbling satellite, and is the only propagator available in the TU Delft Astrodynamics Toolbox used in this work. The quaternion representation of the vehicle orientation is associated to the rotation matrix from the body-fixed frame to the inertial frame as follows [258],

$$q_1 = \frac{1}{4q_4}\left(\boldsymbol{b}_{\mathcal{I}_\oplus\mathcal{B}}(2,3) - \boldsymbol{b}_{\mathcal{I}_\oplus\mathcal{B}}(3,2)\right), \tag{3.8a}$$

$$q_2 = \frac{1}{4q_4}\left(\boldsymbol{b}_{\mathcal{I}_\oplus\mathcal{B}}(3,1) - \boldsymbol{b}_{\mathcal{I}_\oplus\mathcal{B}}(1,3)\right), \tag{3.8b}$$

$$q_3 = \frac{1}{4q_4}\left(\boldsymbol{b}_{\mathcal{I}_\oplus\mathcal{B}}(1,2) - \boldsymbol{b}_{\mathcal{I}_\oplus\mathcal{B}}(2,1)\right), \tag{3.8c}$$

$$q_4 = \frac{1}{2}\sqrt{1 + \boldsymbol{b}_{\mathcal{I}_\oplus\mathcal{B}}(1,1) + \boldsymbol{b}_{\mathcal{I}_\oplus\mathcal{B}}(2,2) + \boldsymbol{b}_{\mathcal{I}_\oplus\mathcal{B}}(3,3)}, \tag{3.8d}$$

these equations are subject to the constraint $\sum_{i=1}^{4} q_i^2 = 1$, which is enforced at each time step of the numerical simulation through a normalisation of the quaternion vector. While quaternions are used to propagate the rotational state in the numerical simulation, the initial state is provided in terms of Euler angles used to define the rotation matrix $\boldsymbol{b}_{\mathcal{I}_\oplus\mathcal{B}}$ using Eq. (3.2). Converting from one representation to another comes back to solving,

$$\boldsymbol{b}_{\mathcal{I}_\oplus\mathcal{B}} = \begin{bmatrix} 1-2(q_2^2+q_3^2) & 2(q_1q_2+q_3q_4) & 2(q_1q_3-q_2q_4) \\ 2(q_2q_1-q_3q_4) & 1-2(q_1^2+q_3^2) & 2(q_2q_3+q_1q_4) \\ 2(q_3q_1+q_2q_4) & 2(q_3q_2-q_1q_4) & 1-2(q_1^2+q_2^2) \end{bmatrix}. \tag{3.9}$$

Equation (3.7) is then completed by,

$$\begin{bmatrix} \dot{q}_1 \\ \dot{q}_2 \\ \dot{q}_3 \\ \dot{q}_4 \end{bmatrix} = \frac{1}{2} \begin{bmatrix} q_4 & -q_3 & q_2 \\ q_3 & q_4 & -q_1 \\ -q_2 & q_1 & q_4 \\ -q_1 & -q_2 & -q_3 \end{bmatrix} \boldsymbol{\omega}_\mathcal{B}, \tag{3.10}$$

which describes the evolution of the quaternion elements based on the rotational velocity with respect to the inertial frame [251].

3.1.4. Resulting State Model Representation

The last two subsections have presented the orbital and attitude dynamics separately. However, the full dynamics is implicitly coupled, and the full state vector needs to be propagated at once. The orbital dynamics is impacted by the orientation of the vehicle due to the Solar Radiation Pressure force (as will be seen in the next subsection) and the attitude dynamics is impacted by the position of the spacecraft in inertial space through the magnitude of this SRP force and the presence of eclipses. Therefore, the fully coupled six-DoFs state vector is given by,

$$\boldsymbol{X} = \begin{bmatrix} p & f & g & h & k & L & \boldsymbol{q}_{\mathcal{I}_\oplus\mathcal{B}}^T & \boldsymbol{\omega}_\mathcal{B}^T, \end{bmatrix} \tag{3.11}$$

which gives the five slow orbital elements describing the orbit shape, the true longitude L variable characterising the fast orbital element, the four quaternion elements $\boldsymbol{q}_{\mathcal{I}_\oplus\mathcal{B}}^T$ describing the rotation matrix from the body-fixed to the inertial reference frames, and the rotational velocity vector of the body-fixed frame with respect to the inertial frame $\boldsymbol{\omega}_\mathcal{B}^T$, expressed in the body-fixed frame. Additionally, the inertial Cartesian position and velocity of the propagated body can be obtained from the first six (orbital) elements, yielding the following processed state vector,

$$\tilde{\boldsymbol{X}} = \begin{bmatrix} \boldsymbol{r}_{\mathcal{I}_\oplus}^T & \boldsymbol{v}_{\mathcal{I}_\oplus}^T & \boldsymbol{q}_{\mathcal{I}_\oplus\mathcal{B}}^T & \boldsymbol{\omega}_\mathcal{B}^T \end{bmatrix} \tag{3.12}$$

3.1.5. External Forces

A number of forces act on a satellite in Earth orbit. From spherical harmonics of the Earth gravity field, third-body effects from other Solar System bodies to Solar Radiation Pressure and aerodynamics forces, Earth-orbiting satellites are subject to a very complex dynamical environment [123]. However, the primary objective of this work is not to produce a high fidelity simulation of a solar-sail in Earth orbit, but rather to investigate the general capability of the vane attitude control system to detumble a spacecraft. Therefore, a simplified dynamical model is employed to reduce the computational time of a single propagation while preserving the most important dynamical aspects. In the following subsubsections, the most important forces acting on Earth-orbiting satellites are reviewed and the final dynamical model is selected.

3.1.5.1. Earth Gravitational Field

As a solar-sail in Earth orbit is considered in this work, the gravitational field of the Earth is the primary force acting on the spacecraft throughout its orbit. The most simple gravitational field model is the central gravitational field acceleration, taking the form [250],

$$\ddot{\boldsymbol{r}}_{\mathcal{I}_\oplus} = -\mu_\oplus \frac{\boldsymbol{r}_{\mathcal{I}_\oplus}}{||\boldsymbol{r}_{\mathcal{I}_\oplus}||^3}, \tag{3.13}$$

where $\mu_\oplus$ is the gravitational parameter of the Earth and $\boldsymbol{r}_{\mathcal{I}_\oplus}$ is the position vector of the spacecraft in the ECI reference frame. This simple central gravity field also results in a gravity gradient torque expressed in the ECI reference frame as [259],

$$\boldsymbol{T}_g = \frac{3\mu_\oplus}{||\boldsymbol{r}_{\mathcal{I}_\oplus}||^5}\boldsymbol{r}_{\mathcal{I}_\oplus} \times (\boldsymbol{I}_\mathcal{B} \cdot \boldsymbol{r}_{\mathcal{I}_\oplus}). \tag{3.14}$$

The effect of this gravity gradient torque is to align the principal axis of (the mass distribution of) the spacecraft with the position vector, which is the direction of the gravity gradient. The effect of this disturbance on the attitude dynamics is therefore stabilising, or providing stiffness, meaning that it makes the detumbling of a spacecraft easier. However, since the Earth is not a perfect sphere, its gravitational field is more accurately described using a spherical harmonics expansion using [260],

$$\ddot{\boldsymbol{r}}_{\mathcal{I}_\oplus} = \nabla U_\oplus, \tag{3.15a}$$

$$U_\oplus = \frac{\mu_\oplus}{||\boldsymbol{r}_{\mathcal{I}_\oplus}||}\sum_{n=0}^{\infty}\sum_{m=0}^{n}\frac{R_\oplus^n}{||\boldsymbol{r}_{\mathcal{I}_\oplus}||^n}P_{n,m}(\sin\phi)(C_{nm}\cos(m\lambda) + S_{nm}\sin(m\lambda)), \tag{3.15b}$$

where $U_\oplus$ is the gravitational potential of the Earth at the considered position, $R_\oplus$ is the mean equatorial radius of the Earth, λ and ϕ are the longitude and the latitude of the spacecraft in an Earth fixed coordinate system, P_{nm} are Legendre Functions of degree n and order m, and C_{nm} and S_{nm} are the associated spherical harmonics coefficients of the same degree and order. The infinite sum described in Eq. (3.15b) is usually truncated at a different degree and order depending on the application. Following from the spherical harmonics expansion of such a gravity field, the higher order gravity gradient torques have been derived by Roithmayr [261], however, these have a much smaller effect than the gravity gradient torque from Eq. (3.14).

In this work, as the first order dynamics are being considered, only the central gravity field described by Eq. (3.13) will be considered. The gravity gradient torque will also be neglected as its effect is largely stabilising and a worst case scenario is desired to assess the capabilities of the vane attitude control system to detumble a solar-sail spacecraft.

3.1.5.2. Solar Radiation Pressure Model

The Solar Radiation Pressure force is a key effect to be accounted for in the dynamics of solar-sails, but as described in Section 2.2.2.3, numerous models of varying fidelity exist. In this work, considered solar-sails are assumed to consist of multiple flat and rigid surfaces, meaning that the total SRP force can be decomposed in the contribution from each panel individually similarly to an N-plates model [131]. Furthermore, the non-constant nature of the sail optical coefficients due to their degradation is neglected as this effect only becomes significant on long-term missions (decades) while the detumbling cases considered in this work will be relatively short-span in comparison (hours to months at most) [154]. For each solar-sail panel, the SRP force is computed according to the O-SRP model from Eq. (2.18) by differentiating between the panel front and the back sides. This yields the following for the SRP force acting on a single panel, where the $\mathcal{I}_\oplus$ subscript was dropped for brevity,

$$\boldsymbol{F}_{SRP} = \frac{WA|\cos(\theta)|}{c}\begin{cases}\left(\alpha_f\left(\boldsymbol{n}_s + \frac{\epsilon_b B_b - \epsilon_f B_f}{\epsilon_f + \epsilon_b}\boldsymbol{n}\right) - 2\rho_{s,f}\cos(\theta)\boldsymbol{n} + \rho_{d,f}\left(\boldsymbol{n}_s - B_f\boldsymbol{n}\right)\right) & \boldsymbol{n}\cdot(-\boldsymbol{n_s}) > 0 \\ \left(\alpha_b\left(\boldsymbol{n}_s + \frac{\epsilon_b B_b - \epsilon_f B_f}{\epsilon_f + \epsilon_b}\boldsymbol{n}\right) - 2\rho_{s,b}\cos(\theta)\boldsymbol{n} + \rho_{d,b}\left(\boldsymbol{n}_s + B_b\boldsymbol{n}\right)\right) & \boldsymbol{n}\cdot(-\boldsymbol{n_s}) < 0\end{cases} \tag{3.16}$$

where $\boldsymbol{n_s}$ was defined in Figure 2.17, subscript f refers to an optical parameter from the front surface, subscript b to an optical parameter from the back surface, and $\boldsymbol{n}$ only refers to the surface normal of the front surface. The change in sign of the $B_{f-b}\boldsymbol{n}$ term in the diffusive reflection part of the reflection law results from $\boldsymbol{n_b} = -\boldsymbol{n_f} = -\boldsymbol{n}$. Furthermore, no similar sign changes appear in the other terms as they would cancel out. Additionally, to analyse the sensitivity of the results obtained in this work with respect to the optical model used, Eq. (3.16) was simplified to a double-sided ideal model ($\rho_{s,f} = \rho_{s,b} = 1$ and all other coefficients are equal to zero) and to a single-sided ideal model ($\rho_{s,f} = 1$ and all other coefficients are equal to zero) for some test case. Based on Eq. (3.16), the torque induced by a single solar-sail panel is given by,

$$\boldsymbol{T}_{SRP,\mathcal{B}} = (\boldsymbol{r}_{panel,\mathcal{B}} - \boldsymbol{r}_{CG,\mathcal{B}}) \times \boldsymbol{F}_{SRP,\mathcal{B}}, \tag{3.17}$$

where $\boldsymbol{r}_{panel,\mathcal{B}}$ is the position vector of the panel centroid and $\boldsymbol{r}_{CG}$ is the position vector of the spacecraft centre of gravity. Following, for the SRP force to be active, the spacecraft needs to be in direct line of sight with the Sun. To account for this effect, the penumbra-umbra eclipse model described by Montenbruck, Gill, and Lutze [260] is used, neglecting the small effect of the atmosphere on the absorption and refraction of light [28].

Additionally, Planetary Radiation Pressure (PRP), being the sum of both the effects of the reflection of SRP on the planet -known as Albedo Radiation Pressure (ARP)- and the thermal radiation emitted by the planet -known as Black-Body Radiation Pressure (BBRP)-, could also be taken into account [211]. While ARP and BBRP have been found to form up to 20% and 10% of the solar-sail acceleration in LEO [123], it was neglected in this work to reduce the computational load of a single propagation and is therefore a clear limitation of this work. On the one hand, as no detumbling manoeuvres can then be performed during eclipses, neglecting PRP will result in longer detumbling times than actually feasible (conservative estimate). On the other hand, this means that the present work is expected to underestimate the effect of long-term effects of tumbling on the orbital dynamics.

3.1.5.3. Third-Body Effects

Other bodies in the solar system exert a gravitational force on spacecrafts in Earth orbit, although the magnitude of the resulting acceleration is much smaller than the Earth's gravitational pull. Similarly to Earth, these bodies are not perfect spheres and their gravitational field is best described by a spherical harmonics expansion. However, the very large distance between the spacecraft and these celestial bodies permits to simplify the gravity field to a point mass modelled through the third-body acceleration formula from Wakker [250],

$$\boldsymbol{a_{tb,i}} = \mu_i \left(\frac{\boldsymbol{r_{\oplus - i}} - \boldsymbol{r}_{\mathcal{I}_\oplus}}{||\boldsymbol{r_{\oplus - i}} - \boldsymbol{r}_{\mathcal{I}_\oplus}||^3} - \frac{\boldsymbol{r_{\oplus - i}}}{||\boldsymbol{r_{\oplus - i}}||^3} \right), \tag{3.18}$$

where μ_i is the gravitational parameter of the ith celestial body and $\boldsymbol{r_{\oplus - i}}$ is the position vector of the third-body in the same reference frame. In case the extended body effects should still be taken into account (eg the Moon), the general form of this expression is given by,

$$\boldsymbol{a_{tb,i}} = \nabla U_\oplus(\boldsymbol{r}_{\mathcal{I}_\oplus}) - \nabla U_\oplus(\boldsymbol{r_i}), \tag{3.19}$$

where $U_\oplus$ is the gravitational potential of the centre body (the Earth in this case). In practice, the Sun and Moon third-body accelerations are the most significant, while the rest of the celestial bodies result in accelerations four orders of magnitudes smaller [262]. As is clear from Eq. (3.18), third-body accelerations have very little to no effect on the spacecraft attitude dynamics, and a minimal effect on its orbital dynamics. Therefore, these effects are neglected in subsequent sections.

3.1.5.4. Aerodynamics Effects

Although the aerodynamics perturbations can be significant for large surface-to-area ratio spacecrafts in Earth-orbit, all cases considered in this work will have an initial altitude of 1000 km or above altitude, which is a realistic altitude regime for potential solar-sails use-cases in Earth orbit [121, 122]. At these altitudes, the atmospheric density is of the order of 10^{-15} to 10^{-18} kg/m^3 depending on the solar activity and time of the day [263], meaning that atmospheric forces and torques are negligible in comparison to the Solar Radiation Pressure, and will be neglected in this work.

3.1.5.5. Final Dynamical Model

In the following sections, if not mentioned otherwise, the dynamical model used in all simulations consists of a central gravity field of the Earth and the SRP force from the Sun. Throughout this work, three reflection models —realistic, single ideal, and double ideal— are used, and the specific model used for each simulation will be clearly indicated. Furthermore, the central gravity field is assumed to only have an effect on the translational dynamics, while the gravity gradient torque is neglected. This reduced dynamical model encapsulates the first order dynamics of an Earth-orbiting solar-sail, permitting to make a primary assessment of the capabilities of the vane attitude control system to detumble such a spacecraft. Additionally, other relatively significant aspects, such as the gravity gradient and aerodynamics torques, would only help the spacecraft detumbling (as explained above). Meaning that the considered dynamical model is a worst-case scenario in terms of spacecraft detumbling.

3.1.6. Ephemeris and Shape Models

As a large amount of propagations will need to be run to generate the results, it is desired to reduce the complexity of the environment and shape models to a maximum to limit the computational time of a single propagation. Therefore, the following models were selected:

- Constant rotation models are used for both the Sun and the Earth as no perturbing acceleration depends on their orientation with respect to the propagated body (such as spherical harmonics).
- The relative position of the Sun with respect to the Earth is retrieved from the SPICE interface[3] throughout the numerical propagation as the numerical overhead associated with the operation was found to be negligible.
- As no atmosphere model is considered in the orbital perturbations, all non-propagated bodies present in the simulation are assumed spherical with the average radius extracted from the SPICE interface.

These assumptions are deemed acceptable given the proof-of-concept nature of the work, which prioritises proving the feasibility over achieving the highest possible accuracy in orbital propagation.

3.2. Numerical Environment

This section briefly presents the numerical environment used in the numerical simulation. Section 3.2.1 gives the numerical integrator selection, and Section 3.2.2 gives the line search method which is used in several algorithms part of the accompanying paper.

3.2.1. Numerical Integrators

Having completely setup the coupled orbit-altitude dynamical model, an appropriate integrator needs to be selected to propagate the equations of motion in time. With numerous methods present in literature [260], the selection of a particular integration scheme requires a trade-off between numerical accuracy and computational time. Three general families of integrators exist and are available in TUDAT:

- Multi-stage Runge-Kutta(-Fehlber) methods aim to solve the Ordinary Differential Equation (ODE) by approximating the solution through a weighted average of the function evaluation at intermediate points within each step. These methods are widely used in initial value numerical simulation due to their simplicity and their robustness [264, 265], but have a generally lower accuracy than the two other families considered here [265]. The general formulation of multi-stage methods is given by Eq. (3.20). These methods can easily be adapted to include a variable step algorithm by comparing schemes of different orders [266], making them particularly suited to the present work.

$$y_{n+1} = y_n + h_{rk} \sum_{i=1}^{s} b_i k_i \tag{3.20}$$

$$\begin{aligned}
k_1 &= f(t_n, y_n), \\
k_2 &= f(t_n + c_2 h_{rk}, y_n + (a_{21} k_1) h_{rk}), \\
k_3 &= f(t_n + c_3 h_{rk}, y_n + (a_{31} k_1 + a_{32} k_2) h_{rk}), \\
&\vdots \\
k_s &= f(t_n + c_s h_{rk}, y_n + (a_{s1} k_1 + a_{s2} k_2 + \cdots + a_{s.s-1} k_{s-1}) h_{rk}).
\end{aligned}$$

- Multi-step methods, such as the explicit Adams-Bashford method shown in Eq. (3.21), aim to derive an interpolated polynomial from previous data points, to extend this polynomial to t_{n+1}, and compute the analytical integral of the interpolation function [265]. The reuse of previous function evaluations permits a more efficient use of computational resources but also requires more memory to store the previous time steps (compared to multi-stage methods). Additionally, the overall concept of the method implies that it is unsuited to dynamical systems comprising discontinuities (such as eclipses). Nevertheless, combined with its variable order and variable step variants (Adams-Bashford-Moulton), it is considered as one of the best trade-offs for integration accuracy and computational time for ODE's with very smooth right-hand sides (if a very dense output is necessary) [265].

[3] URL [accessed on 01/07/2024]: `https://naif.jpl.nasa.gov/naif/`

$$\bar{y}(t_{n+1}) = \bar{y}(t_n) + \Delta t \sum_{j=0}^{s} b_j f(t_{n-j}, \bar{y}_{n-j}) \qquad t_{n-j} = t_n - j\Delta t \tag{3.21}$$

- Extrapolation methods, such as Bulirsch-Stoer schemes, consist of evaluating the same integration step with 2, 4, 8, and so on, integration substeps and to extrapolate the difference in the results between subsequent substeps to infinitely short time steps [265]. While these methods can integrate ODE's with very high accuracy and are considered as the best trade-off between numerical accuracy and computational time when sparse outputs are acceptable [265], they also result in a very sparse output. They are therefore generally used for long-term propagations.

In this work, a variable step size Runge-Kutta method is used. Fixed step methods are inappropriate due to the changing dynamics throughout the numerical simulation: as the sail is detumbled, the rotational velocity becomes smaller and larger time steps can be used. As the attitude dynamics are much faster than the orbital dynamics for large initial rotational velocities, the reduced computational time resulting from the use of a variable step size method (compared to a fixed step method), is significant. Furthermore, multi-step methods are not suited to this work due to the discontinuities in the dynamics arising from eclipses, and extrapolation methods would result in too sparse outputs (as they are better suited for long-duration propagations) [260]. In order to select the most appropriate Runge-Kutta method available in TUDAT, a reference scenario has been setup with pre-determined vane movements to reduce the computational time associated to calls to the vane controller and ensure that the same dynamics are followed by the sailcraft.

On this reference case, integrator errors lower than 1 m, 10^{-3} m/s, and 0.05 deg/s in terms of position, velocity and rotational velocity respectively, are desired. The former two are generally considered large for integration errors but are justified by the low-fidelity dynamical model used in this work: as the dynamical model does is quite far from reality in terms of orbital position and velocity, a very high accuracy integrator would be a waste of computational resources in comparison to running different cases, although the integrator should be able to follow the overall dynamics. However, the rotational velocity error, for which the dynamical model can be considered as medium-to-high fidelity (the most significant aspect for a solar-sail is being considered), is required to be lower as it is the focus of this work. The 0.05 deg/s is selected as 10% of the maximum angular turning rate (0.5 deg/s) of the Advanced Composite solar-sail System (ACS3), which represents the state of the art in terms of Earth-bound solar-sailing [143].

From this reference case, a benchmark was generated based on a fixed step size Runge–Kutta–Fehlberg (RKF) method of order 7 and the robust Cowell propagator, using Figure 3.4 where the maximum propagation error in terms of inertial position and rotational velocity is evaluated for step sizes of 2^{i} for i=7, 6,... ,-3, -4. The error of a propagation with fixed step size Δt is estimated using the subsequent $\Delta t/2$ one, through Eq. (3.22). In the Local Truncation Error (LTE) regime, dividing the time step size by 2 should reduce the error by a factor 128 with a 7th order integrator.

$$\epsilon(t;\Delta t) \approx \bar{y}_1(t;\Delta t) - \bar{y}_2\left(t;\frac{\Delta t}{2}\right) \tag{3.22}$$

Considering Figure 3.4, a benchmark with a fixed time step size of $\Delta t = 2^{-3}$ s is used to assess the error of the different integrators considered. This results in position, velocity, and rotational velocity errors of the order of 0.1 m, 10^{-4} m/s, and 0.005 deg/s respectively - all of which being about 10% lower than the required integrator accuracy. Following, all variable step size multi-stage methods present in TUDAT were considered to propagate the reference case with different relative and absolute tolerances[4], yielding Figure 3.5 showing the maximum integration error and the number of function evaluations (used as a proxy for the computational time) of each option with respect to the benchmark. Based on this figure, the RKF5(6) scheme with absolute and relative tolerances of 10^{-12} was selected as the best trade-off between numerical accuracy and computational time while meeting all accuracy requirements. Note that the error was evaluated by interpolating the benchmark time steps to the integrator steps with an 8th order Lagrange interpolator [267], and discarding the integrator points falling before or after the six first or last benchmark

[4]For each case, the absolute and relative tolerances have been set equal to each other to reduce the amount of cases to be considered.

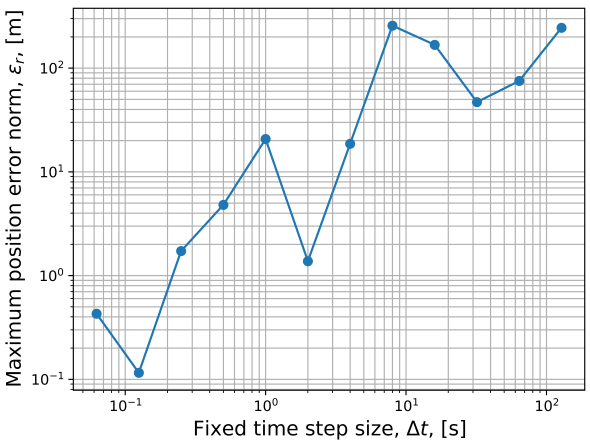

(a) Cartesian position.

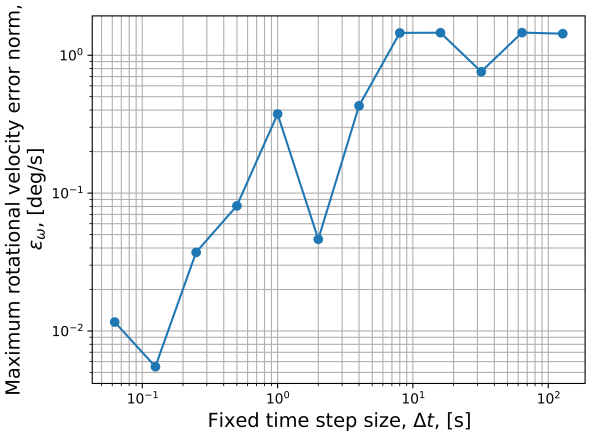

(b) Rotational velocity.

Figure 3.4: Benchmark time step size selection based on the maximum error, for the RKF7 integrator.

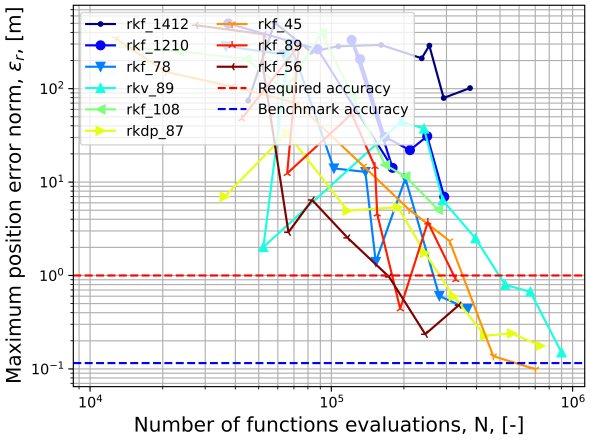

(a) Integrators position error.

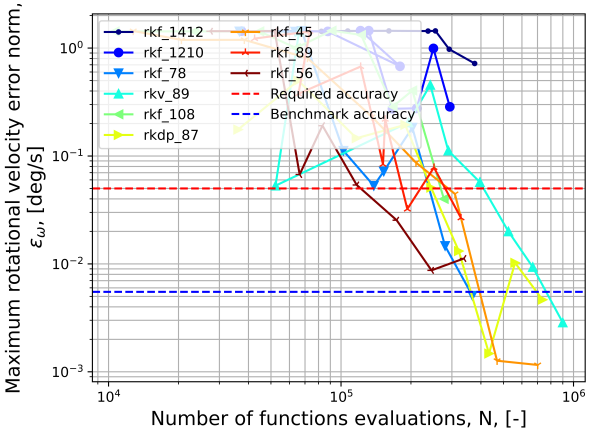

(b) Rotational velocity error.

Figure 3.5: Comparison of multi-stage integrators based on their maximum error and associated number of right-hand side evaluation. The benchmark and required accuracies are indicated with dashed lines.

data points. The latter is necessary to avoid Runge's phenomenon [268], a divergence problem occurring close to the boundaries of the interpolation region, from occurring.

3.2.2. Line Search Methods

A univariate optimisation method was necessary for two aspects of the vane control algorithm presented in the associated paper. From the options available in the SciPy [269] library, the golden section algorithm was selected as it does not require any derivative information and provides a convergence efficiency close to the Fibonacci search with a minimum computational cost [265]. For problems having a discontinuity second (or lower) order derivative, this numerical scheme is the preferred alternative according to Press et al. [265]. When an initial bracket $[x_a, x_b]$ known, as is the case in the present work, the method consists of a sectioning iterative procedure aiming to reduce the interval x_a and x_b by computing x_c and x_d, and redefining the bounds of the interval based on the objective value at points c and d. For $f(x_c) < f(x_d)$: $x_b = x_d$ and $x_d = x_c$, the interval is then reduced and point c is recomputed using Eq. (3.23). Similarly, for $f(x_c) > f(x_d)$: $x_a = x_c$ and $x_c = x_d$, the interval is then reduced and point d is recomputed. This is iterated upon, until the interval length is smaller than a user-specified tolerance.

$$h = x_b - x_a \qquad \text{(3.23a)} \qquad x_c = x_a + \frac{h}{\Phi^2} \qquad \text{(3.23b)} \qquad x_d = x_a + \frac{h}{\Phi} \qquad \text{(3.23c)}$$

where $\Phi = \frac{1+\sqrt{5}}{2}$ is the golden ratio. No interpolation is performed as the tolerance on the interval length can be imposed to be arbitrarily small, rendering the interpolation unnecessary if the residuals are imposed to be lower than the model accuracy. The output value is taken as the final interval bound with the minimum objective function. Furthermore, this algorithm can also be used to find a discontinuity in the bracket.

Part II

Research Paper

Solar-Sail Tumbling and Stabilization using Actuated Tip-Vanes

Lorenz A.V Veithen *
Delft University of Technology, 2629 HS, Delft, The Netherlands

Solar-sailing is a promising propellant-free propulsion method leveraging the momentum of photons to generate a thrust force, making them attractive for long-term missions both in Earth-bound and interplanetary space. In Earth orbit, solar-sails have been envisioned for space debris removal missions aiming to de-orbit multiple defunct satellites. However, their large sail area make them vulnerable to hypervelocity impacts with debris, potentially causing loss of attitude control. Therefore, this paper presents a study of the long-term effects of tumbling on a sail's orbit and of the capability of a modern vane attitude control system to time-optimally stabilise the attitude motion. The tumbling dynamics result in an orbital eccentricity growth which is independent of the tumbling rate, potentially leading to a re-entry of the sail. The vane system is capable of detumbling rotational velocities up to 26 deg/s. For rotational velocities up to 8 deg/s, this system is capable of detumbling the sailcraft at a linear rate of 2 deg/s per day. For larger rotational velocities, the duration of the detumbling manoeuvre grows non-linearly. These results are considered for the specific case study of hypervelocity impacts and the sensitivity of the results to the sail reflectance model, the orbital regime, and the number of degrees of freedom of the vanes is assessed.

I. Introduction

SINCE the launch of Sputnik 1 in 1957 [1], mankind's dependence on space activities has steadily grown. Ranging from global communication to Global Navigation Satellite Systems (GNSS), disaster early warning systems, and climate change monitoring, space technologies have significantly shaped humankind [2]. However, while Sputnik 1 remained in orbit for three months only, Vanguard 1, launched by the United States of America (USA) in 1958, will remain in Medium-Earth Orbit (MEO) for the next 200 years despite having been inactive since 1964 [3]. Since Vanguard 1, the population of artificial objects in Earth orbit has grown steadily, driven by increased launch activities and orbital fragmentation events [4]. Consequently, the Low Earth Orbit (LEO) and Geostationary Orbit (GEO) protected regions have become hostile environments to modern satellites, where collision avoidance manoeuvres are common practice [5].

The large number of uncontrollable objects in Earth orbit also increases the likelihood of the onset of a self-sustaining

*Graduate student, Department of Astrodynamics and Space Missions, Faculty of Aerospace Engineering. lveithen@tudelft.net

collisional cascading process when the number of objects in an orbital region reaches a critical threshold [6]. This phenomenon, theorised by [7] in 1978, is known as the Kessler syndrome and would result in the denial of some orbital regions due to the space-debris build-up on the long-term. This problem is intensified by the recent trends of the NewSpace, with thousands of satellites launched to form mega-constellations in Low Earth Orbit (LEO) [8], and is already observed in debris environment studies [4, 9]. Active Debris Removal (ADR) is therefore considered necessary to delay the onset of the Kessler syndrome and preserve humankind's access to space [10].

One promising ADR method makes use of solar-sails, which generate a thrust force from the Solar Radiation Pressure (SRP) by reflecting photons, to de-orbit high-altitude satellites at their End-of-Life (EoL) [11, 12]. Additionally, their propellant-free nature provides an opportunity for long-term missions aiming to travel to multiple defunct satellites to remove them from orbit, as the sail material degradation is the only constraint on the mission duration [13]. This characteristic also motivates the use of an Attitude Control System (ACS) which relies on SRP, by controlling the position of the sail's centre of pressure (c_p) relative to the centre of mass (c_m) to generate control torques, instead of using a reaction mass [12, 14–16]. An especially attractive type of SRP-based ACS is the two rotational degrees-of-freedom (DoF) tip-vanes system, which controls the sail attitude through reflective vanes placed at the booms' tips [16, 17]. The concept resembles aircraft control surfaces which create a torque by asymmetrically deflecting the airflow on small portions of the wing, except that, in this case, light is reflected instead [18]. Although 2-DoF actuated tip-vanes allow for three-axis stabilization regardless of the sail's initial orientation [17], the system becomes over-constrained when more than three total DoFs are present (two DoFs per vane) [18]. This renders the control system design laborious, therefore, the majority of literature focused on the control of single-DoF vane systems [15, 19]. However, [17] presented a novel control allocation strategy which greatly reduces the control complexity of 2-DoF vanes.

One of the main disadvantages of solar-sails comes from their large sail area, which increases the risk of collisions with orbital debris and results in a high Mass Moment of Inertia (MMI), thereby their manoeuvrability and making them vulnerable to on-orbit collisions. While a large debris impact on a supporting boom may not cause a catastrophic breakup, it can induce significant momentum transfer, perturbing the coupled attitude-orbit dynamics [20]. These collisions are referred to as HyperVelocity Impacts (HVI), where the momentum carried by the colliding debris is distributed across the 1) target body, 2) ejecta from the collision crater, 3) spalled material from the non-impacted surfaces, and 4) downrange ejecta [21]. While for very thin target materials such as solar-sail foils, the momentum transfer to the spacecraft approaches zero [22], large amounts of momentum can be transferred through collisions with thicker targets such as supporting booms [23]. Although [20, 24] found that the effect of this momentum transfer on the attitude and orbital dynamics of conventional satellites is rather small, high area-to-mass ratio bodies are more affected due to the large moment arm of the impulse, possibly resulting in a tumbling motion. As the attitude of a solar-sail directly dictates its thrust direction, an uncontrolled tumbling motion would have direct implications on the spacecraft orbital dynamics [13].

The implications of the tumbling motion on the sail orbital dynamics, and whether the retrieval of attitude control after a hypervelocity impact is feasible using the propellant-free attitude control methods in the Earth-bound environment, are unclear. While the use of solar-sails in Earth orbit is attractive, the current state and trends of the space debris environment raise concerns about the safety of navigating a sailcraft in debris-rich regions. This paper therefore presents a study of the long-term effects of the sail's tumbling dynamics and the capability of a modern vane attitude control system to time-optimally stabilise the attitude motion, using a six-degree-of-freedom attitude-orbit simulator. The results from this study are then linked to the potential perturbation of the sail attitude dynamics from a high-energy collision on a square sail in Earth orbit. These aspects are first studied for the case study of an Advanced Composite solar-sail System (ACS3)-like sail, which is the state-of-the-art in terms of solar-sailing [25]. Subsequently, the sensitivity of the results to different sail reflectance models, orbital regimes and ACS characteristics, are considered.

This paper is structured as follows. First, section II presents the overall dynamical model used throughout the study, including the solar-sail and hypervelocity impact models. Then section III gives a detailed description of the vane system controller used to stabilise a solar-sail in Earth orbit. section IV provides an analysis of the effects of tumbling on the sail dynamics, and section V analyses the detumbling capabilities of the vane system under various scenarios. Then, section VI studies the specific case of hypervelocity impacts causing the tumbling dynamics. At last, the conclusions drawn from the results are summarised in section VII.

II. Dynamical Model

This paper considers a square sail augmented by four 2-DoF tip-vanes, subject to SRP in a central gravity field. All other orbital perturbations are neglected to isolate the effect of SRP, thereby providing better insights into its effect on the tumbling dynamics and attitude recovery. Additionally, the sailcraft is considered in a fully deployed state, and is assumed to be a constant mass and rigid body with flat reflective surfaces where the vanes are allowed to rotate around their attachment point, but the contribution of this movement to the inertia tensor is neglected. Therefore, the vane orientation only affects the SRP force and torques acting on the spacecraft. The solar-sail dynamics are then modelled using a six-DoF attitude-orbit simulator, neglecting the sail structural dynamics. The model was developed using the propagation tools of the TU Delft Astrodynamics Toolbox (TUDAT) [26], which provides numerous libraries supporting astrodynamics and space research, and is available under an open-source license at `https://github.com/LorenzVeithen/SolarSailOrbitAttitudeCoupling`. This section first presents the reference frames and the complete set of Equations of Motion (EoM) for the coupled dynamical system, followed by a detailed description of the solar-sail model considered.

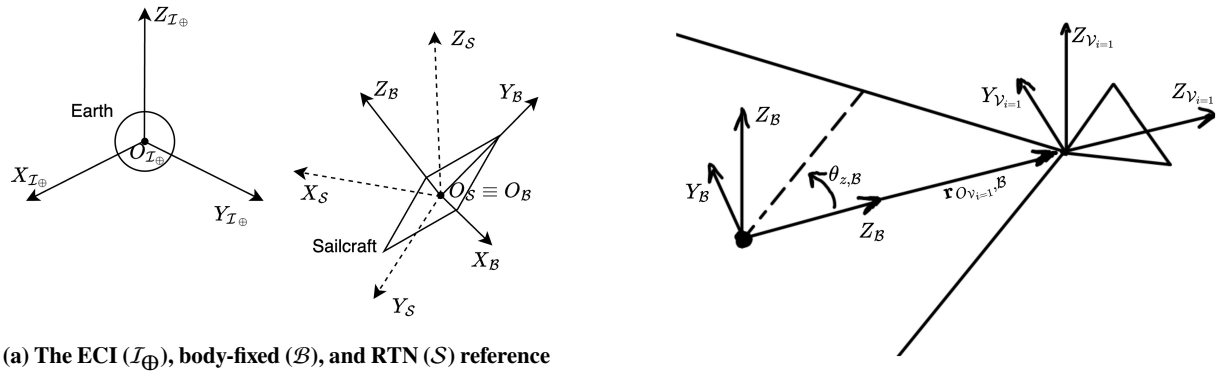

(a) The ECI ($\mathcal{I}_\oplus$), body-fixed ($\mathcal{B}$), and RTN ($\mathcal{S}$) reference frames.

(b) The vane-centered reference frame of vane 1.

Fig. 1 Reference frames.

A. Reference Frames

Figure 1 shows the four reference frames are used to define the dynamics of the sail system in the following sections. These frames are briefly described below:

1) The **Earth-Centered Inertial** (ECI) reference frame, denoted by $\mathcal{I}_\oplus$, has its origin $O_{\mathcal{I}_\oplus}$ at the Center of Mass (CoM) of the Earth, and its orientation is defined based on the J2000 epoch. At J2000, the frame $Z_{\mathcal{I}_\oplus}$-axis points North along the rotational axis of the Earth, the $X_{\mathcal{I}_\oplus}$-axis points in the direction of the vernal equinox, and $Y_{\mathcal{I}_\oplus}$ completes the right-handed coordinate system [27]. The ECI frame is shown in Figure 1a as the only Earth-centered reference frame.

2) The **Radial, Transverse, and Normal** (RTN) frame, denoted by $\mathcal{S}$, is a spacecraft-centered with its origin $O_{\mathcal{S}}$ at the sailcraft CoM, $X_{\mathcal{S}}$ parallel to the radial position vector, $Z_{\mathcal{S}}$ in the direction of the orbital angular momentum vector, and $Y_{\mathcal{S}}$ completes the right-handed coordinate system [28]. The unit vectors of the reference frame are given by,

$$\hat{\boldsymbol{R}}_{RTN} = \frac{\boldsymbol{r}_{\mathcal{I}_\oplus}}{||\boldsymbol{r}_{\mathcal{I}_\oplus}||} \tag{1a}$$

$$\hat{\boldsymbol{N}}_{RTN} = \frac{\boldsymbol{r}_{\mathcal{I}_\oplus} \times \boldsymbol{v}_{\mathcal{I}_\oplus}}{||\boldsymbol{r}_{\mathcal{I}_\oplus} \times \boldsymbol{v}_{\mathcal{I}_\oplus}||} \tag{1b}$$

$$\hat{\boldsymbol{T}}_{RTN} = \frac{\hat{\boldsymbol{N}}_{RTN} \times \hat{\boldsymbol{R}}_{RTN}}{||\hat{\boldsymbol{N}}_{RTN} \times \hat{\boldsymbol{R}}_{RTN}||} \tag{1c}$$

where $\boldsymbol{r}_{\mathcal{I}_\oplus}$ and $\boldsymbol{v}_{\mathcal{I}_\oplus}$ are the inertial position and velocity the vectors respectively, and $\hat{\boldsymbol{R}}$, $\hat{\boldsymbol{T}}$, and $\hat{\boldsymbol{N}}$ are the unit vectors of the RTN reference frame axes expressed in the ECI frame. The rotation matrix from the ECI to the RTN frames is then given by,

$$\boldsymbol{R}_{\mathcal{S}\mathcal{I}_\oplus} = \begin{bmatrix} \hat{\boldsymbol{R}}_{RTN} & \hat{\boldsymbol{T}}_{RTN} & \hat{\boldsymbol{N}}_{RTN} \end{bmatrix}. \tag{2}$$

The RTN frame is shown in Figure 1a as the dashed sailcraft-centered reference frame.

3) The **body-fixed** reference frame, denoted by $\mathcal{B}$, has its origin $O_{\mathcal{B}}$ at the spacecraft CoM, the $Z_{\mathcal{B}}$-axis pointing in

the direction of the sail normal vector, the $X_{\mathcal{B}}$ points along a reference boom of the sail, and $Y_{\mathcal{B}}$ completes the right-handed coordinate system. The initial rotation matrix from the ECI to the body-fixed frame is known for a given case study, and propagated using the equations of rotational motion in subsection II.B. The body-fixed frame is shown in Figure 1a as the solid lines sailcraft-centered reference frame.

4) The **vane-centered** reference frame of the i$^{\text{th}}$ vane, denoted by $\mathcal{V}_i$, has its origin $O_{\mathcal{V}_i}$ located at the vane attachment point*, $X_{\mathcal{V}_i}$ is aligned with the associated boom direction and points outside of the sail, $Z_{\mathcal{V}_i}$ is in the direction of the body-fixed $Z_{\mathcal{B}}$-axis, and $Y_{\mathcal{V}_i}$ completes the right-handed frame. The frame does not move with the vane during its movement, and the transformation from the i$^{\text{th}}$ vane reference frame to the body-fixed frame is given by,

$$\boldsymbol{r}_{\mathcal{B}} = \boldsymbol{r}_{O_{\mathcal{V}_i},\mathcal{B}} + \boldsymbol{R}_{\mathcal{B}\mathcal{V}_i}\boldsymbol{r}_{\mathcal{V}_i} \tag{3}$$

where $\boldsymbol{R}_{\mathcal{B}\mathcal{V}_i}$ is the rotation matrix from the vane to the body-fixed reference frame for the i$^{\text{th}}$ vane, $\boldsymbol{r}_{O_{\mathcal{V}_i},\mathcal{B}}$ is the position of the i$^{\text{th}}$ vane reference frame origin expressed in the body-fixed frame, and $\boldsymbol{r}$ is an arbitrary position vector. The i indices of each vane are described below, but this reference frame is given for vane $i = 1$ in Figure 1b. In this figure, $\theta_{z,\mathcal{B}}$ is the angle of rotation around the $X_{\mathcal{B}}$-axis (drawn positively). The i$^{\text{th}}$ vane is associated with the $\theta^i_{z,\mathcal{B}}$ angle of rotation.

B. Equations of Motion

The sail attitude and orbital dynamics are coupled, as both the sail attitude and position in inertial space have an influence on the SRP force and torque acting on the spacecraft. This coupling is described in the set of EoMs given hereafter, and integrated with a variable step size multi-stage Runge-Kutta-Fehlberg 5(6) (RKF5(6)) integrator with absolute and relative tolerances of 10^{-12}.

1. Translational Equations

The orbital motion is propagated based on the Modified Equinoctial Elements (MEE) formulation of the Gauss perturbation equations with elements p, f, g, h, k, L [29], which describes the motion of the spacecraft's centre of mass (CoM) based on the components of the perturbing acceleration in the RTN frame. Note that this formulation has a singularity at an inclination of $i = 180°$. In this paper, only the SRP force perturbs the orbital motion. With m the spacecraft mass and the SRP acceleration components in the RTN frame given by $[\boldsymbol{a}_{SRP,r} \quad \boldsymbol{a}_{SRP,n} \quad \boldsymbol{a}_{SRP,t}]^T = \boldsymbol{F}_{SRP,\mathcal{S}}/m$, this permits to write [30],

$$\frac{\mathrm{d}p}{\mathrm{d}t} = \frac{2p}{w}\sqrt{\frac{p}{\mu_\oplus}}\boldsymbol{a}_{SRP,t}, \tag{4a}$$

$$\frac{\mathrm{d}f}{\mathrm{d}t} = \sqrt{\frac{p}{\mu_\oplus}}\left[\boldsymbol{a}_{SRP,r}\sin L + ((w+1)\cos L + f)\,\frac{\boldsymbol{a}_{SRP,t}}{w} - (h\sin L - k\cos L)\frac{g\boldsymbol{a}_{SRP,n}}{w}\right], \tag{4b}$$

*Which is always located at the boom tips in this paper.

$$\frac{\mathrm{d}g}{\mathrm{d}t} = \sqrt{\frac{p}{\mu_\oplus}}\left[-\boldsymbol{a}_{SRP,r}\cos L + ((w+1)\sin L + g)\,\frac{\boldsymbol{a}_{SRP,t}}{w} + (h\sin L - k\cos L)\,\frac{f\boldsymbol{a}_{SRP,n}}{w}\right], \tag{4c}$$

$$\frac{\mathrm{d}h}{\mathrm{d}t} = \sqrt{\frac{p}{\mu_\oplus}}\frac{s^2\boldsymbol{a}_{SRP,n}}{2w}\cos L, \tag{4d}$$

$$\frac{\mathrm{d}k}{\mathrm{d}t} = \sqrt{\frac{p}{\mu_\oplus}}\frac{s^2\boldsymbol{a}_{SRP,n}}{2w}\sin L, \tag{4e}$$

$$\frac{\mathrm{d}L}{\mathrm{d}t} = \sqrt{\mu_\oplus p}\left(\frac{w}{p}\right)^2 + \frac{1}{w}\sqrt{\frac{p}{\mu_\oplus}}(h\sin L - k\cos L)\boldsymbol{a}_{SRP,n}, \tag{4f}$$

with,

$$s^2 = 1 + h^2 + k^2, \tag{5a}$$

$$w = 1 + f\cos L + g\sin L, \tag{5b}$$

where t is the time variable, m is the sailcraft mass, and $\mu_\oplus$ is the gravitational parameter of the Earth. The penumbra-umbra eclipse model described in Reference [31] is used, neglecting the small effect of the atmosphere on the absorption and refraction of light [32]. This means that no SRP force is generated when the spacecraft is not in direct line of sight with the Sun.

2. Rotational Equations

The spacecraft attitude dynamics are modelled according to Euler's attitude equation of motion for a rigid body [33],

$$\dot{\boldsymbol{\omega}}_{\mathcal{I}_\oplus\mathcal{B},\mathcal{B}} = (\boldsymbol{I}_\mathcal{B})^{-1}\left(\boldsymbol{T}_{SRP,\mathcal{B}} - \boldsymbol{\omega}_{\mathcal{I}_\oplus\mathcal{B},\mathcal{B}} \times \left(\boldsymbol{I}_\mathcal{B}\boldsymbol{\omega}_{\mathcal{I}_\oplus\mathcal{B},\mathcal{B}}\right)\right), \tag{6}$$

where $\boldsymbol{\omega}_{\mathcal{I}_\oplus\mathcal{B},\mathcal{B}}$ is the rotational velocity vector of the body frame with respect to the ECI and is abbreviated to $\boldsymbol{\omega}_\mathcal{B}$ for brevity, $\boldsymbol{T}_{SRP,\mathcal{B}}$ is the SRP torque vector acting on the spacecraft, and $\boldsymbol{I}_\mathcal{B}$ is the sailcraft inertia tensor, all expressed in the body-fixed frame. Additionally, $\dot{\boldsymbol{I}}_\mathcal{B} \approx 0$ is assumed. Assuming that the inertia tensor is a diagonal matrix and that $I_{xx,\mathcal{B}} = I_{yy,\mathcal{B}}$ but $I_{zz,\mathcal{B}} \neq I_{xx,\mathcal{B}}$, as is the case for a sailcraft, the last term in Eq. (6) can be expanded to reveal the influence of the gyroscopic torque on the rotational velocity vector,

$$\boldsymbol{\omega}_{\mathcal{I}_\oplus\mathcal{B},\mathcal{B}} \times \left(\boldsymbol{I}_\mathcal{B}\boldsymbol{\omega}_{\mathcal{I}_\oplus\mathcal{B},\mathcal{B}}\right) = \underbrace{\begin{bmatrix} \left(-I_{yy,\mathcal{B}}\omega_{y,\mathcal{B}}\omega_{z,\mathcal{B}} + I_{zz,\mathcal{B}}\omega_{z,\mathcal{B}}\omega_{y,\mathcal{B}}\right) \neq 0 \\ \left(I_{xx,\mathcal{B}}\omega_{x,\mathcal{B}}\omega_{z,\mathcal{B}} - I_{zz,\mathcal{B}}\omega_{x,\mathcal{B}}\omega_{z,\mathcal{B}}\right) \neq 0 \\ \left(-I_{xx,\mathcal{B}}\omega_{x,\mathcal{B}}\omega_{y,\mathcal{B}} + I_{yy,\mathcal{B}}\omega_{y,\mathcal{B}}\omega_{x,\mathcal{B}}\right) = 0 \end{bmatrix}}_{\boldsymbol{T}_{\mathrm{Gyro},\mathcal{B}}}, \tag{7}$$

which is the gyroscopic torque, $\boldsymbol{T}_{\mathrm{Gyro},\mathcal{B}}$. Therefore, $\dot{\omega}_{x,\mathcal{B}}$ and $\dot{\omega}_{y,\mathcal{B}}$ are non-zero when $\omega_{z,\mathcal{B}} \neq 0$, yielding variations in the direction of $\hat{\omega}_\mathcal{B}$ while $||\boldsymbol{\omega}_\mathcal{B}||$ remains constant. The gyroscopic torque is a direct result of Euler's attitude equation of motion for a sailcraft, and represents its internal dynamics. Furthermore, the sail orientation is propagated using

quaternion elements, as they allow a singularity-free representation. The link between the rotation matrix describing the body-fixed reference frame orientation with respect to the inertial frame, and the four quaternion elements is given in Reference [34],

$$q_1 = \frac{\left(\boldsymbol{b}_{\mathcal{I}_\oplus\mathcal{B}}(2,3) - \boldsymbol{b}_{\mathcal{I}_\oplus\mathcal{B}}(3,2)\right)}{4q_4}, \tag{8a}$$

$$q_2 = \frac{\left(\boldsymbol{b}_{\mathcal{I}_\oplus\mathcal{B}}(3,1) - \boldsymbol{b}_{\mathcal{I}_\oplus\mathcal{B}}(1,3)\right)}{4q_4}, \tag{8b}$$

$$q_3 = \frac{\left(\boldsymbol{b}_{\mathcal{I}_\oplus\mathcal{B}}(1,2) - \boldsymbol{b}_{\mathcal{I}_\oplus\mathcal{B}}(2,1)\right)}{4q_4}, \tag{8c}$$

$$q_4 = \frac{1}{2}\sqrt{1 + \boldsymbol{b}_{\mathcal{I}_\oplus\mathcal{B}}(1,1) + \boldsymbol{b}_{\mathcal{I}_\oplus\mathcal{B}}(2,2) + \boldsymbol{b}_{\mathcal{I}_\oplus\mathcal{B}}(3,3)}, \tag{8d}$$

$$\sum_{i=1}^{4} q_i = 1, \tag{8e}$$

where $\boldsymbol{b}_{\mathcal{I}_\oplus\mathcal{B}}$ is the rotation matrix from the body-fixed frame to the inertial frame at a given time, $\boldsymbol{b}_{\mathcal{I}_\oplus\mathcal{B}}(i,j)$ is the element of $\boldsymbol{b}_{\mathcal{I}_\oplus\mathcal{B}}$ on the i$^{\text{th}}$ row and j$^{\text{th}}$ column, and $q_{1,2,3,4}$ are the four quaternion elements. As numerical noise can arise in the propagation, the quaternion state vector is normalised at each time step to avoid deviations from Eq. (8e). With $\boldsymbol{\omega}_{\mathcal{I}_\oplus\mathcal{B},\mathcal{B}}$, the sail orientation is propagated using [33],

$$\begin{bmatrix} \dot{q}_1 \\ \dot{q}_2 \\ \dot{q}_3 \\ \dot{q}_4 \end{bmatrix} = \frac{1}{2}\begin{bmatrix} q_4 & -q_3 & q_2 \\ q_3 & q_4 & -q_1 \\ -q_2 & q_1 & q_4 \\ -q_1 & -q_2 & -q_3 \end{bmatrix} \boldsymbol{\omega}_{\mathcal{B}}. \tag{9}$$

C. Solar-Sail Model

Having presented the overall dynamical model considered, this section presents the solar-sail model used to determine $\boldsymbol{F}_{SRP}$ and $\boldsymbol{T}_{SRP}$. Figure 2 shows the fully-deployed rigid square sail model. In this figure, the indices of the wing quadrants and the vanes are indicated with the i superscript, $(X_\mathcal{B}, Y_\mathcal{B}, Z_\mathcal{B})$ give the body-fixed frame described above, and $\boldsymbol{n}^i_{w,\mathcal{B}}$ and $\boldsymbol{n}^i_{v,\mathcal{B}}$ are the unit surface normal vectors, expressed in the body-fixed frame denoted by $\mathcal{B}$, of the i$^{\text{th}}$ wing quadrant and vane respectively. Each wing quadrant of the main sail (labelled w) and tip-vane (labelled v) of the sailcraft is modelled independently by their centroid position[†] ($\boldsymbol{r}^i_{w,\mathcal{B}}$ and $\boldsymbol{r}^i_{v,\mathcal{B}}$, omitted in the figure), surface normal ($\boldsymbol{n}^i_{w,\mathcal{B}}$ and $\boldsymbol{n}^i_{v,\mathcal{B}}$), and surface area, each expressed in the body-fixed frame. In this sail model, the contribution of the spacecraft bus to the SRP force is neglected, although its mass and contribution to the inertia tensor are taken into account, and the spacecraft CoM and centre of gravity are assumed to coincide at the origin of the body-fixed frame.

[†]In Figure 2, the centroid position of each reflective surface is the point of application of the surface normal vectors.

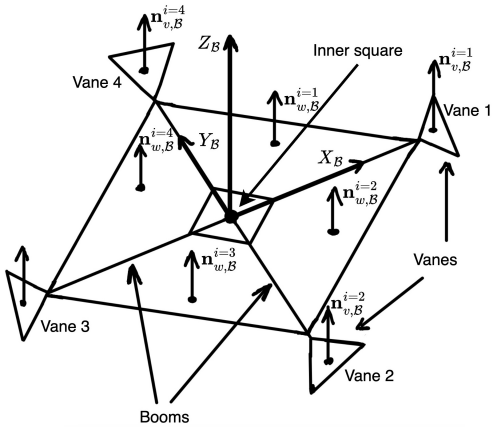

Fig. 2 Square rigid sail with a vane-based attitude control system.

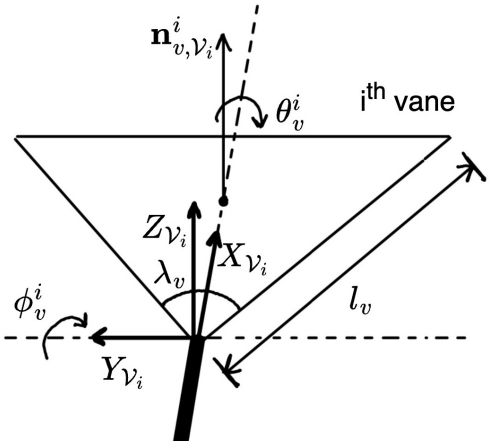

Fig. 3 Vane rotational degrees of freedom in the vane reference frame.

Table 1 Sail model characteristics inspired from [25].

Parameter	Value
Sailcraft mass, m	16 kg
Booms length	7 m
Sail side length	9.9 m
Sail inner square side length	0.9 m
Sailcraft MMI, ($I_{xx,\mathcal{B}}$, $I_{yy,\mathcal{B}}$, $I_{zz,\mathcal{B}}$)	(10.5, 10.5, 21) kg m^2

Table 2 Vane model characteristics.

Parameter	Value
Side length, l_v	0.5 m
Inner angle, λ_v	120°

The ACS3 technology demonstrator mission launched in April 2024 is used as a baseline to formulate the sailcraft model. The main characteristics of the sail are given in Table 1. In this table, the total spacecraft mass does not include the vanes (as their mass is neglected, see below), and the inner square is the gap leaving space for the 12U CubeSat bus in the middle of the sail in Figure 2. Additionally, the gaps between the sail material and each boom are neglected, which results in a sail surface area of 97.18 m^2 rather than 80 m^2 given in Reference [25], resulting in a larger sail lightness number of $\beta = 0.00935$ compared to the ACS3 lightness number of $\beta = 0.0077$.

Additionally, Figure 3 gives the geometry of the vanes considered. In this figure, ($X_{\mathcal{V}_i}, Y_{\mathcal{V}_i}, Z_{\mathcal{V}_i}$) represent the vane reference frame described above, l_v m and λ_v are the side length and the inner angle of the vanes respectively, θ_v^i is the rotation angle around the $X_{\mathcal{V}_i}$-axis (first DoF), and ϕ_v^i is the rotation angle around the $Y_{\mathcal{V}_i}$-axis (second DoF). The contribution of vane material and actuators to the spacecraft mass and inertia tensor is neglected. Therefore, the total spacecraft mass for such a system is slightly underestimated. The values of the vane geometry parameters are given in Table 2. Note that the moment arm of each vane is given by the boom length of 7 m.

Table 3 ACS3 optical coefficients [25].

Sail-side	α	ρ_s	ρ_d	ϵ	B
front, f	0.1	0.74	0.16	0.03	2/3
back, b	0.57	0.23	0.2	0.6	2/3

1. Sail-Photon Interaction Model

Three sail-photon interaction models are considered: a single-sided ideal model (SI-SRP), a double-sided ideal model (DI-SRP), and an optical model (O-SRP) based on the ACS3 [25]. As the former two assume purely specularly reflected photons, they permit to draw noise-free trends in the results. However, the optical model is more realistic by accounting for absorption, specular reflection, and diffuse reflection of photons [13]. All three models can be represented by the reflectance model from [16]. The SRP force acting on the i$^{\text{th}}$ wing, with all vectors expressed in the ECI[‡],

$$\boldsymbol{f}^i_{SRP_w} = \frac{WS^i_w|\cos(\theta^i_{s_w})|}{c}\begin{cases} \left(\alpha_f\left(\boldsymbol{n}_s + \frac{\epsilon_b B_b - \epsilon_f B_f}{\epsilon_f+\epsilon_b}\boldsymbol{n}^i_w\right) - 2\rho_{s_f}\cos(\theta^i_{s_w})\boldsymbol{n}^i_w + \rho_{d_f}\left(\boldsymbol{n}_s - B_f\boldsymbol{n}^i_w\right)\right) & \boldsymbol{n}^i_w\cdot(-\boldsymbol{n_s}) > 0 \\ \left(\alpha_b\left(\boldsymbol{n}_s + \frac{\epsilon_b B_b - \epsilon_f B_f}{\epsilon_f+\epsilon_b}\boldsymbol{n}^i_w\right) - 2\rho_{s_b}\cos(\theta^i_{s_w})\boldsymbol{n}^i_w + \rho_{d_b}\left(\boldsymbol{n}_s + B_b\boldsymbol{n}^i_w\right)\right) & \boldsymbol{n}^i_w\cdot(-\boldsymbol{n_s}) < 0 \end{cases}. \tag{10}$$

In Eq. (10), $\boldsymbol{n}_s$ is the sunlight vector, $\theta^i_{s_w}$ is the angle between the wing surface normal and the sunlight direction such that $\cos\left(\theta^i_{s_w}\right) = \boldsymbol{n}^i_w\cdot(-\boldsymbol{n_s})$, W is the solar irradiance, c is the speed of light, S^i_w is the area of the considered wing, and α, ρ_s, ρ_d ϵ, and B are the absorptivity, specular reflectivity, diffuse reflectivity, emissivity, and Lambertian diffusion optical coefficients of the sail material respectively. The front and back sides of the foil are referred to with the f and b subscripts, respectively. From Eq. (10), the SI-SRP model is obtained by substituting $\rho_{s_f} = 1$ and zeroing all other coefficients, and the DI-SRP model is obtained by substituting $\rho_{s_f} = \rho_{s_b} = 1$ and $\alpha = \rho_d = 0$ for both the front and back sides of the sail. Additionally, the optical characteristics of the ACS3 are used for the O-SRP model, given in Table 3. Eq. (10) can be similarly formulated for a vane reflective surface by substituting all the w subscripts by v. Moreover, it is assumed that the sailcraft wings and tip-vanes can follow different reflectance laws (e.g., the wings follow the O-SRP model while the vanes have the SI-SRP model). In three-dimensional space, the sunlight vector can be expressed in the body-fixed frame using the cone- and clock angles $\alpha_{s,\mathcal{B}}$ and β_s,

$$\boldsymbol{n}_{s,\mathcal{B}} = \begin{bmatrix}\sin\left(\alpha_{s,\mathcal{B}}\right)\cos\left(\beta_{s,\mathcal{B}}\right) & \sin\left(\alpha_{s,\mathcal{B}}\right)\sin\left(\beta_{s,\mathcal{B}}\right) & -\cos\left(\alpha_{s,\mathcal{B}}\right)\end{bmatrix}^T, \tag{11}$$

where $-\pi \leq \alpha_{s,\mathcal{B}} \leq \pi$ and $-\pi \leq \beta_{s,\mathcal{B}} \leq \pi$. The sun angles are shown in Figure 4, which gives the three-dimensional representation of the SRP force in the body-fixed frame [17]. In this figure, $\boldsymbol{F}_{SRP_{XY},\mathcal{B}}$ is the component of the SRP force in the $X_\mathcal{B}Y_\mathcal{B}$ plane, which is the sail plane. Additionally, while the surface normal directions of the wings always points in the $Z_\mathcal{B}$ direction in the body-fixed frame, the vanes' surface normal directions depends on their orientation, as

[‡]omitting the $\mathcal{I}_\oplus$ subscripts for brevity.

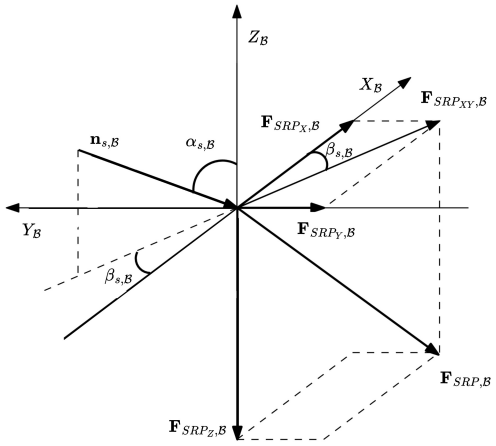

Fig. 4 Three-dimensional representation of the solar radiation pressure force in the body-fixed frame, adapted from [17].

considered in the next section. The body-fixed torque induced by the SRP force acting on the i$^{\text{th}}$ wing, $\boldsymbol{f}^i_{SRP_w}$, can then be obtained from the wing centroid using,

$$\boldsymbol{\tau}^i_{SRP_w,\mathcal{B}} = \boldsymbol{r}^i_{w,\mathcal{B}} \times \boldsymbol{f}^i_{SRP_w,\mathcal{B}}. \tag{12}$$

Again, a similar expression can be obtained for a vane reflective surface by substituting all the w subscripts by v. Additionally, in Eq. (12), it is used that the spacecraft centre of gravity coincides with $O_{\mathcal{B}}$. The total SRP force and torque acting on the sail in a given inertial orientation and position can then be obtained by summing up the contributions of each individual wing and vane,

$$\boldsymbol{F}_{SRP,\mathcal{B}} = \sum_i \boldsymbol{f}^i_{SRP_w,\mathcal{B}} + \sum_i \boldsymbol{f}^i_{SRP_v,\mathcal{B}}, \tag{13a}$$

$$\boldsymbol{T}_{SRP,\mathcal{B}} = \sum_i \boldsymbol{\tau}^i_{SRP_w,\mathcal{B}} + \sum_i \boldsymbol{\tau}^i_{SRP_v,\mathcal{B}}. \tag{13b}$$

2. Vane Dynamical Model

Having obtained formulations for $\boldsymbol{F}_{SRP}$ and $\boldsymbol{T}_{SRP}$, it remains to characterise the dynamical model of the vanes to obtain $\boldsymbol{n}^i_v$ and $\boldsymbol{r}^i_v$ as functions of the vane orientation. As mentioned above, each vane in Figure 2 has up to two rotational DoF around the $X_{\mathcal{V}_i}$ and $Y_{\mathcal{V}_i}$ axes of the vane reference frame shown in Figure 3, given by θ^i_v and ϕ^i_v. It is assumed that both rotational DoF of each vane have a full range of motion, such that $-\pi \leq \theta^i_v \leq \pi$ and $-\pi \leq \phi^i_v \leq \pi$. Based on these angles, the surface normal direction of the considered vane is obtained from,

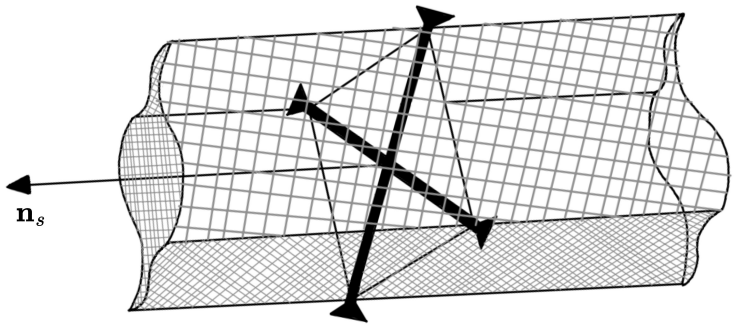

Fig. 5 Vane self-shadowing region.

$$\boldsymbol{n}^i_{v,\mathcal{V}_i} = \left[\sin\left(\phi^i_v\right)\cos\left(\theta^i_v\right) \quad -\sin\left(\theta^i_v\right) \quad \cos\left(\phi^i_v\right)\cos\left(\theta^i_v\right)\right]^T, \tag{14}$$

in the vane reference frame. Additionally, the position of the centroid of the i$^{\text{th}}$ vane can be obtained from,

$$\boldsymbol{r}^i_{v_1,\mathcal{V}_i} = \boldsymbol{R}_y(\phi^i_v)\boldsymbol{R}_x(\theta^i_v)\boldsymbol{r}^i_{v_0,\mathcal{V}_i}, \tag{15}$$

where $\boldsymbol{R}_x$ and $\boldsymbol{R}_y$ are Euler's rotation matrices around $X_{\mathcal{V}_i}$ and $Y_{\mathcal{V}_i}$ respectively, $\boldsymbol{r}^i_{v_0,\mathcal{V}_i}$ is the default vane centroid position vector in the i$^{\text{th}}$ vane reference frame, and $\boldsymbol{r}^i_{v_1,\mathcal{V}_i}$ is the rotated position vector of the vane centroid. Equations (14) and (15) give the vane centroid ($\boldsymbol{r}^i_{v,\mathcal{V}_i} \sim \boldsymbol{r}^i_{v_1,\mathcal{V}_i}$) and surface normal vectors in the i$^{\text{th}}$ vane-centered frame, for a given vane orientation. Converting these vectors to the body-fixed reference frame using Eq. (3) permits to compute the vane's contribution to the body-fixed SRP force and torque using Eqs. (10) and (12).

3. Sail Self-Shadowing Model

Some combinations of the vanes' orientation and the sail attitude may result in one casting shadow over the other. Such self-shadowing occurs if a vane enters the infinite parallelepiped obtained by extruding the sail wings along the sunlight direction. This is shown in Figure 5, where no vane at the boom tips is inside the self-shadowing region. Although the effects of self-shadowing on the SRP force and torque generated by the sail are complex, they are neglected to reduce the computational load. However, they would result in an efficiency loss for both the sail main body and the ACS, making self-shadowing undesirable.

Therefore, vane orientations resulting in self-shadowing are identified to constraint the vane system controller described in section III, thereby avoiding these configurations. This is done by meshing ten equidistant points on each side of the vane model shown in Figure 3, and assessing if any mesh point is inside the infinite parallelepiped shown in Figure 5. If at least one mesh node of the vane is inside the parallelepiped, self-shadowing occurs and the vane orientation is not permitted. Figure 6 gives the permissible domain of $\theta^{i=1}_v$-ϕ^i_v combinations for vane 1 and for sun

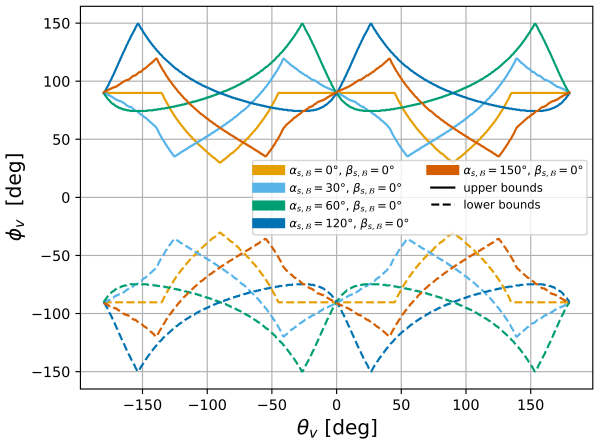

Fig. 6 Domain of the vane angle allocation algorithm under the self-shadowing constraint.

clock angles of $\alpha_{s,\mathcal{B}} = 0, 30, 60, 120, 150°$ and a constant sun cone angle $\beta_{s,\mathcal{B}} = 0°$. In this figure, all combinations of $\theta_v^{i=1}$ and ϕ_v^i between the lower (dashed lines) and upper bounds (solid lines) of the same colour do not result in self-shadowing. Therefore, it can be concluded that while the self-shadowing constraint is more representative for real sailcraft mission operations, it significantly reduces the permissible vane angles. The effects of constraining the permissible vanes' orientation are studied in section V.

D. Tumbling and Hypervelocity Impact Modelling

This paper investigates both the general case of tumbling with an initial rotational velocity and the specific case of attitude disturbances caused by HyperVelocity Impact (HVI). In the former case, initial tumbling rotational velocities between 0.5 deg/s and 15 deg/s are considered, as this range is generally considered as a high tumbling velocity for CubeSats [35]). In the latter case, assuming that the sailcraft is inertially non-rotating prior to the impact, the rotational velocity resulting from an HVI can be formulated as [24],

$$\boldsymbol{\omega}_{0,\mathcal{B}} = \boldsymbol{I}_{\mathcal{B}}^{-1} \left(\boldsymbol{r}_{p,\mathcal{B}} \times \boldsymbol{\Delta p}_{\mathcal{B}} \right), \tag{16}$$

where $\boldsymbol{r}_{p,\mathcal{B}}$ is the impact position on the sail surface in the body-fixed frame and $\boldsymbol{\Delta p}_{\mathcal{B}}$ is the directional linear momentum transferred from the projectile to the sailcraft in the body-fixed frame. Upon impact, the momentum carried by the projectile is transferred to the internal momentum of the spacecraft and the ejecta (back- and downrange) generated by the collision [21]. As the momentum of the ejecta can be in both the projectile direction and opposite to it, momentum enhancement may occur. As a result, more momentum is transferred to the target than was carried by the projectile, as expressed by,

$$\boldsymbol{\Delta p}_{\mathcal{B}} = m_p \boldsymbol{v}_{p,\mathcal{B}} - \sum m_e \boldsymbol{v}_{e,\mathcal{B}} = \beta_E m_p \boldsymbol{v}_{p,\mathcal{B}}, \tag{17}$$

Table 4 Orbital reference cases.

Case	a [km]	e [-]	i [deg]	ω [deg]	Ω [deg]	θ_0 [deg]
O-1	7371	0.004033	98.0	120	27	275
O-2	7371	0.004033	0.0	120	27	275
O-3	16371	0.004033	0.0	120	27	275
O-4	42371	0.004033	0.0	120	27	275

where $0 < \beta_E < 5$ is the momentum enhancement factor, m_p and $\boldsymbol{v}_p$ are the mass and velocity of the projectile in the body-fixed frame respectively, and m_e and $\boldsymbol{v}_e$ are the mass and velocity of the ejecta generated by the collision. Furthermore, the direction of the projectile velocity vector in the body-fixed frame can be expressed similarly to the sunlight vector,

$$\hat{\boldsymbol{v}}_{p,\mathcal{B}} = \begin{bmatrix} \sin\left(\theta_{p,\mathcal{B}}\right)\cos\left(\phi_{p,\mathcal{B}}\right) & \sin\left(\theta_{p,\mathcal{B}}\right)\sin\left(\phi_{p,\mathcal{B}}\right) & -\cos\left(\theta_{p,\mathcal{B}}\right) \end{bmatrix}^T. \tag{18}$$

where $\theta_{p,\mathcal{B}}$ and $\phi_{p,\mathcal{B}}$ are the zenith and azimuth angles of the projectile velocity direction in the body-fixed frame. However, estimating the momentum transfer, and therefore the momentum enhancement factor, resulting from a given HVI is complex and strongly depends on the mass and velocity of the projectile, but also on the shape of the target and the different materials involved [36]. In the very thin target limit where the projectile diameter is ten times larger than the target thickness [37], the momentum transferred to the target tends towards zero as the complete projectile momentum is transferred to the ejecta arising from the collision [22, 38]. As state-of-the-art sailcraft foil thicknesses are of the order of 2.115 µm [39], it can be assumed that collisions with a debris occurring on the sail have a negligible influence on the sailcraft attitude dynamics. In contrast, an impact with one of the sail's supporting booms is much more prone to causing large attitude disruptions. However, as these structures have complex shapes and are made of composite material [39], the effects of HVI on these structures have not yet been considered by literature. Therefore, momentum enhancement factors between 1 and 5 are considered.

E. Orbital and Attitude Reference Cases

A number of initial orbits and attitude relative to the incoming sunlight are used to analyse their effect on the tumbling dynamics and the capabilities of the vane controller to detumble a sailcraft in Earth orbit. The start epoch of all propagations is on the 1st of June 2024 at 00:00, and the end epoch is on the 30th of June 2024 at 00:00 at the latest. Table 4 gives the reference initial orbit cases used, where a is the orbit semi-major axis, e is the orbital eccentricity, ω is the Argument of Pericenter (AoP), and Ω is the Right Ascension of the Ascending Node (RAAN). Case O-1 describes a polar orbit inspired from the ACS3 mission target orbit [25], and comparing cases O-2, O-3, and O-4 gives insights on the orbital altitude. Additionally, two initial sailcraft attitudes are used:

- Case A-1: the body-fixed reference frame has the same orientation as the ECI at the start epoch, that is, $\boldsymbol{R}_{\mathcal{I}_\oplus\mathcal{B}} = \boldsymbol{I}$, where $\boldsymbol{I}$ is the identity matrix. This orientation is arbitrary and is used to demonstrate some properties of the vane

controller in section III.

- Case A-2: the body-fixed reference frame axes are defined in the ECI as,

$$\hat{\boldsymbol{Z}}_{\mathcal{B},\mathcal{I}_\oplus} = \frac{\boldsymbol{r}_{\odot,\mathcal{I}_\oplus}}{||\boldsymbol{r}_{\odot,\mathcal{I}_\oplus}||}, \tag{19a}$$

$$\hat{\boldsymbol{Y}}_{\mathcal{B},\mathcal{I}_\oplus} = \frac{\hat{\boldsymbol{Y}}_{\mathcal{I}_\oplus} \times \hat{\boldsymbol{Z}}_{\mathcal{B},\mathcal{I}_\oplus}}{||\hat{\boldsymbol{Y}}_{\mathcal{I}_\oplus} \times \hat{\boldsymbol{Z}}_{\mathcal{B},\mathcal{I}_\oplus}||}, \tag{19b}$$

$$\hat{\boldsymbol{X}}_{\mathcal{B},\mathcal{I}_\oplus} = \frac{\hat{\boldsymbol{Y}}_{\mathcal{B},\mathcal{I}_\oplus} \times \hat{\boldsymbol{Z}}_{\mathcal{B},\mathcal{I}_\oplus}}{||\hat{\boldsymbol{Y}}_{\mathcal{B},\mathcal{I}_\oplus} \times \hat{\boldsymbol{Z}}_{\mathcal{B},\mathcal{I}_\oplus}||}, \tag{19c}$$

where $\hat{\boldsymbol{X}}_{\mathcal{B},\mathcal{I}_\oplus}$, $\hat{\boldsymbol{Y}}_{\mathcal{B},\mathcal{I}_\oplus}$, and $\hat{\boldsymbol{Z}}_{\mathcal{B},\mathcal{I}_\oplus}$ are the unit vectors of the body-fixed frame axes expressed in the ECI reference frame, $\boldsymbol{r}_{\odot,\mathcal{I}_\oplus}$ is the position vector of the Sun CoM in the ECI frame, and $\hat{\boldsymbol{Y}}_{\mathcal{I}_\oplus} = [0 \quad 1 \quad 0]^T$ is the unit vector of the $\boldsymbol{Y}_{\mathcal{I}_\oplus}$ axis. All results presented in sections IV and V use this initial orientation.

III. Vane System Controller

A vane system controller aiming to time-optimally detumble the sailcraft is presented below, starting with the optimal torque direction. Then, the approach described in Reference [17] is used to determine the required orientation of each vane to generate the desired control torque from the SRP. The approach consists of first solving the body-fixed torques to be generated by each vane, and then individually determining the vane angles producing the assigned torque for each vane. This approach is much simpler than the common approach of solving the optimal control problem for the eight vane angles (two per vane) at a given time, and is less likely to reach a suboptimal solution [17, 40]. At last, the behavior of the vane angles between the controller updates is described. The convergence criterion of the controller is formulated as,

$$\omega_{x,\mathcal{B}} \leq 0.01 \text{ deg/s} \quad \wedge \quad \omega_{y,\mathcal{B}} \leq 0.01 \text{ deg/s} \quad \wedge \quad \omega_{z,\mathcal{B}} \leq 0.01 \text{ deg/s}. \tag{20}$$

Meaning that the controller is turned off as soon as all the inertial rotational velocity components, expressed in the body-fixed frame, are smaller or equal to 0.01 deg/s.

A. Sail Detumbling Strategy

The time-optimal control strategy presented in Reference [41] is used to determine the optimal torque direction to detumble the spacecraft,

$$\boldsymbol{T}^*_{\mathcal{B}} = \frac{-\boldsymbol{I}_{\mathcal{B}}\boldsymbol{\omega}_{\mathcal{B}}}{||\boldsymbol{I}_{\mathcal{B}}\boldsymbol{\omega}_{\mathcal{B}}||}, \tag{21}$$

where $\boldsymbol{T}^*_{\mathcal{B}}$ is the instantaneous optimal torque direction in the body-fixed frame. As the objective is to detumble the sailcraft in the least amount of time possible, the torque magnitude is maximised within the vane system capabilities described hereafter. As expected, Eq. (21) describes a torque along the angular momentum vector, but in the opposite direction.

B. Attainable Moment Set Computation

To be able to assign the components of the detumbling torque in Eq. (21) to the system vanes, the Attainable Moment Set (AMS) of each vane needs to be determined based on their position on the sail, optical properties, solar irradiance, and orientation with respect to the sunlight. The AMS of the i$^{\text{th}}$ vane defines the envelope of torques which are achievable for a given sunlight vector in the i$^{\text{th}}$ vane-centered reference frame. It can be computed for three cases: vanes with two rotational DoF (both θ_v^i and ϕ_v^i are free), vanes with a single rotational DoF (either $\theta_v^i = 0$ or $\phi_v^i = 0$), and vanes without rotational DoF ($\theta_v^i = 0$ and $\phi_v^i = 0$). Previous literature focused on vane systems consisting of 1-DoF vanes to reduce the control complexity compared to the under-constrained control problem of four 2-DoF vanes [15]. However, their steering logic still presents some singularities [15], and the control approach presented in Reference [17] greatly reduced the computational burden of the control problem of 2-DoF vanes.

All AMS are determined from the non-dimensional torque components of the i$^{\text{th}}$ vane in the body fixed frame, $\tilde{\boldsymbol{T}}^i_{\mathcal{B}} = [\tilde{T}^i_{x,\mathcal{B}} \quad \tilde{T}^i_{y,\mathcal{B}} \quad \tilde{T}^i_{z,\mathcal{B}}]$,

$$\tilde{\boldsymbol{T}}^i_{\mathcal{B}}(\theta_v^i, \phi_v^i) = \boldsymbol{\tau}^i_{SRP_v,\mathcal{B}}(\theta_v^i, \phi_v^i) \frac{c}{S_v^i W ||\boldsymbol{r}_{O_{\mathcal{V}_i},\mathcal{B}}||}, \tag{22}$$

this permits to determine a single-time the AMS (as a function of the sunlight angles) of a vane non-dimensionally, and scale it for vanes with different moment arms and area (having the same shape), and to different solar irradiances. Additionally, as will be seen below, in the 2-DoF case, the symmetry in the solar-sail configuration in Figure 2 allow to determine the AMS for a single vane and later adapt it to others. Therefore, the non-dimensional AMS only needs to be computed once for a single vane of given optical properties (but different AMS need to be derived for the SI-SRP, DI-SRP, and O-SRP models).

1. 2-Degrees of Freedom Vane Attainable Moment Set

The aim of this section is to derive an efficient, low-computational method to describe the 2-DoF AMS of a given vane in terms of the sun cone- and clock-angles in the vane-centered frame ($\alpha_{s,\mathcal{V}_i}$ and $\beta_{s,\mathcal{V}_i}$). As the AMS obtained for a single vane can be transformed to others, vane 1 from Figure 2 is considered in the derivation. Its vane-centered frame and the body-fixed frame have the same orientation, meaning that $\hat{\boldsymbol{n}}^{i=1}_{v,\mathcal{V}_1} = \hat{\boldsymbol{n}}^{i=1}_{v,\mathcal{B}}$ and $\hat{\boldsymbol{n}}_{s,\mathcal{V}_1} = \hat{\boldsymbol{n}}_{s,\mathcal{B}}$, however, the same overall approach may be applied to all vanes. An efficient description of the AMS of vane 1 is derived in four steps, as presented in Reference [17]:

1) Iterate through $-\pi \leq \theta_v^{i=1} \leq \pi$ and $-\pi \leq \phi_v^{i=1} \leq \pi$[§] and determine the associated vane torque from Eq. (22) with Eqs. (11), (14), (10), and (12), to generate 10,000 points belonging to the AMS. This is repeated for all combinations of $\alpha_{s,\mathcal{V}_1} = -180°, -178°, ..., 178°, 180°$ and $\beta_{s,\mathcal{V}_1} = -180°, -178°, ..., 178°, 180°$.
2) Determine the convex hull of the generated points for each $(\alpha_{s,\mathcal{V}_1}, \beta_{s,\mathcal{V}_1})$ combination. The convex hull is the

[§]100 equidistant points along both $\theta_v^{i=1}$ and $\phi_v^{i=1}$.

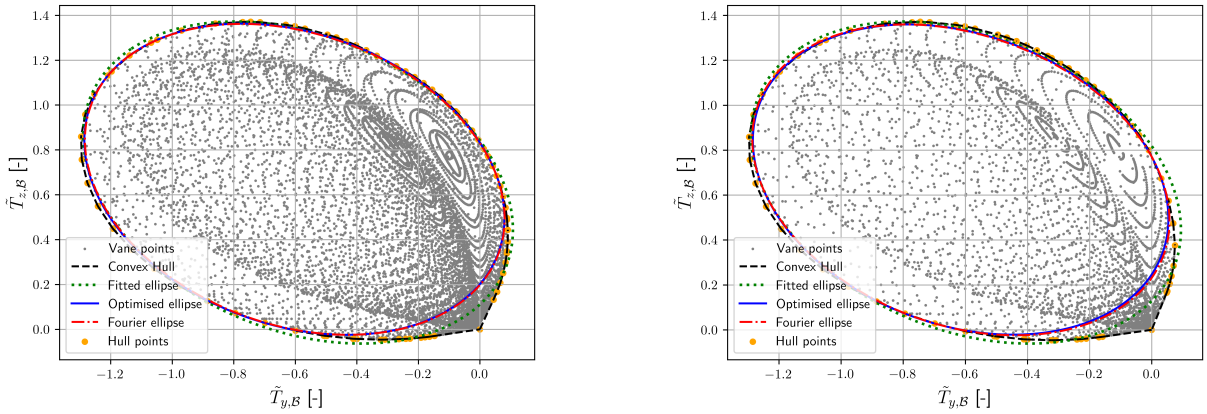

(a) Without shadow constraint. **(b) With shadow constraint.**

Fig. 7 Non-dimensional Attainable moment set of vane 1 with the O-SRP model with and without self-shadowing constraint for $\alpha_{s,\mathcal{V}_1} = -126°$ and $\beta_{s,\mathcal{V}_1} = -54°$.

smallest convex that encloses the set of points generated in step 1 [42].

3) Fit an ellipsoid of the form,

$$\tilde{A}_{y,1}\left(\tilde{T}_{y,\mathcal{B}}\right)^2 + \tilde{B}_{y,1}\tilde{T}_{y,\mathcal{B}}\tilde{T}_{z,\mathcal{B}} + \tilde{C}_{y,1}\left(\tilde{T}_{z,\mathcal{B}}\right)^2 + \tilde{D}_{y,1}\tilde{T}_{y,\mathcal{B}} + \tilde{E}_{y,1}\tilde{T}_{z,\mathcal{B}} + \tilde{F}_{y,1} = 0, \tag{23}$$

to the convex hull points[¶] such that the ellipse is fully contained in the convex hull. In Eq. (23), $\tilde{A}_{y,1} - \tilde{F}_{y,1}$ are the non-dimensional ellipse coefficients of vane 1 in the $\tilde{T}_{y,\mathcal{B}} - \tilde{T}_{z,\mathcal{B}}$ plane, and $\tilde{\boldsymbol{T}}_{\mathcal{B}}$ is a non-dimensional body-fixed torque. All the torque vectors $\tilde{\boldsymbol{T}}_{\mathcal{B}}^{i=1}$ achievable by vane 1 are inside the ellipse described by $\tilde{A}_{y,1} - \tilde{F}_{y,1}$. Note that for vane 1, $\tilde{T}_{x,\mathcal{B}}^{i=1} \approx 0$, meaning that its AMS is only on the $\tilde{T}_{y,\mathcal{B}} - \tilde{T}_{z,\mathcal{B}}$ plane. If a vane is capable of producing both a $\tilde{T}_{x,\mathcal{B}}$ and $\tilde{T}_{y,\mathcal{B}}$ torque, a second AMS in the $\tilde{T}_{x,\mathcal{B}} - \tilde{T}_{z,\mathcal{B}}$ would be considered in the same manner. However, a generalization of the vane 1 AMS to these cases is presented at the end of the section.

4) Derive analytical formulas for the $\tilde{A}_{y,1} - \tilde{F}_{y,1}$ coefficients as functions of $\alpha_{s,\mathcal{V}_1}$ and $\beta_{s,\mathcal{V}_1}$ based on the ellipsoids obtained for each sunlight angle combination.

The result of these steps are seen in Figure 7 which shows the AMS of vane 1 in the non-dimensional $\tilde{T}_{y,\mathcal{B}} - \tilde{T}_{z,\mathcal{B}}$ plane for the O-SRP model with and without self-shadowing constraint, for $\alpha_{s,\mathcal{V}_1} = -126°$ and $\beta_{s,\mathcal{V}_1} = -54°$. This figure shows the results of all the steps of the derivation of the AMS formula and will be referred to throughout this section to illustrate the derivation. At last, a method to transform the $\tilde{A}_{y,1} - \tilde{F}_{y,1}$ coefficients into two sets of $A_{x,i} - F_{x,i}$ and $A_{y,i} - F_{y,i}$ coefficients for any vane of the system is presented, such that the dimensional ellipsoid coefficients of the i$^{\text{th}}$ vane for torques in all three dimensions can be obtained.

The gray points in Figure 7 give the result of the first step of the approach, where the 10,000 combinations of $\theta_v^{i=1}$

[¶]One set of ellipse coefficients per sunlight angles combination.

and $\phi_v^{i=1}$ are shown as a scatter plot for $\alpha_{s,\mathcal{V}_1} = -126°$ and $\beta_{s,\mathcal{V}_1} = -54°$. These points result in a set with an outer boundary resembling an ellipse, within which all non-dimensional body-fixed torques are achievable by the considered vane [17]. Comparing Figure 7a and Figure 7b, which give the AMS without and with the self-shadowing constraint respectively, it appears that the only difference between the two cases is the density of points considered within the set. This is expected as more vane orientations are allowed when no self-shadowing constraint is imposed. Therefore, it can be concluded that the AMS is very similar with and without the self-shadowing constraint. Additionally, studying the sets with the self-shadowing constraint for numerous $(\alpha_{s,\mathcal{V}_1}, \beta_{s,\mathcal{V}_1})$ combinations confirmed that all points within the set outer boundary are always achievable by the vane.

The black dashed line and the orange dots in Figure 7 give the result of the second step of the approach. These points are labelled $\tilde{\boldsymbol{T}}_{ch,\mathcal{B}}^{i=1}$. While such a convex hull describes the attainable moment set of a given vane, it requires storing numerous points for each vane for a wide range of $\alpha_{s,\mathcal{V}_1}$ and $\beta_{s,\mathcal{V}_1}$ combinations, which is computationally inefficient. The third step of the approach then permits to represent the vane AMS with six coefficients for a given $(\alpha_{s,\mathcal{V}_1}, \beta_{s,\mathcal{V}_1})$ combination.

The blue ellipse in Figure 7 gives the result of the third step of the approach. To obtain this ellipse, the convex hull points are first fitted with the direct linear least-square method presented in Reference [43, 44]. This yields the green dotted ellipse in Figure 7, described by $\tilde{A}_{y,1f}\left(\tilde{T}_{y,\mathcal{B}}\right)^2 + \tilde{B}_{y,1f}\tilde{T}_{y,\mathcal{B}}\tilde{T}_{z,\mathcal{B}} + \tilde{C}_{y,1f}\left(\tilde{T}_{z,\mathcal{B}}\right)^2 + \tilde{D}_{y,1f}\tilde{T}_{y,\mathcal{B}} + \tilde{E}_{y,1f}\tilde{T}_{z,\mathcal{B}} + \tilde{F}_{y,1f} = 0$. However, this ellipse violates the boundaries of the convex hull obtained in the second step, meaning that some regions ($\tilde{T}_{y,\mathcal{B}}$-$\tilde{T}_{z,\mathcal{B}}$ combinations) within the fitted ellipse are not achievable by the considered vane [17]. Therefore, the $\tilde{A}_{y,1f} - \tilde{F}_{y,1f}$ coefficients are modified to correct for this discrepancy through a constrained optimization defined as,

$$
\begin{aligned}
&\underbrace{\text{minimise}}_{A,B,C,D,E,F} && -S_{\text{ellipse}} = -\pi a_p b_p \\
&\text{initial guess:} && (A,B,C,D,E,F) = (\tilde{A}_{y,1f}, \tilde{B}_{y,1f}, \tilde{C}_{y,1f}, \tilde{D}_{y,1f}, \tilde{E}_{y,1f}, \tilde{F}_{y,1f}) \\
&\text{subject to} && A + C = 1 \\
& && a_p = \sqrt{\frac{2\left(A\left(\frac{E}{2}\right)^2 + C\left(\frac{D}{2}\right)^2 + F\left(\frac{B}{2}\right)^2 - \frac{BDE}{4} - ACF\right)}{\left(\left(\frac{B}{2}\right)^2 - AC\right)\left(\sqrt{(A-C)^2 + 4\left(\frac{B}{2}\right)^2} - A - C\right)}} \\
& && b_p = \sqrt{\frac{2\left(A\left(\frac{E}{2}\right)^2 + C\left(\frac{D}{2}\right)^2 + F\left(\frac{B}{2}\right)^2 - \frac{BDE}{4} - ACF\right)}{\left(\left(\frac{B}{2}\right)^2 - AC\right)\left(-\sqrt{(A-C)^2 + 4\left(\frac{B}{2}\right)^2} - A - C\right)}} \\
& && A\tilde{T}_{y,\mathcal{B}}^2 + B\tilde{T}_{y,\mathcal{B}}\tilde{T}_{z,\mathcal{B}} + C\tilde{T}_{z,\mathcal{B}}^2 + D\tilde{T}_{y,\mathcal{B}} + E\tilde{T}_{z,\mathcal{B}} + F > 0 \qquad \text{for all } (\tilde{T}_{y,\mathcal{B}}, \tilde{T}_{z,\mathcal{B}}) \text{ in the convex hull} \\
& && B^2 - 4AC < 0
\end{aligned}
$$

where S_{ellipse} is the area of the ellipse, a_p is the ellipse semi-major axis, and b_p is the ellipse semi-minor axis. The optimization then aims to maximise the area of the ellipse defined by the $A - F$ coefficients while staying within the

bounds of the convex hull from step 2. In Eq. (24), $A + C = 1$ excludes the trivial solution $A, B, C, D, E, F = 0$, and the last two equality constraints give the formula for the ellipse semi-major and semi-minor axes in terms of the coefficients $A - F$ [45]. Additionally, the first inequality ensures that the ellipse is bounded by the convex hull[‖] (the convex hull points lie outside the ellipse), and $B^2 - 4AC < 0$ ensures that the conic section remains an ellipse. The optimization is performed with the Sequential Least-Squares Programming (SLSQP) algorithm available in Pygmo [46, 47], resulting in the optimised ellipse shown as the dash-dotted blue line ellipse in Figure 7, and the optimised ellipse coefficients are labelled $\tilde{A}_{y,1o} - \tilde{F}_{y,1o}$.

The solid line red ellipse in Figure 7 gives the result of the fourth step of the approach. Steps 1 to 3 result in 32,400 sets of six ellipse coefficients. To further reduce the computational load of determining the AMS of a vane as part of the vane system controller, a bivariate trigonometric function (also labelled Fourier function) is fitted to this dataset. The fitted function takes the form of, dropping the $\mathcal{V}_1$ subscript of $(\alpha_{s,\mathcal{V}_1}, \beta_{s,\mathcal{V}_1})$ for brevity,

$$\begin{aligned}
\mathcal{F}^{\tilde{A}-\tilde{F}}(\alpha_s, \beta_s) = b_0^{\tilde{A}-\tilde{F}} &+ \sum_{l=0}^{15} \left(b_{1,l}^{\tilde{A}-\tilde{F}} \sin^l(\alpha_s) + b_{2,l}^{\tilde{A}-\tilde{F}} \cos^l(\alpha_s) \right) + \sum_{l=0}^{15} \left(b_{3,l}^{\tilde{A}-\tilde{F}} \sin^l(\beta_s) + b_{4,l}^{\tilde{A}-\tilde{F}} \cos^l(\beta_s) \right) \\
&+ \sum_{l=1}^{15} \sum_{j=1}^{15} \left(b_{5,lj}^{\tilde{A}-\tilde{F}} \sin^l(\alpha_s) \sin^j(\beta_s) + b_{6,lj}^{\tilde{A}-\tilde{F}} \cos^l(\alpha_s) \sin^j(\beta_s) + b_{7,lj}^{\tilde{A}-\tilde{F}} \sin^l(\alpha_s) \cos^j(\beta_s) + b_{8,lj}^{\tilde{A}-\tilde{F}} \cos^l(\alpha_s) \cos^j(\beta_s) \right) \\
&+ \underbrace{\sum_{l=1}^{15} \sum_{j=1}^{15}}_{j=2 \text{ if } l=1} \left(b_{9,lj}^{\tilde{A}-\tilde{F}} \sin(l\alpha_s) \sin(j\beta_s) + b_{10,lj}^{\tilde{A}-\tilde{F}} \cos(l\alpha_s) \sin(j\beta_s) + b_{11,lj}^{\tilde{A}-\tilde{F}} \sin(l\alpha_s) \cos(j\beta_s) + b_{12,lj}^{\tilde{A}-\tilde{F}} \cos(l\alpha_s) \cos(j\beta_s) \right)
\end{aligned} \tag{24}$$

where the $b_{k,lj}^{\tilde{A}-\tilde{F}}$ are constants to be fitted. The $b_{k,lj}^{\tilde{A}-\tilde{F}}$ terms are fitted to the dataset through a linear least-square fit with L_2 norm regularization [48]. This regression is performed for all six ellipse coefficients independently, yielding six functions for each sail-photon interaction model with and without shadow constraint. An indicator of the fit quality is given by the relative area difference between the optimised ellipse resulting from Eq. (24) and the ellipse obtained from evaluating the fitted Fourier functions for the ellipse coefficients, as given by,

$$\Delta S_{\text{rel}} = \frac{S_{\text{Fourier}} - S_{\text{Optimised}}}{S_{\text{Optimised}}}, \tag{25}$$

where S_{Fourier} is the area of the ellipse obtained from the fitted Fourier functions for the ellipse coefficients, $S_{\text{Optimised}}$ is the area of the ellipse obtained from step 3 with the $\tilde{A}_{y,1o} - \tilde{F}_{y,1o}$ coefficients, and ΔS_{rel} is the relative area with respect of S_{Fourier} compared to $S_{\text{Optimised}}$. Note that ΔS_{rel} is computed for each of the 32,400 sets of six ellipse coefficients, meaning that its distribution is used as an indicator of the fit quality. Table 5 gives the statistics of the ΔS_{rel} distribution in terms of its minimum, mean ($\Delta \bar{S}_{\text{rel}}$), maximum, and standard deviation ($\sigma_{\Delta S_{\text{rel}}}$). This table was obtained by reproducing

[‖] Throughout the optimization, the signs of all the coefficients are inverted if a point at infinity yields $Ax_\infty^2 + Bx_\infty y_\infty + Cy_\infty^2 + Dx_\infty + Ey_\infty + F < 0$, as multiplying all ellipse coefficients by the same factor results in the same ellipse but inverts the inequality constraint.

Table 5 Distribution statistics of the ΔS_{rel} fit quality figure of merit for the full Fourier ellipse coefficients.

Model	Shadow constraint?	$\min \Delta S_{\text{rel}}$	$\Delta \bar{S}_{\text{rel}}$	$\max \Delta S_{\text{rel}}$	$\sigma_{\Delta S_{\text{rel}}}$
O-SRP	No	-1.67%	-0.02%	1.10%	0.44%
	Yes	-1.83%	+0.003%	1.47%	0.44%
DI-SRP	No	-0.89%	-0.010%	0.79%	0.27%
	Yes	-1.60%	+0.008%	1.06%	0.34%
SI-SRP	No	-0.87%	-0.009%	0.80%	0.26%
	Yes	-1.70%	+0.009%	1.34%	0.34%

Table 6 Number of terms of the truncated ellipse coefficients Fourier functions and distribution statistics of the ΔS_{rel} fit quality figure of merit.

Model	Shadow constraint?	$\mathcal{F}_{tr}^{\tilde{A}}$	$\mathcal{F}_{tr}^{\tilde{B}}$	$\mathcal{F}_{tr}^{\tilde{C}}$	$\mathcal{F}_{tr}^{\tilde{D}}$	$\mathcal{F}_{tr}^{\tilde{E}}$	$\mathcal{F}_{tr}^{\tilde{F}}$	$\min \Delta S_{\text{rel}}$	$\Delta \bar{S}_{\text{rel}}$	$\max \Delta S_{\text{rel}}$	$\sigma_{\Delta S_{\text{rel}}}$
O-SRP	No	335	164	307	505	166	442	-2.09%	-0.044%	1.66%	0.497%
	Yes	251	146	229	466	165	377	-1.95%	-0.02%	1.46%	0.49%
DI-SRP	No	181	56	160	242	112	368	-2.47%	-0.05%	1.61%	0.49%
	Yes	177	56	165	220	111	303	-1.94%	-0.22%	1.06%	0.49%
SI-SRP	No	182	132	160	397	159	398	-1.52%	-0.09%	2.08%	0.47%
	Yes	219	138	201	415	165	406	-1.93%	-0.17%	1.35%	0.48%

steps 1 to 3 of the approach using $\alpha_{s,\mathcal{V}_1} = -179°, -177°, ..., 177°, 179°$ and $\beta_{s,\mathcal{V}_1} = -179°, -177°, ..., 177°, 179°$, which are not part of the fitted data, and evaluating $\mathcal{F}^{\tilde{A}-\tilde{F}}$ on this new dataset. From Table 5, it is observed that for all reflectance models, the absolute maximum relative area difference is of the order of 1.5%, and that models without the self-shadowing constraint are better fitted.

The high accuracy obtained from fitting Eq. (24) comes at the cost of expensive function evaluations, as each $\mathcal{F}^{\tilde{A}-\tilde{F}}$ contains 1,700 terms. Therefore, these functions are truncated to only retain dominant terms, based on their relative significance, evaluated as the average of the term absolute value on the $(\alpha_{s,\mathcal{V}_1}, \beta_{s,\mathcal{V}_1})$ domain considered. The $\mathcal{F}^{\tilde{A}-\tilde{F}}$ functions are then truncated by optimising the number of terms by minimising $|\sigma_{\Delta S_{\text{rel}}} - 0.5\%|$, meaning that 95.4% of the population is would be within 1% of the mean. This results in Table 6 giving the number of terms present in each function of the truncated functions $\mathcal{F}_{tr}^{\tilde{A}-\tilde{F}}$ and the associated relative area statistics. Comparing Table 6 and Table 5, it appears that while the fit quality reduced, the mean ΔS_{rel} remained around 0% and the maximum absolute deviation is never above 2.5%, and often closer to 2%. Evaluating these functions yields $\tilde{A}_{y,1a} - \tilde{F}_{y,1a}$, which describe the red dash-dotted ellipse in Figure 7.

All the previous step result in six analytical functions of $\alpha_{s,\mathcal{V}_1}$ and $\beta_{s,\mathcal{V}_1}$ giving the six non-dimensional ellipse coefficients, $\tilde{A}_{y,1a} - \tilde{F}_{y,1a}$, describing the vane 1 AMS in the $\tilde{T}_{y,\mathcal{B}} - \tilde{T}_{z,\mathcal{B}}$ plane. These results can be generalised to the i^{th} vane and dimensionalised using,

$$
\begin{aligned}
A_{x,i} &= (\lambda_i)^2\, \mathcal{F}_{tr}^{\tilde{A}}(\alpha_{s,\mathcal{V}_i}, \beta_{s,\mathcal{V}_i}) \\
B_{x,i} &= (\lambda_i)^2 \sin\left(-\theta^i_{z,\mathcal{B}}\right) \mathcal{F}_{tr}^{\tilde{B}}(\alpha_{s,\mathcal{V}_i}, \beta_{s,\mathcal{V}_i}) \\
C_{x,i} &= (\lambda_i)^2 \sin^2\left(-\theta^i_{z,\mathcal{B}}\right) \mathcal{F}_{tr}^{\tilde{C}}(\alpha_{s,\mathcal{V}_i}, \beta_{s,\mathcal{V}_i}) \\
D_{x,i} &= (\lambda_i)^3 \sin\left(-\theta^i_{z,\mathcal{B}}\right) \mathcal{F}_{tr}^{\tilde{D}}(\alpha_{s,\mathcal{V}_i}, \beta_{s,\mathcal{V}_i}) \\
E_{x,i} &= (\lambda_i)^3 \sin^2\left(-\theta^i_{z,\mathcal{B}}\right) \mathcal{F}_{tr}^{\tilde{E}}(\alpha_{s,\mathcal{V}_i}, \beta_{s,\mathcal{V}_i}) \\
F_{x,i} &= (\lambda_i)^4 \sin^2\left(-\theta^i_{z,\mathcal{B}}\right) \mathcal{F}_{tr}^{\tilde{F}}(\alpha_{s,\mathcal{V}_i}, \beta_{s,\mathcal{V}_i})
\end{aligned}
\tag{26a}
$$

$$
\begin{aligned}
A_{y,i} &= (\lambda_i)^2\, \mathcal{F}_{tr}^{\tilde{A}}(\alpha_{s,\mathcal{V}_i}, \beta_{s,\mathcal{V}_i}) \\
B_{y,i} &= (\lambda_i)^2 \cos\left(-\theta^i_{z,\mathcal{B}}\right) \mathcal{F}_{tr}^{\tilde{B}}(\alpha_{s,\mathcal{V}_i}, \beta_{s,\mathcal{V}_i}) \\
C_{y,i} &= (\lambda_i)^2 \cos^2\left(-\theta^i_{z,\mathcal{B}}\right) \mathcal{F}_{tr}^{\tilde{C}}(\alpha_{s,\mathcal{V}_i}, \beta_{s,\mathcal{V}_i}) \\
D_{y,i} &= (\lambda_i)^3 \cos\left(-\theta^i_{z,\mathcal{B}}\right) \mathcal{F}_{tr}^{\tilde{D}}(\alpha_{s,\mathcal{V}_i}, \beta_{s,\mathcal{V}_i}) \\
E_{y,i} &= (\lambda_i)^3 \cos^2\left(-\theta^i_{z,\mathcal{B}}\right) \mathcal{F}_{tr}^{\tilde{E}}(\alpha_{s,\mathcal{V}_i}, \beta_{s,\mathcal{V}_i}) \\
F_{y,i} &= (\lambda_i)^4 \cos^2\left(-\theta^i_{z,\mathcal{B}}\right) \mathcal{F}_{tr}^{\tilde{F}}(\alpha_{s,\mathcal{V}_i}, \beta_{s,\mathcal{V}_i})
\end{aligned}
\tag{26b}
$$

where $\theta^i_{z,\mathcal{B}}$ is the angle of rotation along the $Z_{\mathcal{B}}$ axis such that $\boldsymbol{R}_z(\theta^i_{z,\mathcal{B}}) = R^i_{VB}$ for the i$^{\text{th}}$ vane and with,

$$
\lambda_i = \left(\frac{S^i_v W ||\boldsymbol{r}_{O_{\mathcal{V}_i},\mathcal{B}}||}{c} \right). \tag{27}
$$

The derivation of these equations is given in the appendix. Note that if any of the coefficients is zeroed through the transformation (i.e., $\theta^i_{z,\mathcal{B}} = k\pi$ for $k \in \mathbb{Z}$ for Eq. (26a) and $\theta^i_{z,\mathcal{B}} = \frac{\pi}{2} + k\pi$ for $k \in \mathbb{Z}$ for Eq. (26b)), the ellipse does not exist, meaning that the torque is fully contained in the other plane. The AMS of the i$^{\text{th}}$ vane can be formulated as,

$$
\begin{aligned}
AMS^i_{2-DoF} \equiv \{ & \tau_{2-DoF} = [T_{x,\mathcal{B}}, T_{y,\mathcal{B}}, T_{z,\mathcal{B}}] : \\
& \left(A_{x,i} T^2_{x,\mathcal{B}} + B_{x,i} T_{x,\mathcal{B}} T_{z,\mathcal{B}} + C_{x,i} T^2_{z,\mathcal{B}} + D_{x,i} T_{x,\mathcal{B}} + E_{x,i} T_{z,\mathcal{B}} + F_{x,i} < 0 \right) \quad \wedge \\
& \left(A_{y,i} T^2_{y,\mathcal{B}} + B_{y,i} T_{y,\mathcal{B}} T_{z,\mathcal{B}} + C_{y,i} T^2_{z,\mathcal{B}} + D_{y,i} T_{y,\mathcal{B}} + E_{y,i} T_{z,\mathcal{B}} + F_{y,i} < 0 \right) \}
\end{aligned}
\tag{28}
$$

where the inequalities stipulate that the point is inside both ellipses if they are defined.

2. 1-Degree of Freedom Vane Attainable Moment Set

In case the i$^{\text{th}}$ vane is set to have a single rotational DoF, either around $X_{\mathcal{V}_i}$ or $Y_{\mathcal{V}_i}$, the AMS is determined by generating 150 grid points in the permissible combinations of θ^i_v and ϕ^i_v. From these combinations and a given sunlight vector, the non-dimensional body-torque associated with each vane orientation is computed from Eqs. (14), (10), and (12). That is, for an $X_{\mathcal{V}_i}$-DoF ($Y_{\mathcal{V}_i}$-DoF) vane, 150 equally-spaced points of $\theta^i_v \in [-180°; 180°]$ ($\phi^i_v \in [-180°; 180°]$) are sampled and combined with $\phi^i_v = 0$ ($\theta^i_v = 0$) to obtain the set of permissible vane orientations. These points then form a curve in the $T_{x,\mathcal{B}}$-$T_{z,\mathcal{B}}$ and the $T_{y,\mathcal{B}}$-$T_{z,\mathcal{B}}$ plane, which can be interpolated with Cubic Splines $s^i_x(\alpha_{s,\mathcal{B}}, \beta_{s,\mathcal{B}})$ and $s^i_y(\alpha_{s,\mathcal{B}}, \beta_{s,\mathcal{B}})$ respectively for the i$^{\text{th}}$ vane. Figure 8 gives the non-dimensional AMS of vane 1 with either only a $X_{\mathcal{V}_i}$ rotational DoF (Figure 8a) or a $Y_{\mathcal{V}_i}$ rotational DoF (Figure 8b), for different sunlight angles in the body-fixed frame**. In this figure, for each $(\alpha_{s,\mathcal{B}}, \beta_{s,\mathcal{B}})$ combination, two continuous loops can be observed, which is a result of

**Only 15 of the 150 scatter points used to generate the spline are shown.

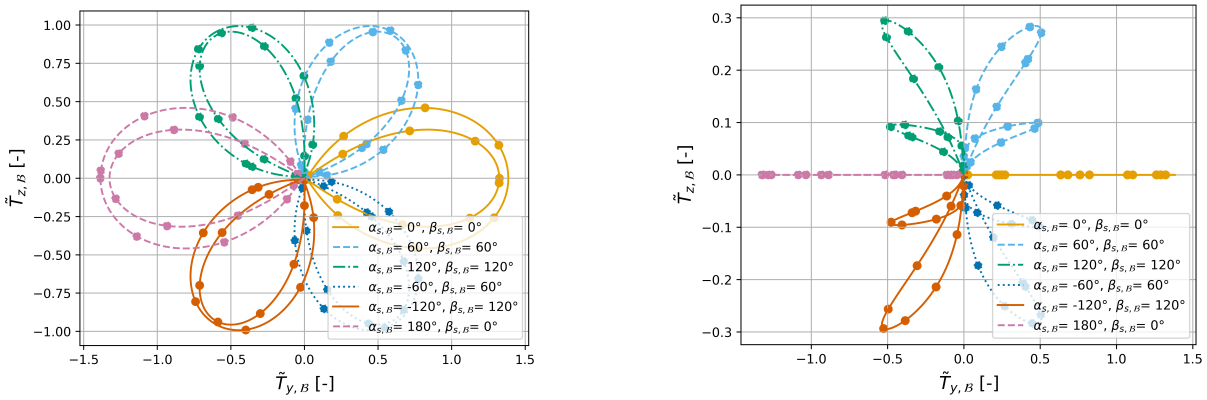

(a) $X_{\mathcal{V}_i}$**-DoF vane,** $\boldsymbol{\phi_v = 0}$

(b) $Y_{\mathcal{V}_i}$**-DoF vane,** $\boldsymbol{\theta_v = 0}$

Fig. 8 Non-dimensional attainable moment set of an $X_{\mathcal{V}_i}$-DoF and a $Y_{\mathcal{V}_i}$-DoF vane for the O-SRP model without self-shadowing constraint, for different sunlight cone-and clock-angles.

the different optical properties of the sail material on its front and back surfaces. For the DI-SRP model, these loops coincide. Furthermore, while the curves in Figure 8 were produced without self-shadowing constraint, the introduction of such a constraint would simply result in gaps in the curve without changing its shape.

The different shapes and the complexity of the curves shown in Figure 8 for different Sun cone-and clock-angles imply that this set cannot be approximated analytically, as was done for the 2-DoF case. Therefore, the generation of the 150 grid points and subsequent interpolation are performed in the loop of the attitude-orbit propagation, resulting in an increased computational time. The AMS can then be formulated as,

$$AMS^i_{1-DoF} \equiv \{\boldsymbol{\tau}_{1-DoF} = [T_{x,\mathcal{B}}, T_{y,\mathcal{B}}, T_{z,\mathcal{B}}] : (T_{x,\mathcal{B}}, T_{z,\mathcal{B}}) \in s^i_x \wedge (T_{y,\mathcal{B}}, T_{z,\mathcal{B}}) \in s^i_y\}. \tag{29}$$

This AMS formulation is then used as a constraint in the control torque allocation problem. Further work could consider producing tabular values of the cubic splines coefficients for different combinations of $(\alpha_{s,\mathcal{B}}, \beta_{s,\mathcal{B}})$ which can be retrieved throughout the propagation to reduce the computational time associated to the computation of these sets.

3. 0-Degree of Freedom Vane Attainable Moment Set

In case a vane is set to have no degrees of freedom from a particular position, its AMS comes back to a single value, $\boldsymbol{\tau}^i_{0-DoF}$, given by Eq. (12) for a given set of vane characteristics and vane angles (θ^i_v, ϕ^i_v). The 0-DoF AMS can be written as,

$$AMS^i \equiv \{\boldsymbol{\tau}^i_{0-DoF}\} \tag{30}$$

C. Vane Torque Allocation Problem

Having determined a general formulation of the AMS for the 2-DoF, 1-DoF, and 0-DoF case as a function of the vane's characteristics, a torque allocation problem is set up to assign the components of the optimal control torque obtained from Eq. (21) to each vane. This takes the form of a quadratic optimization problem that is similar to the one presented in Reference [17] but with a different objective function and an additional constraint on the torque direction. This objective function balances the need for the solution to be close to the desired torque, but also to not be too far from the previous torque allocation solution to avoid fast changes which would result in a faster wear and tear of the vane system. The optimization problem is given by,

$$
\begin{aligned}
&\underbrace{\text{minimise}}_{\boldsymbol{\mathcal{G}}} && \tfrac{2c^2}{3W^2}||\boldsymbol{G}_{\mathcal{B}} - \boldsymbol{T}^*_{\mathcal{B}}||^2 + \tfrac{1c^2}{3W^2}||\boldsymbol{\mathcal{G}} - \boldsymbol{\mathcal{G}}_{\text{pr}}||^2 \\
&\text{initial guess:} && \boldsymbol{\mathcal{G}} = \boldsymbol{\mathcal{G}}_{\text{pr}} \\
&\text{subject to} && \boldsymbol{\mathcal{G}} = [(\boldsymbol{g}^{i=1}_{\mathcal{B}})^T \quad (\boldsymbol{g}^{i=2}_{\mathcal{B}})^T \quad (\boldsymbol{g}^{i=3}_{\mathcal{B}})^T \quad (\boldsymbol{g}^{i=4}_{\mathcal{B}})^T] \\
& && \tfrac{c}{W}\left(\textstyle\sum_{i=1}^{4} \boldsymbol{g}^i_{\mathcal{B}}\right) - \tfrac{c}{W}\boldsymbol{G}_{\mathcal{B}} = 0 \\
& && \tfrac{\boldsymbol{G}_{\mathcal{B}}}{||\boldsymbol{G}_{\mathcal{B}}||} - \tfrac{\boldsymbol{T}^*_{\mathcal{B}}}{||\boldsymbol{T}^*_{\mathcal{B}}||} = 0 \\
& && \tfrac{c}{W}\boldsymbol{g}^i_{\mathcal{B}} \in AMS^i_{\frac{c}{W}} \qquad \text{for i=1, 2, 3, 4}
\end{aligned}
\tag{31}
$$

where $\boldsymbol{G}_{\mathcal{B}}$ is the resultant torque from the vane system expressed in the body fixed frame, $\boldsymbol{\mathcal{G}}$ is a vector containing the twelve variables of the optimization, $\boldsymbol{g}^i_{\mathcal{B}}$ for $i = 1, 2, 3, 4$, which are the three-axis body-fixed torque components of each vane, $\boldsymbol{\mathcal{G}}_{pr}$ is the optimal torque allocation vector from the previous call of the controller, and $AMS^i_{\frac{c}{W}}$ is one of the AMS formulations described above but scaled by a $\frac{c}{W}$ factor. In Eq. (31), the first equality constraint defines the $\boldsymbol{G}_{\mathcal{B}}$ vector in terms of the body-fixed torque vectors to be solved for each vane, and the second one matches the resultant torque of the system with the torque to be generated by each vane. Subsequently, the third one ensures that the resultant torque is in the same direction as the optimal detumbling torque, and the fourth constraint ensures that the torque assigned to each vane is within its capabilities, as defined by its AMS[††]. Additionally, the variables of the optimization are scaled by a c/W factor (which scales the SRP force and torques from Eq. (12)), as optimisers tend to perform better when the variables are $O(1)$ than when they are $O(10^{-6})$ like physical SRP torques. For the general case of four 2-DoF vanes, this problem results in six linear equality constraints, four non-linear inequality constraints, and a quadratic objective function, yielding a convex optimization problem, which guarantees arrival to a global optimum with most common local algorithms [17]. The optimization problem is solved with the COBYLA algorithm from Pygmo [47, 49], as it supports non-linear inequality constraints, and equality constraints can be modelled through a pair of inequality constraints.

[††]Which can be 2-DoF, 1-DoF, or 0-DoF.

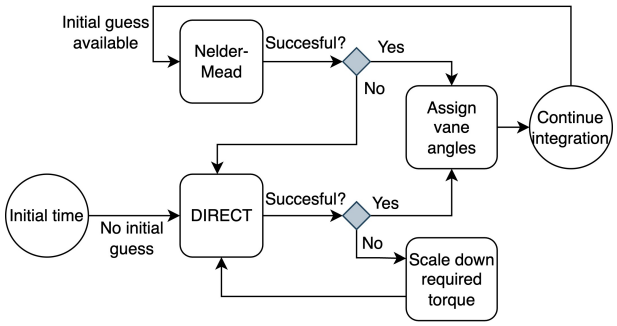

Fig. 9 Flow chart describing whether the DIRECT [50] or the Nelder-Mead [51] optimiser is used, and whether a down scaling of the requested torque is necessary.

D. Vane Angles Allocation Algorithm

Having determined the torque to be produced by the i$^{\text{th}}$ vane, a two-variable optimization is performed to obtain the optimal vane orientation which produces the assigned torque, as described in Reference [40],

$$
\begin{aligned}
&\underbrace{\text{minimise}}_{\theta_v^i,\,\phi_v^i} && \tfrac{1c^2}{3W^2}\left|\left|\boldsymbol{\tau}^i_{SRP_{v,\mathcal{B}}}(\theta_v^i,\phi_v^i)-\kappa \boldsymbol{g}^i_{d,\mathcal{B}}\right|\right|^2 \\
&\text{initial guess:} && \theta_v^i=\theta^i_{v,\text{pr}} \quad \phi_v^i=\phi^i_{v,\text{pr}} \\
&\text{subject to} && -\pi \le \theta_v^i \le \pi \\
& && -\pi \le \phi_v^i \le \pi \\
& && \text{(No self-shadowing)}
\end{aligned}
\tag{32}
$$

where $\boldsymbol{g}^i_{d,\mathcal{B}}$ is the torque to be generated by the i$^{\text{th}}$ vane as output by the optimization in Eq. (31), $\kappa \in [0;1]$ is a scaling factor of the desired torque, $(\theta^i_{v,\text{pr}}, \phi^i_{v,\text{pr}})$ describes the orientation of the vanes obtained from the previous controller call, and $\boldsymbol{\tau}^i_{SRP_{v,\mathcal{B}}}(\theta_v^i,\phi_v^i)$ is the SRP torque generated by the i$^{\text{th}}$ vane as a function of its orientation according to Eqs. (14), (10), and (12). In Eq. (32), the first two inequality constraints define the bounds of the domain and the third constraint is the self-shadowing constraint, which is not always taken. If considered, the self-shadowing constraint is applied through a large penalty added to the objective function. Additionally, similarly to the torque allocation problem, the objective function is scaled by a factor $\frac{c^2}{W^2}$ to aid the optimiser performance. The optimization is then performed for all vanes of the system, resulting in solutions for the eight vane angles. Furthermore, if the final objective function obtained from solving Eq. (32) remains larger than 10^{-3} Nm, the assigned torque $\boldsymbol{g}^i_{d,\mathcal{B}}$ is scaled down as it is not achievable by the vane[‡‡] (i.e., due to a misrepresentation of the AMS while solving Eq. (31) or a failure of the torque allocation algorithm). This is done using a factor κ, which scales down the torque magnitude while retaining its direction. The optimal value of κ is then determined through a golden section search iterating on Eq. (32), aiming to

[‡‡]This was found from tuning the optimiser.

maximise κ such that the final objective function is $\leq \frac{10^{-3}W}{c}$.

Either the DIRECT algorithm [50] or the Nelder-Mead optimiser [51] is used to solve the problem described in Eq. (32). On the one hand, the DIRECT algorithm is a deterministic derivative-free global optimization method which balances both a global exploration search and a local refinement to identify the global optimum [52]. According Reference [52], it is particularly effective on low-dimensionality problems, and it quickly finds the basin of the global optimum, although the method struggles to refine the solution to a high accuracy on a local scale. However, relatively low accuracy of the optimal vane angles is necessary in this case (≈ 0.001 rad). On the other hand, the Nelder-Mead (N-M) algorithm is a gradient-free local optimization method which iteratively adjusts the vertices of a simplex by reflecting the vertex with the largest objective function, to converge towards an optimal solution [51]. While the N-M algorithm lacks in efficiency compared to local methods which assume smooth objective functions [51], a derivative-free method is necessary due to the introduction of a penalty for the self-shadowing constraint yielding a discontinuity in the objective function, and it is recognised as one of the best algorithms in that case [51].

Figure 9 shows the optimiser selection strategy used to perform the optimization in Eq. (32). At the first step of the propagation, no initial guess is available, and the DIRECT algorithm [50, 52, 53] is used to determine the optimal vane angles minimising the objective function from Eq. (32). However, no bias towards a particular part of the domain can be introduced without limiting its boundaries, which would require a good knowledge of the optimization domain. Consequently, between two vane controller calls, the algorithm might identify a global optimum in different parts of the domain, leading to large variations in vane angles, even though a satisfying local minimum might be available near the previous vane angle solution. Such large variations should be avoided to limit the tear and wear of the vane system. Therefore, the N-M algorithm is used when an initial guess is available, which permits reducing the amount of vane angle jumps throughout the detumbling manoeuvre. As a local method, the N-M generally remains close to the initial guess provided, limiting the larger variations in vane angles. However, this also means that it can get stuck in a local minimum if a poor initial guess is given. Therefore, the DIRECT algorithm is called if the direction and the magnitude of the vane torque resulting from the Nelder-Mead vane angles solution is more than 15° and 25% off the desired torque $\kappa \boldsymbol{g}^i_{d,\mathcal{B}}$, respectively. In Figure 9, this happens if the N-M is 'not successful'. Additionally, as the DIRECT method is more robust than the N-M algorithm, it is used when the desired torque requires to be scaled down by the factor κ.

To assess the performance of the hybrid DIRECT/N-M method from Figure 9 in terms of required vane turning rates, it is compared to a solver using only the DIRECT method. This is illustrated in Figure 10, which shows the history of $\theta_v^{i=1}$ for the DIRECT and hybrid solvers for the detumbling of the ACS3-like spacecraft from an initial rotational velocity of $\boldsymbol{\omega}_{0,\mathcal{B}} = [0.5, 0.5, 0.5]$ deg/s. The spacecraft initial orbit and attitude are given by cases O-1, which is representative of the ACS3 mission, and A-1, respectively, from subsection II.E. In Figure 10, it can be seen that the hybrid solver results in much fewer large jumps throughout the detumbling propagation than the DIRECT method. Additionally, the

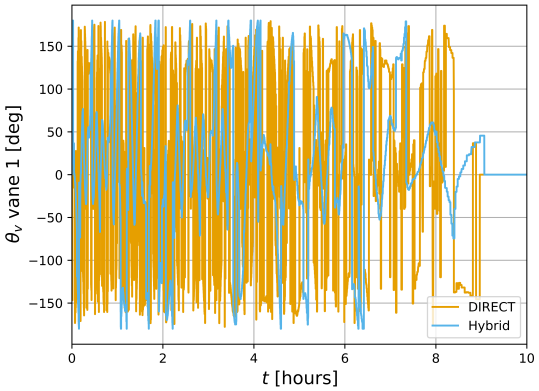

Fig. 10 $\theta_v^{i=1}$ rotation history (around $X_{\mathcal{V}_1}$) for detumbling from $\omega_{0,\mathcal{B}} = [0.5, 0.5, 0.5]$ deg/s with the DIRECT and the hybrid solvers.

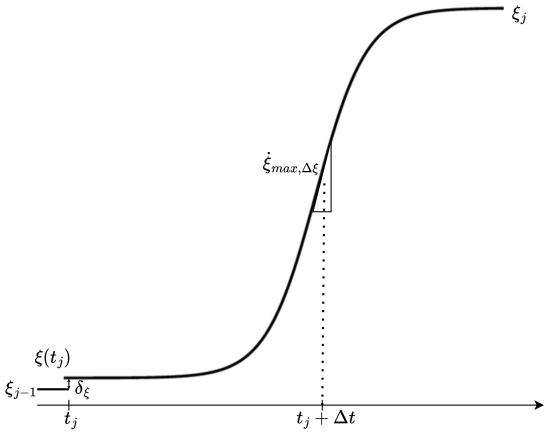

Fig. 11 Transition from a vane angle ξ_{j-1} to ξ_j.

hybrid solver results in a time to stabilization which is only 1% longer.

E. Vane Angles Movement between Controller Invocations

While the controller described has been designed with computational efficiency in mind, it remains expensive to evaluate and cannot be called at every step of the propagation. Therefore, the controller is only called if either the rotational velocity vector or the sunlight vector direction in the body-fixed frame changed by more than 8° and 7°, respectively, with respect to the last vane angle update. These thresholds were found from tuning the detumbling performance of the controller for the $\omega_{0,\mathcal{B}} = [0.5, 0.5, 0.5]$ deg/s scenario with an initial orbit and attitude defined by cases O-1 and A-1 in subsection II.E. Between subsequent controller calls, the vane angles are kept constant, and a smooth transition from $\theta_v^i(t_{j-1})$ ($\phi_v^i(t_{j-1})$) to $\theta_v^i(t_j)$ ($\phi_v^i(t_j)$) is ensured using a modified sigmoid [54],

$$\xi(t) = \xi_{j-1} + \frac{\Delta\xi}{1 + e^{\left(-\gamma(t-(t_j+\Delta t))\right)}}, \tag{33}$$

where $\xi(t)$ is a vane angle (i.e., $\theta_v^i(t)$ or $\phi_v^i(t)$ for the considered vane) at a given time $t \in [t_j; +\infty[$, t_j is the time at which the controller was last updated, ξ_{j-1} is the vane angle as evaluated at the timestamp of the previous controller call t_{j-1}, $\Delta\xi = \xi_j - \xi_{j-1}$ is the angular change between the previous (at t_{j-1}) and new (at t_j) vane angle requested by the controller, γ is a scaling factor defining the steepness of the function, and Δt is a time-shift parameter. In practice, the vane angles determined at t_{j-1} are kept constant until the controller is evaluated again, at t_j. Then, from $t = t_j$ onwards, Eq. (33) is used to describe $\theta_v^i(t)$ and $\phi_v^i(t)$ until the next controller update at t_{j+1}. However, this means that at t_j, a small discontinuity $\delta_\xi = \xi(t_j) - \xi_{j-1}$ is introduced, as $\xi(t_j) \neq \xi_{j-1}$ [§§]. How large this discontinuity is may be specified using the Δt time-shift parameter in Eq. (33), as seen below. A summary of the overall geometry of the

[§§]Note that $\lim_{(t_j+\Delta t)\to+\infty} \delta_\xi = 0$

sigmoid is given by Figure 11, where the gap δ_ξ is exaggerated for illustration.

While the parameters γ and Δt define the shape of the sigmoid, they do not have a direct physical meaning. Therefore, it is desired to relate them to the maximum achievable rotational velocity of the considered vane and the discontinuity at t_j. Based on Eq. (33), the factor γ can be related to the maximum vane rotation speed by considering the derivative of the sigmoid,

$$\frac{\mathrm{d}\xi(t)}{\mathrm{d}t} = \frac{\gamma\Delta\xi e^{\left(-\gamma(t-(t_j+\Delta t))\right)}}{\left(1+e^{\left(-\gamma(t-(t_j+\Delta t))\right)}\right)^2}, \tag{34}$$

which indicates that the maximum vane rotation speed reached during an angular change of $\Delta\xi$, $\dot{\xi}_{max,\Delta\xi}$, is reached at $t = t_j + \Delta t$. In other words, $\dot{\xi}_{max,\Delta\xi}$ is the peak rotational velocity reached by the vane during the transition between $\theta_v^i(t_j)$ and $\theta_v^i(t_{j-1})$ ($\phi_v^i(t_j)$ and $\phi_v^i(t_{j-1})$), with $\Delta\xi = \theta_v^i(t_j) - \theta_v^i(t_{j-1})$ ($\Delta\xi = \phi_v^i(t_j) - \phi_v^i(t_{j-1})$). This permits to express $\dot{\xi}_{max,\Delta\xi}$ as,

$$\dot{\xi}_{max,\Delta\xi} = \frac{\Delta\xi\gamma}{4} \quad \Leftrightarrow \gamma = \frac{4\dot{\xi}_{max,\Delta\xi}}{\Delta\xi}, \tag{35}$$

which may be used to specify the maximum achievable rotational speed of the vane, by considering the largest permissible rotation, such that $\Delta\xi = \Delta\xi_{max}$ in Eq. (35). As $\theta_v^i \in [-\pi;\pi]$ and $\phi_v^i \in [-\pi;\pi]$, the largest angular change between two controller calls is $\Delta\xi_{max} = 2\pi$ in for both rotations around the $X_{\mathcal{V}_i}$ and $Y_{\mathcal{V}_i}$ (from one boundary of their domain to the other). This means that posing,

$$\gamma = \frac{2\dot{\xi}_{max,2\pi}}{\pi}, \tag{36}$$

limits $\dot{\xi}_{max,\Delta\xi}$ to $\dot{\xi}_{max,2\pi}$, which will only be reached for angular changes of $\Delta\xi = 2\pi$ and smaller maximum rotational velocities are reached when $\Delta\xi$ is smaller. Having linked γ to the maximum achievable rotational velocity of a vane, Δt may be related to γ and δ_ξ. Substituting $t = t_j$, and $\xi(t_j) = \xi_{j-1} + \delta_\xi$ in Eq. (33), and isolating Δt permits to write,

$$\Delta t = \frac{\ln\left(\frac{\Delta\xi}{\delta_\xi} - 1\right)}{\gamma}, \tag{37}$$

which can be used to determine Δt as a function of $\gamma(\dot{\xi}_{max,2\pi})$ and a maximum allowable discontinuity δ_ξ at t_j. The δ_ξ offset can be expressed in terms of a fraction of the angle change, such that $\delta_\xi = r_\xi\Delta\xi$. This yields,

$$\Delta t = \frac{\ln\left(\frac{1}{r_\xi} - 1\right)}{\gamma}. \tag{38}$$

In the following, $\dot{\xi}_{max} = 2\pi$ rad/s is assumed, meaning that a complete angular change can be performed in 1 s. Additionally, $r_\xi = 0.0005\%$ is assumed, which was selected to ensure that the discontinuity is small enough to be handled by the integrator. Using Eqs. (36) and (38), these assumptions yield, $\gamma = 4$ and $\Delta t \approx 3$s. It is further assumed that both θ_v^i and ϕ_v^i rotations can be performed simultaneously, and that the vanes are also rotated throughout the eclipse

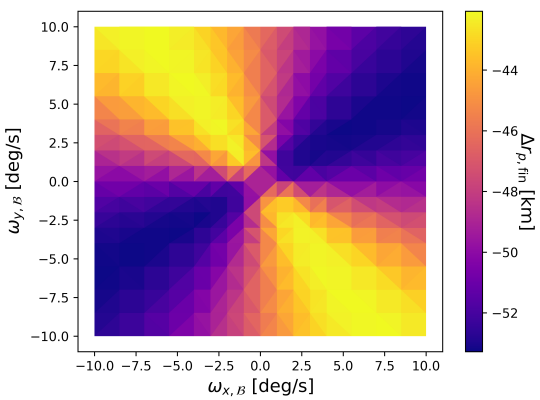

(a) Pericenter deviations.

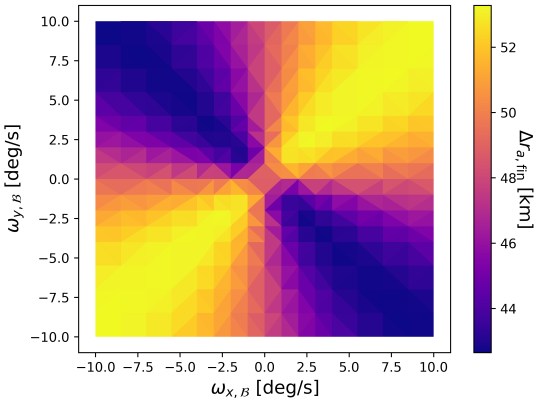

(b) Apocenter deviations.

Fig. 12 Pericenter and apocenter deviations from the case O-1 orbit after 30 days for different combinations of $X_{\mathcal{B}}$ and $Y_{\mathcal{B}}$ rotational velocity components, with the A-2 initial attitude with the DI-SRP model.

times to avoid large jumps at the eclipse end points.

IV. Long-Term Tumbling Analysis

First, the long-term effects of an uncontrolled attitude motion of the sailcraft have been considered to assess how much the sail would diverge from its initial orbit if no detumbling manoeuvre is performed. The sail considered has no tip-vanes and has the characteristics described in subsection II.C. The set of initial rotational velocities considered is defined by $\boldsymbol{\omega}_{0,\mathcal{B}} \in X_{\mathrm{LTT}}$,

$$X_{\mathrm{LTT}} = \{(\pm u, \pm u, 0) | \forall u \in x_{\mathrm{LTT},u}\}, \tag{39}$$

where $x_{\mathrm{LTT},u} = \{0, 1, 2, 3, 4, 5.5, 7, 8.5, 10\}$ deg/s was arbitrarily chosen to sample initial rotational velocities with a magnitude below 15 deg/s while limiting the computational time required. In all considered cases, the rotational velocity around $Z_{\mathcal{B}}$ is zero, $\omega_{z,\mathcal{B}} = 0$, as the self-rotation of the sail has no influence on the SRP force experienced. Although, $\omega_{z,\mathcal{B}} \neq 0$ would result in oscillations in the $\omega_{x,\mathcal{B}}$ and $\omega_{y,\mathcal{B}}$ components of the rotational velocity vector (see Eq. (7)), for a given rotational velocity magnitude, $\omega_{z,\mathcal{B}} \neq 0$ provides gyroscopic stiffness to the sail. This limits the oscillations of sail surface normal direction, which is aligned with $Z_{\mathcal{B}}$, with respect to the local sunlight vector, meaning that situations with $\omega_{z,\mathcal{B}} \neq 0$ are more predictable than with $\omega_{z,\mathcal{B}} = 0$. Therefore, this analysis focused on cases with $\omega_{z,\mathcal{B}} = 0$. Substituting $\omega_{z,\mathcal{B}} = 0$ and $\boldsymbol{T}_{SRP,\mathcal{B}} = \vec{0}$ in Eqs. (6) and (7), it appears that the rotational velocity vector is constant in time and always lies in the sail-plane for the cases considered in X_{LTT}. Therefore, $\boldsymbol{\omega}_{0,\mathcal{B}} = \boldsymbol{\omega}_{\mathcal{B}}(t)$.

A. General Trends

The DI-SRP model is used to assess general trends for the O-1 reference orbit (near-circular, polar orbit) with an initially Sun-pointing attitude (case A-2), but the influence of the reflectance model and sailcraft orbit are later

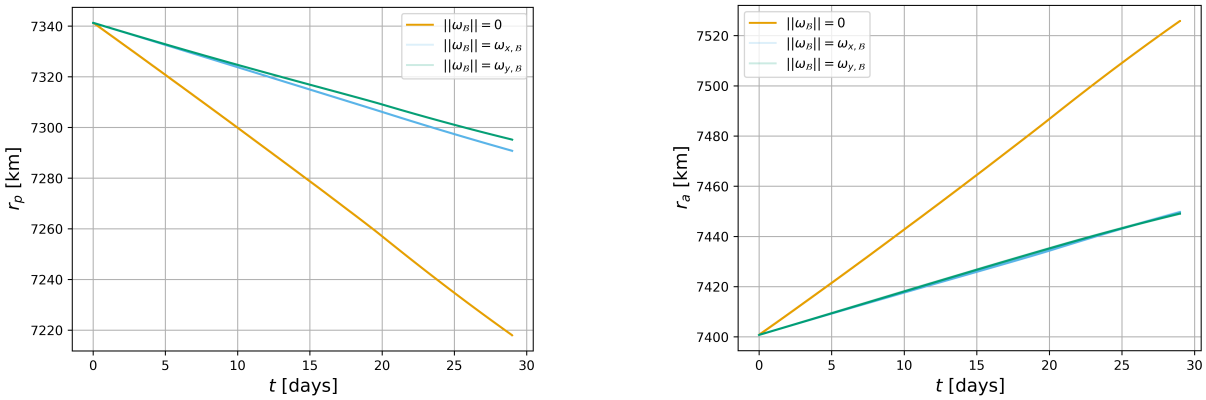

(a) Pericenter evolution. **(b) Apocenter evolution.**

Fig. 13 Pericenter and apocenter evolutions for propagations with $||\omega_{\mathcal{B}}|| = 0$, $||\omega_{\mathcal{B}}|| = \omega_{x,\mathcal{B}}$ and $||\omega_{\mathcal{B}}|| = \omega_{y,\mathcal{B}}$ for the orbital case O-1 and an initial attitude A-2.

considered. In all propagations considered, no plane changes were observed ($\Delta i \approx 0$ and $\Delta\Omega \approx 0$), therefore the subsequent analysis focuses solely on orbit shape metrics within the orbital plane. First, the main features of Figure 12 and Figure 13 are presented, then, their origins are discussed.

Figure 12 gives the pericenter and apocenter deviations at the end of the 30-day propagation, $\Delta r_{p,\text{fin}}$ and $\Delta r_{a,\text{fin}}$, as functions of the $\omega_{x,\mathcal{B}}$ and $\omega_{y,\mathcal{B}}$ rotational velocity components[¶¶]. From this figure, it is observed that the pericenter decreases while the apocenter increases, showing that the orbital eccentricity is growing. This results in a lowering of the pericenter altitude, which could result in a re-entry of the spacecraft on the long-term. Additionally, the graph is centrally symmetric with respect to $(\omega_{x,\mathcal{B}}, \omega_{y,\mathcal{B}}) = (0, 0)$ and the final deviations are independent of the magnitude of the rotational velocity. Particularly, the final deviations are only dependent on the tumbling axis direction in the body-fixed frame, given by the $\omega_{x,\mathcal{B}}/\omega_{y,\mathcal{B}}$ ratio. Furthermore, larger deviations take place if the signs of the rotational velocity components are the same, which results in an asymmetry in Figure 12.

Figure 13 gives the evolution of the pericenter and apocenter radii as a function of time for an initially Sun-pointing sail with $\boldsymbol{\omega}_{\mathcal{B}} = \vec{0}$ (in yellow), and propagations with either $||\boldsymbol{\omega}_{\mathcal{B}}|| = \omega_{x,\mathcal{B}}$ (in blue), or $||\boldsymbol{\omega}_{\mathcal{B}}|| = \omega_{y,\mathcal{B}}$ (in green). In this figure, it can be observed that the $\boldsymbol{\omega}_{\mathcal{B}} = \vec{0}$ propagation shows a severe change in the pericenter and apocenter radii, although the shape of the orbit of a continuously Sun-pointing spacecraft would remain roughly constant. Additionally, comparing the final deviations of the $\boldsymbol{\omega}_{\mathcal{B}} = \vec{0}$ propagation in Figure 13 (~120 km) with the maximum deviations in Figure 12 (~52 km), it appears that the tumbling attitude motion generally reduces the impact (de-orbit speed) of SRP on the sailcraft trajectory compared to the same sailcraft with an initially Sun-pointing attitude and inertially non-rotating. Furthermore, a total of 16 coinciding propagations are shown in Figure 13 for each family of curves with $||\boldsymbol{\omega}_{\mathcal{B}}|| = \omega_{x,\mathcal{B}}$ and $||\boldsymbol{\omega}_{\mathcal{B}}|| = \omega_{y,\mathcal{B}}$ (each curve is 80% transparent). This is consistent with Figure 12 where the final deviations in

[¶¶]Note that the data for $\boldsymbol{\omega}_{\mathcal{B}} = \vec{0}$ deg/s is not included, as it does not exhibit the tumbling dynamics studied.

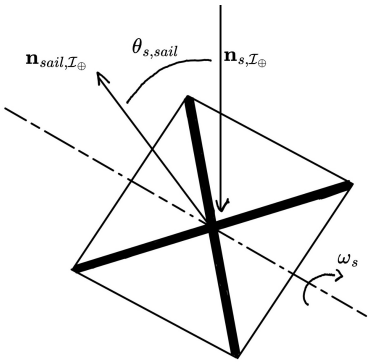

Fig. 14 Tumbling geometry when rotating along an axis in the sail-plane.

pericenter and apocenter are independent of the rotational velocity magnitude for a given tumbling axis, as both groups of curves shares the same axis of rotation within the group.

The central symmetry of the graphs in Figure 12 is expected as $\boldsymbol{\omega}_{\mathcal{B}}$ and $-\boldsymbol{\omega}_{\mathcal{B}}$ describe equal but opposite rotational motions, which results in the same axis of rotation, and equivalent tumbling scenarios with respect to the local sunlight. Subsequently, the independence of the final deviations from the rotational velocity magnitude in Figure 12, as well as the reduced impact of SRP on the tumbling sailcraft trajectory in Figure 13 (compared to an inertially non-rotating sailcraft), can be attributed to the significantly faster attitude motion compared to the orbital motion. For a Sun-pointing initial attitude, over a self-rotation around the tumbling axis, the SRP force components which are not in the direction of the sunlight vector cancel out. Meaning that over the period of the attitude motion, T_ω, the average SRP force is in the local sunlight direction but has a smaller magnitude than the same Sun-pointing sailcraft. It can then be shown that tumbling has the same effect as reducing the effective sail area, $S_{\text{sail,eff}}$. For an initial Sun-pointing orientation and the DI-SRP model, substituting $\rho_{s_f} = \rho_{s_b} = 1$ and considering the complete sail in Eq. (10), the SRP force of the sail can be rewritten as,

$$\boldsymbol{F}_{DI-SRP,\mathcal{I}_\oplus} = \frac{-2W}{c}\left(S_{\text{sail}}|\boldsymbol{n}_{\mathcal{I}_\oplus}(t)\cdot(-\boldsymbol{n}_{s,\mathcal{I}_\oplus})|\left(\boldsymbol{n}_{\mathcal{I}_\oplus}(t)\cdot(-\boldsymbol{n}_{s,\mathcal{I}_\oplus})\right)\boldsymbol{n}_{\text{sail},\mathcal{I}_\oplus}\right), \tag{40}$$

where $\boldsymbol{n}_{\text{sail},\mathcal{I}_\oplus}$ is the sail surface normal direction in the ECI, S_{sail} is the sail area, $\theta_{s,sail}$ is the angle between the local sunlight vector ($\boldsymbol{n}_{s,\mathcal{I}_\oplus}$) and the surface normal direction such that $\cos(\theta_s) = \left(\boldsymbol{n}_{\mathcal{I}_\oplus}\cdot-\boldsymbol{n}_{s,\mathcal{I}_\oplus}\right)$. This situation is illustrated by Figure 14, where $\boldsymbol{\omega}_{\mathcal{B}}$ is the rotational velocity vector and $\theta_{s,sail} = ||\omega_{\mathcal{B}}||t$ from an initial Sun-pointing attitude. As the sail is tumbling, $\boldsymbol{n}_{\text{sail},\mathcal{I}_\oplus} = \boldsymbol{n}_{\text{sail},\mathcal{I}_\oplus}(t)$, and $\boldsymbol{n}_{\text{sail},\mathcal{I}_\oplus}(t=0) = -\boldsymbol{n}_{s,\mathcal{I}_\oplus}(t=0)$. Additionally, as the attitude motion is much faster than the orbital motion, the local sunlight direction $\boldsymbol{n}_{s,\mathcal{I}_\oplus}$ is approximately constant. The evolution of the sail surface normal in the ECI frame is then given by Rodrigues' rotation formula [55],

$$\boldsymbol{n}_{\text{sail},\mathcal{I}_\oplus}(t) = -\boldsymbol{n}_{s,\mathcal{I}_\oplus}\cos(\omega_s t) + \left(\hat{\boldsymbol{\omega}}_{\mathcal{B}}\times-\boldsymbol{n}_{s,\mathcal{I}_\oplus}\right)\sin(\omega_s t) + \hat{\boldsymbol{\omega}}_{\mathcal{B}}\left(\hat{\boldsymbol{\omega}}_{\mathcal{B}}\cdot-\boldsymbol{n}_{s,\mathcal{I}_\oplus}\right)(1-\cos(\omega_s t)), \tag{41}$$

where $\omega_s = ||\boldsymbol{\omega}_{\mathcal{B}}||$ and $\hat{\boldsymbol{\omega}}_{\mathcal{B}}$ is the unit vector of the tumbling axis. For the cases considered, the last term in Eq. (41) is always zero, as the sail surface normal is perpendicular to the sail-plane and the rotational velocities considered are always in the sail-plane***. This permits to determine the average SRP force over one period of the attitude motion, given by,

$$\bar{\boldsymbol{F}}_{DI-SRP,\mathcal{I}_\oplus} = \frac{-2W}{c}\boldsymbol{y}, \tag{42}$$

with,

$$\begin{aligned}
\boldsymbol{y} &= \frac{S}{T_\omega}\int_0^{T_\omega} |\boldsymbol{n}_{\mathcal{I}_\oplus}(t)\cdot(-\boldsymbol{n}_{s,\mathcal{I}_\oplus})|\left(\boldsymbol{n}_{\mathcal{I}_\oplus}(t)\cdot(-\boldsymbol{n}_{s,\mathcal{I}_\oplus})\right)\boldsymbol{n}_{\mathcal{I}_\oplus}(t)\mathrm{d}t \\
&= \frac{S}{T_\omega}\int_0^{T_\omega} |\cos(\omega_s t)|\cos(\omega_s t)\left(-\boldsymbol{n}_{s,\mathcal{I}_\oplus}\cos(\omega_s t) + \left(\hat{\boldsymbol{\omega}}_{\mathcal{B}}\times -\boldsymbol{n}_{s,\mathcal{I}_\oplus}\right)\sin(\omega_s t)\right)\mathrm{d}t \\
&= \underbrace{\frac{4S_{\text{sail}}}{3\pi}}_{S_{\text{sail,eff}}}\left(-\boldsymbol{n}_{s,\mathcal{I}_\oplus}\right).
\end{aligned} \tag{43}$$

From Eqs. (42) and (43), it appears that the effective sail area and SRP force are independent of the rotational velocity magnitude, as was observed in Figure 12 and Figure 13. Therefore, on average, a sailcraft in a sustained tumbling motion (from an initial Sun-pointing attitude) will behave in the same manner as an inertially non-rotating sailcraft with a Sun-pointing attitude of the same mass (and inertia tensor) but with $\approx 42.44\%$ of the area. This model also explains the observation from Figure 13 that tumbling slows down the orbit decay, as a significantly smaller disturbance force is experienced by the spacecraft on average. The performance of the simplified model is given in Figure 15 which shows the pericenter and apocenter evolutions of all the cases in X_{LTT} compared to this simplified model, where the same spacecraft has 42.44% of its initial area. From this figure, it appears that the $S_{\text{sail,eff}} = \frac{4S}{3\pi}$ model performs reasonably well until the tenth day of the propagation. After that point, the effect of the Earth's orbital motion result in the range of deviations observed, as is discussed below.

The eccentricity growth observed for the non-rotating and initially Sun-pointing propagation in Figure 13 is an expected result for a Sun-pointing sailcraft in an orbit which is not perpendicular to the ecliptic. Considering the SRP force in the RTN frame and neglecting the eclipse period, the tangential component of the SRP force cancels out on each side of the orbit, meaning that the orbital semi-major axis evolution is periodic. In contrast, the net radial effect of the force does not cancel out. When the spacecraft is between the Earth and the Sun, the radial component of the SRP force pushes the spacecraft towards the Earth. However, when it is on the other side of the Earth, the same force pushes the spacecraft away from its central body. As a result, a secular eccentricity increase takes place. Additionally, as for an initially Sun-pointing sailcraft a sustained tumbling motion only results in a reduced effective area in comparison to an

*** $\left(\hat{\boldsymbol{\omega}}_{\mathcal{B}}\cdot\boldsymbol{n}_{\text{sail},\mathcal{I}_\oplus}(t=0)\right) = \left(\hat{\boldsymbol{\omega}}_{\mathcal{B}}\cdot -\boldsymbol{n}_{s,\mathcal{I}_\oplus}(t=0)\right) = 0.$

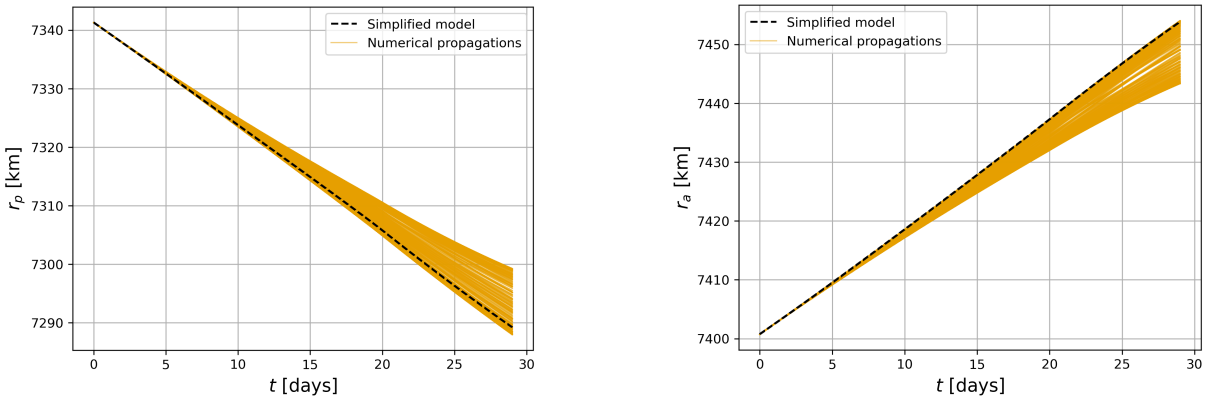

(a) Pericenter evolution. **(b) Apocenter evolution.**

Fig. 15 Pericenter and apocenter evolutions for the case O-1 orbit from the A-2 initial attitude with the DI-SRP model, for the numerical propagations and the analytical model.

inertially non-rotating sail with the same initial attitude (Eq. (42)), this effect also explains the sail orbit decay observed in Figure 12 and why it is slower than a Sun-pointing sailcraft. However, the eccentricity growth is counter-balanced on the opposite side of Earth's orbit around the Sun if the orbit does not precess. Therefore, there is only a risk of sail re-entry if the orbital deviations are significant enough over the space of six months. Whether there is a risk that a sailcraft re-enters as a result of the tumbling motion then depends on the initial orbit being considered.

Furthermore, Earth's motion around the Sun results in the asymmetry observed in Figure 12, as it impacts different tumbling scenarios differently depending on their axis of rotation. Over the span of 30 days, the Earth completes approximately a twelfth of its orbit around the Sun, meaning that the average Sun-spacecraft direction throughout the orbit tilts by roughly 30°. This means that an initially Sun-pointing sailcraft with $\boldsymbol{\omega}_{\mathcal{B}} = \vec{0}$, which does not change attitude in inertial space, is tilted by 30° with respect to the local sunlight direction at the end of the propagation. This effect is at the source of the asymmetry observed in Figure 12. This is illustrated in Figure 16, which shows a sail in a circular heliocentric orbit at its initial orbital position ($t = t_0$) and a quarter of an orbital period T later ($t = t_0 + \frac{T}{4}$), for two tumbling scenarios. In Figures 16a and 16b, the sailcraft have the same initial attitude, but the signs of $\omega_{x,\mathcal{B}}$ and $\omega_{y,\mathcal{B}}$ are equal for (a) and different for (b). As a result, at $t = t_0 + \frac{T}{4}$, (b) is continuously in an edge-on orientation with respect to the Sun (SRP force is zero), while (a) goes through a Sun-pointing attitude once per period of the tumbling motion, although their tumbling motion relative to the local sunlight direction is equivalent at $t = t_0$ (both motions go through a Sun-pointing attitude through one self-revolution). This means that over long-term propagations, (a) experiences an SRP force more often and will deviate more from its initial orbit than (b). This is what is observed with the asymmetry in Figure 12, as a similar argument holds for Earth orbiting spacecraft, as their movement in the solar-system resembles Earth's heliocentric orbit. However, the initial orientation shown in Figure 16 is not exactly the same as case A-2 as this would require the rotation axis in (b) to be aligned with the angular momentum vector of Earth's orbit around the Sun.

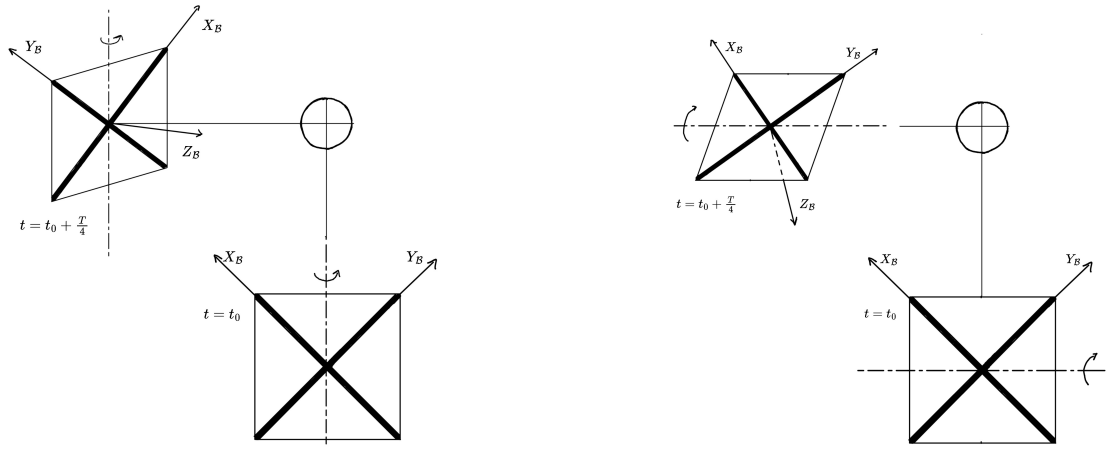

(a) **(b)**

Fig. 16 Effect of the tumbling axis on the attitude of the sail with respect to the Sun at different heliocentric orbital positions.

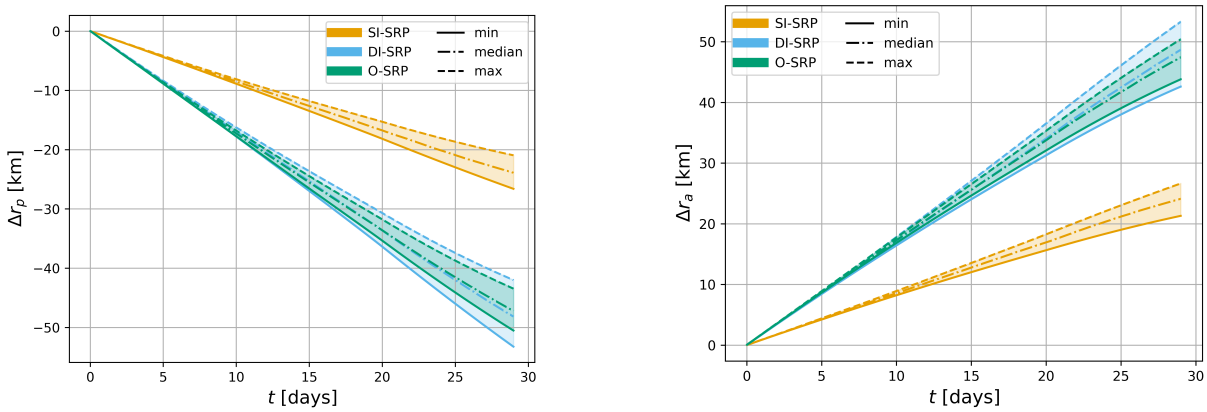

(a) Pericenter time history range. **(b) Apocenter time history range**

Fig. 17 Evolution of the pericenter and apocenter deviations from orbital case O-1 with the initial attitude case A-2 for the SI-SRP, DI-SRP, and O-SRP models.

This means that the results in Figure 12 are slightly shifted with respect to what is expected from the discussion. In Figure 16, the two edge cases of minimum and maximum deviations are exactly $\omega_{x,\mathcal{B}} = \omega_{y,\mathcal{B}}$ and $\omega_{x,\mathcal{B}} = -\omega_{y,\mathcal{B}}$, but in Figure 12, these extrema axes are slightly rotated clockwise with respect to the diagonals of the square.

B. Influence of Reflectance Model

The influence of the reflectance model is studied by further considering the SI-SRP and O-SRP models with the same set of tumbling cases defined by X_{LTT}.

Figure 17 provides the time history of the range of deviations of the pericenter and apocenter altitudes from the initial orbit for the SI-SRP (yellow), DI-SRP (blue), and O-SRP (green) models. In this figure, the shaded regions

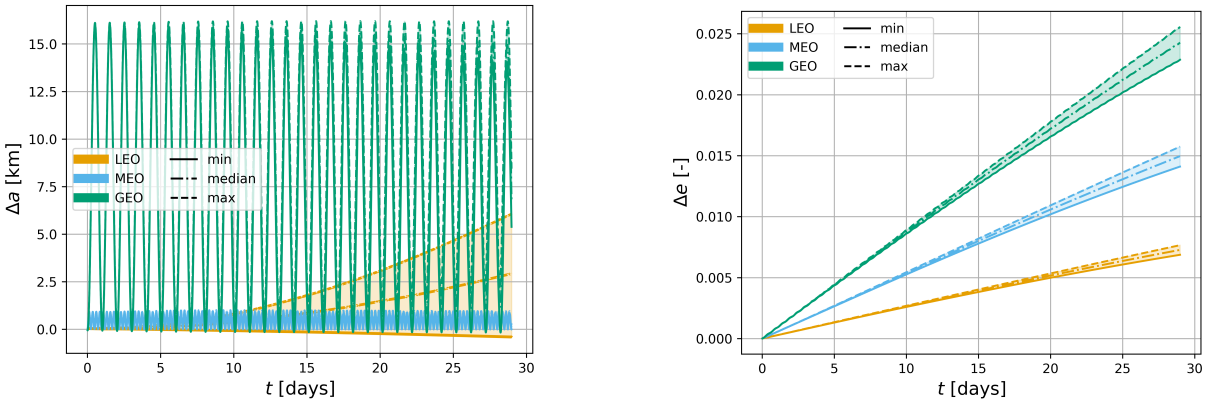

(a) Semi-major axis time history range.

(b) Eccentricity time history range.

Fig. 18 Evolution of the semi-major axis and eccentricity deviations from the initial orbit for the orbital cases O-2 (LEO), O-3 (MEO) and O-4 (GEO), with the initial attitude case A-2 and the DI-SRP model.

provide the range of deviations, and the solid, dash-dotted, and dashed lines give the minimum, median, and maximum deviations as a function of time. From Figure 17, it appears that a tumbling motion with the SI-SRP model results in smaller deviations than the DI-SRP and O-SRP models. This is expected as during the rotational motion, both sides of the sail are exposed to the sunlight. However, for the SI-SRP model, it is assumed that no SRP force is produced by the back of the sail, meaning that, on average, an SRP acceleration is generated only during half of the tumbling period. This contrasts with the DI-SRP and O-SRP models, which produce an SRP acceleration from both sides of the sail, resulting in the large offset observed.

In practice, all realistic sails are expected to yield deviations within the range resulting from the DI-SRP model, as the most efficient moment transfer possible occurs under specularly reflected photons. This is confirmed by Figure 17, shows that the results for the O-SRP model fall within those of the DI-SRP model. Therefore, the DI-SRP model can generally be used to obtain a conservative estimate of the de-orbiting resulting from a tumbling motion.

C. Influence of Orbital Altitude

This section investigates the effect of different orbital altitudes on the orbital decay resulting from the tumbling dynamics defined in by X_{LTT}. . Variations in orbital altitude lead to differing effects of the SRP acceleration on the orbit evolution and result in varying eclipse durations. These factors directly influence the rate of orbital decay.

Figure 18 provides the time evolution of the range of deviations of the semi-major axis and eccentricity from the initial orbit for the orbital cases O-2 (LEO in yellow), O-3 (MEO in blue), and O-4 (GEO in green) from Table 4. In this figure, the shaded regions provide the range of deviations, and the solid, dash-dotted, and dashed lines give the minimum, median, and maximum deviations as a function of time. In Figure 18a, the semi-major axis evolutions of the MEO and GEO orbits are periodic, while the LEO case results in a secular growth. This difference results from

the eclipse times present in LEO that are negligible in MEO and GEO. Due to the slight eccentricity of the orbit, eclipses result in an imbalance between the SRP perturbation on either side of the orbit in LEO, while in GEO the SRP perturbation experienced on one side of the orbit is counter-acted on the other side. The periodic evolution in MEO and GEO also implies that their orbital energy remains approximately constant. Figure 18b shows secular variations of the eccentricity at all three orbital altitudes, with higher altitudes resulting in larger deviations. This is explained by the reduced gravitational acceleration and shorter eclipse times at higher orbital altitudes. In general, longer eclipse times (e.g., for different RAANs of a sun-synchronous LEO) result in smaller orbital deviation, as the SRP perturbation acts for shorter periods of time throughout the mission.

V. Detumbling Analysis

From the results in section IV, it appears that tumbling may result in a re-entry of the sailcraft. This means that regaining attitude control of the sailcraft as fast as possible is capital. Therefore, this section assesses the capabilities of the vane system presented in section III to stabilise a tumbling sailcraft. The complete sail model described in subsection II.C is used with four 2-DoF tip-vanes. However, the influence of the number of degrees of freedom of each vane on the stabilization capabilities is later considered. The set of initial rotational velocities considered in the subsequent analyses is given by $\boldsymbol{\omega}_{0,\mathcal{B}} \in X_{\text{DT}}$,

$$X_{\text{DT}} = X_{\text{DT-1}} \cup X_{\text{DT-2}} \cup X_{\text{DT-3a}} \cup X_{\text{DT-3b}}, \tag{44}$$

with,

$$\begin{aligned} X_{\text{DT-1}} = \{(\pm u, 0, 0) \mid \forall u \in x_{\text{DT-1},u}\} \\ \cup \{(0, \pm u, 0) \mid \forall u \in x_{\text{DT-1},u}\} \\ \cup \{(0, 0, \pm u) \mid \forall u \in x_{\text{DT-1},u}\} \end{aligned} \qquad \begin{aligned} X_{\text{DT-2}} = \{(\pm u, \pm u, 0) \mid \forall u \in x_{\text{DT-2},u}\} \\ \cup \{(0, \pm u, \pm u) \mid \forall u \in x_{\text{DT-2},u}\} \\ \cup \{(\pm u, 0, \pm u) \mid \forall u \in x_{\text{DT-2},u}\} \end{aligned}$$

$$X_{\text{DT-3a}} = \{(\pm u, \pm u, \pm u) \mid \forall u \in x_{\text{DT-3},u}\} \qquad X_{\text{DT-3b}} = \{(\pm u_1, \pm u_2, \pm u_3) \mid \forall u_1, u_2, u_3 \in x_{\text{DT-3},u}\}$$

where $x_{\text{DT-1},u} = \{1, 2, \ldots, 14, 15\}$ deg/s, $x_{\text{DT-2},u} = \{1, 2, 3, 4, 5.5, 7, 8.5, 10\}$ deg/s, and $x_{\text{DT-3},u} = \{1, 2, 3, 4, 5.5, 7, 8.5\}$ deg/s have been arbitrarily chosen to sample initial rotational velocities with magnitudes up to 15 deg/s. In the body-fixed frame, $X_{\text{DT-1}}$, $X_{\text{DT-2}}$, and $X_{\text{DT-3}} = X_{\text{DT-3a}} \cup X_{\text{DT-3b}}$ refer to one-, two-, and three-axes rotational velocities respectively. Additionally, some analyses were performed on $X_{\text{DT, sample}}$, which is a subset of X_{DT}, to reduce the computational time. $X_{\text{DT, s}}$ is defined as,

$$X_{\text{DT, s}} = X_{\text{DT-1}} \cup X_{\text{DT-2}} \cup X_{\text{DT-3a}} \cup X_{\text{DT-3b, s}}, \tag{45}$$

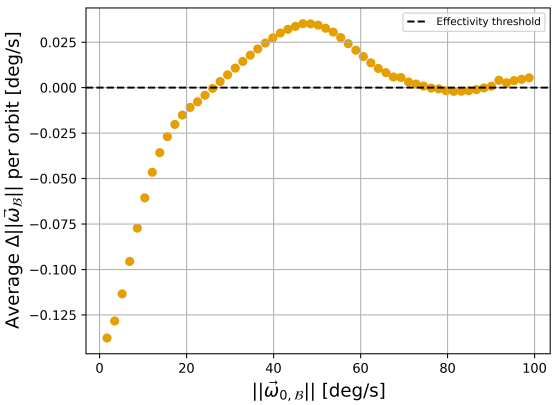

Fig. 19 Average rotational velocity magnitude change over one orbit as a function of $||\omega_{0,\mathcal{B}}||$ for $\omega_{0,\mathcal{B}} \in X_{\text{DT-3c}}$, orbital case O-1, an initial attitude A-2, and the SI-SRP model.

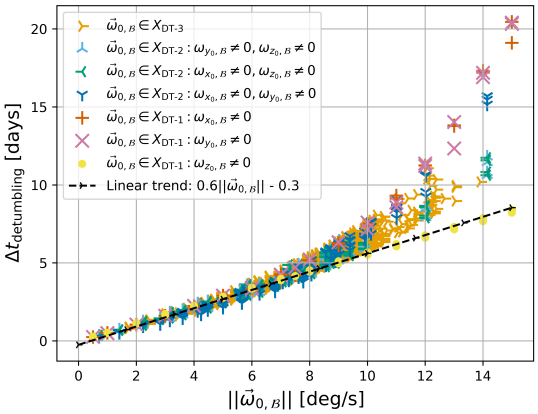

Fig. 20 Detumbling time as a function of the initial rotational velocity magnitude for the orbital case O-1, an initial attitude A-2, and $\omega_{0,\mathcal{B}} \in X_{\text{DT}}$, and the SI-SRP model.

where $X_{\text{DT-3b, s}} \subseteq X_{\text{DT-3b}}$ is a random sample of 250 elements of $X_{\text{DT-3b}}$. At last, the set given by,

$$X_{\text{DT-3c}} = \{(u, u, u) \mid \forall u \in x_{\text{DT-4},u}\}, \tag{46}$$

with $x_{\text{DT-4},u} = \{1, 2, \ldots, 99, 100\}$ deg/s, was used to study the maximum rotational velocity which can physically be handled by the vane system.

A. General Trends

In this section, 2-DoF vanes following the SI-SRP model are used to assess the general trends in the controller detumbling capabilities for the initial rotational velocities given by X_{DT} in the O-1 reference orbit from Table 4 and an initially Sun-pointing attitude defined by case A-2.

Figure 19 shows the average change in rotational velocity magnitude per orbit during the first six orbits of propagation for three-axis tumbling cases from $X_{\text{DT-3c}}$. From this figure, it appears that the considered ACS is more efficient for small initial rotational velocities and that it is capable of reducing the rotational velocity magnitude for $||\omega_{0,\mathcal{B}}|| < 26$ deg/s. Above this threshold, the vane controller is not capable of detumbling the sail, which results in an average increase of the rotational velocity for 26 deg/s $< ||\omega_{0,\mathcal{B}}|| < 76$ deg/s. For $||\omega_{0,\mathcal{B}}|| > 76$ deg/s, the ACS performance oscillates around $\Delta||\omega_{\mathcal{B}}|| = 0$. This behaviour could be the result of the tuning of the controller constants (i.e., how often it is called), which was performed on the $\omega_{0,\mathcal{B}} = [0.5, 0.5, 0.5]$ deg/s case, as mentioned in section III. Overall, it can then be concluded from Figure 19 that the vane system controller presented in section III is capable of detumbling an ACS3-like sailcraft with an initial rotational velocity up to 26 deg/s. However, significantly longer detumbling times

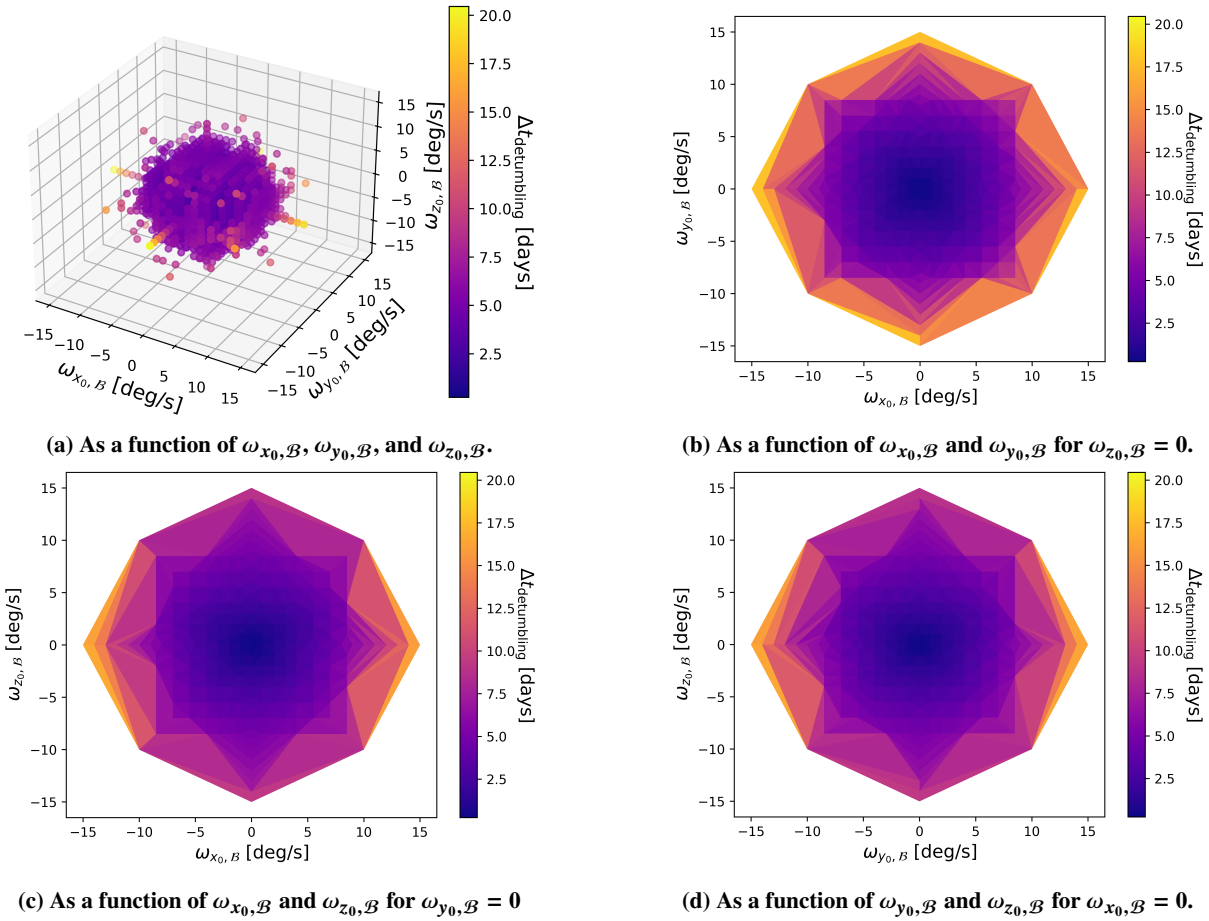

(a) As a function of $\omega_{x_0,\mathcal{B}}$, $\omega_{y_0,\mathcal{B}}$, and $\omega_{z_0,\mathcal{B}}$.

(b) As a function of $\omega_{x_0,\mathcal{B}}$ and $\omega_{y_0,\mathcal{B}}$ for $\omega_{z_0,\mathcal{B}} = 0$.

(c) As a function of $\omega_{x_0,\mathcal{B}}$ and $\omega_{z_0,\mathcal{B}}$ for $\omega_{y_0,\mathcal{B}} = 0$

(d) As a function of $\omega_{y_0,\mathcal{B}}$ and $\omega_{z_0,\mathcal{B}}$ for $\omega_{x_0,\mathcal{B}} = 0$.

Fig. 21 Detumbling time as a function of the rotational velocity components for the O-1 orbital case with an initial attitude A-2, and the SI-SRP model.

can be expected compared to the values displayed in Figure 20.

Figure 20 gives the detumbling time as a function of the initial rotational velocity magnitude for the $X_{\text{DT-1}}$, $X_{\text{DT-2}}$, and $X_{\text{DT-3}}$ sets of initial rotational velocities. From this figure, it can be observed that larger initial rotational velocity magnitudes result in a longer detumbling time and that the stabilization time grows linearly at a rate slightly higher than one day per two deg/s of initial rotational velocity up to $||\boldsymbol{\omega}_{0,\mathcal{B}}|| = 8$ deg/s. These features are expected as larger rotational velocities require the same torque to be applied for longer periods of time prior to reaching stabilization. Furthermore, if the vane system is capable of producing an approximately constant detumbling torque, the time to stabilization is expected to grow linearly for higher initial rotational velocities. However, for $||\boldsymbol{\omega}_{0,\mathcal{B}}|| > 8$ deg/s, only one-axis tumbling scenarios with $\boldsymbol{\omega}_{z_0,\mathcal{B}} \neq 0$ (yellow dots) follow this linear trend, and a maximum detumbling time of 16 days is reached for a two-axes tumbling in the sail-plane ($\omega_{x_0,\mathcal{B}} \neq 0$ and $\omega_{y_0,\mathcal{B}} \neq 0$). This can be explained by the decoupling of $\boldsymbol{\omega}_{z,\mathcal{B}}$ from $\boldsymbol{\omega}_{x,\mathcal{B}}$ and $\boldsymbol{\omega}_{y,\mathcal{B}}$ in the gyroscopic torque given in Eq. (7), and is considered below.

Figure 21 gives the detumbling time as a function of the components of the initial rotational velocity for the tumbling

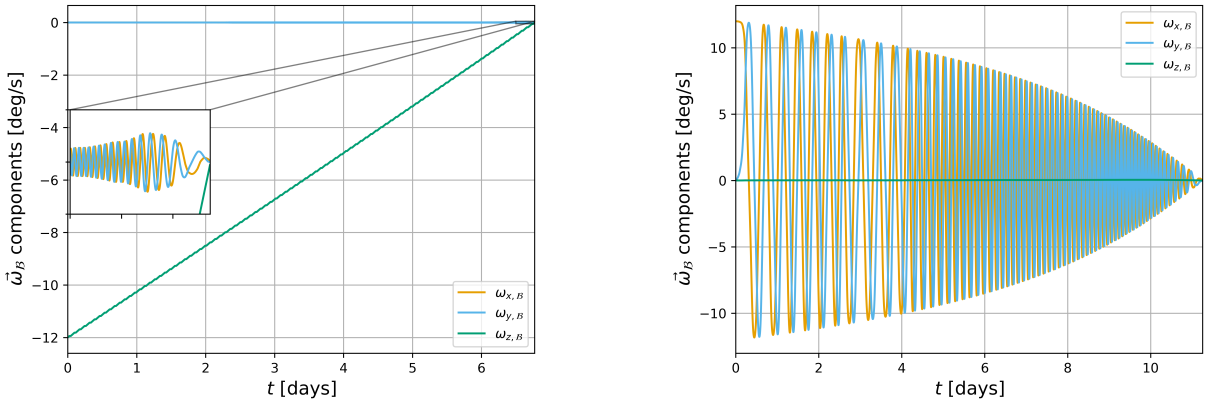

(a) $\boldsymbol{\omega_{0,\mathcal{B}} = [0, 0, -12]}$ **deg/s.** **(b)** $\boldsymbol{\omega_{0,\mathcal{B}} = [12, 0, 0]}$ **deg/s.**

Fig. 22 Evolution of the rotational velocity components as a function of time during a detumbling manoeuvre for the O-1 orbital case and the A-2 initial attitude, and the SI-SRP model.

cases given by X_{DT}. Figure 21a gives the detumbling time associated with all combinations of rotational velocity components, while Figures 21b, 21c, and 21d focus on cases with one of the rotational velocity components equal to zero. From these figures, it appears that larger initial rotational velocity magnitudes result in longer detumbling times, which is consistent with the observations from Figure 20, and that the detumbling time is an even function in all $\boldsymbol{\omega}_{0,\mathcal{B}}$ components. That is, Figures 21b, 21c, and 21d are symmetric with respect to (0, 0). This is expected from the symmetry of the sail. Additionally, it may be observed that for a given $||\boldsymbol{\omega}_{0,\mathcal{B}}||$ magnitude, scenarios with a larger initial $\omega_{z_0,\mathcal{B}}$ component require less time for stabilization. This is seen from Figures 21c and 21d where shorter manoeuvre durations are required for along the vertical axis than the horizontal axis. At last, it appears from Figures 21a and 21b that the scenarios resulting in the longest detumbling times are the ones with large $\omega_{x_0,\mathcal{B}}$ and $\omega_{y_0,\mathcal{B}}$, with the longest recorded cases being when the rotational velocity vector is in the sail plane. This can be observed from Figure 21 particularly, where the longest recorded detumbling times are obtained in the $\omega_{x_0,\mathcal{B}}$-$\omega_{y_0,\mathcal{B}}$ plane. The different impact of $\omega_{z_0,\mathcal{B}}$ from the other rotational velocity components is considered below.

A recurring observation across Figures 20 and 21 is that tumbling cases which involve a non-zero $\omega_{z_0,\mathcal{B}}$ component are less challenging to stabilise. Additionally, it was found that the detumbling time rises sharply for all cases with $||\boldsymbol{\omega}_{0,\mathcal{B}}|| > 8$ deg/s, except for single-axis tumbling scenarios with $\omega_{z_0,\mathcal{B}}$. These aspects result from how quickly the rotational velocity direction, $\hat{\boldsymbol{\omega}}_{\mathcal{B}}$, varies as a result of the gyroscopic torque of the sailcraft. The gyroscopic torque is given by Eq. (7), which reveals a coupling between $\omega_{x,\mathcal{B}}$ and $\omega_{y,\mathcal{B}}$. This means that in the absence of an external torque, if $\omega_{x,\mathcal{B}} \neq 0$ and $\omega_{z,\mathcal{B}} \neq 0$, then $\dot{\omega}_{y,\mathcal{B}} \neq 0$ and $\omega_{y,\mathcal{B}}$ will grow. Similarly, if $\omega_{y,\mathcal{B}} \neq 0$ and $\omega_{z,\mathcal{B}} \neq 0$, then $\dot{\omega}_{x,\mathcal{B}} \neq 0$ and $\omega_{x,\mathcal{B}}$ will grow. This also means that the rotational velocity vector direction is continuously changing in both these cases. In contrast, $\dot{\omega}_{z,\mathcal{B}}$ is always zero in the absence of an external torque, meaning that it is decoupled from $\omega_{x,\mathcal{B}}$ and $\omega_{y,\mathcal{B}}$.

For $\omega_{x_0,\mathcal{B}} = \omega_{y_0,\mathcal{B}} = 0$ and $\omega_{z_0,\mathcal{B}} \neq 0$, the gyroscopic torque is zero and $\hat{\boldsymbol{\omega}}_{\mathcal{B}}$ remains constant in the absence of an external torque. During a detumbling manoeuvre, the fixed direction of $\hat{\boldsymbol{\omega}}_{\mathcal{B}}$ is easily achieved by the ACS (compared to a time-varying direction). This ensures that $\omega_{x_0,\mathcal{B}}$ and $\omega_{y_0,\mathcal{B}}$ remain approximately zero and that the gyroscopic torque does not grow. The constant $\hat{\boldsymbol{\omega}}_{\mathcal{B}}$ explains why one-axis tumbling scenarios with $\omega_{z_0,\mathcal{B}} \neq 0$ follow the linear trend in Figure 20. Additionally, for a given rotational velocity magnitude, a larger $\omega_{z_0,\mathcal{B}}$ component (which does not vary without an external torque) will dominate the rotational velocity direction. This means that the rotational velocity direction will vary less, which is easier to follow for the ACS. Figure 22a gives the evolution of the rotational velocity components as a function of time for $\boldsymbol{\omega}_{0,\mathcal{B}} = [0, 0, -12]$ deg/s, which is an example of the aforementioned case. In this figure, $\omega_{z,\mathcal{B}}$ reaches zero linearly and the $\omega_{x,\mathcal{B}}$ and $\omega_{y,\mathcal{B}}$ components of the rotational velocity vector remain small.

However, even when $\omega_{z,\mathcal{B}} = 0$ at the start epoch, inaccuracies in the ACS torque result in $\omega_{z,\mathcal{B}} \neq 0$ (although remaining very small), which yields a non-zero gyroscopic torque. If the initially non-zero rotational velocity components are large enough, the gyroscopic torque may become significant and result in fast oscillations in $\omega_{x,\mathcal{B}}$ and $\omega_{y,\mathcal{B}}$ due to their coupling in Eq. (7). These oscillations then require the controller to quickly change the vane orientations to avoid a large misalignment between $\hat{\boldsymbol{\omega}}_{\mathcal{B}}$ and the control torque. For large gyroscopic torques, the ACS may not be able to follow the quickly changing rotational velocity direction, which would result in a poorer detumbling performance. This is the case for $||\boldsymbol{\omega}_{0,\mathcal{B}}|| > 8$ deg/s (except for $\boldsymbol{\omega}_{0,\mathcal{B}} \in X_{\text{DT-1}} : \omega_{z,\mathcal{B}} \neq 0$), which results in the deviation from the linear trend shown in Figure 20. Conversely, it appears that the gyroscopic torque remains small enough for all $||\boldsymbol{\omega}_{0,\mathcal{B}}|| < 8$ deg/s, resulting in the linear trend observed in Figure 20. Figure 22b gives the evolution of the rotational velocity components as a function of time for $\boldsymbol{\omega}_{0,\mathcal{B}} = [12, 0, 0]$ deg/s, which is an example of the case discussed. In this figure, $\omega_{y,\mathcal{B}}$ quickly grows from zero due to the large magnitude of $\omega_{x,\mathcal{B}}$ and a small but non-zero $\omega_{z,\mathcal{B}}$ quickly after the start of the propagation. This results in a large gyroscopic torque and fast oscillations in the coupled rotational velocity components, which is difficult to follow for the controller.

B. Influence of Self-Shadowing Constraint and Reflectance Model

This section investigates the impact of the self-shadowing constraint and the vane reflectance model on the detumbling time for 2-DoF vanes. The sailcraft initial state is given by the reference orbital case O-1 and initial attitude A-2 from subsection II.E. Figure 23 gives the detumbling time as a function of the orbital velocity magnitude without and with the self-shadowing constraint for the SI-SRP and O-SRP models in Figures 23a and 23b respectively. Figure 23a shows that only a minor reduction in performance occurs with the addition of the self-shadowing constraint for the SI-SRP model, with an average increase in detumbling time of 0.2%. In contrast, the addition of the constraint results in an improved performance for the O-SRP model (see Figure 23b) with detumbling times up to 40% faster, and 4% faster on average. Upon inspection, it appeared that stabilization of one-axis $\omega_{z_0,\mathcal{B}} \neq 0$ cases is particularly slow for the O-SRP models without the shadowing constraint, as the controller exposed the back-side of some vanes to produce the necessary

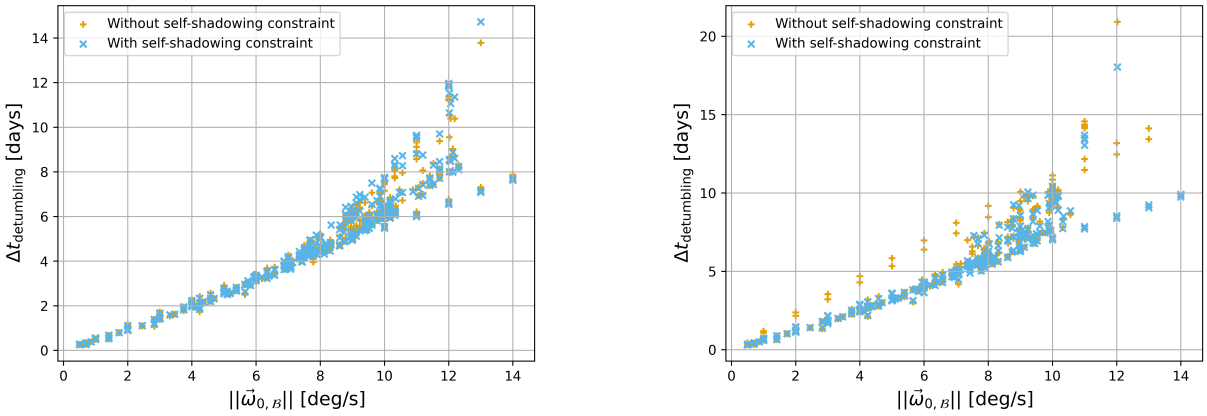

(a) SI-SRP. **(b) O-SRP.**

Fig. 23 Detumbling times with and without self-shadowing constraint for the O-1 orbit, an initial attitude A-2, $\omega_{0,\mathcal{B}} \in X_{\text{DT, s}}$, and the SI-SRP and O-SRP models.

windmill torque. As the back side of the vane has poorer optical properties in the O-SRP model, this results in subpar detumbling performance. This shows that the optimiser is prone to falling into, and remaining in, a local optimum. However, this issue does not occur when the self-shadowing constraint is taken into account, resulting in the improved performance (compared to without the constraint) seen in Figure 23b. The addition of the self-shadowing constraint permits to better bound the vane angle allocation optimization domain (see Figure 6), which improves the optimiser performance to obtain the optimal vane angles generating the desired control torque. In conclusion, the self-shadowing constraint yields only a minimal performance reduction in most cases, and may result in an improved stabilization efficiency in some scenarios. As self-shadowing would likely be avoided for practical solar-sailing, the self-shadowing constraint was used for the majority of the subsequent results, as it yields a more realistic vane movement behaviour.

Figure 24 gives the detumbling time as a function of the rotational velocity magnitude for the SI-SRP (yellow), DI-SRP (blue), and O-SRP (green) models with the self-shadowing constraint, for the orbital case O-1 and initial attitude A-2. From this figure, it appears that the SI-SRP and DI-SRP result in similar detumbling performance and the SI-SRP model performs slightly better for some edge cases beyond the linearity regime ($||\omega_0|| > 8$ deg/s). This result is expected, as the only difference between the SI- and DI-SRP models is that in the SI-SRP model, only one side of the vane is reflective, whereas in the DI-SRP model, both sides are reflective. Furthermore, the full AMS can be achieved with a single side of the vane in both cases, meaning that the SI-SRP model has a smaller domain of feasible vane angles (θ_v^i and ϕ_v^i) with the same performance. This characteristic results in an improved optimiser performance for the vane allocation algorithm, yielding the slightly better performance in the edge cases shown in Figure 24. Conversely, the O-SRP models yields detumbling times 20% longer than the SI-SRP case on average, due to its less efficient thrust generation compared to the idealistic models.

At last, Figure 25 gives the average change in rotational velocity magnitude per orbit during the first six orbits of

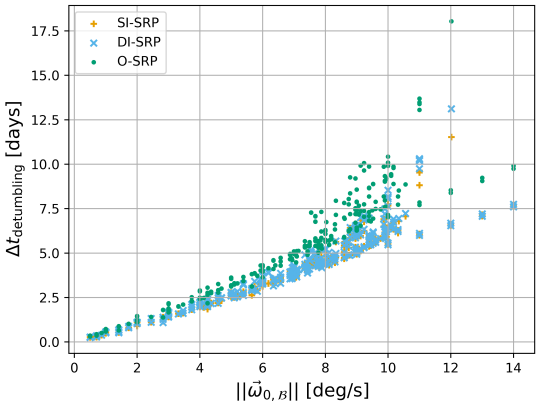

Fig. 24 Detumbling time as a function of the initial rotational velocity magnitude for the reflectance models in the O-1 orbit, with the A-2 initial attitude, with self-shadowing constraint, and $\omega_{0,\mathcal{B}} \in X_{\text{DT, s}}$.

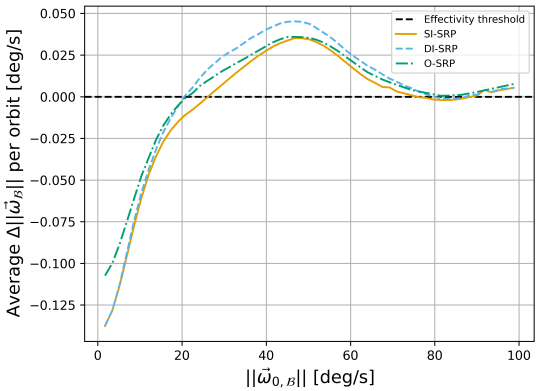

Fig. 25 Average rotational velocity magnitude change over one orbit as a function of $||\omega_{0,\mathcal{B}}||$ for the reflectance models in the O-1 orbit, with the A-2 initial attitude, with self-shadowing constraint, and $\omega_{0,\mathcal{B}} \in X_{\text{DT-3c}}$.

propagation for three-axis tumbling cases from $X_{\text{DT-3c}}$. It can be observed from this figure that the DI-SRP and O-SRP models are capable of detumbling the sailcraft until rotational velocity magnitudes of 20 deg/s while the SI-SRP was found to efficient until $||\omega_{0,\mathcal{B}}|| = 26$ deg/s in Figure 19. Additionally, it appears that the DI-SRP and SI-SRP capabilities match for $||\omega_{0,\mathcal{B}}|| < 26$ deg/s. The better performance of the SI-SRP model compared to the double-sided models at larger rotational velocities is the result of its smaller optimization domain, permitting to find the optimal vane angles more easily.

C. Influence of Orbital Altitude

This section considers the influence of the orbital altitude on the detumbling performance for 2-DoF vanes. Figure 26 shows the evolution of $\omega_{x,\mathcal{B}}$ during an attitude stabilization manoeuvre from $\omega_{0,\mathcal{B}} = [0.5, 0.5, 0.5]$ deg/s and $\omega_{0,\mathcal{B}} = [4, 4, 4]$ deg/s in Figures 26a and 26b respectively, for the orbital cases O-2 (LEO), O-3 (MEO), and O-4 (GEO) from Table 4. In all cases, the sailcraft starts from the Sun-pointing attitude A-2 defined in subsection II.E and follows the SI-SRP reflectance model without self-shadowing constraint. From these figures, it appears that the GEO case is stabilised the fastest, followed by the MEO and at last the LEO cases. This is explained by the difference in eclipse duration between the orbital regimes.

The influence of the orbital regime on the detumbling manoeuvre is straightforward in this model, but the effects of gravity gradient and aerodynamic torques would result in more complex variations. However, both these effects are expected to be stabilising and more significant in LEO. It is then expected that the difference in detumbling manoeuvre duration between different orbital regimes would remain significant, but smaller.

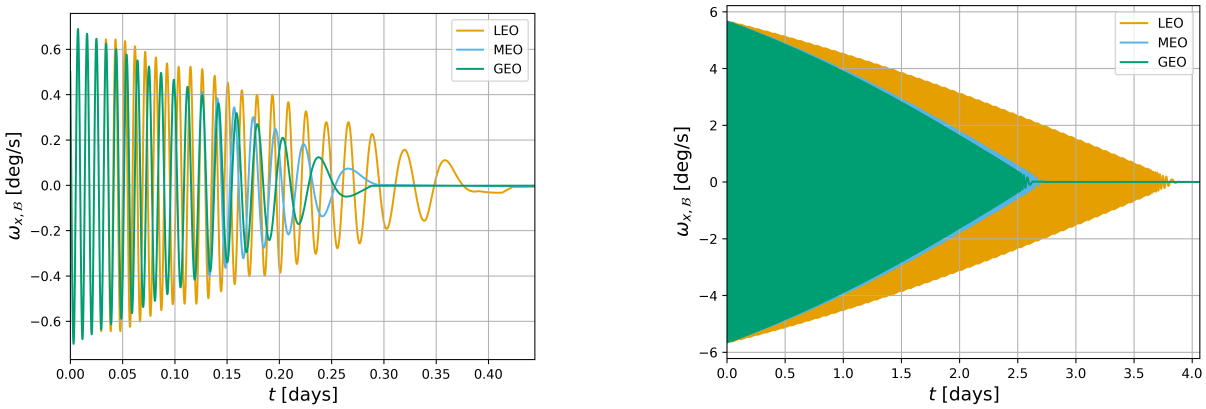

(a) $\omega_{0,\mathcal{B}} = [0.5, 0.5, 0.5]$ **deg/s.** **(b)** $\omega_{0,\mathcal{B}} = [4, 4, 4]$ **deg/s.**

Fig. 26 $\omega_{x,\mathcal{B}}$ **evolution as a function of time during a detumbling manoeuvre for the orbital cases O-2 (LEO), O-3 (MEO) and O-4 (GEO), with the initial attitude case A-2, the SI-SRP model and the self-shadowing constraint.**

Table 7 Degrees of freedom of the vanes in Figure 2 for studied cases.

		Vane 1 DoFs		Vane 2 DoFs		Vane 3 DoFs		Vane 4 DoFs	
System tag	# DoFs	$X_{\mathcal{V}_1}$	$Y_{\mathcal{V}_1}$	$X_{\mathcal{V}_2}$	$Y_{\mathcal{V}_2}$	$X_{\mathcal{V}_3}$	$Y_{\mathcal{V}_3}$	$X_{\mathcal{V}_4}$	$Y_{\mathcal{V}_4}$
D-1	4	✗	✓	✓	✗	✗	✓	✓	✗
D-2	6	✓	✓	✓	✓	✓	✓	✗	✗
D-3	7	✓	✓	✓	✓	✓	✓	✗	✓
D-4	7	✓	✓	✓	✓	✓	✓	✓	✗
Baseline	8	✓	✓	✓	✓	✓	✓	✓	✓

D. Reduced Degrees of Freedom Vane System Performance

This section considers the effect of reduced vane degrees of freedom on the detumbling performance of the vane system. The systems considered are given in Table 7, which gives the DoF of each vane for all cases. In this table, the baseline case is the full 2-DoF system considered in previous analyses, and D-1 is the system presented in Reference [15] to reduce the control complexity compared to the 2-DoF system. Then, all vanes except vane 4 have 2-DoF for cases D-2, D-3, and D-4, where it has neither control over $X_{\mathcal{V}_4}$ nor $Y_{\mathcal{V}_4}$, control over $Y_{\mathcal{V}_4}$ only, and control over $X_{\mathcal{V}_4}$ only, respectively. Lastly, D-5 is a system composed of $X_{\mathcal{V}_i}$-DoF vanes only. All systems are considered with the initial state given by orbit O-1 and the attitude A-2 from subsection II.E, with the SI-SRP reflectance model and neglecting self-shadowing effects.

Figures 27a and 27b give the evolution of the $X_{\mathcal{B}}$ and $Z_{\mathcal{B}}$ rotational velocity components as a function of time for a detumbling manoeuvre from $\omega_{0,\mathcal{B}} = [0.5, 0.5, 0.5]$ deg/s. From these figures, it appears that the baseline system reaches stabilization the fastest, followed closely by system D-4 which has no DoF around $Y_{\mathcal{V}_4}$. All other systems take at least 50% longer to perform the detumbling manoeuvre, with D-2 and D-3 reaching stabilization at similar epochs. Particularly, system D-1 takes approximately twice as long as the baseline configuration These results align with

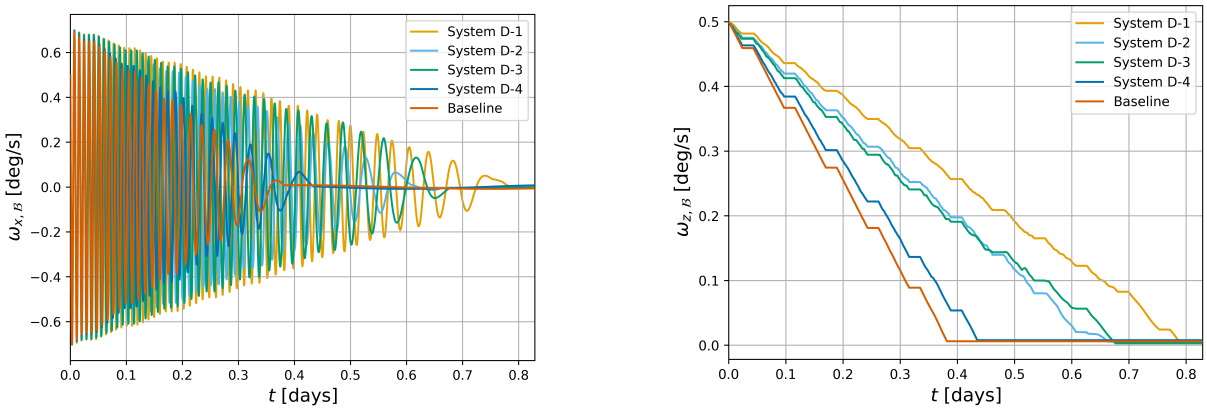

(a) $\omega_{x,\mathcal{B}}$. **(b)** $\omega_{z,\mathcal{B}}$.

Fig. 27 $\omega_{x,\mathcal{B}}$ **and** $\omega_{z,\mathcal{B}}$ **evolution as a function of time during a detumbling manoeuvre from** $\omega_{0,\mathcal{B}} = [0.5, 0.5, 0.5]$ **deg/s for the systems defined by Table 7, from the O-1 orbit and A-2 initial attitude, the SI-SRP model, and neglecting self-shadowing effects.**

expectations, as systems with more DoF perform better than ones with less DoF. An increased number of DoFs allows a larger range of vane orientations to be reached, leading to potentially more optimal vane control solutions. Furthermore, comparing the performance drop of systems D-3 and D-4 compared to the baseline, it appears that one vane losing its $X_{\mathcal{V}_i}$ rotational DoF (D-3) results in a significantly worse performance than the same vane losing its $Y_{\mathcal{V}_i}$ (D-4). This comes from the way a vane-based ACS generates a torque around $X_{\mathcal{B}}$ or $Y_{\mathcal{B}}$ compared to around $Z_{\mathcal{B}}$. While, torques around $X_{\mathcal{B}}$ or $Y_{\mathcal{B}}$ are obtained from an asymmetry between two opposite vanes (vane pairs 1+3 and 2+4 in Figure 2), the torque around $Z_{\mathcal{B}}$ is given by the sum of the contributions from each vane. Particularly, if vane 4 is only capable of rotating around its $Y_{\mathcal{V}_4}$-axis, it is never capable of producing a torque around the $Z_{\mathcal{B}}$-axis. However, if it is only capable of rotating around its $X_{\mathcal{V}_4}$-axis, the vane can both generate a torque around $Z_{\mathcal{B}}$ and a torque around $X_{\mathcal{B}}$ through asymmetry with vane 2. Therefore, the set of attainable torques around $X_{\mathcal{B}}$ remains approximately unchanged if at least one of the vanes of the pair (vane 2 or 4) can orient itself with respect to the other vane. In contrast, the maximum achievable torque around $Z_{\mathcal{B}}$ decreases by 25% if one of the four vanes loses its $X_{\mathcal{V}_i}$ DoF. This also explain the similar performance of systems D-2 and D-3, as both are unable to generate a torque around $Z_{\mathcal{B}}$ from vane 4, and system D-2 is capable of producing a suitable $X_{\mathcal{B}}$ torque by adjusting the orientation of vane 2 compared vane 4 which is fixed.

For practical solar-sailing purposes, the full 2-DoF vane system (baseline system) has demonstrated a superior performance and is robust to malfunctions of single vanes. That is, the configuration is still capable of detumbling the sailcraft under complete or partial failure of one vane (systems D-2, D-3, and D-4) despite a reduced performance. Therefore, the added control complexity of the system is justified.

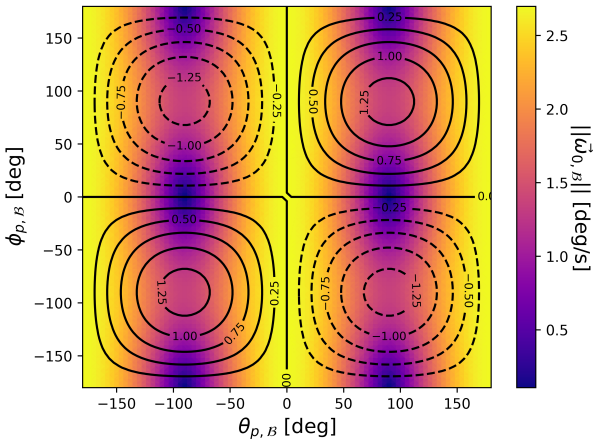

Fig. 28 Rotational velocity magnitude as a function of the collision geometry for a 1 mm diameter debris colliding with the tip of the $X_{\mathcal{B}}$ boom at $||\boldsymbol{v}_p|| = 10$ km/s.

VI. Detumbling after a Hypervelocity Impacts

This section links the results from the previous analyses to the specific case of a hypervelocity impacts with a supporting boom of the sail. Space debris considered are assumed to be spherical and made of aluminium with a density of 2,700 kg/m^2. Eqs. (16), (17), and (18) were iterated upon for momentum enhancement factors in $\beta_E = \{1, 2, 3, 4, 5\}$, projectile diameters in $d_p = \{10^{-7}, 10^{-6}, \ldots 10^{-2}, 10^{-1}\}$ m, and projectile velocity magnitude (in the body-fixed frame) of $||\boldsymbol{v}_{p,\mathcal{B}}|| \in [1; 20]$ km/s. All collisions are assumed to occur at the boom tips, as this results in the largest moment arm and associated attitude disturbance, but these results scale linearly with the projectile moment arm. Additionally, although micrometeoroids can reach impact velocities up to 70 km/s, the majority of them are much less massive than space debris and would not result in a significant disturbance of the attitude dynamics [24]. Therefore, micrometeoroids have been neglected.

Figure 28 gives the rotational velocity magnitude disturbance as a function of the collision geometry in terms of the zenith ($\theta_{p,\mathcal{B}}$) and azimuth ($\phi_{p,\mathcal{B}}$) angles in the body-fixed frame. All collisions are considered at the boom tip for $||\boldsymbol{v}_p|| = 10$ km/s and a momentum enhancement factor of 5. Additionally, contour curves of $\omega_{z,\mathcal{B}}$ are given. From Figure 28, it is observed that larger rotational velocity magnitudes are reached in head-on collisions, resulting in non-zero $\omega_{x,\mathcal{B}}$ or $\omega_{y,\mathcal{B}}$ components. This is expected, as the mass moment of inertia around the $Z_{\mathcal{B}}$ axis is twice as larger as around the $X_{\mathcal{B}}$ and $Y_{\mathcal{B}}$ axes. Combining this observation with the conclusion from subsection V.A that rotational velocities in the $X_{\mathcal{B}}$-$Y_{\mathcal{B}}$ plane are more difficult to stabilise, these results highlight the vulnerability of solar-sails enduring head-on collisions.

Figure 29 gives the rotational velocity magnitude as a function of the projectile linear momentum for collisions at the boom-tip and momentum enhancement factors between 1 and 5. In this figure, the significance level associated with the ACS controller termination condition in Eq. (20) is given by the dashed line, and the dotted-line gives the maximum

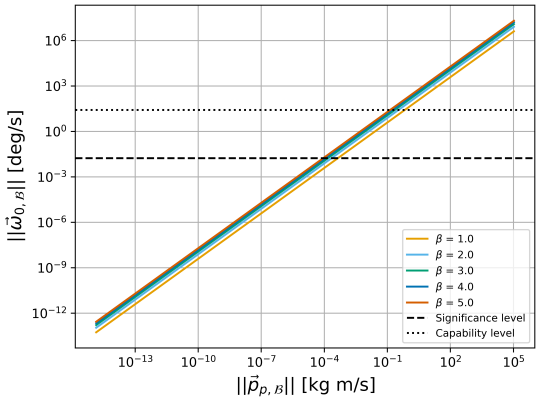

Fig. 29 Rotational velocity magnitude as a function of the projectile linear momentum for a head-on collision at the boom-tip.

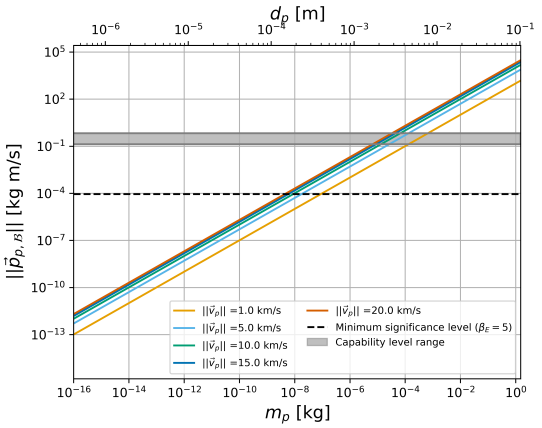

Fig. 30 Linear momentum as a function of the particle mass and velocity.

rotational velocity magnitude which can be stabilised using SI-SRP vanes. Additionally, Figure 30 gives the projectile linear momentum as a function of its mass and velocity. In this figure, the minimum significance level (from $\beta_E = 5$) and the range maximum projectile linear momentum (for $1 \leq \beta_E \leq 5$) which can be tackled by the SI-SRP controller, are also given. Particularly, the range in the latter represents the uncertainty in the effect of the collision on the sailcraft attitude dynamics. From Figures 29 and 30, it appears that the momentum enhancement factor of the collision has a significant impact on whether the ACS would be able to recover the sail attitude. For a collision velocity of 10 km/s, the maximum projectile diameter which can be handled by the ACS in the context of an HVI varies from 0.55 mm to 0.94 mm depending on the momentum enhancement factor at play. Furthermore, from Figure 30, it appears that all projectiles larger than 5 mm diameter would result in a tumbling scenario which cannot be handled by the sail. Nevertheless, less than 10^{-3}% of the impactors have a characteristic size larger than 1 mm in the orbital region of the ACS3 mission, which is similar to Envisat's orbit discussed in Reference [24]. Additionally, the extremely large rotational velocities predicted for these debris sizes indicates the limitations of the rigid plate model used in Eq. (16). Collisions with such debris would likely yield a partial destruction of the boom, which would result in a smaller tumbling velocity. In these scenarios, whether the sail can be recovered after the collision would depend on the state of the structure.

It must be noted, that the results presented in this section assume an impact on a boom rather than the sail, as no momentum transfer would occur during a collision with the sail foil. This means that the probability of collision with one of the booms is very small in comparison to the sail material. Particularly, they only cover approximately 1% of the spacecraft cross-sectional area of the ACS3 spacecraft [25]. Therefore, it can be concluded that a collision with a boom presents a high risk, but the probability of this risk is relatively low. Additionally, collisions with space debris ranging from 10^{-10} kg (at 20 km/s) up to 10^{-6} kg (at 5-10 km/s) would be significant enough to cause an attitude disturbance which can be handled by the vane-based ACS.

VII. Conclusion

This paper studied the post-collision tumbling dynamics and attitude control retrieval of solar-sails by analysing the effects of the tumbling dynamics of a solar-sail on its orbital dynamics, and assessing the capability of a state-of-the-art vane-based attitude control system to retrieve attitude control.

The effect of tumbling dynamics on the sail's orbit depends on the direction of the rotational velocity vector in the body-fixed frame, but not on its magnitude. For an initially Sun-pointing sailcraft, the tumbling motion results in a slower eccentricity growth than for a continuously Sun-pointing sail, but which could still result in the re-entry of the spacecraft. Furthermore, the orbital deviations are larger at higher altitudes and in orbits with smaller eclipse time, but also for sails with more efficient sail reflectance properties. On the short-term, an initially Sun-pointing sail in tumbling motion can be modelled as a Sun-pointing sail of the same mass with 42.44% of the reflective area. On the long-term, the motion of the Earth around the Sun results in deviations from this model.

A vane system composed of four 2-degrees-of-freedom vanes is capable of detumbling an ACS3-like sailcraft from rotational velocities up to 26 deg/s with ideally reflective vanes, and up to 20 deg/s for realistic sail foil reflective properties. For rotational velocity magnitudes below 8 deg/s, the vane system is capable of stabilising the sail craft at a rate of 2 deg/s per day. For higher rotational velocities, the detumbling time grows non-linearly. Additionally, rotational velocities in the sail plane are the most challenging to stabilise due to the coupling of the rotational velocity components around the body-fixed $X_{\mathcal{B}}$ and $Y_{\mathcal{B}}$. The system is robust to the failure of a single vane and to environmental effects, with the eclipse time being the only environmental aspect affecting the system performance, resulting in a down-time.

The vane system can stabilise a sailcraft after a hypervelocity impact with a projectile linear momentum up to 0.13 kgm/s. Particularly, head-on collisions result in the largest attitude disturbance and yield rotational velocities in the sail plane, which are the most difficult to detumble. The vane system is not capable of stabilising the sail after collisions with debris heavier than 0.1 g (4 mm diameter aluminium sphere) at 5 km/s. However, these would likely result in a severe failure of the boom and whether the sail can retrieve control in these cases would depend on the damage made to the structure.

Appendix: Derivation of Vane Coefficients Transformation

The non-dimensionalized truncated Fourier functions for the AMS ellipse coefficients derived for vane 1 from Figure 2 can be generalized to the i$^{\text{th}}$ vane and dimensionalized. For vane 1, $\tilde{T}_{x,\mathcal{B}} \approx 0$, meaning that $\tilde{T}_{y,\mathcal{B}}$ is the complete torque acting in the sail plane. Renaming $\tilde{T}_{y,\mathcal{B}}$ as $\tilde{T}_{xy,\mathcal{B}}$, it can be written that,

$$\tilde{T}_{x,\mathcal{B}} = \sin\left(-\theta_{z,\mathcal{B}}\right)\tilde{T}_{xy,\mathcal{B}} \tag{47a}$$

$$\tilde{T}_{y,\mathcal{B}} = \cos\left(-\theta_{z,\mathcal{B}}\right)\tilde{T}_{xy,\mathcal{B}} \tag{47b}$$

where $\theta_{z,\mathcal{B}}$ is the angle of rotation along the $Z_{\mathcal{B}}$ axis such that $\boldsymbol{R}_z(\theta_{z,\mathcal{B}}) = R^i_{VB}$ for a given vane. Additionally, when considering the i$^{\text{th}}$ vane compared to vane 1, the relative sunlight vector in the i$^{\text{th}}$ vane-centered reference frame

will be different,

$$\boldsymbol{n}_{s,\mathcal{V}_i} = \boldsymbol{R}_{\mathcal{V}_i\mathcal{V}_1}\boldsymbol{n}_{s,\mathcal{V}_1} = \boldsymbol{R}_{\mathcal{V}_i\mathcal{B}}\boldsymbol{n}_{s,\mathcal{B}}, \tag{48}$$

where it was used that $\mathcal{B}$ has the same orientation as $\mathcal{V}_1$ (see Figure 2). This implies that $\alpha_{s,\mathcal{V}_i}$ and $\beta_{s,\mathcal{V}_i}$ should be used when evaluating the non-dimensional truncated Fourier functions $\mathcal{F}_{tr}^{\tilde{A}-\tilde{F}}$ for the i$^{\text{th}}$ vane. Eq. (23) can then be rewritten as,

$$\tilde{A}_{xy,i}\left(\tilde{T}_{xy,\mathcal{B}}\right)^2 + \tilde{B}_{xy,i}\tilde{T}_{xy,\mathcal{B}}\tilde{T}_{z,\mathcal{B}} + \tilde{C}_{xy,i}\left(\tilde{T}_{z,\mathcal{B}}\right)^2 + \tilde{D}_{xy,i}\tilde{T}_{xy,\mathcal{B}} + \tilde{F}_{xy,i}\tilde{T}_{z,\mathcal{B}} + \tilde{F}_{xy,i} = 0, \tag{49}$$

where $\tilde{A}_{xy,i} \rightarrow \tilde{F}_{xy,i} = \mathcal{F}_{tr}^{\tilde{A}}(\alpha_{s,\mathcal{V}_i}, \beta_{s,\mathcal{V}_i}) \rightarrow \mathcal{F}_{tr}^{\tilde{F}}(\alpha_{s,\mathcal{V}_i}, \beta_{s,\mathcal{V}_i})$ are the six non-dimensional ellipse coefficients. Assuming $\theta_{z,\mathcal{B}} \neq k\pi$ for $k \in \mathbb{Z}$ and substituting Eq. (47a) in Eq. (49) yields (dropping the $\mathcal{B}$ subscripts for brevity),

$$\frac{\tilde{A}_{xy,i}}{\sin^2\left(-\theta_z^i\right)}\tilde{T}_x^2 + \frac{\tilde{B}_{xy,i}}{\sin\left(-\theta_z^i\right)}\tilde{T}_x\tilde{T}_z + \tilde{C}_{xy,i}\tilde{T}_z^2 + \frac{\tilde{D}_{xy,i}}{\sin\left(-\theta_z^i\right)}\tilde{T}_x + \tilde{E}_{xy,i}\tilde{T}_z + \tilde{F}_{xy,i} = 0,$$

$$\Leftrightarrow \underbrace{\tilde{A}_{xy,i}}_{=\tilde{A}_{x,i}}\tilde{T}_x^2 + \underbrace{\tilde{B}_{xy,i}\sin\left(-\theta_z^i\right)}_{=\tilde{B}_{x,i}}\tilde{T}_x\tilde{T}_z + \underbrace{\tilde{C}_{xy,i}\sin^2\left(-\theta_z^i\right)}_{=\tilde{C}_{x,i}}\tilde{T}_z^2 + \underbrace{\tilde{D}_{xy,i}\sin\left(-\theta_z^i\right)}_{=\tilde{D}_{x,i}}\tilde{T}_x + \underbrace{\tilde{E}_{xy,i}\sin^2\left(-\theta_z^i\right)}_{=\tilde{E}_{x,i}}\tilde{T}_z + \underbrace{\tilde{F}_{xy,i}\sin^2\left(-\theta_z^i\right)}_{=\tilde{F}_{x,i}} = 0.$$

The $\tilde{A}_{x,i} - \tilde{F}_{x,i}$ coefficients are the non-dimensional ellipse coefficients of the $\tilde{T}_{x,\mathcal{B}} - \tilde{T}_{z,\mathcal{B}}$ AMS of the i$^{\text{th}}$ vane. These coefficients are only valid if the vane is able to generate a $X_{\mathcal{B}}$ torque, that is, if the vane is not on along the $X_{\mathcal{B}}$-axis ($\theta_z^i \neq k\pi$). Similarly, assuming that $\theta_{z,\mathcal{B}} \neq \frac{\pi}{2} + k\pi$ for $k \in \mathbb{Z}$ and substituting Eq. (47b) in Eq. (49) yields (dropping the $\mathcal{B}$ subscripts for brevity),

$$\frac{\tilde{A}_{xy,i}}{\cos^2\left(-\theta_z^i\right)}\tilde{T}_x^2 + \frac{\tilde{B}_{xy,i}}{\cos\left(-\theta_z^i\right)}\tilde{T}_x\tilde{T}_z + \tilde{C}_{xy,i}\tilde{T}_z^2 + \frac{\tilde{D}_{xy,i}}{\cos\left(-\theta_z^i\right)}\tilde{T}_x + \tilde{E}_{xy,i}\tilde{T}_z + \tilde{F}_{xy,i} = 0,$$

$$\Leftrightarrow \underbrace{\tilde{A}_{xy,i}}_{=\tilde{A}_{y,i}}\tilde{T}_x^2 + \underbrace{\tilde{B}_{xy,i}\cos\left(-\theta_z^i\right)}_{=\tilde{B}_{y,i}}\tilde{T}_x\tilde{T}_z + \underbrace{\tilde{C}_{xy,i}\cos^2\left(-\theta_z^i\right)}_{=\tilde{C}_{y,i}}\tilde{T}_z^2 + \underbrace{\tilde{D}_{xy,i}\cos\left(-\theta_z^i\right)}_{=\tilde{D}_{y,i}}\tilde{T}_x + \underbrace{\tilde{E}_{xy,i}\cos^2\left(-\theta_z^i\right)}_{=\tilde{E}_{y,i}}\tilde{T}_z + \underbrace{\tilde{F}_{xy,i}\cos^2\left(-\theta_z^i\right)}_{=\tilde{F}_{y,i}} = 0.$$

The $\tilde{A}_{y,i} - \tilde{F}_{y,i}$ coefficients are the non-dimensional ellipse coefficients of the $\tilde{T}_{y,\mathcal{B}} - \tilde{T}_{z,\mathcal{B}}$ AMS of the i$^{\text{th}}$ vane. At last, an arbitrary ellipse of the form $A_0x^2 + B_0xy + C_0y^2 + D_0x + E_0y + F_0 = 0$ can be stretched by constants λ_x and λ_y along both x and y respectively using,

$$x_s = \lambda_x x, \tag{50a}$$

$$y_s = \lambda_y y. \tag{50b}$$

Substituting Eq. (50) in the general Cartesian ellipse equation yields,

$$
\begin{aligned}
&\frac{A_0}{\lambda_x^2}x_s^2 + \frac{B_0}{\lambda_x\lambda_y}x_s y_s + \frac{C_0}{\lambda_y^2}y_s^2 + \frac{D_0}{\lambda_x}x_s + \frac{E_0}{\lambda_y}y_s + F_0 = 0, \\
\Leftrightarrow\ &\underbrace{A_0\lambda_y^2}_{A_s}\,x_s^2 + \underbrace{B_0\lambda_x\lambda_y}_{B_s}\,x_s y_s + \underbrace{C_0\lambda_x^2}_{C_s}\,y_s^2 + \underbrace{D_0\lambda_x\lambda_y^2}_{D_s} + \underbrace{E_0\lambda_x^2\lambda_y}_{E_s} + \underbrace{F_0\lambda_x^2\lambda_y^2}_{F_s} = 0.
\end{aligned}
\tag{51}
$$

Putting everything together with $\lambda_x = \lambda_y = \lambda_i = \left(\frac{S_v^i W||\boldsymbol{r}_{O_{\mathcal{V}_i},\mathcal{B}}||}{c}\right)$ yields Eqs. (26).

Acknowledgments

The author thanks Dr. Dominic Dirkx for his support with the TU Delft Astrodynamics Toolbox. Additionally, the author acknowledges the use of computational resources of the DelftBlue supercomputer, provided by the Delft High Performance Computing Centre (https://www.tudelft.nl/dhpc).

References

[1] Sagdeev, R., "Sputnik and the Soviets," *Science*, Vol. 318, No. 5847, 2007, pp. 51–52. https://doi.org/10.1126/science.1149240.

[2] Maini, A. K., and Agrawal, V., *Satellite Technology - Principles and Applications*, 3rd ed., Wiley-Blackwell, Hoboken, NJ, 2014.

[3] Hall, L., "The history of space debris," *Space Traffic Management Conference*, Jim Henderson Welcome Center, Embry-Riddle Aeronautical University - Daytona Beach, 2014.

[4] ESA Space Debris Office, "ESA'S Annual Space Environment Report," Tech. rep., European Space Agency, 2023. URL https://www.sdo.esoc.esa.int/environment_report/Space_Environment_Report_latest.pdf.

[5] Johnson, A., "Orbital Debris Quarterly News-Volume 27, Issue 4," *Orbital Debris Quarterly News*, Vol. 27, No. 4, 2023.

[6] Kessler, D. J., Johnson, N. L., Liou, J., and Matney, M., "The kessler syndrome: implications to future space operations," *Advances in the Astronautical Sciences*, Vol. 137, No. 8, 2010, p. 2010.

[7] Kessler, D. J., and Cour-Palais, B. G., "Collision frequency of artificial satellites: The creation of a debris belt," *Journal of Geophysical Research: Space Physics*, Vol. 83, No. A6, 1978, pp. 2637–2646. https://doi.org/https://doi.org/10.1029/JA083iA06p02637.

[8] Pardini, C., and Anselmo, L., "Environmental sustainability of large satellite constellations in low earth orbit," *Acta Astronautica*, Vol. 170, 2020, pp. 27–36. https://doi.org/https://doi.org/10.1016/j.actaastro.2020.01.016.

[9] Lewis, H. G., "Understanding long-term orbital debris population dynamics," *Journal of Space Safety Engineering*, Vol. 7, No. 3, 2020, pp. 164–170. https://doi.org/https://doi.org/10.1016/j.jsse.2020.06.006, space Debris: The State of Art.

[10] Mark, C. P., and Kamath, S., "Review of Active Space Debris Removal Methods," *Space Policy*, Vol. 47, 2019, pp. 194–206. https://doi.org/https://doi.org/10.1016/j.spacepol.2018.12.005.

[11] Trofimov, S. P., and Ovchinnikov, M. Y., "Sail-assisted end-of-life disposal of low-earth-orbit satellites," *Journal of Guidance, Control, and Dynamics*, Vol. 40, No. 7, 2017, pp. 1796–1805.

[12] Gong, S., and Macdonald, M., "Review on solar sail technology," *Astrodynamics*, Vol. 3, No. 2, 2019, pp. 93–125. https://doi.org/10.1007/s42064-019-0038-x.

[13] McInnes, C. R., *Solar sailing: technology, dynamics and mission applications*, Springer Science & Business Media, 2004.

[14] Wie, B., "Solar Sail Attitude Control and Dynamics, Part 1," *Journal of Guidance, Control, and Dynamics*, Vol. 27, No. 4, 2004, pp. 526–535. https://doi.org/10.2514/1.11134.

[15] Wie, B., "Solar Sail Attitude Control and Dynamics, Part Two," *Journal of Guidance, Control, and Dynamics*, Vol. 27, No. 4, 2004, pp. 536–544. https://doi.org/10.2514/1.11133.

[16] Fu, B., Sperber, E., and Eke, F., "Solar sail technology—A state of the art review," *Progress in Aerospace Sciences*, Vol. 86, 2016, pp. 1–19. https://doi.org/https://doi.org/10.1016/j.paerosci.2016.07.001.

[17] Choi, M., and Damaren, C. J., "Control Allocation of Solar Sail Tip Vanes with Two Degrees of Freedom," *Journal of Guidance, Control, and Dynamics*, Vol. 39, No. 8, 2016, pp. 1857–1865. https://doi.org/10.2514/1.G001703.

[18] Mangus, D., and Heaton, A., "Solar Sail Control Actuator Concepts," *Solar Sail Technology and Applications Conference*, 2004.

[19] Prasad, B. A., and Khoral, J. S., "A new mathematical model for the attitude control of a solar sail with spar-tip vanes," *2013 IEEE International Conference on Control Applications (CCA)*, 2013, pp. 574–579. https://doi.org/10.1109/CCA.2013.6662811.

[20] Sagnières, L. B., and Sharf, I., "Evolution of Spacecraft Orbital Motion due to Hypervelocity Impacts with Debris and Meteoroids," *Proceedings of the 7th European Conference on Space Debris, ESA Space Debris Office, Darmstadt, Germany*, 2017.

[21] Alexander, W., and McDonnell, J., "Hypervelocity impact on the GIOTTO Halley Mission dust shield: Momentum exchange and measurement," *Advances in Space Research*, Vol. 2, No. 12, 1982, pp. 185–187. https://doi.org/https://doi.org/10.1016/0273-1177(82)90305-2.

[22] Nysmith, C., and Denardo, B. P., *Experimental investigation of the momentum transfer associated with impact into thin aluminium targets*, National Aeronautics and Space Administration, 1969.

[23] Hayashi, K., Nishida, M., Kurosaki, H., and Yanagisawa, T., "Measurement of Momentum to Move with Hypervelocity Impacts of Projectile," *Transactions of the Japan Society for Aeronautical and Space Sciences, Aerospace Technology Japan*, Vol. 17, No. 4, 2019, pp. 427–431.

[24] Sagnières, L. B., and Sharf, I., "Stochastic modeling of hypervelocity impacts in attitude propagation of space debris," *Advances in Space Research*, Vol. 59, No. 4, 2017, pp. 1128–1143. https://doi.org/https://doi.org/10.1016/j.asr.2016.11.030.

[25] Wilkie, K., and Fernandez, J., "Advanced Composite Solar Sail System (ACS3) Mission Update," *The 6th International Symposium on Space Sailing*, 2023.

[26] Dirkx, D., Fayolle, M., Garrett, G., Avillez, M., Cowan, K., Cowan, S., Encarnacao, J., Lombrana, C. F., Gaffarel, J., Hener, J., et al., "the open-source astrodynamics tudatpy software–overview for planetary mission design and science analysis," *Europlanet Science Congress 2022*, Palacio de Congresos de Granada, Spain, 2022. https://doi.org/https://doi.org/10.5194/epsc2022-253, ePSC2022 (EPSC2022-253).

[27] Wakker, K. F., *Fundamentals of Astrodynamics*, TU Delft Library, 2015.

[28] Casotto, S., "The equations of relative motion in the orbital reference frame," *Celestial Mechanics and Dynamical Astronomy*, Vol. 124, No. 3, 2016, pp. 215–234. https://doi.org/10.1007/s10569-015-9660-1.

[29] Klinkrad, H., *Space debris: models and risk analysis*, Springer Science & Business Media, 2006.

[30] Betts, J. T., "Optimal interplanetary orbit transfers by direct transcription," *Journal of the Astronautical Sciences*, Vol. 42, No. 3, 1994, pp. 247–268.

[31] Montenbruck, O., Gill, E., and Lutze, F., *Satellite orbits: models, methods, and applications*, Springer-Verlag, 2002.

[32] Doornbos, E., *Thermospheric density and wind determination from satellite dynamics*, Springer Science & Business Media, 2012.

[33] Mooij, E., "The motion of a vehicle in a planetary atmosphere," Tech. rep., Delft University of Technology, 1994.

[34] Sidi, M. J., *Spacecraft dynamics and control: a practical engineering approach*, Vol. 7, Cambridge university press, 1997.

[35] Lu, W.-C., Duan, L., and Cai, Y.-X., "De-tumbling Control of a CubeSat," *2018 IEEE International Conference on Advanced Manufacturing (ICAM)*, 2018, pp. 298–301. https://doi.org/10.1109/AMCON.2018.8614819.

[36] Drolshagen, G., "Hypervelocity impact effects on spacecraft," *Meteoroids 2001 Conference*, Vol. 495, 2001, pp. 533–541.

[37] Schonberg, W. P., "A comparison of fragmentation models," *International Journal of Impact Engineering*, Vol. 17, No. 4, 1995, pp. 739–750. https://doi.org/https://doi.org/10.1016/0734-743X(95)99896-Y, hypervelocity Impact Proceedings of the 1994 Symposium.

[38] McDonnell, J., "Momentum enhancement in hypervelocity impacts: Parameters for space debris and meteoroid perturbations," *Proceedings of the Fifth Cranfield Conference on Dynamics and Control of Systems and Structures in Space*, Citeseer, 2002, pp. 1–10.

[39] Wilkie, W. K., "Overview of the NASA advanced composite solar sail system (acs3) technology demonstration project," *AIAA Scitech 2021 Forum*, 2021, p. 1260.

[40] Hassanpour, S., and Damaren, C. J., "Linear Structural Dynamics and Tip-Vane Attitude Control for Square Solar Sails," *Journal of Guidance, Control, and Dynamics*, Vol. 41, No. 11, 2018, pp. 2401–2415. https://doi.org/10.2514/1.G003485.

[41] Aghili, F., "Time-Optimal Detumbling Control of Spacecraft," *Journal of Guidance, Control, and Dynamics*, Vol. 32, No. 5, 2009, pp. 1671–1675. https://doi.org/10.2514/1.43189.

[42] Seidel, R., *Convex hull computations*, Chapman and Hall/CRC, 2017.

[43] Fitzgibbon, A., Pilu, M., and Fisher, R., "Direct least square fitting of ellipses," *IEEE Transactions on Pattern Analysis and Machine Intelligence*, Vol. 21, No. 5, 1999, pp. 476–480. https://doi.org/10.1109/34.765658.

[44] Halır, R., and Flusser, J., "Numerically stable direct least squares fitting of ellipses," *Proc. 6th International Conference in Central Europe on Computer Graphics and Visualization. WSCG*, Vol. 98, Citeseer, 1998, pp. 125–132.

[45] Stewart, J., *Calculus: early transcendentals*, Cengage Learning, 2012.

[46] Kraft, D., "A software package for sequential quadratic programming," *Forschungsbericht- Deutsche Forschungs- und Versuchsanstalt fur Luft- und Raumfahrt*, 1988.

[47] Biscani, F., and Izzo, D., "A parallel global multiobjective framework for optimization: pagmo," *Journal of Open Source Software*, Vol. 5, No. 53, 2020, p. 2338. https://doi.org/10.21105/joss.02338.

[48] McDonald, G. C., "Ridge regression," *WIREs Computational Statistics*, Vol. 1, No. 1, 2009, pp. 93–100. https://doi.org/https://doi.org/10.1002/wics.14.

[49] Powell, M. J., *A direct search optimization method that models the objective and constraint functions by linear interpolation*, Springer, 1994.

[50] Jones, D. R., Perttunen, C. D., and Stuckman, B. E., "Lipschitzian optimization without the Lipschitz constant," *Journal of Optimization Theory and Applications*, Vol. 79, No. 1, 1993, pp. 157–181. https://doi.org/10.1007/BF00941892.

[51] Press, W. H., Vetterling, W. T., Teukolsky, S. A., and Flannery, B. P., *Numerical recipes*, Cambridge University Press, London, England, 1988.

[52] Jones, D. R., and Martins, J. R. R. A., "The DIRECT algorithm: 25 years Later," *Journal of Global Optimization*, Vol. 79, No. 3, 2021, pp. 521–566. https://doi.org/10.1007/s10898-020-00952-6.

[53] Virtanen, P., Gommers, R., Oliphant, T. E., Haberland, M., Reddy, T., Cournapeau, D., Burovski, E., Peterson, P., Weckesser, W., Bright, J., van der Walt, S. J., Brett, M., Wilson, J., Millman, K. J., Mayorov, N., Nelson, A. R. J., Jones, E., Kern, R., Larson, E., Carey, C. J., Polat, İ., Feng, Y., Moore, E. W., VanderPlas, J., Laxalde, D., Perktold, J., Cimrman, R., Henriksen, I., Quintero, E. A., Harris, C. R., Archibald, A. M., Ribeiro, A. H., Pedregosa, F., van Mulbregt, P., and SciPy 1.0 Contributors, "SciPy 1.0: Fundamental Algorithms for Scientific Computing in Python," *Nature Methods*, Vol. 17, 2020, pp. 261–272. https://doi.org/10.1038/s41592-019-0686-2.

[54] Danca, M.-F., and Fečkan, M., "On Numerical Integration of Discontinuous Dynamical Systems," *International Journal of Bifurcation and Chaos*, Vol. 27, No. 14, 2017, p. 1750218. https://doi.org/10.1142/S0218127417502182.

[55] Rodrigues, O., "On the geometrical laws that govern the displacements of a solid system in space, and on the change of coordinates resulting from these displacements considered independently of the causes that can produce them," *J Math Pures Appl*, Vol. 5, 1840, pp. 380–440.

Part III

Closure

4

Conclusion and Recommendations

This thesis aimed to determine the effects of a tumbling motion on the orbital dynamics of solar-sails, and to assess the capability of a state-of-the-art vane system controller to regain attitude control. Additionally, the specific case of hypervelocity impacts causing a disturbance in the attitude dynamics was considered. First, Section 4.1 provides answers to the research questions formulated at the end of the literature review in Section 2.4. Then, Section 4.2 presents recommendations for future research in this field.

4.1. Conclusions

The conclusions on the work performed are presented by answering each research question separately, and then reflecting on the original research objective. The research questions from Section 2.4 were the following:

A) *What is the effect of the tumbling motion on the sail trajectory ?*

The sailcraft moves away from its nominal orbit as a result of the tumbling dynamics, however, this effect is best compared to the cases of a continuously edge-on or Sun-pointing sailcraft. In the edge-on scenario, the sailcraft does not experience any SRP acceleration and remains in its initial orbit. In contrast, a continuously Sun-pointing sailcraft experiences an approximately constant SRP acceleration throughout its orbit, which results in an eccentricity growth. On the long-term, this eccentricity growth could result in a re-entry of the spacecraft if the initial orbit is low enough. For an initially Sun-pointing sailcraft, the net effect of the tumbling dynamics on the sailcraft trajectory is to reduce the impact of the SRP force with respect to the continuously Sun-pointing case. This reduction is independent of the rotational velocity magnitude, but depends on the rotational velocity direction in the body-fixed frame on the long-term. On the short-term (up to 10 days), the effect of tumbling is independent of both the rotational velocity direction and magnitude, under the assumption that the attitude motion is significantly faster than the orbital motion. The deviations from the initial orbit can be quantified using an orbit similar to the Advanced Composite Solar-Sail System (ACS3) mission, a near-polar (inclination of 98°) and near-circular (eccentricity of 0.004) orbit at 1,000 km altitude, and a sail which specularly reflects photons on both of its sides. In this scenario, the sailcraft pericenter and apocenter altitudes decreased and increased by approximately 48 km on average (from 43 to 53 km) respectively after 30 days. Conversely, the same sailcraft in a continuously Sun-pointing orientation in the same orbit would experience pericenter and apocenter deviations of the order of -120 km and +120 km, respectively, over the same period of time. Note in both cases these deviations result from the orbital eccentricity growth, as the semi-major axis only increases by a few kilometres in both cases. Furthermore, neither case results in significant orbital plane changes. Sensitivity studies revealed that larger deviations from the initial orbit result for orbital regions with a weaker gravitational attraction (higher altitudes) and shorter eclipse times (higher altitudes, different RAANs for sun-synchronous orbits, and so on). Additionally, sails with more efficient reflective properties result in larger deviations. On the short-term, the overall effect of the tumbling dynamics can be modelled as a Sun-pointing sailcraft with a sail area reduced by 57.56% ($\approx 1 - \frac{4}{3\pi}$) and the same spacecraft mass. On the long-term, the movement of the Earth around the Sun causes a rotation of the local sunlight direction, which changes the direction of the tumbling axis with respect to the local sunlight, resulting in deviations from this simplified model.

B) *Under which tumbling conditions is the attitude control recovery achievable using a vane-based attitude control system?*

A vane-based ACS consisting of four actuated tip-vanes with 2 rotational degrees-of-freedom each was found to be capable of detumbling an ACS3-like solar-sail for rotational velocity cases up to 26 deg/s (three-axis) for single-sided ideally reflective vanes, and 20 deg/s for vanes having the reflective properties of the ACS3 sail foil material. Note that these values are very large with respect to the maximum turning rate of state-of-the-art solar-sails, as the ACS3 spacecraft can only perform 0.5 deg/s rotation manoeuvres with its ACS [143]. The 26 deg/s threshold was determined by considering the average performance of the vane system over six orbits and assessing whether the rotational velocity magnitude decreases over each orbit. Additionally, the complete detumbling manoeuvre was studied for rotational velocity magnitudes up to 15 deg/s in magnitude, considering one-, two-, and three-axis cases in the body-fixed frame. Over this range, some tumbling scenarios were found to be significantly more challenging to stabilise than others. Particularly, rotational velocities which quickly change direction are the most difficult to detumble as the vane system struggles to follow the optimal detumbling torque direction, which also quickly changes. Such fast changes in rotational velocity direction are the result of the coupling between the $X_{\mathcal{B}}$ and $Y_{\mathcal{B}}$ rotational velocity components in the attitude equations of motion of a rigid sailcraft. Therefore, rotational velocities in the sail plane (with components around the $X_{\mathcal{B}}$ and $Y_{\mathcal{B}}$ body axes only) result in the longest observed detumbling manoeuvre durations. In contrast, rotational velocities around the sail surface normal are significantly easier to stabilise as the $Z_{\mathcal{B}}$ component is decoupled, which that the rotational velocity direction is fixed in inertial space, and the attitude control system can follow the optimal detumbling torque direction more easily.

i) *Is a robust back-up attitude control system necessary to recover attitude control after such collision ?*

Whether a robust ACS is necessary to recover the attitude control of a tumbling sailcraft depends on the likelihood of the occurrence of an attitude disturbance (hypervelocity impact or not) resulting in an attitude disturbance larger than 26 deg/s (20 deg/s for the realistic reflectance model). Considering hypervelocity impacts, the 26 deg/s threshold is equivalent to a head-on collision with a space debris or meteoroid having a linear momentum of 0.13 kgm/s and impacting at one of the booms' tips with a momentum enhancement factor of 5. This linear momentum is equivalent to a 1.66 mm diameter aluminium space debris impacting the sail at a relative velocity of 20 km/s. However, a head-on collision at the boom tip and a momentum enhancement factor of 5 is the absolute worst case scenario and is unlikely for most missions. Mission designers should therefore carefully consider the likelihood of hypervelocity impacts and derive a probability distribution of the resulting attitude disturbance based on the debris flux in the mission target orbit. This information then permits them to trade-off the risk of a hypervelocity impact which cannot be recovered by the vane-based ACS and the cost of the supplementary robust ACS. Furthermore, the rigid plate model used to determine the attitude disturbance resulting from a hypervelocity impact becomes invalid for projectiles with very large linear momentum. Collisions with such particles would likely result in a partial failure of the boom, rather than result in a large momentum transfer of the sail. In these cases, determining whether the attitude recovery of a sailcraft is achievable depends on both the damage to the boom, and the momentum transfer resulting from the impact.

ii) *How long does it take to retrieve attitude control from an initially tumbling state ?*

Larger rotational velocities result in longer detumbling times. For initial rotational velocity magnitudes up to 8 deg/s, the vane-based ACS stabilises the sailcraft at a rate of 2 deg/s per day for ideally reflective vanes, and 1.3 deg/s per day for vanes having the reflective properties of the ACS3 foil. While this linear behaviour continues for larger rotational velocities for initial rotational velocities around the sail surface normal ($Z_{\mathcal{B}}$), the detumbling time grows non-linearly for $||\boldsymbol{\omega}_{0,\mathcal{B}}|| > 8$ deg/s for all other tumbling cases. The non-linear behaviour is a result of the quickly changing rotational velocity direction resulting from the coupling between the $X_{\mathcal{B}}$ and $Y_{\mathcal{B}}$ rotational velocity components mentioned above. For ideally reflective vanes, a maximum detumbling time of 20 days was reached for a rotational velocity of 15 deg/s in the sail plane, which is the worst case tumbling geometry mentioned above.

iii) *What parameters influence the recovery time the most ?*

The sensitivity of the detumbling performance with respect to the orbital regime, the reflectance properties of the sail, and the degrees-of-freedom of the sail was analysed. First, the detumbling performance was considered in equatorial near-circular (eccentricity of 0.004) orbits with altitudes of 1,000 km (LEO), 10,000 km (MEO), and 36,000 km (GEO). This test case showed that the eclipse time has a major impact on the length of the stabilisation manoeuvre, as the system cannot generate any torque during an eclipse. Therefore, eclipses result in a down-time of the ACS and stabilisation manoeuvres are shorter in GEO (where the spacecraft does not experience eclipse times) than in LEO. Second, the capabilities of the vane system are severely impacted by the vane optical characteristics. Vanes having the reflective properties of the ACS3 sail foil result in a 30% increase of the detumbling time on average with respect to ideally reflective vanes. At last, reducing the number of degrees of freedom of the vane system was found to have a direct impact on the detumbling performance. Particularly, the system presented by Wie [179], which has four degrees-of-freedom (two $X_{\mathcal{V}}$-DoF and two $Y_{\mathcal{V}}$-DoF vanes), takes about twice as long as the full 2-DoF system to stabilise a $\boldsymbol{\omega}_{0,\mathcal{B}} = [0.5, 0.5, 0.5]$ deg/s tumbling scenario. Additionally, the full 2-DoF system is robust to the complete failure of one of its vanes. This means that if one of the four vanes of the system were to lose its two degrees-of-freedom and remain fixed in the body-fixed frame, the vane system would still be able to detumble the sailcraft, although with a significantly reduced performance.

C) What collision geometries are the most difficult to recover from ?

Considering an initially inertially non-rotating sail, a head-on collision at a boom's tip would result in the largest sailcraft tumbling motion. This is a result of the smaller mass moment of inertia of the sail around its in-plane body axes ($X_{\mathcal{B}}$ and $Y_{\mathcal{B}}$). In such collision geometry, the projectile velocity vector is perpendicular to the sail plane, resulting in a sailcraft rotational velocity in the sail plane. As mentioned above, these tumbling scenarios are also the most difficult to stabilise due to the coupling between the $X_{\mathcal{B}}$ and $Y_{\mathcal{B}}$ rotational velocity components. In this configuration, the maximum mass of the debris which could be stabilised by the system for a collision at 5 km/s is of the order of 0.1 g (or a 4 mm diameter aluminium sphere). However, note that the tumbling dynamics described in this thesis would only occur from a hypervelocity impact in case of a collision with a boom, as a collision with the sail foil would result in a negligible momentum transfer due to its very small thickness (2.115 μm for the ACS3 [118]). As the booms represent approximately 1% of the sail cross-sectional area, collisions of large debris with a boom presents a high risk with a low probability for the sailcraft survivability. Additionally, less than 10^{-3}% of the impactors have a characteristic size larger than 1 mm in the orbital region of the ACS3 mission [230].

The research objective of this thesis was to characterise the effect of a high-energy on-orbit debris/solar-sail collision with orbital debris on the sailcraft attitude and trajectory dynamics and assess the capability of an actuated tip-vane system to retrieve attitude control from a tumbling state. Based on the answers of the above research questions, this research objective has been met and showed that the detumbling of a sailcraft using the a, actuated tip-vanes system is possible up to some extent. This also disproves the statement from Wie et al. [199] that propellantless attitude control system cannot be used to recover a sail from a tumbling state, as it was shown that it is at least possible to do so with actuated tip-vanes.

4.2. Recommendations and Future Work

A number of recommendations on future work to be performed in the field are given in this section. These are divided into work related to the dynamical model in Section 4.2.1, recommendations regarding improving the vane controller performance in Section 4.2.2 and future research using the vane system controller from this thesis in Section 4.2.3.

4.2.1. Dynamical Model

A relatively simple dynamical model including solely the central gravity field and SRP accelerations, and the SRP torques, was used throughout this thesis. Future work should consider a higher-fidelity model of the near-Earth space environment, focusing specifically on perturbing torques such as the gravity gradient and aerodynamic (in LEO) torques. These perturbing torques are particularly important when considering the detumbling manoeuvres performance. Additionally, including other major orbital perturbations (like

Earth's oblateness, atmospheric drag, and third-body accelerations) would permit to assess how the orbital deviations resulting from the tumbling motion compare to those from these other forces.

As the number of artificial objects in Earth orbit continues to rise, a deeper understanding of hypervelocity impact dynamics on complex aerospace structures is becoming increasingly more important. Particularly, better knowledge of the momentum enhancement factor at play during one of these collisions with the composite booms of the ACS3 mission would permit to better pinpoint what kind of debris result in collisions which cannot be recovered from by the vane-based attitude control system. Such knowledge would then better aid mission designers in their trade-off on whether a robust attitude control system should be included on-board of the spacecraft, for example. Additionally, better knowledge of the hypervelocity impact at play would permit to assess on which cases a boom would be significantly damage.

4.2.2. Vane System Controller

The vane controller developed for this thesis extended the work performed by Choi and Damaren [270] to include non-ideal reflectance models of the vanes, a self-shadowing constraint, and variations in the number of degrees-of-freedom of each vane. However, there remains a number of aspects which can be tackled to improve the controller performance. Some of these are listed below in no particular order:

- A more computationally efficient method to describe the 1-DoF vane attainable moment set, similar to the ellipse approach for the 2-DoF could be developed. This would be particularly valuable if such vane controller is envisioned to run on-board of a sailcraft.
- The controller performance can be enhanced by further preventing the occurrence of sudden large changes in vane angles from one controller call to the other. These large jumps reduce the efficiency of the system due to the time taken by the vane to rotate to the new orientation.
- Determining under which conditions the controller tends to fall into local minima and further preventing these occurrences.
- Tuning the controller tolerances (such as under what conditions the vane angles are updated) to improve its performance on tumbling cases close to the 26 deg/s threshold. The controller tolerances used throughout this thesis were obtained from tuning its performance on a tumbling case defined by $\boldsymbol{\omega}_{0,\mathcal{B}} = [0.5, 0.5, 0.5]$ deg/s, which is very far from the maximum capabilities of the controller, but was necessary due to the high computational cost of propagations with large initial rotational velocities

4.2.3. Future Research

Future research on the use of the vane system controller developed throughout this work could include further sensitivity analyses related to the maximum vane speed, the domain of permissible orientations of each vane, the relative size of the vanes compared to the sail, the initial orientation of the sailcraft, and the vanes shapes, among others. Additionally, the controller was assumed to have a perfect knowledge of the sail position and orientation in inertial space, and of the material reflective properties. Therefore, studying the performance of the controller as a result of an imperfect knowledge of these aspects is fundamental if the controller is to be used on-board of a sailcraft in the future. Additionally, the probability of a hypervelocity impact was not considered in this thesis. However, an assessment of which collision geometries and projectile linear momentum are most likely in a given orbit would help to better contextualise the capabilities of the vane system with respect to hypervelocity impacts. At last, the capabilities of other propellantless attitude control systems to detumble a sailcraft should be investigated such that the most promising system can be selected for future solar-sailing missions.

References

[1] D. J. Kessler and B. G. Cour-Palais. “Collision frequency of artificial satellites: The creation of a debris belt”. In: *Journal of Geophysical Research: Space Physics* 83.A6 (1978), pp. 2637–2646. DOI: https://doi.org/10.1029/JA083iA06p02637.

[2] R. Sagdeev. “Sputnik and the Soviets”. In: *Science* 318.5847 (2007), pp. 51–52. DOI: 10.1126/science.1149240.

[3] A. K. Maini and V. Agrawal. *Satellite Technology - Principles and Applications*. 3rd ed. Hoboken, NJ: Wiley-Blackwell, 2014.

[4] L. Hall. “The history of space debris”. In: *Space Traffic Management Conference*. 2014.

[5] D. J. Kessler, N. L. Johnson, J. Liou, and M. Matney. “The kessler syndrome: implications to future space operations”. In: *Advances in the Astronautical Sciences* 137.8 (2010), p. 2010.

[6] C. Pardini and L. Anselmo. “Environmental sustainability of large satellite constellations in low earth orbit”. In: *Acta Astronautica* 170 (2020), pp. 27–36. ISSN: 0094-5765. DOI: https://doi.org/10.1016/j.actaastro.2020.01.016.

[7] J. Sankaran. “Russia’s anti-satellite weapons: A hedging and offsetting strategy to deter Western aerospace forces”. In: *Contemporary Security Policy* 43.3 (2022), pp. 436–463.

[8] P. Anz-Meador, J. Opiela, and J.-C. Liou. *History of on-orbit satellite fragmentations*. Tech. rep. 2023.

[9] R. Miller. “Orbital Debris Quarterly News-Volume 25, Issue 4”. In: *Orbital Debris Quarterly News* 25.4 (2021).

[10] ESA Space Debris Mitigation Working Group. *ESA Space Debris Mitigation Requirements*. Tech. rep. European Space Agency, 2023. URL: https://technology.esa.int/upload/media/ESA-Space-Debris-Mitigation-Requirements-ESSB-ST-U-007-Issue1.pdf.

[11] ESA Space Debris Office. *ESA’S Annual Space Environment Report*. Tech. rep. European Space Agency, 2023. URL: https://www.sdo.esoc.esa.int/environment_report/Space_Environment_Report_latest.pdf.

[12] A. Witze. “SpaceX launch highlights threat of “mega-constellations””. In: *Nature* 575.7782 (2019), pp. 268–269.

[13] A. Johnson. “Orbital Debris Quarterly News-Volume 27, Issue 4”. In: *Orbital Debris Quarterly News* 27.4 (2023).

[14] M. Mejía-Kaiser. “Taking Garbage Outside: The Geostationary Orbit and Graveyard Orbits”. In: *Proceedings of the 49th IISL Colloquium on the Law of Outer Space*. 2006.

[15] D. S. McKnight, R. Maher, and L. Nagl. *Fragmentation Algorithms for Satellite Targets (FAST) empirical breakup model*. 1992.

[16] M. Schimmerohn, P. Matura, E. Watson, N. Durr, A. Altes, T. Cardone, D. de Wilde, H. Krag, and F. Schäfer. “Numerical investigation on the standard catastrophic breakup criteria”. In: *Acta Astronautica* 178 (2021), pp. 265–271. ISSN: 0094-5765. DOI: https://doi.org/10.1016/j.actaastro.2020.09.014.

[17] S. Flegel, J. Gelhaus, C. Wiedemann, P. Vorsmann, M. Oswald, S. Stabroth, H. Klinkrad, and H. Krag. “The MASTER-2009 space debris environment model”. In: *Fifth European Conference on Space Debris*. Vol. 672. European Space Agency/European Space Operations Centre Darmstadt, Germany. 2009, pp. 1–8.

[18] H. Klinkrad. *Space debris: models and risk analysis*. Springer Science & Business Media, 2006.

[19] D. Wright. “Colliding satellites: consequences and implications”. In: *Union of Concerned Scientists* 26 (2009).

[20] W. Nozawa, K. Kurita, T. Tamaki, and S. Managi. “To What Extent Will Space Debris Impact the Economy?” In: *Space Policy* 66 (2023), p. 101580. ISSN: 0265-9646. DOI: https://doi.org/10.1016/j.spacepol.2023.101580.

[21] S. Tkatchova. *Emerging Space Markets*. Springer, 2018.

[22] J. Mason, J. Stupl, W. Marshall, and C. Levit. “Orbital debris–debris collision avoidance”. In: *Advances in Space Research* 48.10 (2011), pp. 1643–1655. ISSN: 0273-1177. DOI: https://doi.org/10.1016/j.asr.2011.08.005.

[23] J. L. Forshaw, G. S. Aglietti, N. Navarathinam, H. Kadhem, T. Salmon, A. Pisseloup, E. Joffre, T. Chabot, I. Retat, R. Axthelm, S. Barraclough, A. Ratcliffe, C. Bernal, F. Chaumette, A. Pollini, and W. H. Steyn. “RemoveDEBRIS: An in-orbit active debris removal demonstration mission”. In: *Acta Astronautica* 127 (2016), pp. 448–463. ISSN: 0094-5765. DOI: https://doi.org/10.1016/j.actaastro.2016.06.018.

[24] X. Li, D. Yang, and H. Liu. “China’s space robotics for on-orbit servicing: the state of the art”. In: *National Science Review* 10.5 (2022), nwac129. ISSN: 2095-5138. DOI: 10.1093/nsr/nwac129.

[25] R. Biesbroek, S. Aziz, A. Wolahan, S.-f. Cipolla, M. Richard-Noca, and L. Piguet. “The clearspace-1 mission: ESA and clearspace team up to remove debris”. In: *Proc. 8th Eur. Conf. Sp. Debris*. 2021, pp. 1–3.

[26] G. Vukovich and Y. Kim. “Satellite orbit decay due to atmospheric drag”. In: *International Journal of Space Science and Engineering* 5.2 (2019), pp. 159–180. DOI: 10.1504/IJSPACESE.2019.097438.

[27] E. M. Alessi, G. Schettino, A. Rossi, and G. B. Valsecchi. “Natural highways for end-of-life solutions in the LEO region”. In: *Celestial Mechanics and Dynamical Astronomy* 130.5 (2018), p. 34.

[28] E. Doornbos. *Thermospheric density and wind determination from satellite dynamics*. Springer Science & Business Media, 2012.

[29] L. Liu and X. Wang. “On the orbital lifetime of high-altitude satellites”. In: *Chinese Astronomy and Astrophysics* 24.3 (2000), pp. 284–288. ISSN: 0275-1062. DOI: https://doi.org/10.1016/S0275-1062(00)00055-2.

[30] W. C. Rochelle, R. E. Kinsey, E. A. Reid, R. C. Reynolds, and N. L. Johnson. “Spacecraft orbital debris reentry: Aerothermal analysis”. In: *Proceedings of the Eighth Annual Thermal and Fluids Analysis Workshop: Spacecraft Analysis and Design*. Vol. 3359. National Aeronautics and Space Administration. 1997.

[31] T. Lips, B. Fritsche, G. Koppenwallner, and H. Klinkrad. “Spacecraft destruction during re-entry – latest results and development of the SCARAB software system”. In: *Advances in Space Research* 34.5 (2004). Space Debris, pp. 1055–1060. ISSN: 0273-1177. DOI: https://doi.org/10.1016/j.asr.2003.01.012.

[32] ChoiEun-Jung, ChoSungki, LeeDeok-Jin, KimSiwoo, and J. Hyun. “A Study on Re-entry Predictions of Uncontrolled Space Objects for Space Situational Awareness”. In: *Journal of Astronomy and Space Sciences* 34.4 (2017), pp. 289–302.

[33] R. Kumar, R. Singh, A. Chinnappan, and A. Appar. “Simulation of the orbital decay of a spacecraft in low Earth orbit due to aerodynamic drag”. In: *The Aeronautical Journal* 126.1297 (2022), pp. 565–583. DOI: 10.1017/aer.2021.83.

[34] T. Lips and B. Fritsche. “A comparison of commonly used re-entry analysis tools”. In: *Acta Astronautica* 57.2 (2005). Infinite Possibilities Global Realities, Selected Proceedings of the 55th International Astronautical Federation Congress, Vancouver, Canada, 4-8 October 2004, pp. 312–323. ISSN: 0094-5765. DOI: https://doi.org/10.1016/j.actaastro.2005.03.010.

[35] T. Lips and B. Fritsche. “A comparison of commonly used re-entry analysis tools”. In: *Acta Astronautica* 57.2 (2005). Infinite Possibilities Global Realities, Selected Proceedings of the 55th International Astronautical Federation Congress, Vancouver, Canada, 4-8 October 2004, pp. 312–323. ISSN: 0094-5765. DOI: https://doi.org/10.1016/j.actaastro.2005.03.010.

[36] Z. WU, R. HU, X. QU, X. WANG, and Z. WU. “Space Debris Reentry Analysis Methods and Tools”. In: *Chinese Journal of Aeronautics* 24.4 (2011), pp. 387–395. DOI: 10.1016/S1000-9361(11)60046-0.

[37] D. King-Hele and D. M. Walker. “Predicting the orbital lifetimes of Earth satellites”. In: *Acta Astronautica* 18 (1988), pp. 123–131. ISSN: 0094-5765. DOI: https://doi.org/10.1016/0094-5765(88)90093-8.

[38] S. Khodairy, M. Sharaf, M. Awad, R. A. Hamed, and M. Hussein. “Impact of solar activity on Low Earth Orbiting satellites”. In: *Journal of Physics: Conference Series* 1523.1 (2020), p. 012010. DOI: 10.1088/1742-6596/1523/1/012010.

[39] J. M. Picone, A. E. Hedin, D. P. Drob, and A. C. Aikin. “NRLMSISE-00 empirical model of the atmosphere: Statistical comparisons and scientific issues”. In: *Journal of Geophysical Research: Space Physics* 107.A12 (2002), SIA 15-1-SIA 15–16. DOI: https://doi.org/10.1029/2002JA009430.

[40] V. Braun, A. Horstmann, S. Lemmens, C. Wiedemann, and L. Böttcher. “Recent developments in space debris environment modelling, verification and validation with MASTER”. In: *8th European Conference on Space Debris*. ESA Space Debris Office Darmstadt, Germany. 2021, p. 18.

[41] D. L. Mains and M. E. Sorge. “The IMPACT satellite fragmentation model”. In: *Acta Astronautica* 195 (2022), pp. 547–555. ISSN: 0094-5765. DOI: https://doi.org/10.1016/j.actaastro.2022.03.030.

[42] N. Johnson, P. Krisko, J.-C. Liou, and P. Anz-Meador. “NASA’s new breakup model of evolve 4.0”. In: *Advances in Space Research* 28.9 (2001), pp. 1377–1384. ISSN: 0273-1177. DOI: https://doi.org/10.1016/S0273-1177(01)00423-9.

[43] R. Reynolds, A. Bade, P. Eichlez, A. Jackson, P. Krisko, M. Matney, D. Kessler, and P. Anz-Meador. *NASA Standard Breakup Model 1998 Revision*. Tech. rep. Lockheed Martin Space Mission Systems and Services, 1998.

[44] N. Cimmino, G. Isoletta, R. Opromolla, G. Fasano, A. Basile, A. Romano, M. Peroni, A. Panico, and A. Cecchini. “Tuning of NASA Standard Breakup Model for Fragmentation Events Modelling”. In: *Aerospace* 8.7 (2021). ISSN: 2226-4310. DOI: 10.3390/aerospace8070185.

[45] J. Schuhmacher. “Efficient Implementation and Evaluation of the NASA Breakup Model in modern C++”. In: (2021).

[46] R. L. Andrisan, A. Ionita, R. D. González, N. S. Ortiz, F. P. Caballero, and H. Krag. “Fragmentation event model and assessment tool (fremat) supporting on-orbit fragmentation analysis”. In: *7th European Conference on Space Debris*. 2016.

[47] D. A. Vallado and D. L. Oltrogge. “Fragmentation event debris field evolution using 3D volumetric risk assessment”. In: *7th ECSD, Darmstadt* (2017).

[48] T. Hanada. “Developing a Low-Velocity Collision Model Based on the Nasa Standard Breakup Model”. In: *Space Debris* 2.4 (2000), pp. 233–247.

[49] S. Diserens, H. G. Lewis, and J. Fliege. “NewSpace and its implications for space debris models”. In: *Journal of Space Safety Engineering* 7.4 (2020), pp. 502–509. ISSN: 2468-8967. DOI: https://doi.org/10.1016/j.jsse.2020.07.027.

[50] J. Beck. *Review of Space Debris Population Prediction Methodologies and Results*. Tech. rep. Belstead Research Ltd, 2013.

[51] T. Wang. “Analysis of Debris from the Collision of the Cosmos 2251 and the Iridium 33 Satellites”. In: *Science & Global Security* 18.2 (2010), pp. 87–118. DOI: 10.1080/08929882.2010.493078.

[52] R. Jehn. “Dispersion of debris clouds from on-orbit fragmentation events”. In: *Dresden International Astronautical Federation Congress*. 1990.

[53] J. D. Slotten. “Examination of debris cloud density resulting from precession of argument of perigee due to J2 effect”. In: *7th European Conference on Space Debris*. 2017, p. 131.

[54] C. F. Gauss. “Exposition d’une nouvelle méthode de calculer les perturbations planétaires avec l’application au calcul numérique des perturbations du mouvement de Pallas”. In: *Hrsg. Gesellschaft der Wissenschaften zu Göttingen, K. von der Göttingen* 7 (1870), pp. 439–472.

[55] J. C. Bennett and J. Sang. “Modelling the evolution of the low-Earth orbit debris population”. In: *11th Australian Space Science Conference, Canberra, Australia*. Citeseer. 2011, pp. 165–178.

[56] H. G. Lewis. “Understanding long-term orbital debris population dynamics”. In: *Journal of Space Safety Engineering* 7.3 (2020). Space Debris: The State of Art, pp. 164–170. ISSN: 2468-8967. DOI: https://doi.org/10.1016/j.jsse.2020.06.006.

[57] A. Horstman et al. “Enhancement of s/c Fragmentation and Environment Evolution Models”. In: *Final Report, Contract N. 4000115973/15/D/SR, Institute of Space System, Technische Universität Braunschweig* 26.08 (2020).

[58] A. B. Vavrin, A. P. Manis, J. Seago, D. Gates, P. Anz-Meador, Y.-L. Xu, R. Barahona, A. Malachi, I. Bigger, M. J. Matney, et al. *NASA Orbital Debris Engineering Model ORDEM 3.1-Software User Guide*. Tech. rep. 2019.

[59] A. Horstmann, A. Manis, V. Braun, M. Matney, A. Vavrin, D. Gates, J. Seago, P. Anz-Meador, C. Wiedemann, and S. Lemmens. “Flux Comparison of MASTER-8 and ORDEM 3.1 Modelled Space Debris Population”. In: *8th European Conference on Space Debris*. 2021.

[60] J.-C. Liou, D. Hall, P. Krisko, and J. Opiela. “LEGEND – a three-dimensional LEO-to-GEO debris evolutionary model”. In: *Advances in Space Research* 34.5 (2004). Space Debris, pp. 981–986. ISSN: 0273-1177. DOI: https://doi.org/10.1016/j.asr.2003.02.027.

[61] D. Mehrholz, L. Leushacke, W. Flury, R. Jehn, H. Klinkrad, and M. Landgraf. “Detecting, tracking and imaging space debris”. In: *ESA Bulletin(0376-4265)* 109 (2002), pp. 128–134.

[62] G. Muntoni, G. Montisci, T. Pisanu, P. Andronico, and G. Valente. “Crowded Space: A Review on Radar Measurements for Space Debris Monitoring and Tracking”. In: *Applied Sciences* 11.4 (2021). ISSN: 2076-3417. DOI: 10.3390/app11041364.

[63] C. P. Mark and S. Kamath. “Review of Active Space Debris Removal Methods”. In: *Space Policy* 47 (2019), pp. 194–206. ISSN: 0265-9646. DOI: https://doi.org/10.1016/j.spacepol.2018.12.005.

[64] J. L. Rhatigan and W. Lan. “Drag-enhancing deorbit devices for spacecraft self-disposal: A review of progress and opportunities”. In: *Journal of Space Safety Engineering* 7.3 (2020). Space Debris: The State of Art, pp. 340–344. ISSN: 2468-8967. DOI: https://doi.org/10.1016/j.jsse.2020.07.026.

[65] K. P. Alsup, F. Anantachaisilp, J. L. Komma, K. B. Lobo, B. L. Lovdahl, J. R. Shapiro, J. L. Rhatigan, M. Romano, and J. Virgili-Llop. “Drag-Enhancing Deorbit Devices for Mid-Sized Spacecraft Self-Disposal”. In: *2019 IEEE Aerospace Conference*. 2019, pp. 1–16. DOI: 10.1109/AERO.2019.8741759.

[66] P. C. Roberts and P. G. Harkness. “Drag sail for end-of-life disposal from low earth orbit”. In: *Journal of Spacecraft and Rockets* 44.6 (2007), pp. 1195–1203.

[67] A. J. Petro. “Techniques for orbital debris control”. In: *Journal Of Spacecraft and Rockets* 29.2 (1992), pp. 260–263.

[68] K. Meyer and C. Chao. “Atmospheric reentry disposal for low-altitude spacecraft”. In: *Journal of Spacecraft and Rockets* 37.5 (2000), pp. 670–674.

[69] S. Campbell, C.-C. Chao, A. Gick, and M. Sorge. “Orbital stability and other considerations for US Government guidelines on post-mission disposal of space structures”. In: *Space Debris* 473 (2001), pp. 835–839.

[70] G. Bonin, J. Hiemstra, T. Sears, and R. Zee. “The CanX-7 drag sail demonstration mission: enabling environmental stewardship for nano-and microsatellites”. In: (2013).

[71] A. Viquerat, M. Schenk, B. Sanders, and V. Lappas. “Inflatable rigidisable mast for end-of-life deorbiting system”. In: *European conference on spacecraft structures, materials and environmental testing (SSMET)*. Vol. 2014. 2014, pp. 1–10.

[72] D. Zanutto et al. “Analysis of propellantless tethered system for the de-orbiting of satellites at end of life”. In: (2013).

[73] B. Hawe. *Analysis of Passive Attitude Stabilisation and Deorbiting of Satellites in Low Earth Orbit*. 2016.

[74] G. Sarego, L. Olivieri, A. Valmorbida, A. Brunello, E. C. Lorenzini, L. Tarabini Castellani, E. Urgoiti, A. Ortega, G. Borderes-Motta, and G. Sánchez-Arriaga. “Deployment requirements for deorbiting electrodynamic tether technology”. In: *CEAS Space Journal* 13.4 (2021), pp. 567–581.

[75] A. Valmorbida, L. Olivieri, A. Brunello, G. Sarego, G. Sánchez-Arriaga, and E. Lorenzini. “Validation of enabling technologies for deorbiting devices based on electrodynamic tethers”. In: *Acta Astronautica* 198 (2022), pp. 707–719. ISSN: 0094-5765. DOI: https://doi.org/10.1016/j.actaastro.2022.06.013.

[76] V. Morand, H. Fraysse, A. Lamy, C. Le Fevre, and R. Pinede. “End of life disposal of satellites in the GEO region, the issue of high inclinations”. In: *24th Internaional Symposium on Space Flight Dynamics*. 2014.

[77] R. Longstaff, M. Hempsell, and S. Alexandra. “Study into the sustainable disposal of end of life GEO satellites”. In: *J. Br. Interplanet. Soc* 69 (2016), pp. 429–438.

[78] E. Cabot Costa. “Study of end-of-life disposal options for highly-inclined geosynchronous satellites”. B.S. thesis. Universitat Politècnica de Catalunya, 2016.

[79] M. Hu, Y. Ruan, H. Zhou, J. Xu, and W. Xue. “Long-Term Orbit Prediction and Deorbit Disposal Investigation of MEO Navigation Satellites”. In: *Aerospace* 9.5 (2022), p. 266.

[80] A. Rossi, L. Anselmo, C. Pardini, and R. Jehn. “Effectiveness of the de-orbiting practices in the MEO region”. In: *Proceedings of the Fifth European Conference on Space Debris, ESA SP-672, CD-ROM, ESA Communication Production Office, Noordwijk, The Netherlands*. 2009.

[81] R. Dominguez-Gonzalez, J. Radtke, N. Sánchez-Ortiz, and K. Merz. “Long-Term Implications of GNSS Disposal Strategies for the Space Debris Environment”. In: *Proceedings of the 7th European Conference on Space Debris, Darmstadt, Germany*. 2017, pp. 18–21.

[82] F. Letizia, S. Sanvido, S. Lemmens, K. Merz, R. Southworth, and B. Sousa. “ESA’s current approaches to end-of-life strategies for HEO missions”. In: *Journal of Space Safety Engineering* 10.4 (2023), pp. 407–413. ISSN: 2468-8967. DOI: https://doi.org/10.1016/j.jsse.2023.08.004.

[83] C. Colombo, E. M. Alessi, W. van der Weg, S. Soldini, F. Letizia, M. Vetrisano, M. Vasile, A. Rossi, and M. Landgraf. “End-of-life disposal concepts for Libration Point Orbit and Highly Elliptical Orbit missions”. In: *Acta Astronautica* 110 (2015). Dynamics and Control of Space Systems, pp. 298–312. ISSN: 0094-5765. DOI: https://doi.org/10.1016/j.actaastro.2014.11.002.

[84] I. Newton. *Philosophiae Naturalis Principia Mathematica*. 1687. DOI: 10.3931/e-rara-440.

[85] R. H. Goddard. *R. H. Goddard: An Autobiography*. Vol. 4. Robert H. Goddard Notebook dated September 6, 1906. Publisher, 1959.

[86] E. Stuhlinger. *Ion propulsion for space flight*. McGraw-Hill New York, 1964.

[87] E. Stuhlinger. “Electric space propulsion systems”. In: *Space Science Reviews* 7.5-6 (1967), pp. 795–847.

[88] L. Garrigues and P. Coche. “Electric propulsion: comparisons between different concepts”. In: *Plasma Physics and Controlled Fusion* 53.12 (2011), p. 124011. DOI: 10.1088/0741-3335/53/12/124011.

[89] D. Lev, R. M. Myers, K. M. Lemmer, J. Kolbeck, H. Koizumi, and K. Polzin. “The technological and commercial expansion of electric propulsion”. In: *Acta Astronautica* 159 (2019), pp. 213–227. ISSN: 0094-5765. DOI: https://doi.org/10.1016/j.actaastro.2019.03.058.

[90] D. A. Spencer, L. Johnson, and A. C. Long. “Solar sailing technology challenges”. In: *Aerospace Science and Technology* 93 (2019), p. 105276. ISSN: 1270-9638. DOI: https://doi.org/10.1016/j.ast.2019.07.009.

[91] C. R. McInnes. *Solar sailing: technology, dynamics and mission applications*. Springer Science & Business Media, 2004.

[92] S. Gong and M. Macdonald. “Review on solar sail technology”. In: *Astrodynamics* 3.2 (2019), pp. 93–125. DOI: 10.1007/s42064-019-0038-x.

[93] R. Broucke. “The celestial mechanics of gravity assist”. In: *Astrodynamics Conference*. 1988, p. 4220.

[94] M. M. Munk and S. A. Moon. “Aerocapture Technology Development Overview”. In: *2008 IEEE Aerospace Conference*. 2008, pp. 1–7. DOI: 10.1109/AERO.2008.4526545.

[95] J. L. Prince, R. W. Powell, and D. Murri. “Autonomous aerobraking: A design, development, and feasibility study”. In: *2011 AAS/AIAA Astrodynamics Specialist Conference*. NF1676L-12519. 2011.

[96] P. Janhunen. “Electric Sail for Spacecraft Propulsion”. In: *Journal of Propulsion and Power* 20.4 (2004), pp. 763–764. DOI: 10.2514/1.8580.

[97] R. M. Zubrin and D. G. Andrews. “Magnetic sails and interplanetary travel”. In: *Journal of Spacecraft and Rockets* 28.2 (1991), pp. 197–203. DOI: 10.2514/3.26230.

[98] J. Kepler. *Ioannis Kepleri mathematici Cæsarei Dissertatio cum Nuncio sidereo: nuper ad mortales misso à Galilæo Galilæo mathematico Patavino*. H.F. Schulz in Kommission, 1610.

[99] B. Fu, E. Sperber, and F. Eke. “Solar sail technology—A state of the art review”. In: *Progress in Aerospace Sciences* 86 (2016), pp. 1–19. ISSN: 0376-0421. DOI: https://doi.org/10.1016/j.paerosci.2016.07.001.

[100] J. C. Maxwell. *A treatise on electricity and magnetism*. Vol. 1. Clarendon press, 1873.

[101] P. Lebedew. “The physical causes of the deviations from Newton’s law of gravitation”. In: *Astrophysical Journal, vol. 16, p. 155* 16 (1902), p. 155.

[102] E. F. Nichols and G. F. Hull. “The pressure due to radiation”. In: *Proceedings of the American Academy of Arts and Sciences*. Vol. 38. 20. JSTOR. 1903, pp. 559–599.

[103] K. E. Tsiolkovsky. “Extension of man into outer space”. In: *Proceedings of the Symposium on Jet Propulsion*. Vol. 2. 1921.

[104] F. A. Tsander. *From a scientific heritage*. Vol. 540. National Aeronautics and Space Administration, for sale by the Clearinghouse …, 1969.

[105] C. Wiley. “Clipper ships of space”. In: *Astounding Science Fiction* 5 (1951), p. 135.

[106] R. L. Garwin. *Solar sailing-a practical method of propulsion within the solar system*. 1958.

[107] P. E. Zadunaisky, I. I. Shapiro, and H. M. Jones. “Experimental and theoretical results on the orbit of Echo 1”. In: *SAO Special Report# 61 (1961)* 61 (1961).

[108] C. R. McInnes. “Space-based geoengineering: Challenges and requirements”. In: *Proceedings of the Institution of Mechanical Engineers, Part C: Journal of Mechanical Engineering Science* 224.3 (2010), pp. 571–580. DOI: 10.1243/09544062JMES1439.

[109] M. Macdonald, C. McInnes, and G. Hughes. “Technology Requirements of Exploration Beyond Neptune by Solar Sail Propulsion”. In: *Journal of Spacecraft and Rockets* 47.3 (2010), pp. 472–483. DOI: 10.2514/1.46657.

[110] M. Macdonald and C. McInnes. “Solar sail science mission applications and advancement”. In: *Advances in Space Research* 48.11 (2011). SOLAR SAILING: CONCEPTS, TECHNOLOGY, AND MISSIONS, pp. 1702–1716. ISSN: 0273-1177. DOI: https://doi.org/10.1016/j.asr.2011.03.018.

[111] M. Shan, J. Guo, and E. Gill. “Review and comparison of active space debris capturing and removal methods”. In: *Progress in Aerospace Sciences* 80 (2016), pp. 18–32. ISSN: 0376-0421. DOI: https://doi.org/10.1016/j.paerosci.2015.11.001.

[112] J. A. Borja and D. Tun. “Deorbit Process Using Solar Radiation Force”. In: *Journal of Spacecraft and Rockets* 43.3 (2006), pp. 685–687. DOI: 10.2514/1.9508.

[113] C. Lücking, C. Colombo, and C. McInnes. “A passive de-orbiting strategy for high altitude CubeSat missions using a deployable reflective balloon”. In: *8th IAA symposium on small satellites*. 2011.

[114] P. Zhao, C. Wu, and Y. Li. “Design and application of solar sailing: A review on key technologies”. In: *Chinese Journal of Aeronautics* 36.5 (2023), pp. 125–144. ISSN: 1000-9361. DOI: https://doi.org/10.1016/j.cja.2022.11.002.

[115] J. L. Wright. *Space sailing*. Taylor & Francis, 1992.

[116] Y. Tsuda, O. Mori, R. Funase, H. Sawada, T. Yamamoto, T. Saiki, T. Endo, K. Yonekura, H. Hoshino, and J. Kawaguchi. “Achievement of IKAROS — Japanese deep space solar sail demonstration mission”. In: *Acta Astronautica* 82.2 (2013). 7th IAA Symposium on Realistic Advanced Scientific Space MissionsAosta, Italy, July 2011, pp. 183–188. ISSN: 0094-5765. DOI: https://doi.org/10.1016/j.actaastro.2012.03.032.

[117] D. A. Spencer, B. Betts, J. M. Bellardo, A. Diaz, B. Plante, and J. R. Mansell. “The LightSail 2 solar sailing technology demonstration”. In: *Advances in Space Research* 67.9 (2021). Solar Sailing: Concepts, Technology, and Missions II, pp. 2878–2889. ISSN: 0273-1177. DOI: https://doi.org/10.1016/j.asr.2020.06.029.

[118] W. K. Wilkie. “Overview of the NASA advanced composite solar sail system (acs3) technology demonstration project”. In: *AIAA Scitech 2021 Forum*. 2021, p. 1260.

[119] J. M. Longuski, R. E. Todd, and W. W. Konig. “Survey of nongravitational forces and space environmental torques-Applied to the Galileo”. In: *Journal of guidance, control, and dynamics* 15.3 (1992), pp. 545–553.

[120] A. Capannolo, E. Paolini, A. Colagrossi, V. Pesce, and S. Silvestrini. “Chapter Three - The space environment”. In: *Modern Spacecraft Guidance, Navigation, and Control*. Ed. by V. Pesce, A. Colagrossi, and S. Silvestrini. Elsevier, 2023, pp. 77–129. ISBN: 978-0-323-90916-7. DOI: https://doi.org/10.1016/B978-0-323-90916-7.00003-2.

[121] M. Macdonald. *Advances in solar sailing*. Springer Science & Business Media, 2014.

[122] L. Carzanaa, P. Vissera, and J. Heiligersa. “A New Model for the Planetary Radiation Pressure Acceleration for Optical Solar Sails”. In: *6th International Symposium on Space Sailing*. 2023.

[123] L. Carzana, P. Visser, and J. Heiligers. “Locally optimal control laws for Earth-bound solar sailing with atmospheric drag”. In: *Aerospace Science and Technology* 127 (2022), p. 107666. ISSN: 1270-9638. DOI: https://doi.org/10.1016/j.ast.2022.107666.

[124] A. Einstein. “Does the inertia of a body depend upon its energy-content”. In: *Annalen der physik* 18.13 (1905), pp. 639–641.

[125] A. P. French. *Special relativity*. CRC Press, 2017.

[126] V. Koblik, E. Polyakhova, and L. Sokolov. “Solar sail near the Sun: Point-like and extended models of radiation source”. In: *Advances in Space Research* 48.11 (2011). SOLAR SAILING: CONCEPTS, TECHNOLOGY, AND MISSIONS, pp. 1717–1739. ISSN: 0273-1177. DOI: https://doi.org/10.1016/j.asr.2011.04.024.

[127] R. Forward. “Grey solar sails”. In: *25th Joint Propulsion Conference*. 1989, p. 2343.

[128] J. J. Lissauer and I. De Pater. *Fundamental planetary science: physics, chemistry and habitability*. Cambridge University Press, 2013.

[129] L. Wald. *Basics in solar radiation at Earth surface*. 2018. URL: https://minesparis-psl.hal.science/hal-01676634.

[130] A. M. Markhoos. “Solar sailing near the Sun: A comparison study between point-like and spherical-like Sun models”. In: *Acta Astronautica* 173 (2020), pp. 9–18. ISSN: 0094-5765. DOI: https://doi.org/10.1016/j.actaastro.2020.01.040.

[131] L. I. Zardaín Rodríguez. “Developing an efficient algorithm for computing Solar Radiation Pressure”. MA thesis. Universitat Politècnica de Catalunya, 2019.

[132] J. W. McMahon and D. J. Scheeres. “Improving Space Object Catalog Maintenance Through Advances in Solar Radiation Pressure Modeling”. In: *Journal of Guidance, Control, and Dynamics* 38.8 (2015), pp. 1366–1381. DOI: 10.2514/1.G000666.

[133] D. M. Lucchesi. “Reassessment of the error modelling of non-gravitational perturbations on LAGEOS II and their impact in the Lense–Thirring determination. Part I”. In: *Planetary and Space Science* 49.5 (2001), pp. 447–463. ISSN: 0032-0633. DOI: https://doi.org/10.1016/S0032-0633(00)00168-9.

[134] Z. Jin and W. Tianshu. “Coupled Attitude-Orbit Control of Flexible Solar Sail for Displaced Solar Orbit”. In: *Journal of Spacecraft and Rockets* 50.3 (2013), pp. 675–685. DOI: 10.2514/1.A32369.

[135] A. Farrés and À. Jorba. “Station keeping of a solar sail around a Halo orbit”. In: *Acta Astronautica* 94.1 (2014), pp. 527–539. ISSN: 0094-5765. DOI: https://doi.org/10.1016/j.actaastro.2012.07.002.

[136] G. Aliasi, G. Mengali, and A. A. Quarta. “Artificial equilibrium points for a solar balloon in the α Centauri system”. In: *Acta Astronautica* 104.2 (2014). Future of Space Exploration: Towards the Stars, pp. 464–471. ISSN: 0094-5765. DOI: https://doi.org/10.1016/j.actaastro.2014.03.006.

[137] K. Parsay and H. Schaub. “Designing solar sail formations in sun-synchronous orbits for geomagnetic tail exploration”. In: *Acta Astronautica* 107 (2015), pp. 218–233. ISSN: 0094-5765. DOI: https://doi.org/10.1016/j.actaastro.2014.11.018.

[138] B. Dachwald. “Optimal Solar Sail Trajectories for Missions to the Outer Solar System”. In: *Journal of Guidance, Control, and Dynamics* 28.6 (2005), pp. 1187–1193. DOI: 10.2514/1.13301.

[139] B. Dachwald and B. Wie. “Solar Sail Trajectory Optimization for Intercepting, Impacting, and Deflecting Near-Earth Asteroids”. In: *AIAA Guidance, Navigation, and Control Conference and Exhibit*. 5. DOI: 10.2514/6.2005-6176.

[140] B. Dachwald and W. Seboldt. “Multiple near-Earth asteroid rendezvous and sample return using first generation solar sailcraft”. In: *Acta Astronautica* 57.11 (2005), pp. 864–875. ISSN: 0094-5765. DOI: https://doi.org/10.1016/j.actaastro.2005.04.012.

[141] G. Mengali and A. A. Quarta. “In-orbit repositioning of multiple solar sail spacecraft”. In: *Aerospace Science and Technology* 12.7 (2008), pp. 506–514. ISSN: 1270-9638. DOI: https://doi.org/10.1016/j.ast.2007.12.003.

[142] V. Lappas, G. Mengali, A. A. Quarta, J. Gil-Fernandez, T. Schmidt, and B. Wie. “Practical Systems Design for an Earth-Magnetotail-Monitoring Solar Sail Mission”. In: *Journal of Spacecraft and Rockets* 46.2 (2009), pp. 381–393. DOI: 10.2514/1.32040.

[143] K. Wilkie and J. Fernandez. “Advanced Composite Solar Sail System (ACS3) Mission Update”. In: *The 6th International Symposium on Space Sailing*. 2023.

[144] L. Rios-Reyes and D. J. Scheeres. “Generalized Model for Solar Sails”. In: *Journal of Spacecraft and Rockets* 42.1 (2005), pp. 182–185. DOI: 10.2514/1.9054.

[145] L. Rios-Reyes and D. J. Scheeres. “Solar-Sail Navigation: Estimation of Force, Moments, and Optical Parameters”. In: *Journal of Guidance, Control, and Dynamics* 30.3 (2007), pp. 660–668. DOI: 10.2514/1.24340.

[146] T. Yamaguchi, Y. Mimasu, Y. Tsuda, R. Funase, H. Sawada, O. Mori, M. Y. Morimoto, H. Takeuchi, and M. Yoshikawa. “Trajectory Analysis of Solar Sail Spacecraft Considering the Large Uncertainty of Solar Radiation Pressure”. In: 2009.

[147] L. Rios-Reyes and D. Scheeres. “Applications of the Generalized Model for a Solar Sail”. In: *AIAA Guidance, Navigation, and Control Conference and Exhibit*. 2004, p. 5434.

[148] D. Scheeres. “The dynamical evolution of uniformly rotating asteroids subject to YORP”. In: *Icarus* 188.2 (2007), pp. 430–450. ISSN: 0019-1035. DOI: https://doi.org/10.1016/j.icarus.2006.12.015.

[149] Y. Tsuda, T. Saiki, R. Funase, and Y. Mimasu. “Generalized Attitude Model for Spinning Solar Sail Spacecraft”. In: *Journal of Guidance, Control, and Dynamics* 36.4 (2013), pp. 967–974. DOI: 10.2514/1.59516.

[150] A. Heaton, N. Ahmad, and K. Miller. “Near earth asteroid scout solar sail thrust and torque model”. In: *International Symposium on Solar Sailing (ISSS 2017)*. M16-5470. 2017.

[151] S. Kikuchi, Y. Tsuda, and J. Kawaguchi. “Orbit-Attitude Coupled Dynamics of Solar Sail Spacecraft around Small Bodies”. In: (2017).

[152] G. Mengali, A. A. Quarta, C. Circi, and B. Dachwald. “Refined solar sail force model with mission application”. In: *Journal of Guidance, Control, and Dynamics* 30.2 (2007), pp. 512–520.

[153] G. Vulpetti and S. Scaglione. “The Aurora project: Estimation of the optical sail parameters”. In: *Acta Astronautica* 44.2 (1999). Missions to the Outer Solar System and Beyond, pp. 123–132. ISSN: 0094-5765. DOI: https://doi.org/10.1016/S0094-5765(99)00038-7.

[154] B. Dachwald, G. Mengali, A. A. Quarta, and M. Macdonald. “Parametric Model and Optimal Control of Solar Sails with Optical Degradation”. In: *Journal of Guidance, Control, and Dynamics* 29.5 (2006), pp. 1170–1178. DOI: 10.2514/1.20313.

[155] C. R. McInnes. “Approximate Closed-Form Solution for Solar Sail Spiral Trajectories with Sail Degradation”. In: *Journal of Guidance, Control, and Dynamics* 37.6 (2014), pp. 2053–2057. DOI: 10.2514/1.G000225.

[156] B. Dachwald, M. Macdonald, C. R. McInnes, G. Mengali, and A. A. Quarta. “Impact of optical degradation on solar sail mission performance”. In: *Journal of Spacecraft and Rockets* 44.4 (2007), pp. 740–749.

[157] J. He, S. Gong, and J. Li. “A curved surface solar radiation pressure force model for solar sail deformation”. In: *Science China Physics, Mechanics and Astronomy* 55.1 (2012), pp. 141–155.

[158] T. Ingrassia, V. Faccin, A. Bolle, C. Circi, and S. Sgubini. “Solar sail elastic displacement effects on interplanetary trajectories”. In: *Acta Astronautica* 82.2 (2013). 7th IAA Symposium on Realistic Advanced Scientific Space MissionsAosta, Italy, July 2011, pp. 263–272. ISSN: 0094-5765. DOI: https://doi.org/10.1016/j.actaastro.2012.11.015.

[159] J. Zou, D. Li, and J. Wang. “High-precision numerical calculation method of solar radiation pressure force for wrinkled solar sails”. In: *Proceedings of the Institution of Mechanical Engineers, Part G: Journal of Aerospace Engineering* 236.12 (2022), pp. 2463–2471. DOI: 10.1177/09544100211063681.

[160] R. Y. Kezerashvili and J. F. Vázquez-Poritz. “Effect of a drag force due to absorption of solar radiation on solar sail orbital dynamics”. In: *Acta Astronautica* 84 (2013), pp. 206–214. ISSN: 0094-5765. DOI: https://doi.org/10.1016/j.actaastro.2012.11.005.

[161] B. Wie. “Solar Sail Attitude Control and Dynamics, Part 1”. In: *Journal of Guidance, Control, and Dynamics* 27.4 (2004), pp. 526–535. DOI: 10.2514/1.11134.

[162] E. Sperber. *Attitude Dynamics and Control of Solar Sails*. University of California, Davis, 2014.

[163] L. Boni, A. Quarta, and G. Mengali. “Thermal-structural analysis of a square solar sail”. In: *Acta Astronautica* 154 (2018). DOI: 10.1016/j.actaastro.2018.03.037.

[164] J. Heiligers, D. Guerrant, and D. Lawrence. “Exploring the Heliogyro’s Orbital Control Capabilities for Solar Sail Halo Orbits”. In: *Journal of Guidance, Control, and Dynamics* 40.10 (2017), pp. 2569–2586. DOI: 10.2514/1.G002184.

[165] W. K. Wilkie, J. E. Warren, L. G. Horta, K. H. Lyle, J.-N. Juang, J. D. Littell, R. G. Bryant, M. W. Thomson, P. E. Walkemeyer, D. V. Guerrant, et al. “Heliogyro solar sail research at NASA”. In: *Advances in Solar Sailing* (2014), pp. 631–650.

[166] R. H. MacNeal. *The heliogyro-an interplanetary flying machine*. Tech. rep. 1967.

[167] L. Friedman. *Solar Sailing Development Program (FY 1977) Final Report Vol I*. 1978.

[168] D. Guerrant and D. Lawrence. “Tactics for Heliogyro solar sail attitude control via blade pitching”. In: *Journal of Guidance, Control, and Dynamics* 38.9 (2015), pp. 1785–1799.

[169] J. Kang and K.-C. Park. “Computational multibody dynamics of heliogyro solar sail under spin-deployment”. In: *AIAA Scitech 2020 Forum*. 2020, p. 2164.

[170] J. Kang and K.-C. Park. “Flexible heliogyro solar sail under solar radiation pressure and gravitational force”. In: *Acta Astronautica* 179 (2021), pp. 186–196.

[171] Y. Tsuda. “On-orbit sail quality evaluation utilizing attitude dynamics of spinner solar sailer IKAROS”. In: *Utilizing Attitude Dynamics of Spinner Solar Sailer IKAROS, 22nd AAS/AIAA Space Flight Mechanics Meeting Charleston. USA 2012*. 2012.

[172] C. R. McInnes. “Solar sail mission applications for non-Keplerian orbits”. In: *Acta Astronautica* 45.4 (1999). Third IAA International Conference on Low-Cost Planetary Missions, pp. 567–575. ISSN: 0094-5765. DOI: https://doi.org/10.1016/S0094-5765(99)00177-0.

[173] J. R. Mansell, J. M. Bellardo, B. Betts, B. Plante, and D. A. Spencer. “LightSail 2 Solar Sail Control and Orbit Evolution”. In: *Aerospace* 10.7 (2023). ISSN: 2226-4310. DOI: 10.3390/aerospace10070579.

[174] E. Sperber, B. Fu, and F. O. Eke. “Large Angle Reorientation of a Solar Sail Using Gimballed Mass Control”. In: *The Journal of the Astronautical Sciences* 63.2 (2016), pp. 103–123.

[175] D. Mangus and A. Heaton. “Solar Sail Control Actuator Concepts”. In: *Solar Sail Technology and Applications Conference*. 2004.

[176] D. Romagnoli and T. Oehlschlägel. “High performance two degrees of freedom attitude control for solar sails”. In: *Advances in Space Research* 48.11 (2011). SOLAR SAILING: CONCEPTS, TECHNOLOGY, AND MISSIONS, pp. 1869–1879. ISSN: 0273-1177. DOI: https://doi.org/10.1016/j.asr.2011.04.027.

[177] B. Wie and D. Murphy. “Solar-sail attitude control design for a flight validation mission”. In: *Journal of Spacecraft and Rockets* 44.4 (2007), pp. 809–821.

[178] A. Bolle and C. Circi. “Solar sail attitude control through in-plane moving masses”. In: *Proceedings of the Institution of Mechanical Engineers, Part G: Journal of Aerospace Engineering* 222.1 (2008), pp. 81–94. DOI: 10.1243/09544100JAERO223.

[179] B. Wie. “Solar Sail Attitude Control and Dynamics, Part Two”. In: *Journal of Guidance, Control, and Dynamics* 27.4 (2004), pp. 536–544. DOI: 10.2514/1.11133.

[180] D. M. Murphy, T. W. Murphey, and P. A. Gierow. “Scalable Solar-Sail Subsystem Design Concept”. In: *Journal of Spacecraft and Rockets* 40.4 (2003), pp. 539–547. DOI: 10.2514/2.3975.

[181] M. Choi and C. J. Damaren. “Structural Dynamics and Attitude Control of a Solar Sail Using Tip Vanes”. In: *Journal of Spacecraft and Rockets* 52.6 (2015), pp. 1665–1679. DOI: 10.2514/1.A33179.

[182] Z. Kun. “Control Capability and Allocation of Solar Sail Tip Vanes over Bounded Movement”. In: *Journal of Guidance, Control, and Dynamics* 38.7 (2015), pp. 1340–1344. DOI: 10.2514/1.G000938.

[183] M. B. Quadrelli and J. West. “Sensitivity studies of the deployment of a square inflatable solar sail with vanes”. In: *Acta Astronautica* 65.7 (2009), pp. 1007–1027. ISSN: 0094-5765. DOI: https://doi.org/10.1016/j.actaastro.2009.03.015.

[184] R. Funase, Y. Shirasawa, Y. Mimasu, O. Mori, Y. Tsuda, T. Saiki, and J. Kawaguchi. “On-orbit verification of fuel-free attitude control system for spinning solar sail utilizing solar radiation pressure”. In: *Advances in Space Research* 48.11 (2011). SOLAR SAILING: CONCEPTS, TECHNOLOGY, AND MISSIONS, pp. 1740–1746. ISSN: 0273-1177. DOI: https://doi.org/10.1016/j.asr.2011.02.022.

[185] A. Borggräfe, J. Heiligers, M. Ceriotti, and C. McInnes. “Optical control of solar sails using distributed reflectivity”. In: *Spacecraft Structures Conference*. 2014, p. 0833.

[186] J. M. Fernandez. “Low-cost gossamer systems for solar sailing & spacecraft deorbiting applications”. In: *University of Surrey* (2014).

[187] B. Fu and F. O. Eke. “Attitude Control Methodology for Large Solar Sails”. In: *Journal of Guidance, Control, and Dynamics* 38.4 (2015), pp. 662–670. DOI: 10.2514/1.G000048.

[188] B. Fu and F. Eke. “Further investigation of the body torques on a square solar sail due to the displacement of the sail attachment points”. In: *Aerospace Science and Technology* 50 (2016), pp. 281–294. ISSN: 1270-9638. DOI: https://doi.org/10.1016/j.ast.2016.01.007.

[189] B. Fu, G. Gede, and F. O. Eke. “Controllability of a square solar sail with movable membrane tips”. In: *Proceedings of the Institution of Mechanical Engineers, Part G: Journal of Aerospace Engineering* 231.6 (2017), pp. 1065–1075. DOI: 10.1177/0954410016647533.

[190] R. S. Blomquist. *Heliogyro control*. Carnegie Mellon University, 2009.

[191] W. K. Wilkie, J. Warren, L. G. Horta, K. H. Lyle, J.-N. Juang, S. C. Gibbs, E. Dowell, D. V. Guerrant, and D. A. Lawrence. “Recent advances in heliogyro solar sail structural dynamics, stability, and control research”. In: *2nd AIAA Spacecraft Structures Conference*. 2015, p. 0431.

[192] A. R. Pimienta-Penalver. “Attitude Dynamics, Stability, and Control of a Heliogyro Solar Sail”. PhD thesis. State University of New York at Buffalo, 2017.

[193] D. Guerrant and D. Lawrence. “Tactics for Heliogyro Solar Sail Attitude Control via Blade Pitching”. In: *Journal of Guidance, Control, and Dynamics* 38.9 (2015), pp. 1785–1799. DOI: 10.2514/1.G000861.

[194] X. Hu, S. Gong, and J. Li. “Attitude stability criteria of axisymmetric solar sail”. In: *Advances in Space Research* 54.1 (2014), pp. 72–81. ISSN: 0273-1177. DOI: https://doi.org/10.1016/j.asr.2014.03.008.

[195] D. A. Lawrence and M. S. Whorton. “Solar Sail Dynamics and Coning Control in Circular Orbits”. In: *Journal of Guidance, Control, and Dynamics* 32.3 (2009), pp. 974–985. DOI: 10.2514/1.35970.

[196] S. Gong, J. Li, and K. Zhu. “Dynamical analysis of a spinning solar sail”. In: *Advances in Space Research* 48.11 (2011). SOLAR SAILING: CONCEPTS, TECHNOLOGY, AND MISSIONS, pp. 1797–1809. ISSN: 0273-1177. DOI: https://doi.org/10.1016/j.asr.2011.06.012.

[197] B. Wie, D. Murphy, M. Paluszek, and S. Thomas. “Robust Attitude Control Systems Design for Solar Sails (Part 2): MicroPPT-based Backup ACS”. In: *AIAA Guidance, Navigation, and Control Conference and Exhibit*. 2004, p. 5011.

[198] S. Gong and J. Li. “Fuel consumption for interplanetary missions of solar sailing”. In: *Science China Physics, Mechanics and Astronomy* 57.3 (2014), pp. 521–531.

[199] B. Wie, D. Murphy, M. Paluszek, and S. Thomas. “Robust attitude control systems design for solar sails (Part 1): propellantless primary ACS”. In: *AIAA Guidance, Navigation, and Control Conference and Exhibit*. 2004, p. 5010.

[200] N. Adeli, T. Theodorou, and V. Lappas. “Ground demonstration of a solar sail attitude control actuator”. In: *AIAA Guidance, Navigation, and Control Conference*. 2010, p. 8071.

[201] M. Macdonald and C. R. McInnes. “Analytical control laws for planet-centered solar sailing”. In: *Journal of Guidance, Control, and Dynamics* 28.5 (2005), pp. 1038–1048.

[202] C. R. McInnes, M. Macdonald, V. Angelopolous, and D. Alexander. “GEOSAIL: Exploring the Geomagnetic Tail Using a Small Solar Sail”. In: *Journal of Spacecraft and Rockets* 38.4 (2001), pp. 622–629. DOI: 10.2514/2.3727.

[203] V. L. Coverstone and J. E. Prussing. “Technique for escape from geosynchronous transfer orbit using a solar sail”. In: *Journal of Guidance, Control, and Dynamics* 26.4 (2003), pp. 628–634.

[204] M. Macdonald and C. R. McInnes. “Realistic earth escape strategies for solar sailing”. In: *Journal of Guidance, Control, and Dynamics* 28.2 (2005), pp. 315–323.

[205] M. Leipold. “Solar Sail Mission Design”. PhD thesis. DLR Deutsches Zentrum fuer Luft- und Raumfahrt e.V., Koeln (Germany). Inst. fuer Weltraumsensorik und Plantetenerkundung; Technische Univ. Muenchen (Germany). Fakultaet fuer Maschinenwesen, 2000.

[206] R. J. McKay, M. Macdonald, J. Biggs, and C. McInnes. “Survey of Highly Non-Keplerian Orbits with Low-Thrust Propulsion”. In: *Journal of Guidance, Control, and Dynamics* 34.3 (2011), pp. 645–666. DOI: 10.2514/1.52133.

[207] C. R. McInnes. “Dynamics, Stability, and Control of Displaced Non-Keplerian Orbits”. In: *Journal of Guidance, Control, and Dynamics* 21.5 (1998), pp. 799–805. DOI: 10.2514/2.4309.

[208] C. R. McInnes and J. F. L. Simmons. “Solar sail halo orbits. Part I - Heliocentric case.” In: *Journal of Spacecraft and Rockets* 29.4 (1992), pp. 466–471. DOI: 10.2514/3.25487.

[209] C. R. McInnes and J. F. L. Simmons. “Solar Sail Halo Orbits Part II - Geocentric Case”. In: *Journal of Spacecraft and Rockets* 29.4 (1992), pp. 472–479. DOI: 10.2514/3.55639.

[210] A. De Iuliis, F. Ciampa, L. Felicetti, and M. Ceriotti. “Sailing with solar and planetary radiation pressure”. In: *Advances in Space Research* 67.9 (2021). Solar Sailing: Concepts, Technology, and Missions II, pp. 2795–2811. ISSN: 0273-1177. DOI: https://doi.org/10.1016/j.asr.2019.11.036.

[211] A. Barles, M. Ceriotti, F. Ciampa, and L. Felicetti. “An optimal steering law for sailing with solar and planetary radiation pressure”. In: *Aerospace Science and Technology* 118 (2021), p. 107051. ISSN: 1270-9638. DOI: https://doi.org/10.1016/j.ast.2021.107051.

[212] G. Mengali and A. A. Quarta. “Near-Optimal Solar-Sail Orbit-Raising from Low Earth Orbit”. In: *Journal of Spacecraft and Rockets* 42.5 (2005), pp. 954–958. DOI: 10.2514/1.14184.

[213] V. Stolbunov, M. Ceriotti, C. Colombo, and C. R. McInnes. “Optimal Law for Inclination Change in an Atmosphere Through Solar Sailing”. In: *Journal of Guidance, Control, and Dynamics* 36.5 (2013), pp. 1310–1323. DOI: 10.2514/1.59931.

[214] G. Leemans, L. Carzana, and J. Heiligers. “Many-revolution Earth-centred solar-sail trajectory optimisation using differential dynamic programming”. In: *AIAA SCITECH 2022 Forum*. 2022, p. 1776.

[215] S. Gong, H. Baoyin, and J. Li. “Solar sail three-body transfer trajectory design”. In: *Journal of guidance, control, and dynamics* 33.3 (2010), pp. 873–886.

[216] X. Zeng, G. Vulpetti, and C. Circi. “Solar sail H-reversal trajectory: A review of its advances and applications”. In: *Astrodynamics* 3.1 (2019), pp. 1–15.

[217] B. Dachwald. “Optimization of interplanetary solar sailcraft trajectories using evolutionary neurocontrol”. In: *Journal of Guidance, Control, and Dynamics* 27.1 (2004), pp. 66–72.

[218] L. B. Sagnières and I. Sharf. “Evolution of Spacecraft Orbital Motion due to Hypervelocity Impacts with Debris and Meteoroids”. In: *Proceedings of the 7th European Conference on Space Debris, ESA Space Debris Office, Darmstadt, Germany*. 2017.

[219] J. McDonnell. “Momentum enhancement in hypervelocity impacts: Parameters for space debris and meteoroid perturbations”. In: *Proceedings of the Fifth Cranfield Conference on Dynamics and Control of Systems and Structures in Space*. Citeseer. 2002, pp. 1–10.

[220] A.-M. Lanouette. *Évaluation de l’effet structurel de l’impact d’un micrométéorite ou d’un débris orbital sur le bras canadien 2*. 2014.

[221] C. Ryan. *Momentum Transfer due to Hypervelocity Impacts into Spacecraft Solar Arrays*. 2021.

[222] J. McDonnell. “Factors affecting the choice of foils for penetration experiments in space”. In: *Space Research* 10 (1970), pp. 314–325.

[223] M. Lambert. “Hypervelocity impacts and damage laws”. In: *Advances in Space Research* 19.2 (1997), pp. 369–378.

[224] D. L. Edwards, C. Semmel, M. A. Hovater, M. Nehls, P. A. Gray, W. S. Hubbs, and G. Wertz. “Solar sail material performance property response to space environmental effects”. In: *Photonics for Space Environments IX*. Ed. by E. W. Taylor. Vol. 5554. International Society for Optics and Photonics. SPIE, 2004, pp. 80–91. DOI: 10.1117/12.562809.

[225] J. Murakami, T. Hanada, J. Liou, and E. Stansbery. “Micro-satellite impact tests to investigate multi-layer insulation fragments”. In: *Orbital Debris Quarterly News* 13.2 (2009).

[226] E. Grün, B. A. Gustafson, S. Dermott, and H. Fechtig. *Interplanetary dust*. Springer Science & Business Media, 2012.

[227] M. Rival and J. C. Mandeville. “Modeling of Ejecta Produced upon Hypervelocity Impacts”. In: *Space Debris* 1.1 (1999), pp. 45–57.

[228] G. Drolshagen. “Impact effects from small size meteoroids and space debris”. In: *Advances in Space Research* 41.7 (2008), pp. 1123–1131. ISSN: 0273-1177. DOI: https://doi.org/10.1016/j.asr.2007.09.007.

[229] G. Drolshagen. “Hypervelocity impact effects on spacecraft”. In: *Meteoroids 2001 Conference*. Vol. 495. 2001, pp. 533–541.

[230] L. B. Sagnières and I. Sharf. “Stochastic modeling of hypervelocity impacts in attitude propagation of space debris”. In: *Advances in Space Research* 59.4 (2017), pp. 1128–1143. ISSN: 0273-1177. DOI: https://doi.org/10.1016/j.asr.2016.11.030.

[231] E. Schneider and A. Stilp. “Meteoroid/debris simulation at Ernst-Mach-Institut(EMI)- Experimental methods and recent results”. In: *Proceedings of the First European Conference on Space Debris, Darmstadt, Germany*. 1993, pp. 401–404.

[232] A. F. Cheng, A. M. Stickle, E. G. Fahnestock, E. Dotto, V. Della Corte, N. L. Chabot, and A. S. Rivkin. “DART mission determination of momentum transfer: Model of ejecta plume observations”. In: *Icarus* 352 (2020), p. 113989. ISSN: 0019-1035. DOI: https://doi.org/10.1016/j.icarus.2020.113989.

[233] J. D. Walker and S. Chocron. “Momentum enhancement in hypervelocity impact”. In: *International Journal of Impact Engineering* 38.6 (2011). Hypervelocity Impact selected papers from the 2010 Symposium, A1–A7. ISSN: 0734-743X. DOI: https://doi.org/10.1016/j.ijimpeng.2010.10.026.

[234] W. Alexander and J. McDonnell. “Hypervelocity impact on the GIOTTO Halley Mission dust shield: Momentum exchange and measurement”. In: *Advances in Space Research* 2.12 (1982), pp. 185–187. ISSN: 0273-1177. DOI: https://doi.org/10.1016/0273-1177(82)90305-2.

[235] M. Ikeda, M. Tanaka, D. Yokoo, T. Koura, and Y. Akahoshi. “Study of the Effects of Projectile Shape in the Asteroid Orbit Change by Spacecraft Impact”. In: *Procedia Engineering* 204 (2017). 14th Hypervelocity Impact Symposium 2017, HVIS2017, 24-28 April 2017, Canterbury, Kent, UK, pp. 138–145. ISSN: 1877-7058. DOI: https://doi.org/10.1016/j.proeng.2017.09.766.

[236] K. Hayashi, M. Nishida, H. Kurosaki, and T. Yanagisawa. “Measurement of Momentum to Move with Hypervelocity Impacts of Projectile”. In: *TRANSACTIONS OF THE JAPAN SOCIETY FOR AERONAUTICAL AND SPACE SCIENCES, AEROSPACE TECHNOLOGY JAPAN* 17.4 (2019), pp. 427–431.

[237] C. Nysmith and B. P. Denardo. *Experimental investigation of the momentum transfer associated with impact into thin aluminium targets*. National Aeronautics and Space Administration, 1969.

[238] W. P. Schonberg. “A comparison of fragmentation models”. In: *International Journal of Impact Engineering* 17.4 (1995). Hypervelocity Impact Proceedings of the 1994 Symposium, pp. 739–750. ISSN: 0734-743X. DOI: https://doi.org/10.1016/0734-743X(95)99896-Y.

[239] T. McDonnell, N. McBride, S. F. Green, P. R. Ratcliff, D. J. Gardner, and A. D. Griffiths. “Near Earth Environment”. In: *Interplanetary Dust*. Ed. by E. Grün, B. Å. S. Gustafson, S. Dermott, and H. Fechtig. Berlin, Heidelberg: Springer Berlin Heidelberg, 2001, pp. 163–231. ISBN: 978-3-642-56428-4. DOI: 10.1007/978-3-642-56428-4_4.

[240] J. McDonnell, E. Grün, G. Evans, J. Firth, W. Carey, H. Kuczera, W. Alexander, D. Clark, R. Grard, and M. Hanner. “A dust impact detection system for the Giotto Halley Mission”. In: *ESA Scientific and Experimental Aspects of the Giotto Mission* (1981), pp. 61–75.

[241] R. Tennyson and C. Lamontagne. “Hypervelocity impact damage to composites”. In: *Composites Part A: Applied Science and Manufacturing* 31.8 (2000), pp. 785–794. ISSN: 1359-835X. DOI: https://doi.org/10.1016/S1359-835X(00)00029-4.

[242] E. Giannaros, A. Kotzakolios, S. Tsantzalis, V. Kostopoulos, and G. Campoli. “Numerical Simulation of Composite Deployable Boom Response Subjected to Hypervelocity Impact”. In: *European Conference on Spacecraft Structures, Materials and Environmental*. 2018.

[243] M. Hosseini and H. Abbas. “Growth of hole in thin plates under hypervelocity impact of spherical projectiles”. In: *Thin-Walled Structures* 44.9 (2006), pp. 1006–1016. ISSN: 0263-8231. DOI: https://doi.org/10.1016/j.tws.2006.08.024.

[244] D. Gardner, J. McDonnell, and I. Collier. “Hole growth characterisation for hypervelocity impacts in thin targets”. In: *International Journal of Impact Engineering* 19.7 (1997), pp. 589–602. ISSN: 0734-743X. DOI: https://doi.org/10.1016/S0734-743X(96)00047-4.

[245] S. A. Hill. “Determination of an empirical model for the prediction of penetration hole diameter in thin plates from hypervelocity impact”. In: *International Journal of Impact Engineering* 30.3 (2004), pp. 303–321. ISSN: 0734-743X. DOI: https://doi.org/10.1016/S0734-743X(03)00079-4.

[246] M. Hosseini, H. Abbas, and N. Gupta. “Growth of hole in thin plates under hypervelocity impact of cylindrical projectiles”. In: *Proceedings of the IMPLAST Conference*. 2010, pp. 12–14.

[247] L. J. De Chant. “An explanation for the minimal effect of body curvature on hypervelocity penetration hole formation”. In: *International Journal of Solids and Structures* 41.15 (2004), pp. 4163–4177. ISSN: 0020-7683. DOI: https://doi.org/10.1016/j.ijsolstr.2004.02.053.

[248] K. Dhote and P. Verma. “Investigation of hole formation by steel sphere impacting on thin plate at hypervelocity”. In: *Thin-Walled Structures* 126 (2018). Special Issue on Plasticity and Impact Mechanics (IMPLAST 2016), pp. 38–47. ISSN: 0263-8231. DOI: https://doi.org/10.1016/j.tws.2017.05.012.

[249] D. Dirkx, M. Fayolle, G. Garrett, M. Avillez, K. Cowan, S. Cowan, J. Encarnacao, C. F. Lombrana, J. Gaffarel, J. Hener, et al. “the open-source astrodynamics tudatpy software–overview for planetary mission design and science analysis”. In: *Europlanet Science Congress 2022*. 2022. DOI: https://doi.org/10.5194/epsc2022-253,2022.

[250] K. F. Wakker. *Fundamentals of Astrodynamics*. TU Delft Library, 2015.

[251] E. Mooij. *The motion of a vehicle in a planetary atmosphere*. Tech. rep. Delft University of Technology, 1994.

[252] S. Casotto. “The equations of relative motion in the orbital reference frame”. In: *Celestial Mechanics and Dynamical Astronomy* 124.3 (2016), pp. 215–234. DOI: 10.1007/s10569-015-9660-1.

[253] K. R. Pollock. “An analysis of orbital propagators for low earth orbit rendezvous”. MA thesis. Naval Postgraduate School, 1994.

[254] G. Xu and J. Xu. “On the singularity problem in orbital mechanics”. In: *Monthly Notices of the Royal Astronomical Society* 429.2 (Dec. 2012), pp. 1139–1148. ISSN: 0035-8711. DOI: 10.1093/mnras/sts403.

[255] J. T. Betts. “Optimal interplanetary orbit transfers by direct transcription”. In: *Journal of the Astronautical Sciences* 42.3 (1994), pp. 247–268.

[256] D. Dirkx. *Tudat mathematical model definition*. Tech. rep. Delft University of Technology, 2022.

[257] H. Schaub. “Attitude Dynamics Fundamentals”. In: *Encyclopedia of Aerospace Engineering*. John Wiley & Sons, Ltd, 2010. ISBN: 9780470686652. DOI: https://doi.org/10.1002/9780470686652.eae295.

[258] M. J. Sidi. *Spacecraft dynamics and control: a practical engineering approach*. Vol. 7. Cambridge university press, 1997.

[259] M. Paluszek. “Chapter 8 - Disturbances”. In: *ADCS - Spacecraft Attitude Determination and Control*. Ed. by M. Paluszek. Elsevier, 2023, pp. 117–145. ISBN: 978-0-323-99915-1. DOI: https://doi.org/10.1016/B978-0-32-399915-1.00019-X.

[260] O. Montenbruck, E. Gill, and F. Lutze. *Satellite orbits: models, methods, and applications*. Springer-Verlag, 2002.

[261] C. M. Roithmayr. “Contributions of Spherical Harmonics to Gravitational Moment”. In: *AIAA Journal* 57.10 (2019), pp. 4291–4299. DOI: 10.2514/1.J057227.

[262] D. King-Hele. *Theory of satellite orbits in an atmosphere*. London (Butterworths Mathematical Texts), 1964.

[263] D. Weidner, C. Hasseltine, R. Smith, and S. Mills. *Models of Earth’s Atmosphere (120 to 1000 km)*. Tech. rep. National Aeronautics and Space Administration, 1969.

[264] E. B. Shanks. “Solutions of differential equations by evaluations of functions”. In: *Mathematics of Computation* 20.93 (1966), pp. 21–38.

[265] W. H. Press, W. T. Vetterling, S. A. Teukolsky, and B. P. Flannery. *Numerical recipes*. Cambridge University Press, London, England, 1988.

[266] P. Deuflhard and F. Bornemann. *Scientific computing with ordinary differential equations*. Vol. 42. Springer Science & Business Media, 2012.

[267] B. Das and D. Chakrabarty. “Lagrange’s interpolation formula: representation of numerical data by a polynomial curve”. In: *International Journal of Mathematics Trends and Technology-IJMTT* 34 (2016).

[268] C. Runge et al. “Über empirische Funktionen und die Interpolation zwischen äquidistanten Ordinaten”. In: *Zeitschrift für Mathematik und Physik* 46.224-243 (1901), p. 20.

[269] P. Virtanen et al. “SciPy 1.0: Fundamental Algorithms for Scientific Computing in Python”. In: *Nature Methods* 17 (2020), pp. 261–272. DOI: 10.1038/s41592-019-0686-2.

[270] M. Choi and C. J. Damaren. “Control Allocation of Solar Sail Tip Vanes with Two Degrees of Freedom”. In: *Journal of Guidance, Control, and Dynamics* 39.8 (2016), pp. 1857–1865. DOI: 10.2514/1.G001703.

[271] F. Aghili. “Optimal control of a space manipulator for detumbling of a target satellite”. In: *2009 IEEE International Conference on Robotics and Automation*. 2009, pp. 3019–3024. DOI: 10.1109/ROBOT.2009.5152235.

A

Software Verification

This appendix provides key aspects of the verification process of the software developed for the thesis. For brevity, this chapter focuses on system-level tests, although numerous unit-level tests were performed throughout the project and any identified deficiencies have been corrected. Unit-tests of key functionalities of the software are also briefly mentioned, such as the self-shadowing constraint and the optical reflection law. It is noted that the TU Delft Astrodynamics Toolbox (TUDAT) used as the backbone of this research has been fully verified and has a history of being used by students and researchers in astrodynamics research, meaning that its verification has not been necessary. Therefore, the orbital and attitude propagators, integrators, interpolators, and so on, used in this work have not been unit-tested individually, but system- and acceptance-level tests were performed to ensure that these tools were used appropriately.

No validation of the code could be performed, as the attitude control system considered in this thesis has never been flown before, and no reliable dataset on the attitude dynamics of solar-sails could be accessed.

A.1. Unit-Level Tests

Among the many unit tests performed to verify the code functionalities, two are highlighted below. The verification of the new reflection law implemented in the C++ libraries of TUDAT is described in Section A.1.1, and the verification of the novel self-shadowing constraint developed in this thesis is discussed in Section A.1.2.

A.1.1. Reflectance Model

The reflectance model given in Eq. (3.16) was implemented in TUDAT and exposed to TUDATpy for this thesis. A thorough verification of the reflection law was performed by considering a single panel with different orientations at different points in a heliocentric orbit with an isotropic point source model for the Sun, and comparing the obtained values with ones computed manually. Once the new functionality was completely integrated, a regression test was performed by running all the tests of the TUDAT libraries to ensure that the addition of the new reflection law did not impair the functionality of other parts of the program.

A.1.2. Self-shadowing Constraint

The self-shadowing constraint described in the paper was tested comparing the output of the algorithm, which specifies where a vane is inside the shadow of the sailcraft or casts shadow on it, through visualisation checks. The convex hull of the infinite parallelepiped created by the sailcraft surface and the local sunlight direction was displayed with the position of the nodes of the meshed sides of vane 1. Twenty vane orientation for various Sun cone- and clock-angles were considered, permitting to conclude that the self-shadowing constraint functions as expected.

A.2. System-Level Tests

A number of system-level tests were performed on different aspects of the software to ensure that it works correctly. Particularly, Section A.2.1 considers the entire the attitude segment of the software, Section A.2.2 examines the attainable moment set computation, Section A.2.3 considers the complete vane system

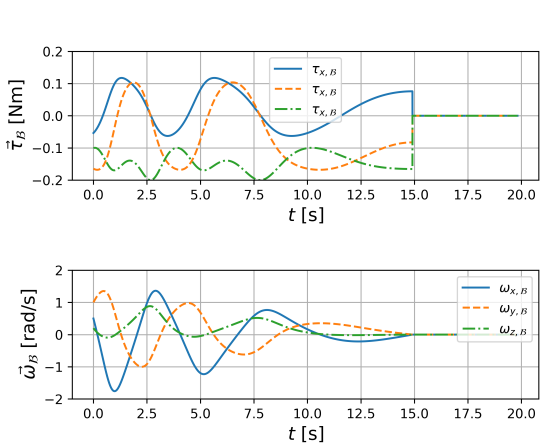

(a) Software developed in this thesis.

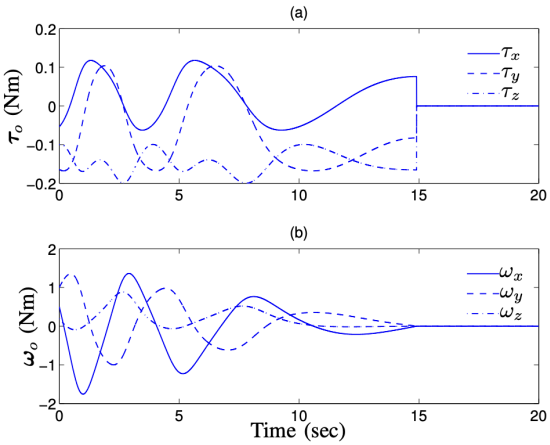

(b) Example from Aghili [271].

Figure A.1: Detumbling manoeuvre of a spacecraft with the inertia tensor from Eq. (A.1) and initial rotational velocity of Eq. (A.2).

controller segment of the software, and subsections A.2.4 and A.2.5 consider the link between the SRP force and torque and the attitude and orbital dynamics.

A.2.1. Time-Optimal Detumbling Torque

The time-optimal detumbling manoeuvre presented by Aghili [271] is reproduced to verify the implementation of the optimal torque direction, and ensure that the attitude dynamics behave as expected. The detumbling torque is imposed through the custom torque interface in TUDATpy, meaning that it is not directly generated by the vanes, but is applied directly to the spacecraft. Considering a three-axis (in the body-fixed frame) initial rotational velocity, this test then permits to verify the complete attitude dynamics part of the software. The case described by Aghili [271] is given as follows,

$$\boldsymbol{I}_{\mathcal{B}} = \begin{bmatrix} 1 & 0.5 & -1 \\ 0.5 & 2 & 1 \\ -1 & 1 & 5 \end{bmatrix}, \qquad \text{(A.1)} \qquad \boldsymbol{\omega}_{0,\mathcal{B}} = \begin{bmatrix} 0.5 \\ 1.0 \\ 0.2 \end{bmatrix} \text{ rad/s}, \qquad \text{(A.2)}$$

with a maximum detumbling torque magnitude of 0.2 Nm. Figure A.1 gives the detumbling torque and rotational velocity of the spacecraft as a function of time, from the software developed in this thesis (Figure A.1a) and the study from Aghili [271] (Figure A.1b). From these figures, it appears that the detumbling torque and attitude dynamics match very closely.

A.2.2. Attainable Moment Set Computation

The derivation of the 2-DoF Attainable Moment Set (AMS) of the vanes of the system is a key part of the torque allocation algorithm of the vane system controller. The overall concept of the method was first presented by Choi and Damaren [270], which provides a number of graphs of the construction of the AMS. Figure A.2 provides the AMS obtained in this thesis for the single-ideal SRP model with $\alpha_{s,\mathcal{B}} = 0°$ and $\beta_{s,\mathcal{B}} = 0°$, and the final graph from Choi and Damaren [270]. The linestyles of the different ellipses match between the figures, such that the convex hull (Vane 1 convex Hull), the fitted ellipse (Vane 1 Ellipse Fitz.), the optimised ellipse (Vane 1 Ellipse Interior), and the Fourier ellipse (Vane 1 F.Series Ellipse) of the AMS are given. In both figures, the torque achievable by vane 1 is non-dimensionalised, but Choi and Damaren [270] also normalized it such that the torques considered remain between -1 and 1. This explains the factor 2 difference between Figures A.2a and A.2b. Nevertheless, it appears from these figures that the constructed ellipses match closely. Combined with the unit tests performed for each element of the construction of the Fourier ellipse, Figure A.2 confirms that the AMS derived is correct.

Furthermore, a novel 1-DoF AMS formulation was derived in this work, and could not be compared to previous literature. Therefore, the cubic splines representing the 1-DoF AMS of vane 1 for both a rotational degree of freedom around $X_{\mathcal{V}_1}$ and $Y_{\mathcal{V}_1}$, were compared to 1,000 numerical points belonging to the AMS,

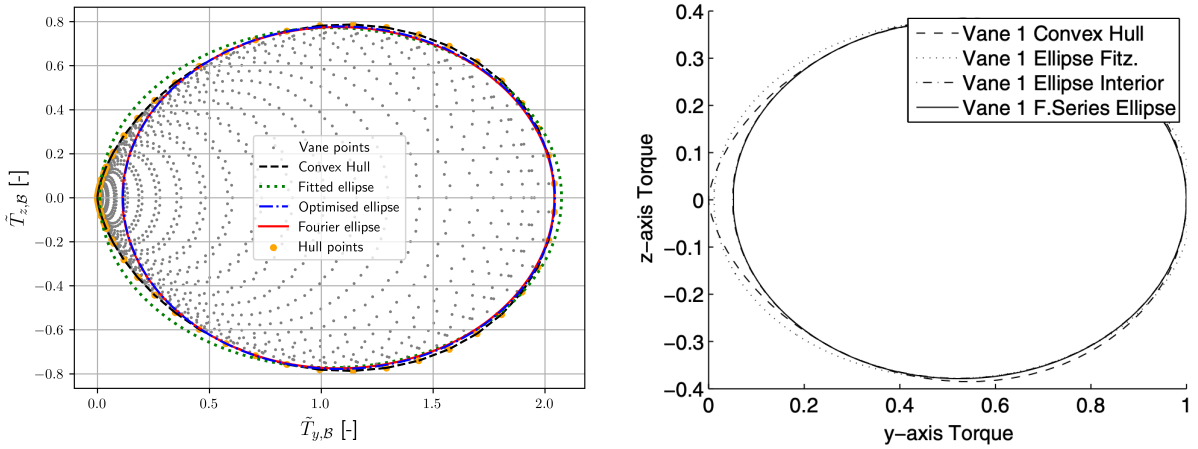

(a) AMS for vane 1 in this thesis.

(b) AMS representation in [270].

Figure A.2: Attainable moment set shape for the SI-SRP model and $(\alpha_{s,\mathcal{B}}, \beta_{s,\mathcal{B}}) = (0, 0)$ from this work and from Choi and Damaren [270].

Table A.1: Expected and numerical SRP acceleration and torque for the SI-SRP model.

Variable	Expected value	Numerical value
Sail SRP acceleration [m/s/s]	5.36959e-5	5.369934e-5
Vane SRP torque [Nm]	6.851043e-6	6.851664e-6

showing a good match between the two.

A.2.3. Complete Vane System Controller

A test of the complete vane system controller was performed by requesting the eight vane angles solution; two angles per vane in the 2-DoF case, for a desired torque of $\boldsymbol{T}_{\mathcal{B}} = [10; 10; 10]$ Nm. This torque lies outside the capabilities of the vane system, meaning that it is automatically scaled down such that the resultant torque direction is conserved. This property was indeed observed. Figure A.3 gives the numerical AMS of vane 4 for $\alpha_{s,\mathcal{B}} = 75°$ and $\beta_{s,\mathcal{B}} = 45°$ for two configurations: all vanes have two rotational DoFs (Figure A.3a) and all vanes have 2 rotational DoFs except vane 4 which can rotate only around its $X_{\mathcal{V}_4}$ axis (Figure A.3b). In these figures, the orange line is the AMS of the vane if it only has a DoF around $X_{\mathcal{V}_4}$, the blue line is the AMS of the vane if it only has a DoF around $Y_{\mathcal{V}_4}$, and the green triangle is the AMS of the vane if it has no degrees of freedom. Additionally, the blue triangle gives the torque allocated to the vane by the torque allocation algorithm, and the orange triangle gives the torque resulting from the selected vane angles. In both these figures, it can be observed that the torque allocated to the vane is inside its AMS. The torque solution in Figure A.3a lies on the ellipse boundary, which shows that the requested torque was scaled down only as much as necessary, and the solution lies on the $X_{\mathcal{V}_4}$ AMS in Figure A.3b. Furthermore, it can be observed that the torques resulting from the torque and vane angle allocation algorithms match very closely, meaning that the vane angle allocation algorithm performs well. Similar plots were also obtained for the other vanes, showing no deficiencies compared to the expected behaviour.

This test was performed for different sunlight cone- and clock-angles and desired torques inside and outside the capabilities of the system, and resulted in the expected behaviour consistently. Combined with the time-optimal detumbling torque test from Section A.2.1 and underlying unit tests, this confirms that the vane system controller functions as intended.

A.2.4. SRP Effect on Attitude Dynamics

A test was set up to verify the interface between the SRP torque (and force) and the attitude dynamics. The sailcraft model from the paper is used, and is initially Sun-pointing in a circular orbit at 1,000 km

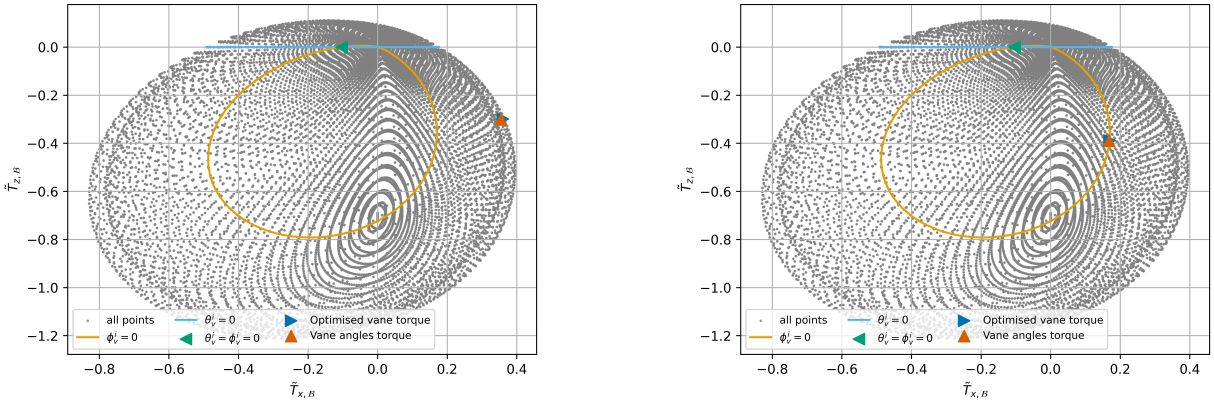

(a) Vane 4 torque with 2-DoF.

(b) Vane 4 torque with $X_{\mathcal{V}_4}$-DoF only.

Figure A.3: Numerical AMS of vane 4 for $\alpha_{s,\mathcal{B}} = 75°$ and $\beta_{s,\mathcal{B}} = 45°$.

altitude with an inclination of 60°. Additionally, the sailcraft follows the single-sided SRP reflectance model, and has a single vane positioned at the tip of its positive $Y_{\mathcal{B}}$-axis, resulting in a moment arm of 7.17 m (including the centroid of the vane). This configuration permits to verify that a torque is generated around the $X_{\mathcal{B}}$-axis (negatively), along which the sail starts tumbling.

Table A.1 gives the expected and numerical SRP force and torque acting on the sail at the start of the propagation, when the sailcraft is in a Sun-pointing orientation. This expected values were obtained from Equation 3.16 adapted for the SI-SRP model and with a solar irradiance of 1323.7 W/m^2. The solar irradiance value used was approximated as it could not be directly extracted from the numerical simulation. Nevertheless, the expected and numerical values are very close to each other in both cases.

Figure A.4 gives the $X_{\mathcal{B}}$ rotational velocity component evolution as a function, as a result of the torque on the single vane of the system considered. From this figure, it appears that the rotational velocity magnitude keeps increasing, as expected. The steady rotational velocity increase is a result of the SI-SRP reflectance model. As the vane is reflective on one of its sides only, the torque exerted on the vane is always in the same direction in the body-fixed frame, and is not counter-acted by the back side of the vane on the other side of the self-rotation. The increase found is also consistent with the torque magnitude from Table A.1. Similar studies were performed for the other torque components, yielding results which are consistent with the expectations.

At last, Figure A.5 gives the magnitude of the SRP acceleration acting on the sailcraft as a function of time and resulting from the induced rotational motion. In this figure, it can be observed that the SRP acceleration oscillates between its maximum value (Sun-pointing orientation) and zero, as it rotates around its $X_{\mathcal{B}}$-axis. This is expected, as through one self-rotate, the sailcraft goes from a Sun-pointing orientation to an edge-on orientation periodically. Additionally, the rate of the oscillations increases as the rotational velocity increases (see Figure A.4), as expected.

Overall, the results obtained for this test match the expectations, meaning that the interface between the SRP effects and the attitude dynamics functions as intended.

A.2.5. SRP Effect on Orbital Dynamics

It remains to verify that the SRP acceleration has the correct effect on the sail orbital dynamics. In this test, the sailcraft model from the paper is used, and is initially Sun-pointing in a circular orbit at 42,300 km altitude with an inclination of 0°. The Sun-line lies in the orbital plane of the sailcraft. Additionally, the sailcraft follows the single-sided SRP reflectance model, but has no vane. This means that no torque is acting on the spacecraft throughout this test case. Moreover, as the spacecraft is at very high altitudes, it does not experience any eclipse time. Note that no plane changes were observed throughout this test.

Figure A.6 gives the evolution of the orbit semi-major axis and eccentricity as a function of time. From Figure A.6a, it appears that the semi-major axis evolution is periodic, with an amplitude of 42.117 km. The value of this amplitude can be verified with [91],

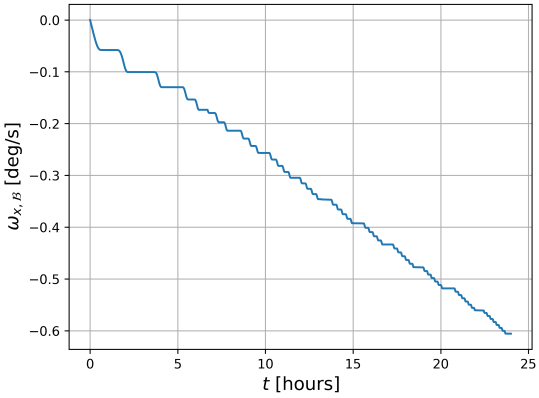

Figure A.4: $X_{\mathcal{B}}$ component of the rotational velocity vector as a function of time.

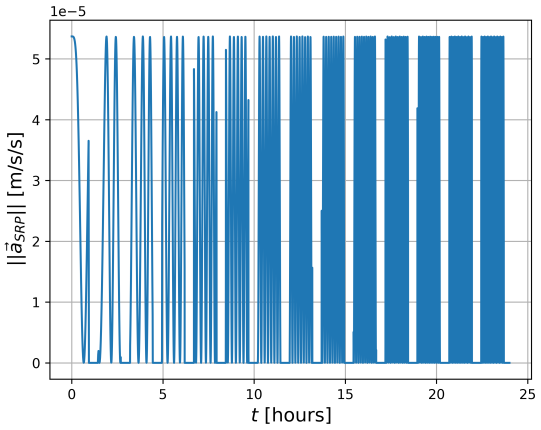

Figure A.5: SRP acceleration as a function of time.

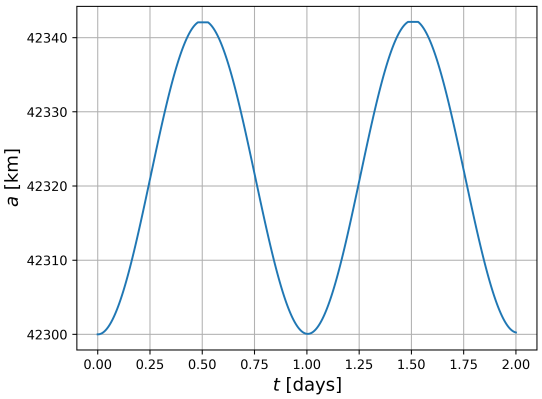

(a) Semi-major axis.

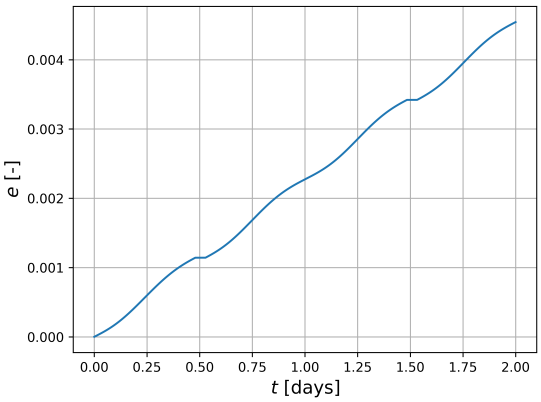

(b) Eccentricity.

Figure A.6: Semi-major axis and eccentricity evolution as a function of time.

$$\Delta a = \frac{4a_0}{\mu_{\oplus}} a^3, \tag{A.3}$$

which provides the maximum achievable semi-major axis increase during half of an orbit by a continuously Sun-pointing solar-sail in Earth orbit. Note, however, that the spacecraft considered here is not continuously pointing towards the Sun as it is inertially non-rotating with an initially Sun-pointing attitude. In Eq. (A.3), Δa is the change in semi-major axis through the half-orbit. For the case considered, Δa should give a good approximate of the amplitude of the oscillation in Figure A.6a. For this test case, Eq. (A.3) yields 42.243 km (using the numerical SRP acceleration from Table A.1), which is within 0.2% of the numerical value obtained. Deviations from this idealistic value can be the result of the changing SRP acceleration due to the rotation of the Sun-line at a rate of 0.986° per day, variations in the solar-irradiance experienced by the spacecraft throughout the orbit (assumed constant by McInnes [91]), and the time-varying eccentricity ($e = 0$ is assumed by McInnes [91]). Nevertheless, the analytical and numerical values are very close to each other.

Conversely, Figure A.6b shows a secular evolution of the eccentricity as a function of time. This behaviour is expected as the SRP acceleration acts to stretch the orbit along the Sun-line. When the spacecraft is the closest to the Sun, the SRP acceleration pushes the spacecraft towards the Earth. In contrast, when the spacecraft is the furthest away from the Sun (other side of the Earth), the SRP acceleration pushes the spacecraft away from the Earth. This means that the orbital eccentricity will

increase.

Overall, the observed effects of SRP on the orbital dynamics are consistent with the expectations.

B

Project Management

This appendix provides the final Work Breakdown Structure and Gantt Chart of the project.

The main work packages which need to be completed throughout the thesis to answer the research questions defined in Section 2.4 have been divided in five categories, as shown in the WBS in Figure B.1. The overall approach to complete the research objective consists in setting up a numerical simulation propagating the sailcraft attitude and trajectory as a result of a hypervelocity impact, and analysing different configurations.

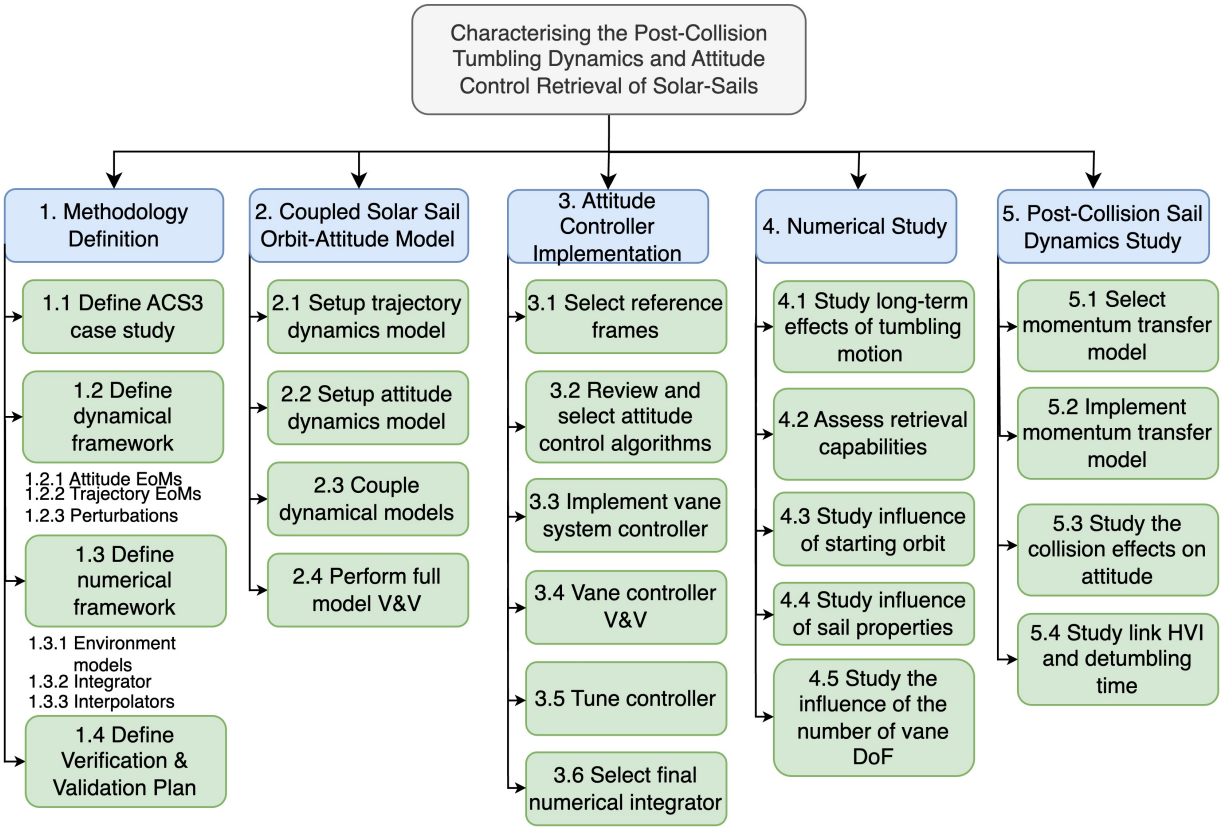

Figure B.1: Work Breakdown Structure of the work packages completed throughout the thesis.

The timeline of the project, reflecting the order in which each work package presented in the previous section will be tackled, is shown on the following page.

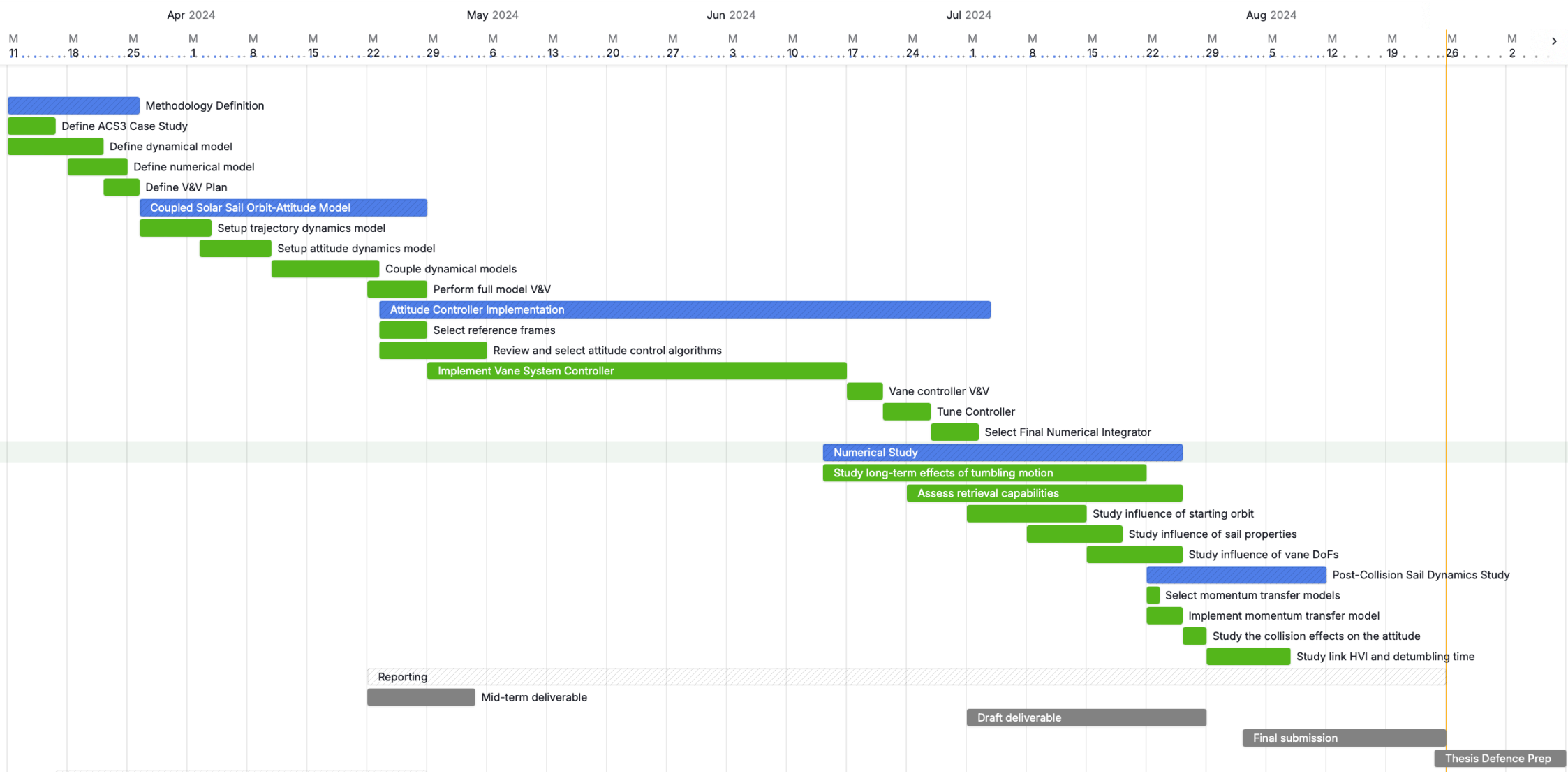
Apr 2024
May 2024
Jun 2024
Jul 2024
Aug 2024
M 11
M 18
M 25
M 1
M 8
M 15
M 22
M 29
M 6
M 13
M 20
M 27
M 3
M 10
M 17
M 24
M 1
M 8
M 15
M 22
M 29
M 5
M 12
M 19
M 26
M 2
Methodology Definition
Define ACS3 Case Study
Define dynamical model
Define numerical model
Define V&V Plan
Coupled Solar Sail Orbit-Attitude Model
Setup trajectory dynamics model
Setup attitude dynamics model
Couple dynamical models
Perform full model V&V
Attitude Controller Implementation
Select reference frames
Review and select attitude control algorithms
Implement Vane System Controller
Vane controller V&V
Tune Controller
Select Final Numerical Integrator
Numerical Study
Study long-term effects of tumbling motion
Assess retrieval capabilities
Study influence of starting orbit
Study influence of sail properties
Study influence of vane DoFs
Post-Collision Sail Dynamics Study
Select momentum transfer models
Implement momentum transfer model
Study the collision effects on the attitude
Study link HVI and detumbling time
Reporting
Mid-term deliverable
Draft deliverable
Final submission
Thesis Defence Prep